The Properties and Origins of Spiral Structure across the Galaxy Population

Ross Edward Hart

University of Nottingham
UK | CHINA | MALAYSIA

Thesis submitted to the University of Nottingham
for the degree of Doctor of Philosophy, March 2018

"I heard someone say 'I can't wait until I can finally say I've made it'. The day you think you've 'made it' is the day you begin your decline."

– J. J. Watt

Supervisor:	Dr. Steven Bamford
Examiners:	Dr. Victor Debattista (University of Central Lancashire) Prof. Alfonso Aragón-Salamanca (University of Nottingham)
Submitted:	23 March 2018
Examined:	20 April 2018
Final version:	4 May 2018

Abstract

Spiral galaxies are the most numerous type of massive galaxy in the low-redshift Universe. There have been a number of mechanisms proposed for their origin, including global density waves and swing amplified arms growing around local density perturbations. In order to understand the origin of arms fully, one requires a detailed study of all types of spiral structure. This thesis examines the global properties of the spiral galaxy population in large, complete samples of low-redshift galaxies. We utilise data from Galaxy Zoo, which provides visual classifications for a flux-limited sample of Sloan Digital Sky Survey (SDSS) galaxies, complete for $m_r \leq 17.0$.

In order to study galaxy morphology, we developed techniques to measure the two fundamental properties to fully describe spiral arms: the arm number and pitch angle (how tightly wound the arms are). Accurate arm number measurements were obtained from the Galaxy Zoo 2 dataset. This required the development of a new method to remove the effect of redshift-dependent classification bias, an effect that galaxies viewed from further away have more difficult to distinguish features. To measure pitch angles, we used a tool called SPARCFIRE. This automatically detects spiral arms in input images, and measures a number of properties of the detected arms, including pitch angles. Accurately measuring pitch angles required the use of a machine learning algorithm trained on a subset of images checked by human inspection. Our method achieves a completeness of 75 per cent and contamination of 19 per cent in detecting real spiral arms in images.

Using these data, the demographics of spiral galaxies with different spiral arm numbers are compared. It is found that whilst all spiral galaxies occupy similar ranges of stellar mass and environment, many-armed galaxies display much bluer colours than their two-armed counterparts. I also combined UV and mid-IR photometry from GALEX and WISE to measure the rates and relative fractions of obscured and unobscured star formation in a sample of low-redshift SDSS spirals. Total star formation rate has little dependence on spiral arm multiplicity, but two-armed spirals convert their gas to stars more efficiently. I find significant differences in the fraction of obscured star formation: an additional ~ 10 per cent of star formation in two-armed galaxies is identified via mid-IR dust emission, compared to that in many-armed galaxies. The latter are also significantly offset below the IRX-β relation for low-redshift star forming galaxies. I present several explanations for these differences versus arm number: variations in the spatial distribution, sizes or clearing timescales of star forming regions (i.e., molecular clouds), or contrasting recent star formation histories.

I also compare overall demographics with respect to arm pitch angle. A stellar mass-complete sample of $\sim 6,000$ SDSS spiral galaxies was selected. The star formation properties of galaxies vary significantly with arm number, but not pitch angle. We find that galaxies hosting strong bars have spiral arms substantially $(4-6°)$ looser than un-

barred galaxies. Accounting for this, spiral arms associated with many-arm structures are looser (by 2°) than those in two-arm galaxies. In contrast to this average trend, galaxies with greater bulge-to-total stellar mass ratios display both fewer and looser spiral arms. This effect is primarily driven by the galaxy disc, such that galaxies with more massive discs contain more spiral arms with tighter pitch angles. This implies that galaxy central mass concentration is not the dominant cause of pitch angle and arm number variations between galaxies, which in turn suggests that not all spiral arms are governed by classical density waves or modal theories.

Finally, I confront analytical predictions for swing amplified arms. By using a number of measured properties of galaxies, and scaling relations where there are no direct measurements, I model samples of SDSS and S^{4}G spiral galaxies in terms of their relative halo, bulge and disc mass and size. Using these models, I test predictions of swing amplification theory with respect to directly measured spiral arm numbers from Galaxy Zoo 2. We find that neither a universal cored or cuspy inner dark matter profile can correctly predict observed number of arms in galaxies. However, by invoking a halo contraction/expansion model, a clear bimodality in the spiral galaxy population emerges. Approximately 40 per cent of unbarred spiral galaxies at $z \lesssim 0.1$ and $\mathrm{M}_* \gtrsim 10^{10}\mathrm{M}_\odot$ have spiral arms that can be modelled by swing amplification. This population displays a significant correlation between predicted and observed spiral arm numbers, evidence that they are swing amplified modes. The remainder are dominated by two-arm systems for which the model predicts significantly higher arm numbers. These are likely driven by tidal interactions or other mechanisms.

Acknowledgements

My first and foremost thanks go to my supervisor, Steven. After three and a half years of your diligent tutelage and hard work on both our parts, we seem to have had a few successes! I will always be grateful for your patience, your support, and all of the time and effort you have put in from the very start of my PhD to now (which has been a lot!). Thanks also for all of the drinks you have bought me over the years (which I may pay back one day) and, of course, for teaching me how great Python is.

I would also like to thank all of the members of my collaboration that have made the work in this thesis possible, and for all of the helpful comments which have shaped and improved my papers. Thank you to Becky, Bill, Brooke, Chris, Karen, Kyle, Sandor and the countless other members of Galaxy Zoo – I truly believe you are the best collaboration in astronomy. Thanks for being great scientists, and above all genuinely great people. Thanks for all your support, thanks for making the work in my PhD so easy, and thanks for the awesome week we had at Galaxy Zoo 10. I would also like to acknowledge all of the enthusiastic volunteers out there who have classified our galaxies; this thesis would not have been possible without you.

I have really enjoyed my time in the Nottingham astronomy department, mainly thanks to all of the amazing colleagues I have had the pleasure of spending time with. Thanks to my various office mates over the years – James, Martha, Tom, Ulli, and Simon for making our office a great place to work (and chat when I needed a break). Thanks also goes to Jake, Rachel, Lizzie and Tom my fellow Inflativerse managers over the years. It's been nice to have something non-academic to focus on that took me away from my desk! Genuinely, working with you all has been an enjoyable and rewarding experience, and I hope we have really made a difference in the community through all of our hard work. I would also like to thank Becky and Tom – thank you for your friendship and all your advice (and telling me to take a holiday when I really needed it!). I'd like to give a big thanks to everybody in the department for making this such a fun and enjoyable place to work during my time here.

I would also like to thank my family. Thanks to Mom, Dad and Scott for everything you've given me and teaching me the value of hard work and dedication – I certainly wouldn't have been able to do this PhD without all of your help over the years.

My studies were funded by a studentship from the STFC, for which I am grateful. I have also benefited from two RAS grants to assist with travel to conferences, for which I am also grateful.

Published work

Much of the work presented in this thesis has previously been presented in four papers:

I Hart R. E., Bamford S. P., Willett, K. W., Masters K. L., Cardamone C. N., Lintott C. J., Mackay R. J., Nichol R. C.; Rosslowe C. K., Simmons B. D.; Smethurst R. J., 2016, "Galaxy Zoo: comparing the demographics of spiral arm number and a new method for correcting redshift bias", MNRAS, 461, 3663

II Hart R. E., Bamford S. P., Casteels K. R. V., Kruk S. J., Lintott, C. J., Masters K. L., 2017a, "Galaxy Zoo: star formation versus spiral arm number", MNRAS, 468, 1850

III Hart R. E., Bamford S. P., Hayes W. B., Cardamone C. N., Keel, W. C., Kruk S. J., Lintott C. J., Masters K. L., Simmons B. D., Smethurst R. J., 2017b, "Galaxy Zoo and SpArcFiRe: constraints on spiral arm formation mechanisms from spiral arm number and pitch angles ", MNRAS, 472, 2263

IV Hart R. E., Bamford S. P., Keel W. C., Kruk, S. J., Masters K. L., Simmons B. D., Smethurst R. J., 2018, "Galaxy Zoo: constraining the origin of spiral arms", MNRAS in press

Paper I details the work presented in sections 3.2.1 and 4.1 of this thesis. Paper II describes the work presented in 4.2. Paper III describes the work in sections 3.3, 3.4 and chapter 5. Paper IV describes all of the work presented in chapter 6. The vast majority of the work in this thesis was performed by the author with advice from the co-authors listed above. Material resulting from collaborative work is listed at the beginning of each chapter.

Contents

List of Figures

List of Tables

Chapter 1

Introduction

This thesis primarily studies the visual characteristics of spiral galaxies. With the advent of large surveys in astronomy, morphological galaxy studies have become somewhat challenging. Measuring galaxy colours and luminosities accurately in these surveys is comparatively simple, meaning that studies of galaxy colours vs. other properties are popular. Accurate visual morphologies instead require detailed inspection of galaxy images, which proves to be a time consuming task. Thus, studies of spiral galaxies are usually limited to samples of order ~ 1000 galaxies or less. In order to measure morphologies in large, complete samples, I make use of the visual classifications of Sloan Digital Sky Survey (SDSS;York *et al.* 2000) galaxies using the data collected from Galaxy Zoo (Lintott *et al.*, 2008). This was a citizen science project in which members of the public were asked a number of questions about the physical appearance of low-redshift galaxies, including whether or not they had bars and spiral arms, and how many spiral arms there were. This approach means that we have visual classifications for complete samples of low-redshift galaxies in the SDSS regions.

Galaxy Zoo has already proven to be a valuable resource for understanding the galaxy morphology, with ~ 50 papers published by the collaboration itself, and hundreds of others using its published data for their own studies. The detailed information about spiral arm morphology was, however, an untapped resource at the commencement of the work presented in this thesis. The goal of this thesis is to use these data to investigate spiral galaxies in a more complete, unbiased manner than ever before. The links between visual spiral morphology and global galaxy properties, including stellar mass, star formation rate, colour and environment, are presented for large samples of SDSS galaxies, with particular emphasis on their implications for how spiral arms form.

The relevant background material and motivation for the work in this thesis are summarised in the rest of this chapter. Section 1.1 details a historical overview of morphological galaxy studies. Section 1.2 presents a summary of our current understanding of how spiral arms form and evolve, combining the perspectives from observational data, theory, and simulations. In chapter 2, I present all of the data that is used in this thesis. In chapter 3, details of new statistical techniques are described with the goal of converting raw citizen science data products to clean, unbiased datasets. Chapters 4 and 5 describe how I used these data to study the overall properties of galaxies with respect to two fundamental properties of visually classified spiral structure, arm number (chapter 4) and pitch angle (chapter 5). Chapter 6 describes work confronting direct predictions of swing amplification theory (introduced in section 1.3.2) with our mea-

sured properties of galaxies. Finally, the key conclusions of the thesis in the context of relevant theory, and future work related to the work presented are summarised in chapter 7.

Throughout this thesis, the cosmological parameters are the concordance values of $\Omega_\Lambda = 0.7$, $\Omega_\mathrm{m} = 0.3$ and $H_0 = 70$ kms^{-1}Mpc^{-1} as supported by WMAP and Planck (Spergel *et al.*, 2003; Planck Collaboration *et al.*, 2016). All logarithms are base-10, unless otherwise specified.

1.1 Galaxy morphology

The classification of galaxies into different groups by their appearance is a science older than the firm conclusion that galaxies exist outside our own Milky Way. The existence of 'nebulae' with distinct spiral features dates back to Rosse (1850), where observations of the galaxy M51 were obtained with a 6-foot reflecting telescope. Rosse identified a distinct spiral structure and point sources in M51, shown in Fig. 1.1, indicating that these nebulae were not simply gas clouds. It was not until the 1920s that distances to these nearby nebulae could be accurately measured with Cepheid variables to prove that these objects were galaxies outside of our own (Hubble, 1926a, 1929).

The first comprehensive attempt to organise galaxies by their visual appearance was detailed in Hubble (1936). The Hubble classification scheme broadly separated galaxies by the presence of two components: bars and spiral arms. Early-type galaxies, labelled E0–E7, are typically spheroidal objects. Later type galaxies, labelled as 'S' are instead characterised by the presence of a bulge and disc component. S0 galaxies have discs with no arms, S galaxies have spiral arms and SB galaxies have arms and flat bar features in the centres of galaxies. An entire sample of galaxies can be classified with T-types –5 to 10, with values T < 0 indicating early-type morphology, T $= 0$ indicating S0/lenticular morphology and T > 0 indicating late-type morphology. Spiral galaxies are assigned a T-type between 0 and 10, depending on either the prominence of their bulge and/or how tightly wound the arms are (this is discussed in more detail in section 1.2.2). The Hubble classification scheme with subsequent updates to account for features not observed in Hubble's original work, such as diffuse irregular spiral arms and rings (de Vaucouleurs, 1959, 1963), is still the most commonly applied technique for purely visual classification of galaxies.

The complicating factor for any study of visual morphology concerns the means by which one classifies galaxies. The largest atlases of galaxies have historically relied upon the inspection of galaxy images by individuals or small teams of professional astronomers (e.g. Sandage 1961; de Vaucouleurs *et al.* 1991). However, measurement of morphology is subjective – the classifications of a single object by two individuals can vary by as much as 1–2 Hubble T-types (Naim *et al.*, 1995; Nair & Abraham, 2010). In order to achieve less subjectiveness, more quantitative measures of visual morphology have been sought. In principle there are two ways in which this can be achieved. The first measures a number of statistics on galaxy images (e.g. Lahav *et al.* 1995; Ball *et al.* 2004; Abraham, van den Bergh & Nair 2003; Conselice 2006; Sreejith *et al.* 2018). These techniques use a number of measured parameters including colour, asymmetry and spectral features to group galaxies. These measures cannot, however, give a true sense of the morphology of galaxies, given that there may be unquantifiable biases in these proxies for galaxy morphology (Lintott *et al.*, 2008, 2011). The most notable

Figure 1.1: Sketch of nebula M51. Figure reproduced from *Observations on the Nebulae* (Rosse, 1850).

example is red spirals – elliptical galaxies are generally redder than spirals, so this leads to a mis-classification of a subsample of the red galaxy population as ellipticals, even if they actually show strong spiral features (Masters *et al.*, 2010a). A more promising approach that has been developed in recent years is the use of machine learning based algorithms. These have been shown to be able to recover galaxy morphological information to high accuracies of $\gtrsim 90$ per cent (Dieleman, Willett & Dambre, 2015; Domínguez Sánchez *et al.*, 2017), and unsupervised algorithms even predict the two distinct groups of early and late-type galaxies as devised by Edwin Hubble (Hocking *et al.*, 2018). In order to obtain more detailed classifications and classify more subtle variations between galaxies to, for example, reproduce the Hubble sequence requires supervised learning. However, these classifiers are usually trained on images where there is a clear consensus in morphology; it remains to be seen whether they can also produce accurate classifications for objects where the classification is more uncertain.

1.1.1 Galaxy properties with respect to morphology

The importance of galaxy morphology in the study of galaxy evolution stems from the idea that both secular and environmental processes can change a galaxy's structure (Kormendy & Bender, 2012; Buta, 2013). That galaxy morphology is linked to the physical mechanisms responsible for galaxy evolution dates back to Holmberg (1958), where it was discovered that spiral galaxies are bluer in colour than elliptical galaxies, which was linked to differing rates of star formation and star formation histories (SFHs) in Roberts (1963). Subsequent studies confirm a clear, systematic trend between Hubble type and galaxy colour (Kennicutt, 1983; Romanishin, 1990; Roberts & Haynes, 1994; Blanton & Moustakas, 2009).

More recent surveys show that galaxy colour-magnitude and colour-mass distributions are bimodal, with a red sequence of passive galaxies and a blue cloud of star-forming galaxies (Strateva *et al.*, 2001; Baldry *et al.*, 2004, 2006). The red population is generally more massive, with a clear offset towards the more massive end observed in the galaxy stellar mass function (GSMF) for the red population. Morphologically, a similar trend is observed – early-type galaxies have greater stellar masses than more disc-dominated late-type galaxies (Kelvin *et al.*, 2014a). A clear environmental dependence is also observed with respect to both morphology and colour (Dressler, 1980; Kauff-

mann *et al.*, 2004), indicating that the red population may consist of elliptical galaxies formed by dry mergers (Brinchmann *et al.*, 2004). If one instead considers kinematics, then red galaxies can generally be subdivided into rotationally supported 'fast rotators' and dispersion dominated 'slow rotators' (Emsellem *et al.*, 2007; Cappellari *et al.*, 2007). According to the ATLAS^{3D} project, $\sim 80-90$ per cent of early-type galaxies (defined as galaxies without spiral arms) are fast rotators (Emsellem *et al.*, 2011). The massive end of the red sequence consists of more slow rotators, which can be considered as classical elliptical galaxies. The lower mass end of the red sequence instead consists of a majority of fast rotators – these galaxies must have transitioned from red to blue via processes that have ceased star formation yet kept the rotation of the galaxy intact, and can thus be considered as quenched discs. Additionally, the existence of a passive population of red spirals shows that the morphological transformation of galaxies may take much longer than the processes which cease the star formation and transform galaxies from blue and star-forming to red and passive (Bamford *et al.*, 2009; Masters *et al.*, 2010a).

1.2 Spiral galaxies

Through the fitting of galaxy profiles, it has been shown that galaxies often comprise a rotationally supported, kinematically cool disc and a hotter, pressure supported bulge (e.g. Tabor *et al.* 2017). Rotationally supported discs with in-situ star formation and spiral arms have been observed as far as $z = 2-3$ (Jones *et al.*, 2016; Yuan *et al.*, 2017). Given that the majority of stars in the Universe formed in discs (van der Wel *et al.*, 2014), the role of spiral structure in regulating and arranging star formation is an important question. In this section I outline the origins of discs and spiral arms in galaxies, and outline some of the key influences that spiral arms are predicted to have on their discs.

1.2.1 The growth of discs

Current theory postulates that galaxy formation is hierarchical. The smallest dark matter potential wells formed from density perturbations in the early Universe, and accreted to form the larger structures we see at $z \sim 0$ (White & Rees, 1978). These initial dark matter haloes gain angular momentum via their gravitational interactions with other haloes (Silk, 2003). These haloes then accrete gas, from which stars can begin to form. In high mass galaxies ($\mathrm{M}_* \gtrsim 10^{10}\mathrm{M}_\odot$), smooth 'hot mode' accretion dominates (Fall & Efstathiou, 1980). As gas accretes onto a halo, it is heated by dynamical friction to high enough temperature that it is in dynamical equilibrium with the dark matter. This gas then radiates away its thermal energy, losing its pressure support and settling into a disc. In lower mass galaxies, gas accretion is instead dominated by 'cold mode' accretion along filaments (Binney, 1977; Katz, Quinn & Gelb, 1993; Katz *et al.*, 1994; Kereš *et al.*, 2005), where gas is not heated by friction. Both modes of accretion lead to the formation of a dynamically cool disc from which stars, and subsequently galaxies, form.

Star formation in discs can usually be modelled by two phases. The first is often referred to as a growth phase. The growth phase is characterised by a slowly declining total star formation rate (SFR) in normal star-forming galaxies (Noeske *et al.*, 2007b).

Galaxies generally lie on a well-defined stellar mass-SFR plane, often described as the 'star formation main sequence' (SFMS). The SFR for a given stellar mass falls in the time between $z \approx 1$ and $z \approx 0$. The second phase is a 'quenching' phase, where galaxies experience a decline in star formation, putting them well below the main sequence. The most massive galaxies exhaust their gas supply most quickly (Noeske *et al.*, 2007a; Saintonge *et al.*, 2016), and are therefore more likely to be red, passive galaxies. It is well established that discs have negative colour gradients (Gonzalez-Perez, Castander & Kauffmann, 2011; Kennedy *et al.*, 2016; García-Benito *et al.*, 2017). This leads to a natural conclusion that discs either grow or quench 'inside-out' (i.e. either stars form earlier or star formation ceases earlier at smaller radii). Recent studies show that in order to reproduce the range of observed colour gradients at low-redshift, discs must form via an inside-out mechanism (Lian *et al.*, 2017; Ellison *et al.*, 2018).

During the growth phase, discs are not simply smooth features. The light profile of discs indicate that secular processes alter the shape of discs. Classically, discs were fit with single exponential profiles (de Vaucouleurs, 1959). However, it was soon shown that some discs were not well fit by the single exponential profile, and require inner and outer disc profiles (Freeman, 1970). Therefore, a smoothly varying inside-out mechanism falls short in explaining disc growth. This is evidence that secular processes are at play during a disc's growth phase. Disc profiles can be described as the result of secular processes such as bars and spiral arms causing radial migration of stars (Debattista *et al.*, 2006; Roškar *et al.*, 2008a,b).

With the gas accretion mechanisms discussed above, one might expect star formation to be an efficient process. However, star formation is inefficient, with only ~ 2 per cent of the mass in molecular clouds converted into stars (Evans *et al.*, 2009). Results from the FIRE simulation suggest that feedback from young stars regulates star formation, meaning that the process is relatively inefficient (Hopkins, Quataert & Murray, 2011; Hopkins *et al.*, 2014). It is now well established that galaxy morphology is an important factor in regulating star formation. The broad morphological evolution from late-type disc to early-type spheroid can significantly reduce total SFRs in galaxies (Kawata, Cen & Ho, 2007; Martig *et al.*, 2009, 2013). One reason for this is the effect of shear. Differential rotation acts to shear star-forming features in the disc and effectively stretch them out, which significantly reduces the star formation efficiency. Galaxies with falling rotation curves have high shear, and galaxies with rising rotation curves have low shear. Stable discs have much lower rates of shear than spheroids (Martig *et al.*, 2013), so actively form stars. Another reason why total SFRs typically falls in spheroid-dominated systems is because there is less total molecular gas, which means that the gas density is lower for a given total gas mass (Combes, Young & Bureau, 2007; Krips *et al.*, 2010; Saintonge *et al.*, 2011). Spiral arms also have a significant impact on the regulation of star formation. They are able to grow from gravitationally unstable regions via a swing amplified mechanism (see section 1.3 for detailed discussion about the mechanisms from which arms can form), and would not be present if the rate of shear was too high. The role that arms play in star formation is discussed further in section 1.2.3.

1.2.2 Classifying spiral galaxies

Classic studies of spiral galaxies focused on the link between the galaxy bulge and the spiral arms in the disc. In the Hubble sequence, discs are classified from Sa–Sc (or given a T-type between 0–10) depending on two criteria: the prominence of the bulge and the pitch angle of the spiral arms. A correlation between these two quantities is expected from theory, if one considers the shear in a galaxy disc. If there is a high level of shear, caused by a greater central mass concentration, the spiral arms should be tighter. A strong correlation has been proven between black hole mass and spiral arm pitch angle (Seigar *et al.*, 2006; Davis, Graham & Seigar, 2017; Mutlu-Pakdil *et al.*, 2018), albeit with small samples of nearby spirals with two-arm, grand design structure. There is an established correlation between black hole mass and bulge mass (e.g. Kormendy & Richstone 1995; Ferrarese & Merritt 2000; Gebhardt *et al.* 2000; Häring & Rix 2004). This holds when there is a massive disc present, as the growth of a disc affects both the growth of the central black hole and compresses the bulge, increasing its velocity dispersion (Debattista, Kazantzidis & van den Bosch, 2013). One might therefore expect a strong correlation between bulge-to-total ratio (mass 'concentration') and spiral arm pitch angle. However, if one considers the entire population of spiral galaxies, rather than a small sample of grand design spirals, there is no correlation between the two fundamental quantities underpinning the Hubble classification of spirals (Kennicutt, 1981; Seigar & James, 1998b; Masters *et al.*, in prep).

A more comprehensive spiral galaxy classification was described in Elmegreen & Elmegreen (1982). Unlike the Hubble classification scheme, this scheme is only concerned with the spiral arms in galaxies, rather than any correlations between the spiral arms and other galactic properties. This Elmegreen classification scheme principally groups galaxies into three types: grand design, many-arm and flocculent. Grand design spiral structure is associated with two symmetric spiral arms; multiple-armed structure is associated with more than two spiral arms and flocculent structure describes galaxies with many, shorter, less well-defined arms. The distinct advantage to classifying spiral galaxies in this way is that contrasting physical mechanisms are thought to play a role in the formation of these different types of spiral structure. Grand design spirals are thought to be induced secularly by density waves or the growth of strong bars in galaxy discs (Kormendy & Norman, 1979). They can also be induced via tidal interactions between galaxies (Dobbs *et al.*, 2010). Many-arm structures instead arise readily in simulations, and tend to grow due to more local gravitational processes in discs, such as swing amplification (Carlberg & Freedman, 1985). More details about these mechanisms can be found in section 1.3. The most recent simulations show that flocculent structure may actually be a transient feature of spiral galaxies, with spiral arms continually being made and destroyed (Bottema, 2003; Baba *et al.*, 2009; Grand, Kawata & Cropper, 2012a; Baba, Saitoh & Wada, 2013; D'Onghia, Vogelsberger & Hernquist, 2013), rather than a single, long-lasting structure. Evidence for these differing formation mechanisms came from early observations: grand design spirals are more common in higher density environments where interactions are frequent, and in galaxies with bars (Elmegreen & Elmegreen, 1982; Elmegreen, Elmegreen & Dressler, 1982; Elmegreen & Elmegreen, 1987b). Despite this clear dichotomy between grand design and many-arm/flocculent structures, many-arm galaxies can still exist with bars and in high density environments, and grand design galaxies can exist in low density

environments without bars (Elmegreen & Elmegreen, 1982). A potentially complicating factor is the wavelength of the observation – earlier studies suggested that galaxies with many-arm structures in the younger optical stellar population may be grand design in the near-infrared old stellar population (Block & Wainscoat, 1991; Block *et al.*, 1994; Thornley, 1996). A more recent study of a large sample of galaxies has, however, suggested that this phenomenon is rare (Elmegreen *et al.*, 2011).

1.2.3 Star formation in spiral galaxies

In the low-redshift Universe, overall SFRs follow scaling relations with respect to galaxy stellar mass (Brinchmann *et al.*, 2004; Salim *et al.*, 2007) and gas density (Kennicutt, 1998). The tightness of the relationship between total SFR and stellar mass indicates that the processes responsible for star formation are regulated (Bouché *et al.*, 2010; Lilly *et al.*, 2013; Hopkins *et al.*, 2014), and apply to all galaxies, irrespective of morphology. Further relations between SFR density and gas density within individual galaxies (Kennicutt, 1998; Bigiel *et al.*, 2008; Leroy *et al.*, 2008) and of SFR with total gas mass (Saintonge *et al.*, 2016) indicate that the current SFR of low-redshift galaxies is primarily tied to the availability of gas to form new stars (Saintonge *et al.*, 2013; Genzel *et al.*, 2015), and that star formation efficiency varies little within or between galaxies (Kennicutt, 1998; Saintonge *et al.*, 2011).

In the interstellar medium (ISM) of the Milky Way, a warm ionised medium of hydrogen in the form of ionised hydrogen (HII) and neutral hydrogen (HI) exists. The coldest structures are molecular clouds, from which stars form (Kennicutt & Evans, 2012). These clouds form via self-gravity (Tan, 2000; Kim & Ostriker, 2002; Dobbs, 2008) and cloud-cloud interactions (Casoli & Combes, 1982; Dobbs, 2008). Observations of the Milky Way show that these clouds are highly filamentary, with gravity, turbulence and magnetic fields all playing a role in the formation and suppression of cloud formation (e.g. Padoan *et al.* 2016; Burkhart, Stalpes & Collins 2017). Dense cores exist inside these molecular clouds, the sites of the formation of individual stars (Williams, Blitz & McKee, 2000). Inside these molecular clouds, dust grains grow and attenuate the light from young stars, making the overall spectrum of a galaxy redder. Standard radiative transfer models predict that dust primarily exists in two components – a warm component associated with the HII clouds where stars form, which emit at shorter wavelength (Silva *et al.*, 1998), and a more diffuse component that emits at the longer wavelength, far-infrared end of the spectrum (Charlot & Fall, 2000; Popescu *et al.*, 2000). The existence of both components is required to match both the colour and the total IR (infrared) luminosity in nearby galaxies (Calzetti, Kinney & Storchi-Bergmann, 1994; Tuffs *et al.*, 2004; Wild *et al.*, 2011).

Spiral arms have been associated with star formation since the discovery that the Milky Way's arms have enhanced concentrations of young stars (Morgan, Whitford & Code, 1953). CO cores of mass $\sim 10^7 \mathrm{M}_\odot$ are located in the spiral arms of the Milky Way and nearby galaxies (McGee & Milton, 1964; Grabelsky *et al.*, 1987; Elmegreen & Elmegreen, 1987a; Lada *et al.*, 1988; Pety *et al.*, 2013; Bolatto *et al.*, 2017). Given that molecular gas density and SFR correlate tightly down to sub-kpc scales (Schruba *et al.*, 2010; Onodera *et al.*, 2010; Khoperskov & Vasiliev, 2017), then it follows that spiral arms are the primary sites of star formation in disc galaxies. Calzetti *et al.* (2005) presented maps of dust and star formation features in M51 indicating the young

stars (measured at UV (ultraviolet) wavelength with the GALEX FUV band) and the dust emission (measured in the Spitzer 24μm mid-IR band). Both are tracers of the star formation, and both are primarily located in the spiral arms of M51. The mid-IR emission is strongly associated with the cores of the spiral arms, coincident with the Hα emission, the most direct measure of star formation (Hao *et al.*, 2011; Murphy *et al.*, 2011). The UV emission from young stars free of dust obscuration is also located in the spiral arm regions, albeit at the edge of the arms. Spiral arms are the locations where stars preferentially form in discs, and their inner regions are also locations where the dust opacity is high (Holwerda *et al.*, 2005).

The role that the spiral arms play in the conversion of gas to stars is still unclear. Vogel, Kulkarni & Scoville (1988) and Elmegreen (2002) argue that total SFRs are consistent across the entire population of spirals. This is because the majority of the gas within discs that can turn molecular in shielded regions at low enough pressure already does so, irrespective of whether there are any arms present. Spiral arms cannot enhance the efficiency of formation of molecular clouds, and thus the efficiency of star formation. Star formation can therefore be thought of as saturated (Elmegreen, 2011). Evidence that this is the case can be found from hydrodynamical simulations. The presence of stronger spiral arms increases the frequency of cloud-cloud collisions in galaxies, meaning clouds merge frequently. Without strong spiral arms, clouds tend to condense from gravitational instabilities alone. Strong spiral arms tend to form fewer, larger molecular clouds, without increasing the total SFR in the host galaxy (Dobbs, Burkert & Pringle, 2011; Dobbs, Pringle & Burkert, 2012), in agreement with the picture described in Elmegreen (2011). Preliminary observational evidence that molecular cloud properties vary between galaxies was demonstrated in Hughes *et al.* (2016) – local massive spirals such as M51 have more massive giant molecular clouds (GMCs) than low-mass irregular galaxies. Resolved studies of M51 also show that GMC masses are greater in the centre of spiral arms (Colombo *et al.*, 2014).

The picture becomes more complex when one considers resolved studies of individual arms of nearby galaxies. Weaver (1970) demonstrated that the arms of nearby galaxies are actually irregular structures, with several clumpy spurs. These spurs are usually coincident with extinction features, called feathers (Lynds, 1970; La Vigne, Vogel & Ostriker, 2006), and molecular gas overdensities (Corder *et al.*, 2008). Schinnerer *et al.* (2017) presented a high resolution study of the molecular gas and star formation geometry along a spiral arm of M51, showing the clear presence of spur and feather features. Molecular clouds were more bound, with a higher fraction of the gas in GMCs than in the arm itself, with massive star formation preferentially located in these spurs. This suggests that spiral arms themselves may not be ideal sites for star formation, possibly caused by an increase in the dynamical pressure due to a streaming motion through spiral arms (Meidt *et al.*, 2013). The potential origin of such a streaming motion is discussed in section 1.3.1.

1.3 Spiral theory

There are a number of theories of why spiral arms exist in disc galaxies. Generally, they can be considered as one of two types. The first describes a global phenomenon across the disc of galaxies. This usually predicts a long-lived, symmetric, two-arm mode in the disc, with visible spiral arms being the regions where the density is greatest. These

arms are often referred to as quasi-stationary density waves. The second describes a more bottom-up approach to spiral arm formation. In this scenario, spiral arms grow around any small density enhancements in discs. Discs can display spiral arms of this type for long periods of time, but individual modes are usually of much higher order and more short-lived than those predicted in two arm spirals.

1.3.1 Density wave theory

One theory to explain the presence of spiral arms in galaxies is density wave theory. If spiral arms are material structures, then a problem exists often described as the 'arm winding problem'. Measurements of local disc galaxies such as M31 had already established that the rotation curves of discs were flat (Babcock, 1939). Stars and gas at all radii rotate with similar orbital speeds, $V(r)$, but because stars further from the galactic centre move in larger orbits, they take longer to complete a single rotation. Thus, a material arm will 'wind up' over time, and eventually become indistinguishable from the galaxy disc. Prendergast & Burbidge (1960) explained that one of the following three statements must be untrue: that all material moved on circular orbits in discs; their velocities remain constant over time and that material which starts in a spiral arm remains in that same spiral arm over several rotations. Density wave theory was proposed as a way in which arms could form, by violating the third of the statements in Prendergast & Burbidge (1960). As suggested by Oort (1962), arms are able to be sustained if matter is to be constantly added to their inner edges, and lost from their outer edges.

Density waves can exist in a number of configurations. Density wave-driven spiral arms which evolve over time are often described as kinematic density waves, whereas spiral arms which retain their structure (arm number and pitch angle) over several rotations can be described as quasi-stationary density waves. Density wave theory is rooted in the early works of Bertil Lindblad. His earliest works demonstrated that an oval distortion to a galaxy disc, or an external perturber, causes a disc to grow an inner lens-like structure with density waves extending outwards into the disc (Lindblad, 1927). Lindblad (1963, 1964) demonstrated an N-body model of a flat disc with a long-lived, trailing two-arm system with stars flowing through the spiral arms, as expected from a self-consistent density wave theory.

Quasi-stationary density wave theory reached its maturity in the early 1960s in the publication of Lin & Shu (1964) (meaning it is often referred to as the Lin-Shu hypothesis). This paper has often been described as 'elementary' to understanding spiral structure (Bertin & Lin, 1996; Pasha, 2004). These arms are described as quasi-stationary, as they rotate around the galactic centre and do not wind up over time. Lin & Shu (1964) further demonstrated the existence of long-lived spiral patterns in galaxy discs directly from arguments from fluid dynamics. This paper demonstrated stable two-arm modes in between inner and outer Lindblad resonance radii. An early diagram of a density wave pattern in this region for the Milky Way is shown in Fig. 1.2. If particles are moving on elliptical orbits, then their motion can be described by two parameters. The first is Ω, the frequency of the orbit. Elliptical orbits also mean that the radius to the centre of the system varies. The frequency of these oscillations is denoted with κ. The corotation radius r_c is the radius where the pattern speed of the spiral matches the rotation speed of the galaxy, i.e. $\Omega(r_c) = \Omega_{\rm p}$. The Lindblad resonances occur at the radii

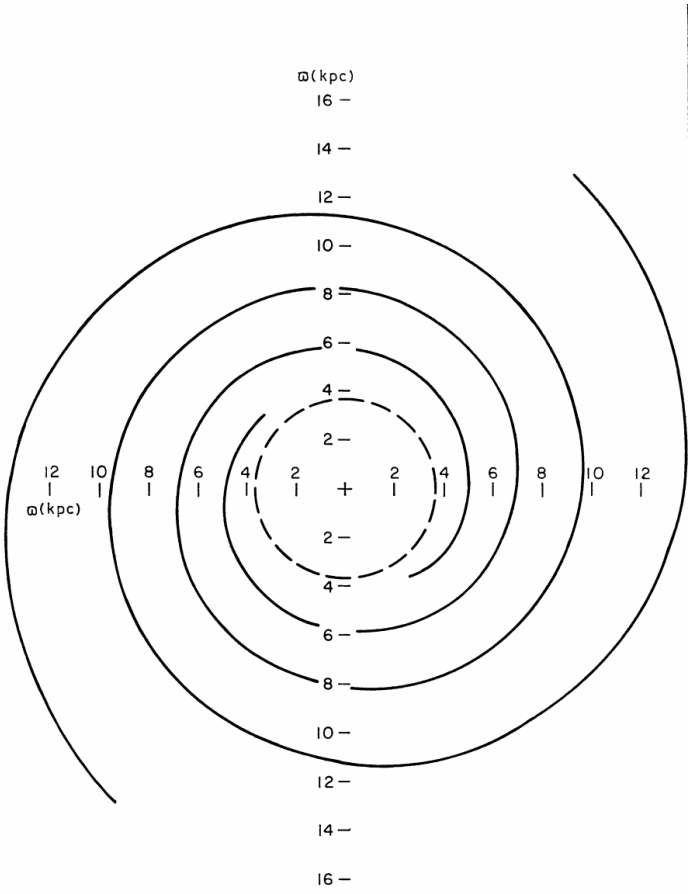

Figure 1.2: Diagram of a density wave pattern for the Galaxy (Lin & Shu, 1967), with the Galaxy's rotation curve measured in Schmidt (1965). The model is a quasi-stationary density wave with $\Omega_{\rm p} = 11$ kms^{-1}kpc^{-1}. The quantity $\tilde{\omega}$ is the radius from the Galactic centre. The inner Lindblad resonance (the radius at which the arms start) is 3.75 kpc.

where $\Omega_{\rm p} = \Omega \pm \frac{\kappa}{2}$.

1.3.2 Swing amplification theory

An altogether different theory to explain the existence of spiral arms in galaxies is swing amplification theory. This differs from density wave theory in that it is principally concerned with local density variations in galaxy discs, rather than the existence of global density wave modes. Swing amplification is a theory via which any instability can grow, so can be considered relevant in all types of spiral galaxy. The key motivation for this alternative to the Lin-Shu hypothesis is the requirement for a theory to explain all of the types of spiral structure in the local Universe, from grand design to many-arm structures (Goldreich & Lynden-Bell, 1965).

Swing amplification predicts that spiral arms start as local material instabilities in discs, but grow to form non-stationary kinematic density waves. Some of the earliest work described in Julian & Toomre (1966) showed that small overdensities could be amplified to form arm-like structures due to self-gravity in the disc. A diagram of a dense spiral arm region growing around a local gravitational instability is shown in Fig. 1.3. A more complete analysis of a rotating disc outlined in Toomre (1981) showed that as

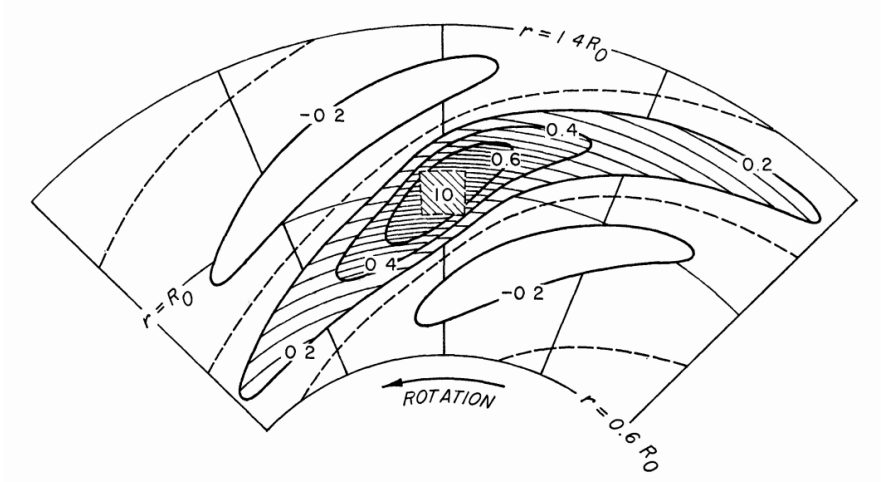

Figure 1.3: Diagram of a spiral arm overdensity caused by swing amplification (Julian & Toomre, 1966). The diagram is for a galaxy with a flat rotation curve ($V_{\rm rot}(r)$ = constant, shear = 1). The contours show lines of equal stellar density.

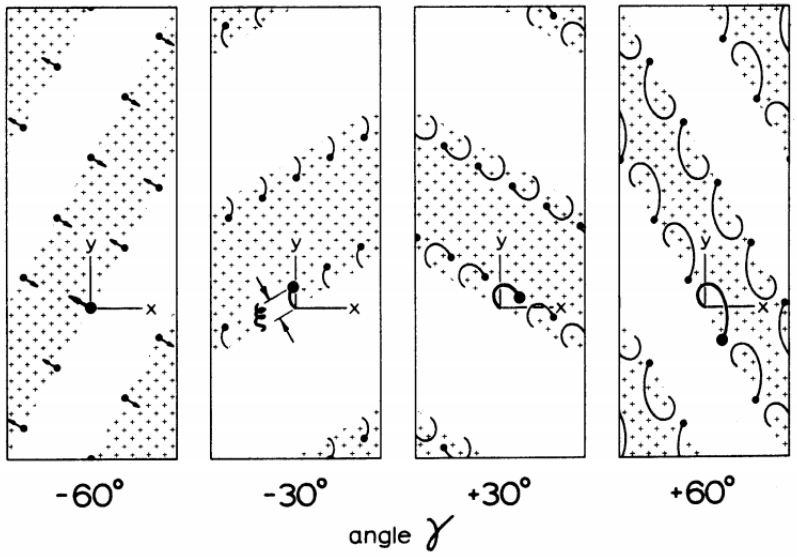

Figure 1.4: Diagram of a swing amplified feature undergoing rotation (Toomre, 1981). The points indicate the positions of stellar particles. The shear of the feature means that star particles linger in small circular orbits, amplifying spiral arms.

the disc rotates, the self-gravity of an enhanced density region causes stars to fall into the dense arm region and stay trapped in there for a 56 per cent longer time period than expected from the linear equations described in Julian & Toomre (1966). The diagram of the 'shearing wavelet' presented in Toomre (1981), which depicts the orbits of stellar particles temporarily trapped by the swing amplification mechanism, is shown in Fig. 1.4. Swing amplification itself is a manifestation of a balance between shear and self gravity. Shear tends to break up the largest structures over time, and can also suppress the formation of molecular clouds (Seigar, 2005): spiral arms form in unstable regions where self gravity dominates, but are eventually broken up by the disc shear. The shear in the galaxy disc causes an initial gravitational instability to form a distinct trailing spiral arm as the disc rotates. Such a phenomenon was predicted in both the gas component (Goldreich & Lynden-Bell, 1965) and the stellar component of discs (Julian & Toomre, 1966).

1.3.3 Tidally induced spiral arms

It may of course be the case that spiral structures do not arise internally in the discs of galaxies; rather, they may be triggered by an outside influence of a companion galaxy. Initial evidence for this was presented in section 1.2.2, that grand design spiral arms are more common in higher density environments where interactions are more frequent. Kendall, Clarke & Kennicutt (2015) showed that the arm vs. inter-arm contrast, or strength of grand design spiral features, is tightly correlated with the tidal forcing from companion galaxies, evidence that galaxy-galaxy interactions may play a role in inducing grand design spiral structure in discs. That interactions between galaxies can alter their morphology is well established. Historically, the presence of tidal bridges and tails between interacting galaxies has been noted (Arp, 1966; Hodge & Merchant, 1966), and recent works statistically confirm that galaxies are more asymmetric when a close companion (projected distance $r_{\rm p} \lesssim 50$ kpc) is present (Ellison *et al.*, 2010; Casteels *et al.*, 2013; Patton *et al.*, 2016; Holincheck *et al.*, 2016). Models of interacting galaxies producing tidal bridges and tails have long been established (Toomre & Toomre, 1972a,b). Examples of spiral arms produced in this way are shown in Fig. 1.5. High resolution N-body simulations (Oh *et al.*, 2008; Oh, Kim & Lee, 2015) and full hydrodynamical simulations (Dobbs *et al.*, 2010) show that the classic grand design two-arm pattern can be achieved by interaction between two galaxies. M51 is a classic example of a supposed tidally interacting spiral structure – both its morphology and its orbit can be well explained with a tidal interaction between it and its companion, NGC 5195 (Salo & Laurikainen, 2000; Theis & Spinneker, 2003; Dobbs *et al.*, 2010).

Rather than considered as a separate type of spiral structure, the arms produced by galaxy-galaxy interactions may instead be similar to the arms generated secularly. Simulations show that the spiral arms produced by interactions are initially material in nature, but form two-arm density wave structures over time (Sundelius *et al.*, 1987; Dobbs *et al.*, 2010). The produced density waves are, however, different to those produced by the Lin-Shu hypothesis, and do wind up over time, albeit more slowly than material arms. Both simulations and observations predict that tidally induced spiral arms are themselves transient phenomena, lasting $\sim 0.1 - 1$ Gyr (Merrifield, Rand & Meidt, 2006; Oh *et al.*, 2008; Struck, Dobbs & Hwang, 2011). From measurements of the fraction of grand design spirals in groups, Elmegreen & Elmegreen (1983) predicted that grand design spirals should last ~ 5 Gyr, or that the interaction distance for triggering grand design structure must be several galactic radii. Given the measurements of the persistence of grand design arms by interactions discussed here, fleeting interactions must play a significant role in producing spiral arms.

1.3.4 The role of bars

Bars are a common feature in disc galaxies: the fraction of spiral galaxies which have strong bars is reported to be ~ 0.3 from traditional 'by-eye' morphological measurements (de Vaucouleurs *et al.*, 1991; Barazza *et al.*, 2009; Masters *et al.*, 2011), increasing to ~ 0.6 if weaker bars are considered (Sellwood & Wilkinson, 1993; Moles, Marquez & Perez, 1995). Bars have a significant impact on the evolution of galaxy discs, as they are theorised to transfer angular momentum in discs (Combes & Sanders, 1981; Weinberg, 1985; Debattista & Sellwood, 2000; Berentzen, Shlosman & Jogee, 2006; Debattista *et al.*, 2006; Roškar *et al.*, 2008a,b). This potentially leads to gas inflows

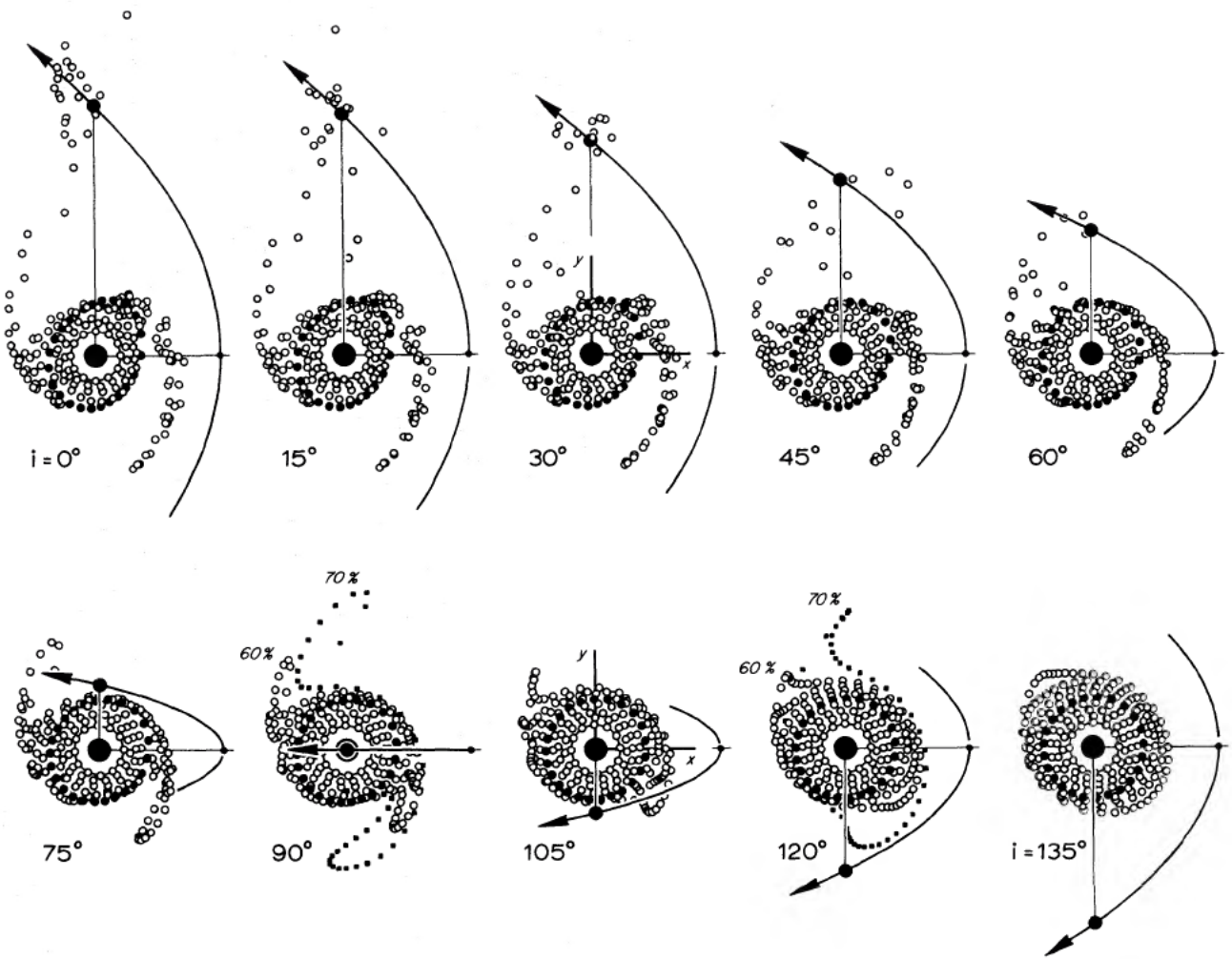

Figure 1.5: N-body simulation of the encounter between a disc and a companion (Toomre & Toomre, 1972a). The massive disc is rotating counter-clockwise. Each encounter is a parabolic passage of a companion of a quarter of the disc mass. The inclination, i, of the encounter plays a significant role in the shape of tidal bridges and tails and the resulting spiral arms.

towards the centre of galaxies, causing episodes of star formation (Hawarden *et al.*, 1986; Kruijssen *et al.*, 2014; Krumholz & Kruijssen, 2015) and the growth of galactic bulges (Weinzirl *et al.*, 2009; Masters *et al.*, 2011). This process has been used to explain observational results that bars exist in redder (Giordano *et al.*, 2010; Masters *et al.*, 2011; Hoyle *et al.*, 2011) and more gas poor galaxies (Davoust & Contini, 2004; Masters *et al.*, 2012), as bars exhaust the gas supply, and therefore the raw materials for star formation.

The link between bars and spiral arms has been established since the discovery that grand design spiral arms are more common when bars are present (Elmegreen & Elmegreen, 1982). That bars can influence spiral arms is not surprising, given that bars have been predicted to alter the underlying kinematics of discs (Miller, Prendergast & Quirk, 1970; Hohl, 1971). A common interpretation is that bars directly drive spiral arms (bar forcing) due to resonances between the rotation of the bar and disc. Bar forcing occurs when the ends of the bars are at the corotation radius of galaxies, causing corotating spiral waves to trail outwards into the disc (Elmegreen & Elmegreen, 1985). A related mechanism is called invariant manifold theory (Romero-Gómez *et al.*, 2006, 2007; Athanassoula, Romero-Gómez & Masdemont, 2009; Athanassoula *et al.*, 2009, 2010; Athanassoula, 2012). This describes a scenario where spiral arms emanate not as extensions of the bar, but from two unstable Lagrangian points at the ends of the bar. The orbital paths that stars take in order to maintain kinetic energy and angular momentum are governed by manifolds, which take the form of trailing ring-like or spiral arm-like structures. The bar causes any stars near the Lagrangian points to take these specific orbits, invoking arm structures without the need for density waves or swing amplification. Bar forcing is predicted to have a profound influence on spiral structure. Spiral arms produced in this way are likely to appear connected to the ends of bars, and be more material in nature than those produced by density waves (Roca-Fàbrega *et al.*, 2013). This could lead to the spiral arms not having a typical logarithmic spiral shape, instead having a hyperbolic spiral shape (Seiden & Gerola, 1979; Kennicutt, 1981). Athanassoula *et al.* (2010) also predict that galaxies with stronger bars should have looser spiral arms, and stronger arm vs. inter-arm contrasts.

The exact nature of the bar-spiral arm relationship is not yet fully understood. Some studies report clear evidence for the bar driven spiral mechanisms described above, with correlations between bar strength and spiral arm strength (Block *et al.*, 2004; Salo *et al.*, 2010), whereas others find no clear correlation (Seigar & James, 1998b; Kendall, Kennicutt & Clarke, 2011). The existence of other theories predicting a non-linear coupling between the bar and spiral arms (Tagger *et al.*, 1987; Sellwood & Sparke, 1988; Masset & Tagger, 1997), and that bars need to grow sufficiently strong before they can influence spiral structure (Grand, Kawata & Cropper, 2012b; Roca-Fàbrega *et al.*, 2013) means that a single theory may not explain the wide variety of bar-spiral patterns in discs (Rautiainen & Salo, 1999). This does, however, highlight the importance of bars when one considers studies of spiral galaxies: some galaxies will be strongly influenced by the bar, so care must be taken if one wants to study the role of spiral arms alone, independent of the effect of bars.

1.3.5 Spiral modes

Spiral structure can often be described in terms of 'modes'. Modes can be considered as standing waves reflecting at two ends. An ingoing trailing mode travelling from corotation to the galaxy centre can be reflected into a swing amplified leading wave travelling from the galaxy centre to corotation. These modes can grow over time, and are described as cavity modes (Sellwood & Carlberg, 2014).

Of key concern to this thesis is the difference between long-lived disc modes, that persist over several rotations of the galaxy, or randomly excited, short-lived waves. Generally speaking, a quasi-stationary, grand design two arm pattern can be considered as a long-lived $m = 2$ mode, where m denotes the number of spiral arms. Conversely, many-arm patterns tend to fluctuate over time, and can be considered as somewhat random, short-lived modes.

1.3.6 Models of long-lived spiral structure

Simulations have the potential to shed some light on what mechanisms are at play in spiral galaxies. Disc simulations give us a unique opportunity to study how forces act to introduce or amplify spiral arms. The pioneering work of Sellwood & Carlberg (1984) and Sellwood (1985) showed that N-body simulations of isolated galaxy discs can lead to the growth of spiral modes which form arm-like spiral structures, through gravitational mechanisms such as swing amplification. These simulations suggested that spiral patterns are short-lived, many-arm features. Although these early simulations could not produce long-lived patterns, they did show that spiral arms are indeed possible simply due to gravitational processes in the disc, without an explicit requirement for gas and star formation feedback. The most recent disc simulations are now at the stage where realistic spiral arm patterns can be modelled in galaxy discs. Advances in simulation resolution have also shown us that discs can sustain spiral structure over many rotations, and the short-lived nature was an artefact of the low resolution in the earlier simulations (Sellwood, 2011; Fujii *et al.*, 2011).

That local gravitational instabilities can grow to form sheared spiral arm structures is predicted from the most recent simulations of secularly evolving disc galaxies. A simulation of particular interest for this thesis is the one presented in D'Onghia, Vogelsberger & Hernquist (2013). The simulation consisted of a live disc of stars in a rigid dark matter halo. In order to create spiral arms, a number of GMCs randomly form throughout the disc – these form the initial density fluctuations. Spiral arms then grow around these initial density fluctuations due to swing amplification, leading to kinematic density waves. In order for such structures to persist for longer than one or two rotation periods, and solve the 'winding problem', individual spiral arms have to be short-lived features that can be replenished over time. The disc forms 'self-perpetuating' spiral arms – even after the removal of the initial density fluctuation, the model predicts spiral arms which break and replenish over time. This effect is shown in Fig. 1.6. Spiral arms created in this way cannot be considered as long-lived modes: they are short-lived features that are constantly broken and remade.

When simulating spiral structure, two-arm modes must be given strong consideration. Evidence suggests that the majority of spirals at low-redshift exhibit two-arm spiral structure (see section 1.2.2). A number of studies have therefore attempted to produce long-lived, quasi-stationary density waves in discs. The earliest N-body simula-

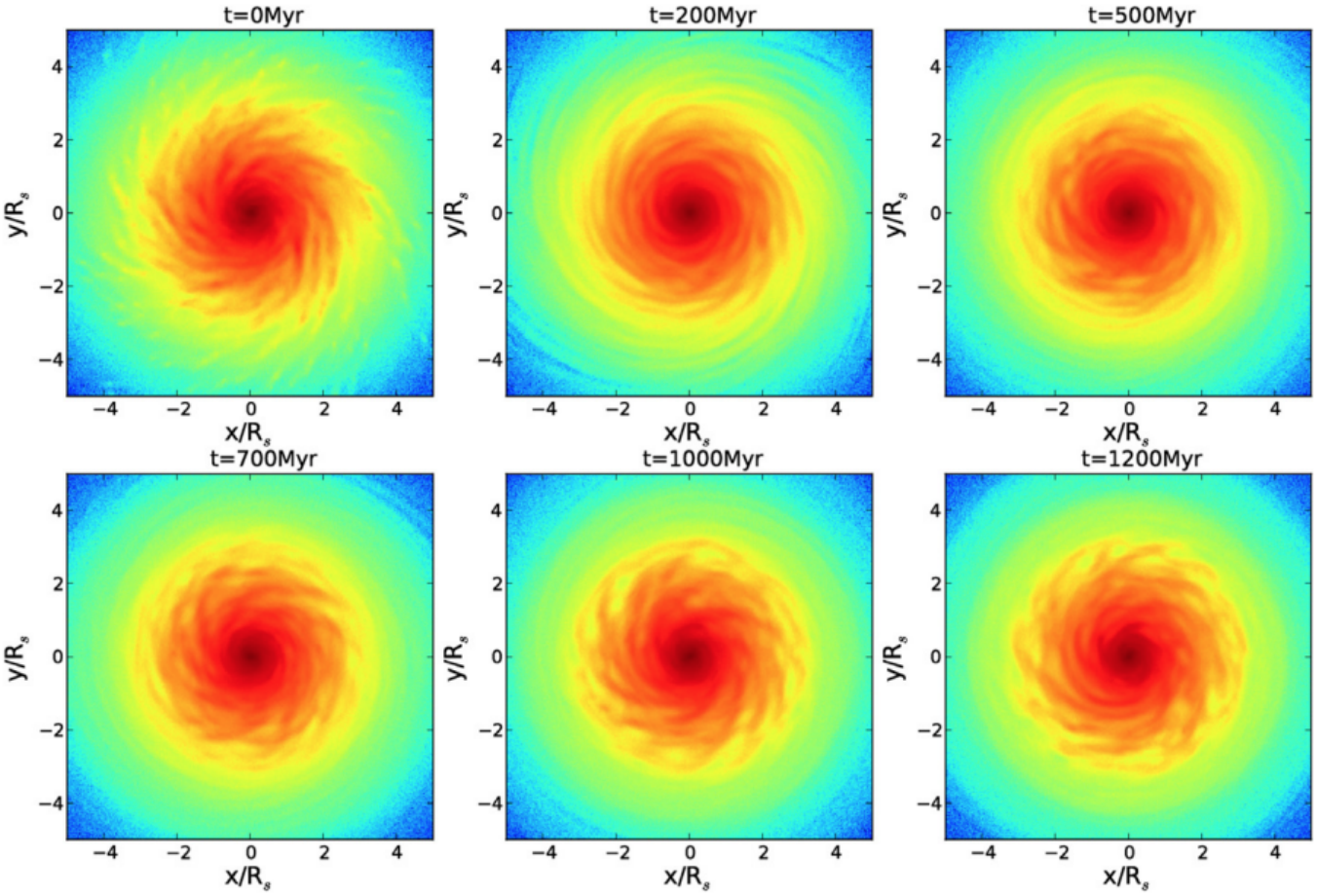

Figure 1.6: Simulation of self-perpetuating spiral arms in a disc galaxy. The simulation is of a thin exponential stellar disc comprising 10^8 stars and a static Hernquist dark matter halo using the GADGET-3 code (Springel, 2005). Stars are randomly selected to form GMCs of mass $9.5 \times 10^5 \mathrm{M}_\odot$ and spiral arms form via gravitational instabilities. At $t = 0$ Myr, these GMCs are removed and replaced with stellar particles. Despite the removal of the initial perturbation, the disc forms self-perpetuating, dynamic, swing amplified arms.

tions struggled to produce realistic spiral arms, with two-arm modes quickly leading to the growth of a bar (Miller, Prendergast & Quirk, 1970; Hohl, 1971; Kalnajs & Athanassoula-Georgala, 1974; Zang, 1976). In order to stop the rapid formation of a bar, Ostriker & Peebles (1973) (and also Hohl 1976) demonstrated that the addition of a spherical dark matter halo component makes cold discs more stable. A more recent simulation of has shown that two-arm structure can persist for long periods of time. Roškar *et al.* (2012) ran high resolution simulations of discs with gas and dark matter particles. As stars generally become dynamically hot compared to the disc over time, an injection of cool gas from which dynamically cool young stars can form is required in order to sustain spiral structure, a phenomenon first noted in Sellwood & Carlberg (1984). Over the lifetime of the spiral simulation, a number of spiral modes were excited. High order modes existed for short periods of time, but a long-lived two-arm mode persisted for the lifetime of the simulation (10 Gyr). This spiral mode cannot be considered as a quasi-stationary density wave, as the two-arm spiral pattern changed its structure over time, and even briefly disappeared for 1 Gyr. It does, however, provide the first evidence that long-lived, two-arm modes can be sustained in discs.

A potential uncertainty in any analysis of spiral structure concerns the existence of multiple modes in discs. The most obvious case of this concerns galaxies with both spirals and bars. Simulations have often formed spiral arms of this type, and bars and spirals often appear to join up in such simulations (Sellwood, 1985; Sellwood & Athanassoula, 1986; Sparke & Sellwood, 1987). One may therefore believe that the spiral arms and the bars form a single extended structure with a constant pattern speed. Further analysis of the bar and spiral arms reveal that they comprise two separate structures, with an rapidly rotating inner bar and a more slowly rotating outer $m = 2$ spiral pattern. The existence of multiple modes in what seem to be single spiral patterns has also been noted: Grand, Kawata & Cropper (2012a) presented a spiral simulation with extended spiral arms. However, the arms cannot be considered as long-lived modes as they change their shape over time. Further analysis proved this to be the case: Sellwood & Carlberg (2014) demonstrated that spiral arms formed in this way actually consist of multiple modes at different radii throughout the disc, with varying pattern speeds. For the purposes of this thesis, we generally consider spiral arms as single mode structures. Understanding the complex interplay of multiple modes in galaxies requires complicated analysis. We instead draw upon measurements which provide single measurements of spiral arm number for each galaxy, and pitch angle for each spiral arm. Whilst this is an approximation, it gives an idea of the dominant behaviour of the modes in each spiral galaxy, and can give an insight into the role spiral arms play across the entire low-redshift galaxy population.

1.3.7 Observational expectations

A common prediction of density waves is that gas can be 'shocked' into star formation. Fundamental to this argument is the role of gas and stars in the discs of galaxies. Gas in spiral arms has less pressure than stars, so the density contrast between the arm and inter-arm regions caused by density waves can be much larger. Simulations suggest gas is underdense in the regions entering density wave driven arms and overdense in the regions exiting the arms. Density waves can also cause vertical compression of gas inside the corotation radius (Debattista, 2014). Gas under the influence of density waves can therefore reach very high densities, dense enough to induce star formation

in spiral arms (Fujimoto, 1968; Roberts, 1969). Observationally, one would therefore predict that galaxies with stronger two-arm structures, indicative of stronger density waves, should have enhanced SFRs compared with galaxies where little or no density wave is present. One would also predict a clear gradient in the age of the stellar population across a spiral arm. Pour-Imani *et al.* (2016) describe this scenario in terms of spiral arm pitch angle (pitch angle is introduced in more detail in chapter 5). If one were to look at an image of the gas distribution of a galaxy, it would be on the leading edge of the spiral arm, as it precedes the formation of stars (Haynes *et al.*, 2011). The star formation should trail this gas, and an older stellar population should trail further still, leading to a tightening of the spiral arm pitch angle with age of the component. Evidence for the first of these predictions was provided by Romanishin (1985), where galaxies with strong two-arm structures were found to be bluer and hence more star-forming than many-arm structures. However, subsequent work on a larger sample of galaxies with measurements of both colour and Hα-derived SFR showed that there was no correlation between SFR and Elmegreen arm class (Elmegreen & Elmegreen, 1986; Kendall, Clarke & Kennicutt, 2015). Evidence for clear age gradients across the arms of nearby galaxies including M51 and M81 have also proven to be inconclusive (Foyle *et al.*, 2010, 2011; Choi *et al.*, 2015). If density waves are indeed present, they do not seem to significantly trigger or enhance star formation, but instead serve only to move the star-forming material around in galaxy discs (Vogel, Kulkarni & Scoville, 1988; Elmegreen, 2002; Moore *et al.*, 2012; Dobbs, Burkert & Pringle, 2011).

If spiral arms exist as swing amplified random instabilities, we expect that the spiral arm number should be affected by the mass distribution in galaxies. Although spiral arms can be broken and remade, the average total spiral arm number, or dominant mode, will exist beyond the lifetime of a single spiral arm. The nature of this dominant mode is directly related to the underlying mass distribution of galaxy discs. Notably, swing amplified models have predicted that spiral arm number should depend on the relative bulge, disc and halo mass distributions in spiral galaxies (Athanassoula, Bosma & Papaioannou, 1987; Athanassoula & Bosma, 1988; Bosma, 1999). The most obvious example of this is the prediction presented in D'Onghia (2015), where spiral arm number is predicted with respect to the properties of the bulge, disc and halo. However, there is no prior confirmation that such a relationship does exist and that many-arm spirals exist in this way.

Chapter 2

Data

2.1 Overview

This thesis primarily investigates the visual morphology of galaxies. The main intention is to study large populations of galaxies in statistically meaningful ways, with thought given to sample completeness. For this, a statistically complete sample of visual classifications is required.

An approach that has been successfully employed to visually classify galaxies in large surveys is citizen science, which asks many volunteers to morphologically classify galaxies rather than relying on a small number of experts. Galaxy Zoo 1 (GZ1; Lintott *et al.*, 2008, 2011) was the first project to collect visual morphologies using citizen science, by asking volunteers to classify galaxies from the SDSS as either 'elliptical' or 'spiral'. Using this method, each galaxy is classified by many (typically > 40) individuals, and a likelihood or 'vote fraction' of each galaxy having a particular feature is assigned as the fraction of classifiers who saw that feature. GZ1 classifications collected in this way have been used to compare galaxy morphology with respect to colour (Bamford *et al.*, 2009; Masters *et al.*, 2010a,b), environment (Bamford *et al.*, 2009; Skibba *et al.*, 2009; Darg *et al.*, 2010a,b), and star formation properties (Tojeiro *et al.*, 2013; Schawinski *et al.*, 2014; Smethurst *et al.*, 2015).

Following from the success of GZ1, more detailed visual classifications were sought, including the presence of bars, the presence of spiral arms, and spiral arm winding and multiplicity properties. Thus, Galaxy Zoo 2 (GZ2) was created (Willett *et al.*, 2013, hereafter W13), in which volunteers were asked more questions about a subsample of GZ1 SDSS galaxies. The main difference between GZ2 and GZ1 was that visual classifications were collected using a 'question tree' in GZ2, to gain a more exhaustive set of morphological information for each galaxy. GZ2 has already been used to compare the properties of spiral galaxies with or without bars (Masters *et al.*, 2011, 2012; Cheung *et al.*, 2013), look for interacting galaxies (Casteels *et al.*, 2013), and look for relationships between spiral arm structure and star formation (Willett *et al.*, 2015). This 'question tree' method has since been used in a similar way to measure the presence of detailed morphological features in higher redshift galaxy surveys (e.g. Melvin *et al.* 2014; Simmons *et al.* 2014), and other citizen science projects. These Galaxy Zoo data were used for visual classifications for the majority of this thesis. Section 2.2 outlines the sample selection and raw photometric data used in this thesis. Section 2.3 describes the GZ2 classifications in more detail. Section 2.4 describes any derived data

products employed in this thesis, including stellar mass and SFR estimates.

2.2 Sample selection and photometry

Galaxies with reliable visual classifications are taken from the GZ2 data catalogue. The galaxies classified by GZ2 were taken from the SDSS Data Release 7 (DR7; Abazajian *et al.* 2009). All galaxies are taken from the SDSS main galaxy sample (MGS, Strauss *et al.* 2002). The primary sample used in GZ2 consisted of the brightest $\sim 250,000$ galaxies in the SDSS region. To ensure that galaxies were bright enough to see detailed features, several cuts were employed. The final sample contains essentially all well-resolved galaxies in DR7, with spectroscopic redshifts in the range $0.0005 < z \leq 0.25$, Petrosian half-light magnitudes brighter than $m_r = 17.0$ and $R_{90,r}$ (90 per cent Petrosian light radius) greater than 3 arcsec. Deeper imaging data were obtained for the Stripe82 region, with limiting magnitudes down to $m_r = 17.77$. For the purpose of this thesis, we exclude these deeper images from any analysis, instead using only the normal depth imaging.

Petrosian aperture photometry in optical $ugriz$ filters is obtained from the SDSS DR7 catalogue. Rest-frame absolute magnitudes corrected for Galactic extinction are those computed by Bamford *et al.* (2009), using KCORRECT (Blanton & Roweis, 2007). These magnitudes were available for all galaxies in the SDSS sample described above. In chapters 4 and 5, photometry from the UV, near-IR (NIR) and mid-IR (MIR) were also used. UV absolute magnitudes are obtained from the GALEX GR6 catalogue (Martin *et al.*, 2005). These are included in the NASA Sloan Atlas (NSA; Blanton *et al.* 2011). NIR and MIR photometry are from the AllWISE catalogue of galaxies from the WISE mission (Wright *et al.*, 2010), and obtained from the reduced catalogue of Chang *et al.* (2015). We only match WISE detections to galaxies where there is only one WISE source within 6 arcsec of a galaxy, in line with Donoso *et al.* (2012), Yan *et al.* (2013) and Chang *et al.* (2015).

2.3 Galaxy Zoo

In this section I outline the main steps involved in obtaining visual morphology measurements with Galaxy Zoo. A full description is included in the GZ2 data release (W13). The key steps relevant to this thesis are described below.[1]

2.3.1 Image creation

In Galaxy Zoo, images of individual SDSS galaxies were presented to users or classifiers via a web-based interface.[2] Each image was a gri composite colour image, with each filter scaled with an asinh function using a modified version of the SDSS SkyServer asinh stretch code (Lupton *et al.*, 2004). To alleviate any potential resolution-dependent bias, all images were presented with 424×424 pixels, with each pixel scaled to $0.02 \times R_{90,r}$. Some randomly selected example composite images that were classified in GZ2 are shown in Fig. 2.1.

[1] All data products from Galaxy Zoo described in this chapter are available from data.galaxyzoo.org

[2] The current version of Galaxy Zoo is at www.galaxyzoo.org

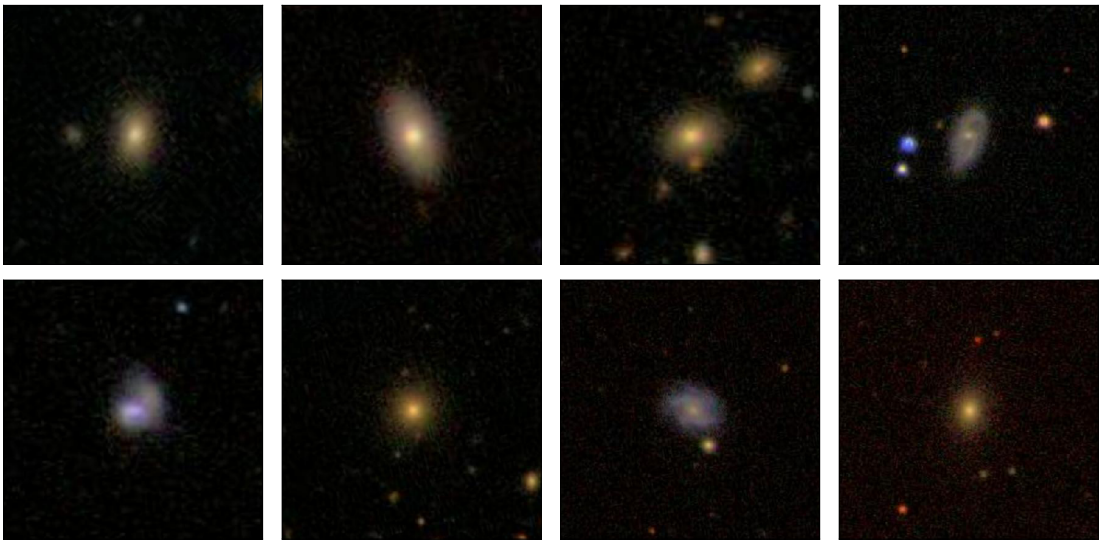

Figure 2.1: Eight randomly-selected GZ2 images presented to users. The images are created as gri composite images scaled by an asinh function. All images are scaled to the galaxy's Petrosian radius to ensure there is no systematic size effect in classifications.

2.3.2 Classification

In GZ2, morphological information for each galaxy was obtained by asking participants to answer a series of questions. The structure of this question tree is shown in Fig. 2.2. No user will explicitly answer every question in the tree for a particular galaxy; they instead follow a specific branch of the tree. To reach the questions further down the tree, it is required that another question has been answered with a specific response. For each question, the responses are each represented by the 'vote fraction', p, assigned to each possible answer. For any given question, the sum of the vote fractions for all possible answers adds up to one. Considering the 'edge-on' question (T01 in Fig. 2.2), a classifier would only answer that question if they answered 'features or disc' for T00. For example; if a galaxy was classified by 40 people, and 30 of those said they saw features, whilst the other 10 claimed it was smooth, then the corresponding vote fractions are $p_{\rm features} = 0.75$ and $p_{\rm smooth} = 0.25$. Only the 30 classifiers who saw 'features' would then answer the 'edge-on' question (T11 of Fig. 2.2). If 15 of those said the galaxy was edge-on, and 15 said it was not, the corresponding vote fractions would be $p_{\rm edge-on} = 0.5$ and $p_{\rm not\,edge-on} = 0.5$. The GZ2 main sample finished with a median of 44 individual classifications per galaxy, with 99.9 per cent of galaxies having ≥ 28 classifications.

In order to reduce the influence of unreliable classifiers, W13 down weighted individual volunteers who had poor agreement with the other classifiers. Throughout this thesis, these weighted vote fractions are referred to as the 'raw' quantities. Before using these GZ2 vote fractions to study the galaxy population, we must first consider the issue of classification bias, as we shall see in section 3.2.2.

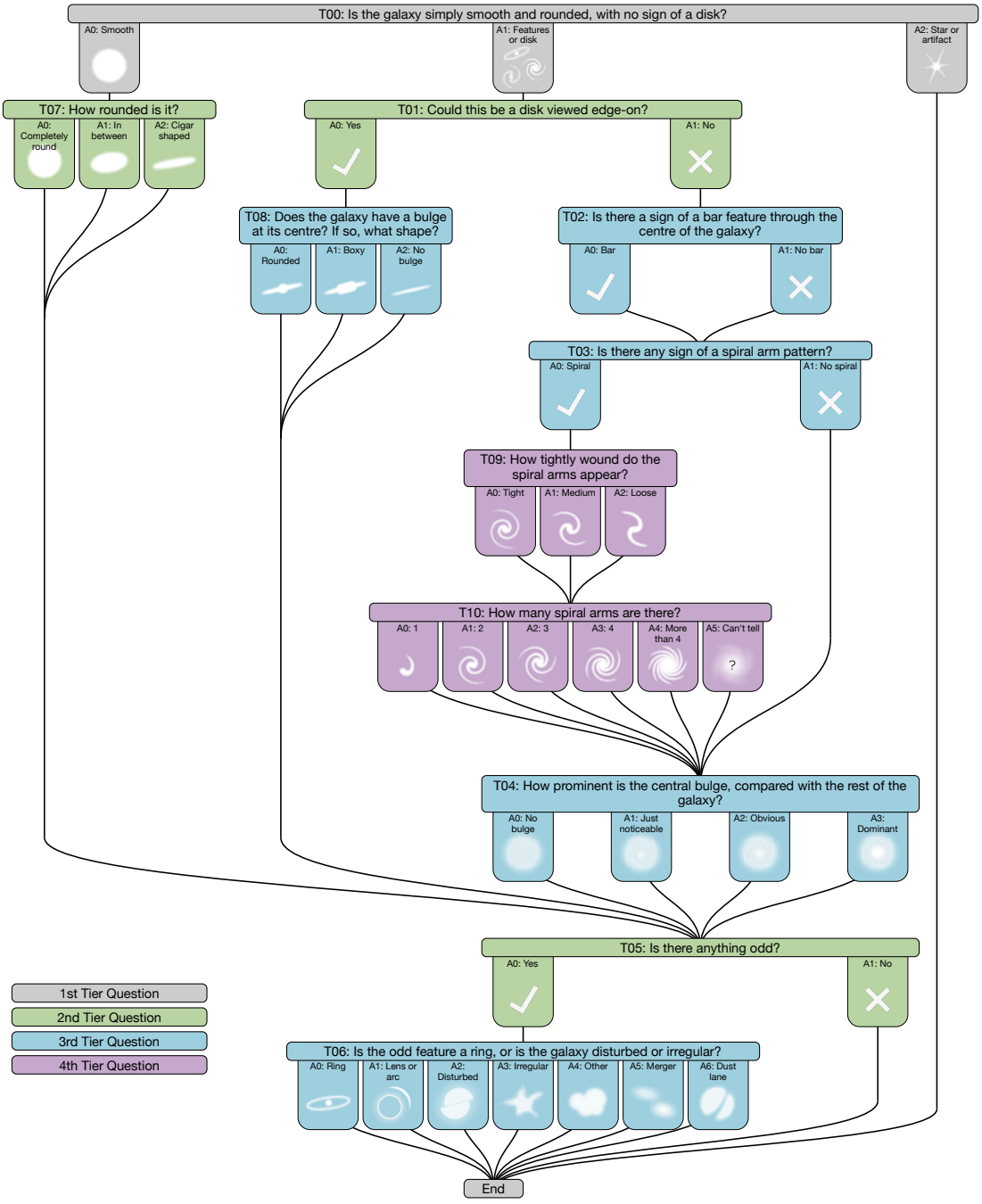

Figure 2.2: Diagram of the question tree used to classify galaxies in GZ2. The tasks are colour-coded by their depth in the question tree. As an example, the arm number question (T10) is a fourth-tier question – to answer that particular question about a given galaxy, a participant needs to have given a particular response to three previous questions (that the galaxy had features, was not edge-on and had spiral arms).

2.4 Ancillary data

2.4.1 Stellar masses

In principle, there are a number of ways in which one can measure the stellar mass of a galaxy. At different stages, I use three independently derived stellar mass estimates. The first stellar mass estimates are from the colour-luminosity technique of Baldry *et al.* (2006). A simple relation was used, with a constant assumed mass-to-light ratio as a function of colour similarly to Bell & de Jong (2001). A simple relationship between the two quantities was obtained by fitting to the stellar masses obtained from more sophisticated models presented in Kauffmann *et al.* (2003) and Glazebrook *et al.* (2004), which used stellar population synthesis models.

The work in section 4.2 uses only galaxies where reliable NIR and MIR photometry were obtained from the WISE data. As the NIR is usually the wavelength of choice for accurate stellar mass estimates of galaxies (Glazebrook *et al.*, 2004; Eskew, Zaritsky & Meidt, 2012; Meidt *et al.*, 2012), IR derived stellar masses were used. These are obtained from Chang *et al.* (2015), and used full photometric fits of the galaxy spectra from the optical (SDSS $ugriz$) and the IR (WISE 3.4, 4.6, 12 and 22μm) with MAGPHYS (da Cunha, Charlot & Elbaz, 2008).

For chapters 5 and 6, bulge+disc mass estimates were required. Stellar masses were from the Mendel *et al.* (2014) method, which fit optical $ugriz$ photometry with GIM2D (Simard *et al.*, 2002). Given that three separate stellar mass estimates are used at various points of this thesis, we check their consistency in Fig. 2.3. All galaxies with stellar mass estimates in the redshift range $0.02 < z \leq 0.055$ are used for this purpose, and the sample consists of 43,534 galaxies. I note here that the Baldry *et al.* (2006) stellar mass estimate uses a Kroupa (2001) IMF, different to the other stellar mass estimates that both use a Chabrier (2003) IMF. For the purpose of this comparison, the Baldry *et al.* (2006) stellar masses are scaled down by –0.03 dex to account for the IMF difference, as suggested in Zahid *et al.* (2012) and Speagle *et al.* (2014). The three stellar mass estimates are generally very consistent with scatter of ~ 0.1 dex between the different estimates. The Chang *et al.* (2015) and Mendel *et al.* (2014) are systematically slightly higher by 0.10 and 0.14 dex respectively, but there appears to be no errant behaviour – galaxies more massive with one measure are generally more massive with another, with little scatter. These small differences are consistent enough to justify that there are no significant deviations depending on which estimate was used.

2.4.2 Star formation rates

In chapters 4 and 5, I derive a measure of SFR directly from UV and MIR fluxes, which indicate the emission directly from young stars and dust heated by star formation respectively. I also use another measure of SFR from the widely-used MPA-JHU catalogue. These are obtained from the SDSS spectra of the inner region of galaxies. Any missed star formation from outside the fibre are corrected using galaxy colours and colour gradients, trained on UV-optical SED fits (Brinchmann *et al.*, 2004; Salim *et al.*, 2007). Comparisons with more recent SED models confirm that these SFRs are likely the most accurate measures of total SFR for SDSS galaxies (Salim *et al.*, 2016).

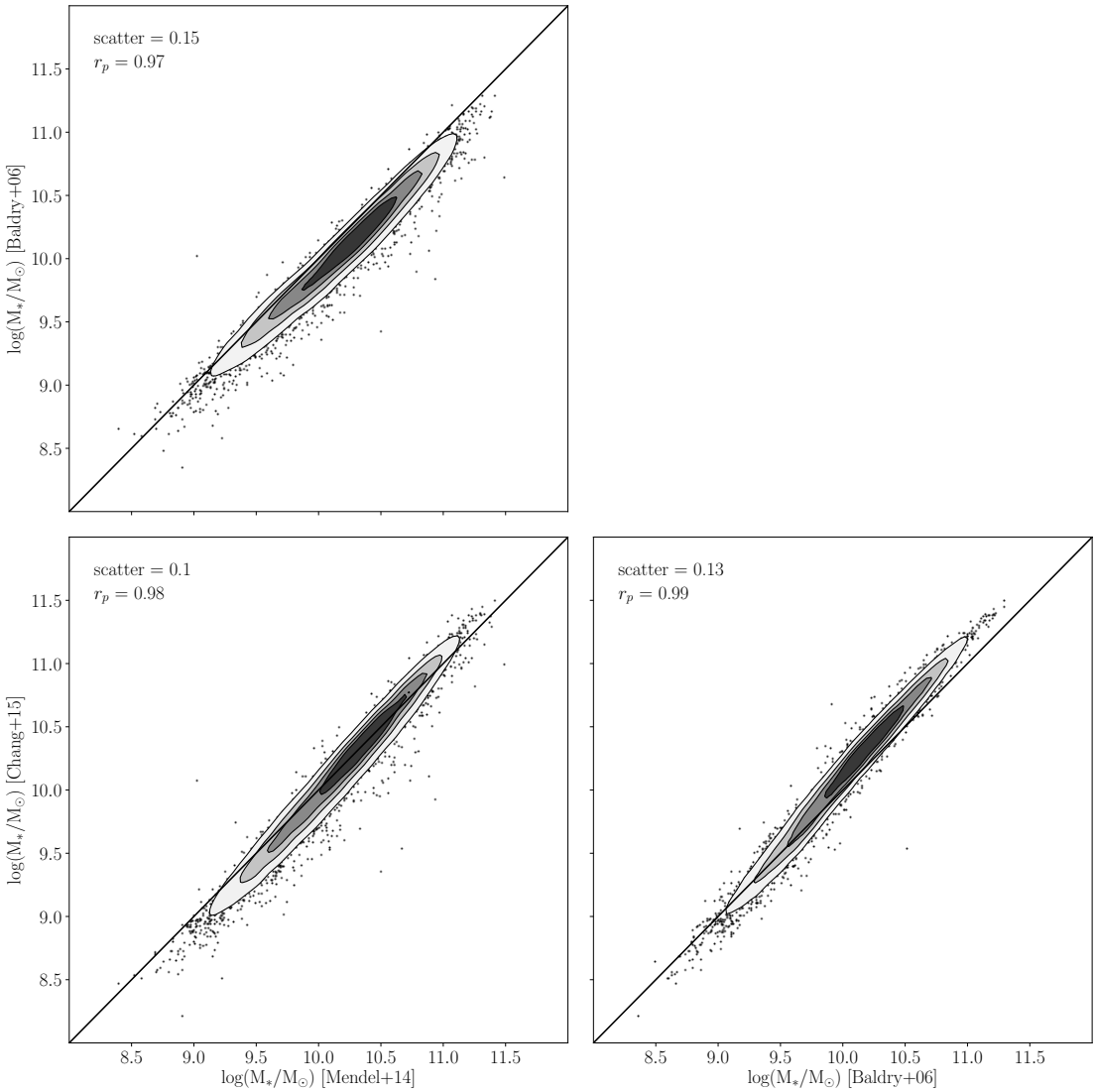

Figure 2.3: Comparison of stellar mass estimates used in this thesis. All galaxies in the redshift range $0.02 < z \leq 0.055$ which have mass estimates in all three catalogues, irrespective of morphology, are shown in this figure. The grey contours show the regions where 20, 40, 60 and 80 per cent of the galaxies lie in each sub plot. The stellar mass estimates are consistent, despite the differences in the techniques employed to measure them.

2.4.3 HI fluxes and masses

For SDSS galaxies, measurements of HI flux and associated errors are from the Arecibo Legacy Fast ALFA survey (ALFALFA; Giovanelli *et al.* 2005; Haynes *et al.* 2011). The survey has significant overlap with the North Galactic Cap region of Sloan, the principal region of the GZ2 dataset, as shown in Fig. 2.4. The published α70 data was used, which included all of the data for ~ 70 per cent of the total ALFALFA survey area. At the time of the publication of the work using the ALFALFA data, the collection and reduction of the full α100 dataset had not yet been completed. I selected reliable HI detections using objects with ALFALFA detcode = 1 or 2 (described in Haynes *et al.* 2011) and a single SDSS matched optical counterpart in the galaxy sample within the redshift range $0.02 \leq z \leq 0.05$. Objects with detcode = 1 are considered as reliable detections and objects with detcode = 2 are described as 'priors' – these are objects with a lower signal-to-noise than the threshold required to be a reliable detection, but

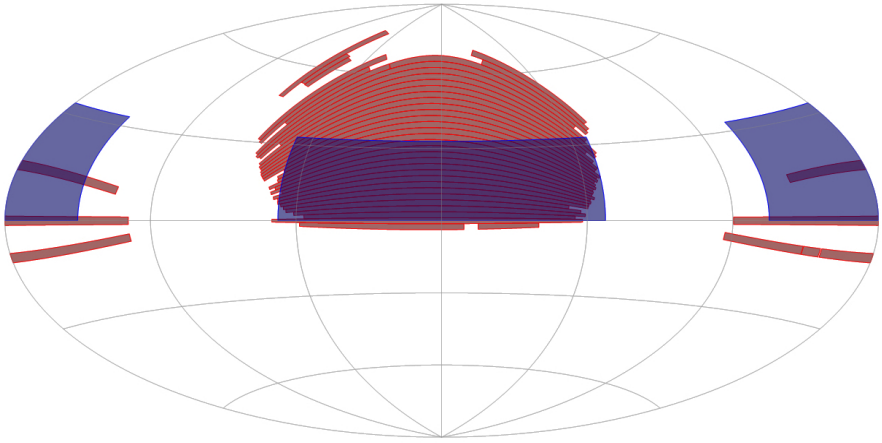

Figure 2.4: Footprints of the SDSS and ALFALFA surveys. The red regions show the footprint of SDSS DR7, and the blue regions show the footprint of $\alpha 100$ upon completion. As the Arecibo telescope is static, it cannot survey the entire SDSS region. Image obtained from http://egg.astro.cornell.edu/index.php/images/alfalfa_sdss_coverage.jpg.

have a matched optical counterpart, making them likely to be real detections. Only detections with $z < 0.05$ are considered because detections above this redshift suffer with contamination due to radio interference caused by the San Juan airport radar (Haynes *et al.*, 2011). Due to the restrictions on the $\alpha 70$-SDSS footprint and the imposed limiting redshift of $z \leq 0.05$, not all galaxies have been surveyed by ALFALFA – the fraction of galaxies with reliable detections are discussed in section 4.2.6. HI fluxes were converted to HI masses using the conversion outlined in Haynes *et al.* (2011):

$$\mathrm{M_{HI}} = 2.356 \times 10^5 D^2_{\mathrm{Mpc}} S_{21}, \tag{2.1}$$

where S_{21} is the integrated 21cm line HI flux density, and D_{Mpc} is the distance to the galaxy measured in Mpc.

Chapter 3

Methods for measuring morphologies and data analysis

All work described in this chapter which relate to spiral arm number was first published in Hart *et al.* (2017a). The work related to spiral arm pitch angle was published in Hart *et al.* (2017b). All work was undertaken by the author with advice from Steven Bamford, Wayne Hayes, and the co-authors of the aforementioned papers. The creation of SPIRALSPOTTER was the work of Steven Bamford with the ZOONIVERSE project builder interface. The creation of the input images for SPIRALSPOTTER was the work of the author with advice from Steven Bamford. The running of the SPARCFIRE code was performed by Wayne Hayes. Technical assistance in the writing of the GZ2 debiasing code was provided by Steven Bamford.

3.1 Overview

Grouping and studying galaxies by their visual appearance has been a well established science since the work of Hubble (1926b). The appearance, or *morphology* of galaxies gives us an insight into the physical processes that shape the evolution of galaxies: the processes that affect how stars and gas evolve in galaxies can also leave lasting imprints on their structure. This leads to broad correlations between galaxy morphology and other fundamental characteristics, including colour and gas fraction (Roberts & Haynes, 1994).

The advent of the largest surveys, including the SDSS (York *et al.*, 2000) and the Galaxy and Mass Assembly survey (GAMA, Robotham *et al.* 2010) presents a challenge to studying visual morphologies in galaxies. The majority of visual morphology catalogues compiled throughout the 20th century required by eye visual inspection by individual astronomers or small groups of astronomers (Sandage, 1961; de Vaucouleurs *et al.*, 1991). Even the largest catalogues of professionally inspected SDSS galaxies consist of only $\sim 10^4$ galaxies, approximately two orders of magnitude smaller than the number of classifiable galaxies in the SDSS (Fukugita *et al.*, 2007; Nair & Abraham, 2010). In principle, one can approach the problem of obtaining visual morphologies of large galaxy samples in two ways. The number of people classifying galaxies can be increased or one can develop a computer algorithm to automatically sort galaxies. I describe examples where these two methods have been applied in this chapter, to measure both spiral arm numbers and pitch angles.

3.2 Galaxy Zoo visual morphologies

3.2.1 Quantifying morphology in Galaxy Zoo

In GZ1, galaxies were classified as simply spiral or elliptical. In GZ2, morphological information for each galaxy was obtained by asking participants to answer a series of questions. The structure of this question tree is shown in Fig. 2.2. Typically, each image was viewed by $\gtrsim 40$ people (W13), although no user will explicitly answer every question in the tree for a particular galaxy. The way in which classifications were combined to give a vote fraction was introduced in section 2.3.2.

Traditional morphologies assign each galaxy to a specific class, usually determined by one, or occasionally a few, experts. In contrast, Galaxy Zoo provides a large number of independent opinions on specific morphological features for each galaxy. This allows one to consider both the inherent 'subjectiveness' and observational uncertainties of galaxy morphology, and hence control the compromise between sample contamination and completeness.

There are two principal ways in which galaxy morphologies can be quantified using Galaxy Zoo vote fractions. The first is to consider averages of the vote fractions over specific samples or bins divided by some other property. These average vote fractions can then be used to study variations in the morphological content of the galaxy population. Individual galaxies are not given specific classifications. There is no population of 'unclassified', and hence ignored, galaxies. This approach has been taken by Bamford *et al.* (2009), Casteels *et al.* (2013), Willett *et al.* (2015), and various other studies. With this method, the vote fractions of all galaxies can be considered together; even galaxies with a small (but non-zero) vote fraction for a given property count towards the statistics. Effectively, this approach considers the vote fractions as an estimate of the probability of a galaxy belonging to a particular class.

The second approach is to divide the galaxy sample into different morphological categories, either by applying a threshold on the vote fractions, or choosing the class with the largest vote fraction. Such methods have been used by Land *et al.* (2008), Skibba *et al.* (2009), Galloway *et al.* (2015) and many more. One advantage of this approach is that each galaxy is assigned to a definite class, with the threshold tuned to ensure a desired level of classification certainty. However, a set of 'uncertain' or 'unclassified' galaxies may remain. In some analyses these require special attention.

These different approaches are also relevant for how questions at different levels in the tree are combined. For example, a participant is only asked if they can see spiral arms when they have already answered that they can see features in the galaxy and that the galaxy is not an edge-on disc. The vote fraction for spiral arms therefore represents the conditional probability of spiral arms *given that* features are discernible *and* that the galaxy is not edge-on. When considering whether a galaxy displays spiral arms, one should account for the answers to these previous questions in the tree. One can treat vote fractions as probabilities, multiplying them to obtain a combined 'probability' that a galaxy displays any features, is not edge-on and possesses spiral arms. Alternatively, one may select a set of galaxies that display features, are not edge-on and possess spiral arms, by applying some thresholds to the vote fractions for each question in turn. (See Casteels *et al.* (2013) for a more thorough discussion of these issues.)

The primary morphological features we use in this thesis are the apparent number of spiral arms displayed by a galaxy and how tightly wound those arms are (T09 and

T10 of Fig. 2.2). Some of the classes for spiral arm number, contain a relatively low fraction of the total spiral population, however. In addition, the vote fractions for the preferred answer are often fairly low, with votes distributed over several answers. In such cases, averaging the vote fractions over the full sample does not work particularly well, as noise from more common galaxy classes overwhelms the subtle signal from rarer classes. In this thesis we often prefer to assign galaxies to morphological samples by applying a threshold or taking the answer with the largest vote fraction for this reason.

3.2.2 Biases in the Galaxy Zoo sample

An issue that arises in both visual and automated methods of morphological classification is that detailed features are more difficult to observe in lower signal-to-noise images (i.e. observed from a greater distance). In Galaxy Zoo, this has been termed as *classification bias*. If a sample is significantly biased, it leads to issues with contamination and incompleteness. Incompleteness and contamination are defects that arise in a sample where an inherent redshift bias affects the classifications. Incompleteness affects the 'harder to see' features: the vote fractions for these features decrease with redshift, leaving us with poor number statistics for a sample we wish to define as having that feature. Contamination is the converse effect that appears in the 'easier to see' categories. For these responses, the vote fractions decrease with redshift, meaning that any samples defined using the Galaxy Zoo classifications will also include mis-classified galaxies that should have actually been included in one of the 'harder to see' categories. Any intrinsic differences between samples that one wishes to compare may therefore be negated. If galaxies are not correctly assigned into the correct categories, then the samples will be contaminated and any significant differences between the categories can be significantly reduced.

In GZ1, there was a clear example of redshift-dependent classification bias. Galaxies of a given size and luminosity appear fainter and smaller in the SDSS images if they are at higher redshifts. Galaxy images in GZ1 and GZ2 are scaled by Petrosian radius (see section 2.3.1). As this means that equivalent galaxies at further distances are scaled to have the same angular size, their pixel resolution is lower. Detailed features can therefore be more difficult to distinguish in galaxies at higher redshift. As a result, visual galaxy classifications are biased, as fewer galaxies are classified as having the more detailed features at higher redshift, making a sample of galaxies with the these features incomplete. In GZ1, galaxies at higher redshift had lower 'spiral' vote fractions, which were corrected using a statistical method developed in Bamford *et al.* (2009).

Debiasing the GZ2 data is, however, somewhat more complicated for two reasons. In GZ1 morphologies are a binary choice of spiral or elliptical; this is not the case for GZ2. Many of the GZ2 questions have multiple possible answers, including the spiral arm number and spiral arm tightness questions which are of principal concern in this chapter. Any debiasing method must distribute the votes among *all* of the categories fairly. Secondly, a number of the questions depend on questions which have come previously. Again, the spiral arm questions fall into this category – these are 'fourth order' questions, so depend on how the questions further up the tree were debiased.

It should be noted that such biases are not exclusive to Galaxy Zoo. Difficulty in detecting faint features in lower signal-to-noise images is an inherent property of any

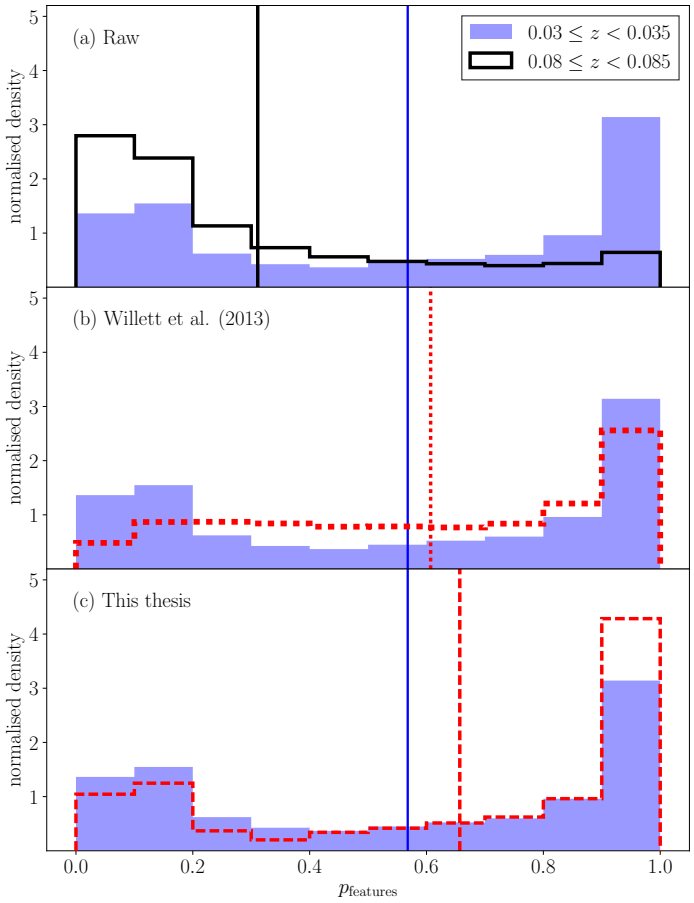

Figure 3.1: Histograms of vote fractions for the 'features' response to the 'smooth or features' question in GZ2. In each of the panels, the blue filled histogram shows the raw vote distribution for a low-redshift $0.03 \leq z < 0.035$ slice of the *luminosity-limited sample*. The unfilled histograms show the equivalent distribution for a higher-redshift $0.08 < z \leq 0.085$ sample. The vertical lines show the mean vote fractions.

visual or automated method of galaxy classification. The advantage of using Galaxy Zoo classifications is that they give a statistical method of measuring galaxy morphology. As each of the galaxies in the *full sample* has been visually classified by a number of independent observers, the apparent evolution in the presence of features can be modelled, and biases corrected accordingly.

The effect of redshift bias is shown in Fig. 3.1a, where the answer to the 'smooth or features' question is compared for high and low-redshift samples in GZ2. This sample is a *luminosity-limited sample* in the redshift range $0.03 < z < 0.085$, complete for galaxies brighter than $M_r = -21$. The redshift range of the SDSS sample is shallow enough to argue that there should be minimal change in the overall population of galaxies (Bamford *et al.* 2009; W13). In a *luminosity-limited sample*, the level of completeness should also be the same at all redshifts, meaning that the overall populations of the high and low redshift samples should be equivalent. However, Fig. 3.1a shows that the higher redshift vote fractions are dramatically skewed to lower values – generally, people have greater difficulty in detecting the presence of features in the higher redshift images. Thus, there are fewer votes for galaxies showing 'features' and consequently more votes for galaxies being 'smooth'. If one wished to compare a sample of galaxies with 'features' against one that is 'smooth' using the raw vote fractions, the number of galaxies with 'features' would be incomplete relative to the low redshift bin

and the 'smooth' sample would be contaminated.

3.2.3 The previous method for redshift bias correction

The previous debiasing procedure applied to both GZ1 and GZ2 focused on correcting the vote fractions of the galaxy samples by adjusting the mean vote fractions as a function of redshift. The method was first proposed in Bamford *et al.* (2009), and updated for GZ2 in W13. The method successfully adjusts the mean vote fractions for questions with two dominant answers, as can be seen from the vertical lines in Fig. 3.1b: the mean of the debiased high-redshift sample is much closer to the mean of the low-redshift sample than for raw vote distributions (Fig. 3.1a).

However, this technique has two limitations that make it unsuitable if we want to divide a galaxy sample into different morphology subsets. The first issue is that adjustment of the mean vote fraction does not necessarily lead to correct adjustment of individual vote fractions. This can be seen in Fig. 3.1b. Although the mean vote fraction for the high-redshift sample has been correctly adjusted to approximately match the low-redshift sample, the overall distribution does not match. There is an excess of debiased votes in the middle of the distribution, and fewer votes for the tails of the distribution at $p \approx 0$ and $p \approx 1$. This effect is important if we wish to divide the sample into different subsets by morphological type. As the shape of the histograms is not consistent with redshift, the fraction of galaxies with p_{features} greater than a given threshold can also vary with redshift, which will affect any cuts we wish to make by combining questions at various stages in the question tree.

As described in section 3.1, GZ2 utilises multiple-answer questions to obtain more detailed classifications than GZ1. In cases where the votes are split between multiple categories, the debiasing method from W13 does not always adjust the vote fractions correctly. I show this effect for the 'spiral arm number' question (T10 of Fig. 2.2), in Fig. 3.2. We select a sample of 'secure' spiral galaxies with $p_{\mathrm{features}} \cdot p_{\mathrm{not\,edge-on}} \cdot p_{\mathrm{spiral}} > 0.5$, (with the vote fractions corresponding to the debiased values from W13), and plot the mean vote fractions with respect to redshift for each of the arm number responses. A clear trend in p_m (where m is the spiral arm number) is observed: the mean vote fractions vary systematically with redshift, even after the W13 correction has been applied. For this question, the answers with more spiral arms (3, 4, or 5+ spiral arms) are the 'harder to see' features, equivalent to the spiral response in GZ1. This means that there are fewer votes for these categories at higher redshift, which instead increase the 1 and 2 arm vote fractions. The 3, 4 and 5+ spiral arm samples of spiral galaxies therefore suffer from incompleteness. This is of particular importance in this case for two reasons. Firstly, three questions must have been answered 'correctly' previously for a galaxy to be classified as spiral as this is a 'fourth order' question, as can be seen in Fig. 2.2. This means the sample size is limited. Secondly, the 3, 4 and 5+ arm responses have low mean vote fractions overall, of $\lesssim 0.1$. Thus, the number statistics for these categories are very low, meaning they will suffer from high levels of noise. Correspondingly, the 1 and 2 armed spiral samples would suffer from contamination from galaxies that should have been classified as 3, 4 or 5+ armed.

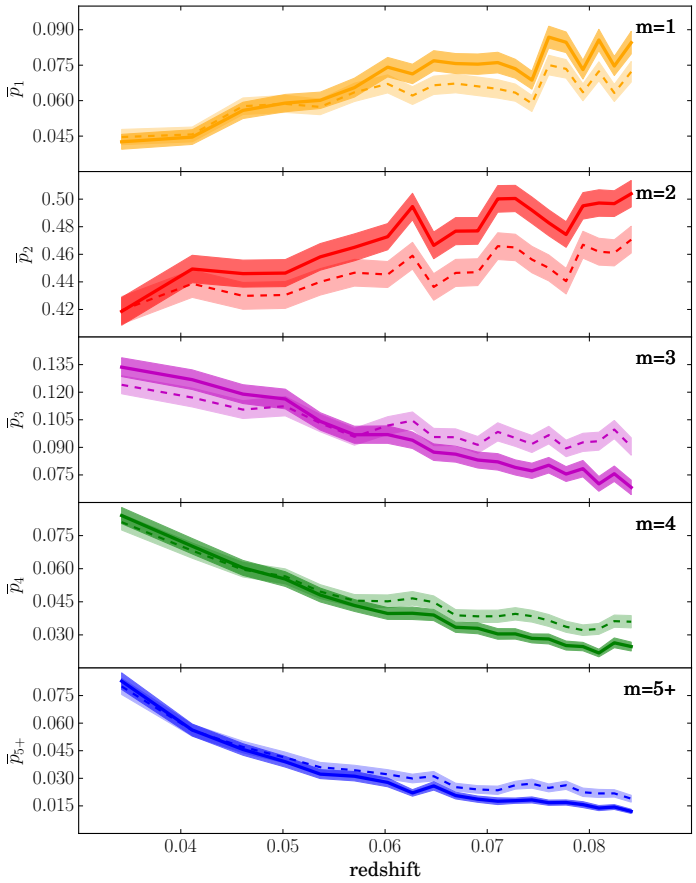

Figure 3.2: Mean vote fractions for each of the responses to the 'arm number' question (T10 in Fig. 2.2). The sample consists of galaxies from the *luminosity-limited sample*, with $p_{\rm features} \cdot p_{\rm not\ edge-on} \cdot p_{\rm spiral} > 0.5$ (with vote fractions taken from the W13 debiased catalogue). The solid lines show the mean arm number vote fractions obtained using the raw vote classifications, and the dashed lines indicate the same quantity obtained using the W13 debiased values. The shaded regions indicate the 1σ error on the mean.

3.2.4 A new method for correcting redshift bias

Given the limitations described in section 3.2.3, I constructed a new method of debiasing the GZ2 data more effectively. As discussed in section 3.2.1, there are two distinct ways in which one can quantify morphology with the GZ2 dataset. When considering a question further down the question tree with low number statistics, such as the spiral arm question, a thresholding technique is preferred rather than using the weighted vote fractions (see section 3.2.1). The spiral arm number question is an example where this thresholding technique is applied later on in this thesis. Fig. 3.2 shows that the '2 spiral arms' response dominates the overall vote fraction, making up ~ 60 per cent of the votes, even at the lowest redshifts. The rarer responses of 3, 4 or 5+ arms have much lower number statistics overall, with only ~ 10 per cent of the votes. The mean values can therefore be affected by the noise in the dominant category, which will be much larger than the noise for the rarer categories. I therefore divide the galaxy sample into different sub-samples when comparing galaxies by spiral arm number.

Unlike the debiasing method in W13, my new method aims to make the vote distributions themselves as consistent as possible rather than purely aiming for consistency in the mean vote fraction values. As each galaxy is classified by 40 or more volunteers (W13), I have enough data to model the evolution of the vote distributions as a function

of redshift. Different classifiers will have different sensitivity to picking out the most detailed features. Thus, as samples at higher redshift are considered, and hence with poorer image quality, I expect the vote fraction distributions to also evolve as some classifiers become less able to see the most detailed features. I aim to account for this bias by modelling the vote fraction distributions as a function of redshift, and correcting the higher redshift vote distributions to be as similar as possible to equivalent vote distributions at low redshift.

3.2.4.1 Sample selection for each question

As GZ2 morphologies are classified with a decision tree (see section 2.3), not all of the questions were answered by each of the volunteers for a given galaxy. Answering the spiral arm number question is not appropriate for all of the galaxies in the sample: if a galaxy has no spiral features, yet a volunteer answered the spiral arm question, that galaxy would contribute 'noise' to the answers to that question. To avoid 'noise' introduced by incorrectly classified galaxies, clean galaxy samples are defined with $p > 0.5$. For the first question, this corresponds to all of the galaxies, as each classifier answered that particular question for each galaxy. However, when questions further down the tree are considered, this is not the case. The equivalent $p > 0.5$ for the spiral arm question would only include the galaxies with $p_{\text{features}} \cdot p_{\text{not edge-on}} \cdot p_{\text{spiral}} > 0.5$.
For each of the questions in turn, I define a sample of galaxies with which I will apply the new debiasing procedure. These samples are defined using a cut of $p > 0.5$ (corresponding to $p_{\text{features}} \cdot p_{\text{not edge-on}} \cdot p_{\text{spiral}} > 0.5$ for the spiral arm question for example). A further cut of $N \geq 5$ (where N is the number of classifications) is also imposed to ensure that each galaxy has been classified by a significant number of people to reduce the effects of Poisson noise. In this case, the vote fractions must be the debiased vote values, to ensure each sample is as complete as possible (see section 3.2.2) as I look at each question. The order in which the questions are debiased is important: to define a complete sample of galaxies to be used for the debiasing of a particular question, all questions further up the question tree must have been debiased beforehand.

3.2.4.2 Binning the data

It must be noted that such a method could still be limited by small-number statistics, which is particularly common at higher redshifts. In the case that a feature's vote fraction drops to zero, I can not 'add' votes for a feature – it is only possible to debias the galaxies with $p > 0$, where there is evidence for a feature being present. This remains a problem for the categories where the vote fractions are lowest, such as in the responses to the odd feature question (T06 in Fig. 2.2).
It is expected that the ability to discern the presence of a particular feature will depend on intrinsic galaxy properties. For example, larger, brighter galaxies may be easier to classify over a wider redshift range. Conversely, fainter galaxies may show stronger features, as both overall galaxy morphology (Maller, 2008; Bamford *et al.*, 2009) and spiral arm morphology (Kendall, Clarke & Kennicutt, 2015) have stellar mass dependences. To account for this, the galaxy sample for each question was divided into bins of galaxies with similar overall surface brightness properties. This is achieved by Voronoi binning the sample by the intrinsic properties of size (r-band Petrosian half

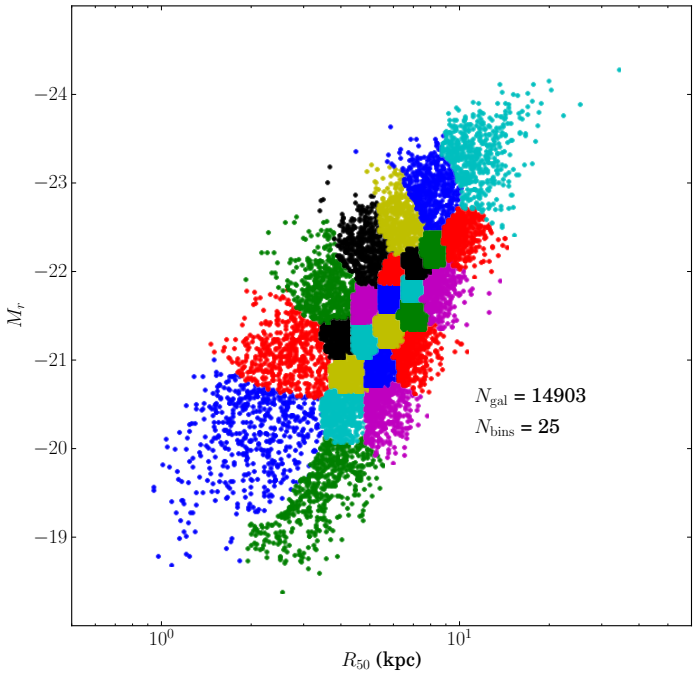

Figure 3.3: Voronoi bins for the 5+ arms (A4) answer to the spiral arm number question (T10). The sample is defined using the method described in section 3.2.4.2, and binned in terms of $\log(R_{50})$ and M_r. Different bins are defined with different colours. Each Voronoi bin is further subdivided into several redshift bins.

light radius, R_{50}) and brightness (r-band Petrosian absolute magnitude, M_r). I used the `voronoi_2d_binning` package from Cappellari & Copin (2003), to ensure the bins will have an approximately equal number of galaxies. Fig. 3.3 shows an example of the Voronoi binning for the 5+ arms response to the arm number question. When Voronoi binning the data for each of the answers, only the galaxies with $p > 0$ are included ($N_{\rm gal}$), meaning that the 'signal' of galaxies is evened out over all of the Voronoi bins. I aim to have ~ 30 Voronoi bins for each of the questions, so the desired number of galaxies in each bin is given by $N_{\rm gal}/30$. After Voronoi binning the data in terms of their intrinsic properties of size and brightness, I further divide each bin into redshift bins, to allow us to study how the vote distributions change with redshift. Each redshift bin is constrained to contain ≥ 50 galaxies, with an exception for the case where the number of galaxies in a Voronoi bin was < 250 – in this case, the galaxies were divided into 5 bins with the same number of galaxies in each redshift bin. This binned data is used for the debiasing methods described in section 3.2.4.3.

3.2.4.3 Modelling redshift bias

For each of the possible responses to each question, a method is applied to correct for the redshift bias in the sample, aiming to make the vote distributions for each answer consistent with redshift. In this thesis, I developed two methods to achieve this task, which are detailed in this section.

The first method I utilised to remove redshift bias simply matches the shapes of the histograms on a bin-by-bin basis. The cumulative distribution for the lowest redshift sample in a given Voronoi bin is used as a reference for how the shape of the histogram would look if it were viewed at low redshift. An example of this method is shown in Fig. 3.4, in which the 'features or disc' answer to the 'smooth or features' question is

considered – in section 3.2.2, I showed that this is an example of where the previous debiasing method failed to reproduce the vote distribution correctly, which may become an issue further down the question tree. For both the low redshift bin and each of the high redshift bins in turn, the vote fractions are ranked in order of low to high. Each of the galaxies in each high redshift bin is then matched to its low redshift equivalent by finding the galaxy with the closest cumulative fraction in the low redshift bin. An example of this technique is shown by the vertical lines of Fig. 3.4. In this case, a galaxy with cumulative fraction of ≈ 0.8 in the high redshift bin has $p_{\mathrm{features}} \approx 0.18$. A galaxy at the same cumulative fraction in the low-redshift bin has $p_{\mathrm{features}} \approx 0.65$, so this is the debiased value assigned to that galaxy. This is repeated for each galaxy and for each of the high redshift bins in turn. Applying a vote fraction threshold for a given response gives the same fraction of the population above that threshold in all of the redshift bins, with the galaxies most likely to have a feature making up the population of galaxies above that threshold.

The main strength of this method is that any vote distribution can be modelled in this way, irrespective of the overall shape. However, a potential weakness is that noise can be introduced due to the discretisation of the data. To limit this issue, each redshift bin has a 'good' signal of ≥ 50 galaxies. This effectively 'blurs' any trends with redshift, and can actually lead to an over-correction of vote fractions, which can be seen in Fig. 3.1c. Although the overall histogram shape is well matched when a slice at $0.08 \leq z < 0.085$ is considered, there are too many galaxies with $p \approx 1$ compared to the low redshift data. This issue is purely caused by the discretisation of the individual bins: although the trends can be modelled overall, any trends within individual bins cannot. If there is a redshift trend *within* a bin, then the fraction of galaxies with the more difficult to see features will preferentially reside in the lower redshift ends of the bins. This effect leads to an overestimate of the number of galaxies with the more difficult to see features. Fig. 3.6a shows the debiased trends of the 'features or disc' question, which was debiased using the 'bin-by-bin' method, which shows that the method slightly over-corrects the redshift trend in the number of galaxies classified with $p_{\mathrm{features}} > 0.5$.

A potential solution would be to bin the data more finely. However, there is no 'ideal' solution to this problem, as fewer galaxies in each bin would mean that the redshift range that each bin occupies is smaller, but the noise in each of the bins is larger.

To correct this problem with the bin-by-bin method, I also developed a technique to model all of the distributions with functions, whose parameters can be modelled with respect to size, luminosity and redshift. For each of the redshift bins, I plot a cumulative histogram of $\log(p)$ against the cumulative fraction. Examples of some of these cumulative histograms are plotted as the solid lines in Fig. 3.5. It can be seen that there is a clear variation in the distributions with redshift. This effect is most prominent in the 4 and 5+ arms responses, where the distributions shift so that there are fewer galaxies with higher vote fractions. Each of the cumulative histograms can be fit to an analytic function, and the parameters of the function modelled in terms of M_r, R_{50} and z. After much experimentation, two functions were used to model the distributions:

$$f(p) = e^{kp^c}, \tag{3.1}$$

and

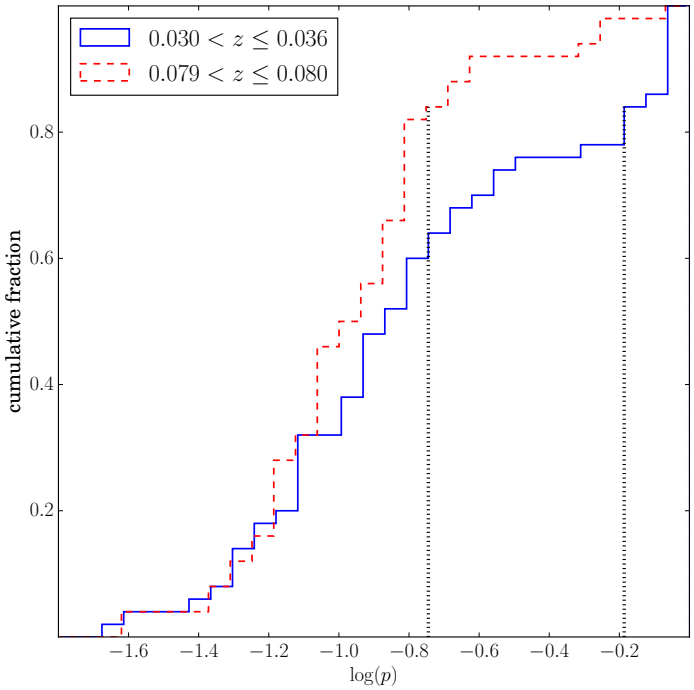

Figure 3.4: An example of vote distributions for an example Voronoi bin for the 'features or disc' answer to the 'smooth or features' question at high and low redshift. Each of the galaxies in the high-redshift bin (red dashed line) is matched to its closest equivalent low-redshift galaxy (blue solid line) in terms of cumulative fraction. The dotted lines indicate the 'matched' values for an example galaxy with $\log(p) \approx -0.8$, and an equivalent low-redshift value of $\log(p) \approx -0.2$ (corresponding to $p_{\rm raw} = 0.18$ and $p_{\rm debiased} = 0.65$). $\log(p)$ is plotted on the x-axis rather than p to make the two distributions more easily discernible.

$$f(p) = \frac{L}{1 + e^{-kp+c}}, \tag{3.2}$$

where k and c are parameters fit to each of the curves. The parameter L in Eq. 3.2 is given by $L = 1 + e^c$ for the function to be correctly bounded (i.e. go through $\log(p) = 0$, cumulative fraction = 1). In practice, Eq. 3.1 does a better job of modelling the distributions with higher overall vote fractions (e.g. the $m = 2$ case), and Eq. 3.2 models the rarer classes better (e.g. all but the $m = 2$ case for the arm number question). Best-fit k and c values are found for each of the bins, indicated by the dashed lines in Fig. 3.5. When fitting, the cumulative histogram is sampled evenly in $\log(p)$ to avoid the fit being weighted to the steepest parts of the curves.

After finding k and c for each of the bins, I attempt to quantify how these parameters change with respect to M_r, $\log(R_{50})$ and z. A 2σ clipping is applied to all of the k and c values to remove any fits where discrepant k or c values have been found. The data is then fitted using a continuous function of the following form:

$$A_{\rm fit}(M_r, R_{50}, z) = A_0 + A_M(f_M(-M_r)) + A_R(f_R(\log(R_{50}))) + A_z(f_z(z)), \tag{3.3}$$

where A corresponds to either k or c and f_M, f_R and f_z are functions that can be either logarithmic ($\log x$), linear (x) or exponential (e^x). The values A_0, A_M, A_R and A_z are constants that parameterise the shape of the fit with respect to each of the terms. When fitting the data, M_r, $\log(R_{50})$ and z correspond to their respective mean values calculated using all of the galaxies in that bin. The best combination of functions is chosen by calculating A_0, A_M, A_R and A_z for each combination of f_M, f_R and f_z, and

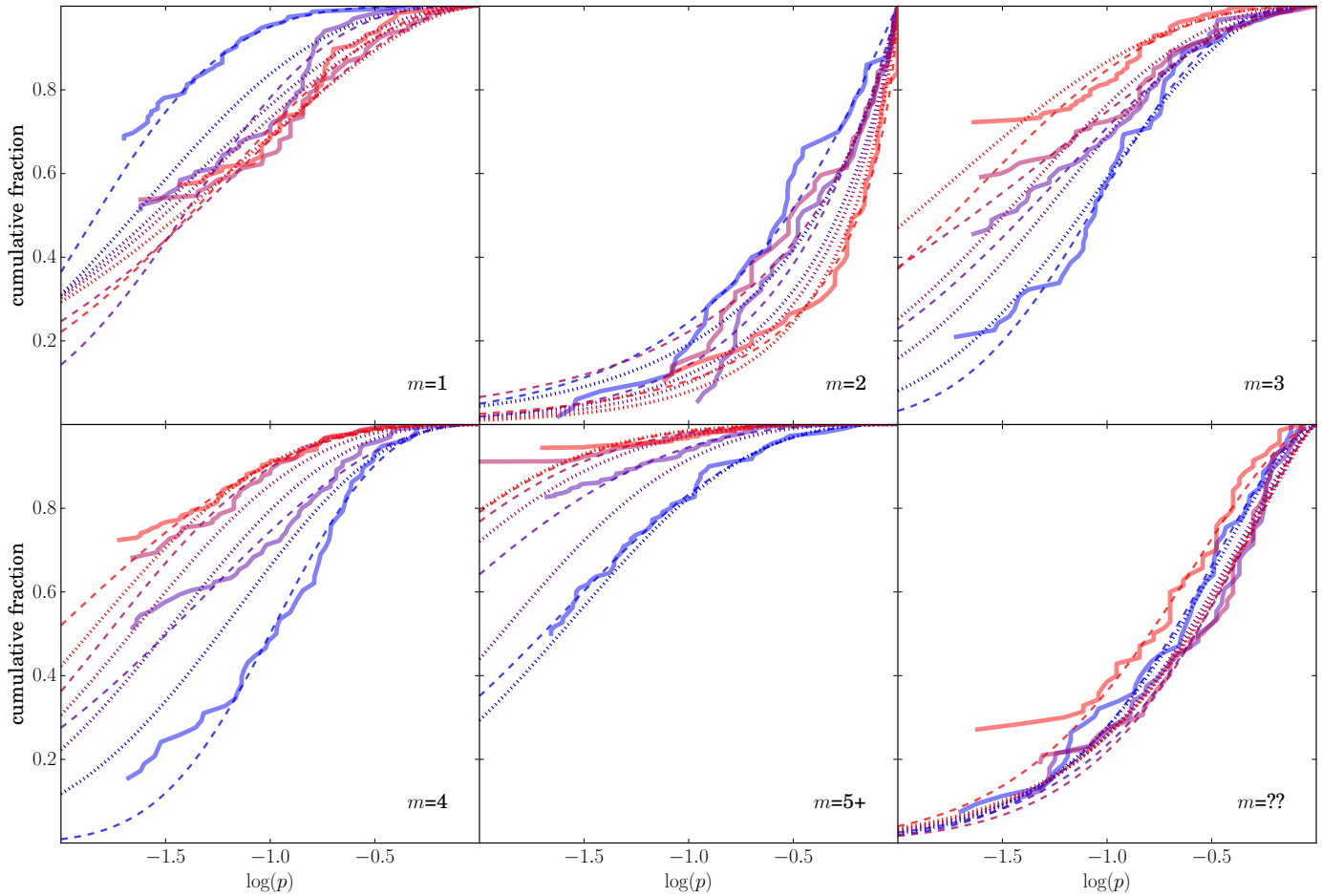

Figure 3.5: An example of a single Voronoi bin function fit for the *arm number* question. The red line indicates the highest redshift bin, and the blue line indicates the lowest redshift bin. The solid lines indicate the raw p histograms, and the dashed lines show the best fit function to each of them. The dotted lines show the corresponding approximation from the continuous fit to the k and c values.

selecting the function that has the lowest squared residuals. I then clip any values with a $> 2\sigma$ residual to this fit and re-fit the data to find a final functional form for k and c with respect to M_r, R_{50} and z. The resulting modelled cumulative histograms for the spiral arm number question are shown by the dotted lines of Fig. 3.5. Limits are also applied to k and c to avoid unphysical fits at extreme values of M_R, R_{50} and z, set by the upper and lower limits of all of the fit k and c values within the 2σ clipping.

After finding a functional form for k and c with respect to M_r, $\log(R_{50})$ and z, each of the galaxies in the sample is debiased to find its equivalent value at low redshift. To do this for an individual galaxy, a cumulative histogram is estimated using $k_{\rm fit}(M_r, R_{50}, z)$ and $c_{\rm fit}(M_r, R_{50}, z)$, where M_r, R_{50} and z are the properties for that particular galaxy, giving the cumulative fraction for a galaxy's raw vote fraction. The equivalent cumulative histogram at $z = 0.03$ (the low redshift limit of the *luminosity-limited sample*) is also found, using $k_{\rm fit}(M_r, R_{50}, 0.03)$ and $c_{\rm fit}(M_r, R_{50}, 0.03)$. The vote fraction for the corresponding cumulative fraction is read off from the low redshift cumulative histogram in a similar way as in the 'bin-by-bin' method, this time using the fitted curves rather than the raw histograms. This is repeated for each of the galaxies in the sample to generate a set of debiased values for the *full sample* of galaxies.

As mentioned previously, function fitting avoids issues related to the discretisation of the data. However, it does introduce its own biases, as an assumption is made that the cumulative histograms can all be well-fit by a particular set of continuous functions. This may not always be the case, so I must consider which of the above methods does the best overall job of removing redshift bias. To do this, the distributions of votes for a low-redshift reference sample are compared to the distributions of higher redshift bins. Using the *luminosity-limited sample*, which is free from redshift bias across all $M_r - R_{50}$ bins, a reference sample with $0.03 \leq z < 0.035$ is defined. The rest of the *luminosity-limited sample* is then split into 10 redshift slices, and the total square residual of the vote fractions from the bin-by-bin debiasing method is compared to the resulting distributions from the fitting methods using the two different functional forms (Eqs. 3.1 and 3.2). The method with the lowest total square residual is used to compute the final debiased values.

3.2.5 Results from the new debiasing method

To test how successful the new debiasing method is at defining populations of galaxies above a given threshold with redshift, the fraction of galaxies with $p > 0.5$ for each of the questions is plotted in Fig. 3.6. It can be seen that in most cases, the new debiasing method does keep the fraction of the population with $p > 0.5$ constant with redshift, as expected. This effect is most evident when looking at the 'spiral' question (T03 in Fig. 2.2), in Fig. 3.6d. The original debiasing method does not adequately remove redshift bias, with fewer galaxies exhibiting spiral structure at higher redshift. However, my new method does keep this fraction approximately constant with redshift, which means the spiral sample will be more complete if we wish to use a thresholding technique to define a sample of galaxies with spiral structure.

Fig. 3.6 only shows the specific example of the threshold of $p > 0.5$. This does not give any insight into the overall vote fraction distribution, which can vary with redshift as shown in Fig. 3.1. Therefore, overall distributions are compared for two redshift slices in Fig. 3.7. The new method does not always 'match' the low and high redshift

samples exactly, an effect that is most obvious in the 'spiral' question. Rather than getting an excess of votes towards the middle of the distribution, excesses are more generally seen at the tails of the distributions at $p \approx 0$ and $p \approx 1$. This is because my method preferentially matches the $p \approx 1$ end of the distribution. As can be seen by the 'spiral = yes' response in Fig. 3.7, the top ends of the distributions are usually correctly matched; the scarcity of votes for the intermediate values of p are caused by the excess of galaxies with $p = 0$ that cannot be corrected.

In order to use the outputs from the new debiasing method described in this chapter, the data is output to a table. Alongside the raw vote fractions, the new debiased vote fractions are listed, as well as a $gz2\_class$ and flags for 'securely' detected spiral or elliptical galaxies – these are galaxies where $p_{\rm spiral}$ or $p_{\rm smooth}$ are greater than 0.8. A portion of the full table is shown in Table 3.1. A string-format overall morphology description is also provided, described in detail in W13.

If the debiasing procedure worked perfectly, then we would expect convergence between the raw and debiased lines as we approach $z = 0$. We can see from the dotted lines that this is not the case for the W13 method (e.g. the 'smooth or features?' question in Fig. 3.6a). This is because the W13 method does not make a low redshift cut, so all values are debiased to $z \approx 0$, rather than $z = 0.03$ which we use in this thesis. We also see that our debiasing method does not converge perfectly for all questions. This is an artefact of the fitting method we employ, which means that we may smooth out subtle variations, and may not perfectly match the behaviour as we approach $z = 0.03$. However, we do see that for the majority of questions the method does a good job of converging close to the expected fractions for $z = 0.03$.

3.2.5.1 The spiral arm number question

As a final check, particular focus is put on the spiral arm number question. The new debiasing procedure must make the sample sizes of galaxies with more spiral arms, which tend to drop off with redshift (see Fig. 3.2), as consistent as possible with redshift. In order to compare different spiral samples, we defined a secure sample of spirals. The sample is defined by selecting galaxies with $p_{\rm features} \cdot p_{\rm not\ edge\text{-}on} \cdot p_{\rm spiral} > 0.5$. A further cut is also imposed where only galaxies with $N_{\rm spiral} - N_{\rm can't\ tell} \geq 5$ are selected, meaning that *at least five people* classified the spiral arm number of each of the spiral galaxies, reducing the effects of noise due to low numbers of classifications. Each galaxy is then assigned a specific spiral arm number m, of either 1, 2, 3, 4 or 5+ arms, depending on which response has the highest debiased vote fraction. For the purpose of these plots, we removed the *can't tell* responses, and the response of the other five questions with the highest fraction was used. The *debiased* vote fractions for each of the arm number responses are hereafter referred to as p_m, where m is either 1, 2, 3, 4 or 5+.

The debiasing procedure applied to this question has shifted the vote fractions for the multiple-armed ($m = 3$, 4, 5+) answers upwards overall, as can be seen in Fig. 3.8.[1]

[1]Cameron (2011) describe a method for estimating binomial confidence intervals for populations. The paper argues that the 'normal approximation' (also described as the Poisson error) significantly underestimates the confidence interval, particularly for small samples. The paper suggests that binomial distributions can be well-modelled by β-distributions, examples of which can be seen in Fig. 1 of Cameron (2011). Errors on binomial quantities (i.e. fractions) are estimated using this method for the remainder of this thesis.

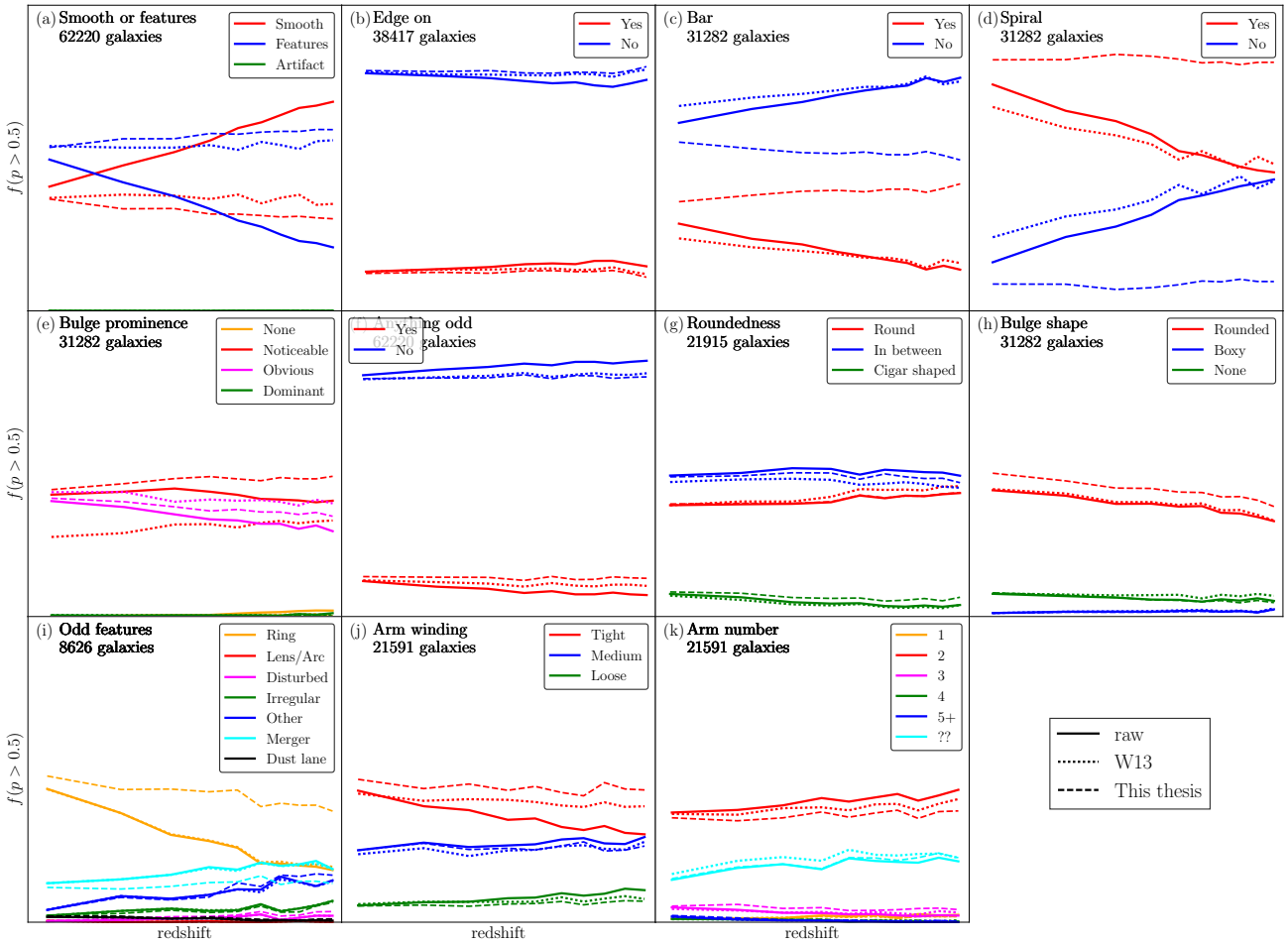

Figure 3.6: Number of galaxies with $p > 0.5$ for each of the questions with vote fractions from using the new debiasing method. The solid lines indicate the raw vote fractions and the dashed lines indicate the debiased vote fractions. The dotted lines indicate the same fractions using the W13 debiasing method. The total sample here is composed of galaxies in the *luminosity-limited sample* with $p > 0.5$ (as described in section 3.2.4.1).

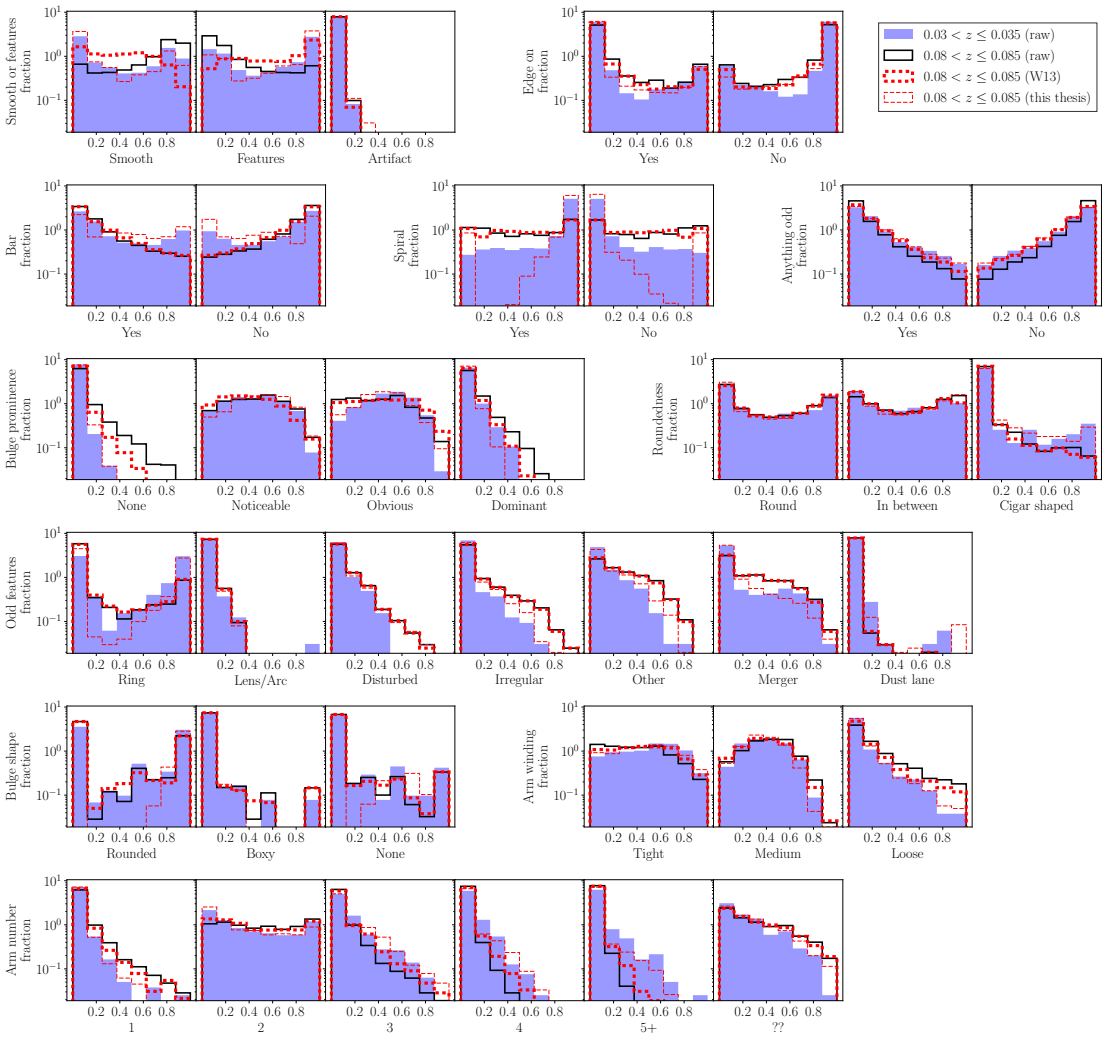

Figure 3.7: Vote distribution histograms for each of the answers in the GZ2 question tree for raw and debiased data from the old and new method. The blue filled histogram shows the distribution for galaxies with $0.03 < z \leq 0.035$, which should have minimal redshift-dependent bias. The black solid, red dotted and red dashed histograms show the distribution of galaxies at $0.08 < z \leq 0.085$ using the raw, W13 debiased, and debiased data from the method described in this chapter, respectively. All samples use only galaxies with $p > 0.5$ (as described in section 3.2.4.1) from the *luminosity-limited sample*.

Table 3.1: Example portion of the output table from the new debiasing method, showing the results from the 'smooth or features' question (T11), and 'smooth' answer (A0). The full, machine-readable version of this table is available at http://data.galaxyzoo.org. The columns are: (1) DR7 object ID in the SDSS database, (2) Right ascension (SDSS DR7), (3) Declination (SDSS DR7), (4) GZ2 classification (described in W13), (5) The number of unique volunteers that classified the galaxy, (6) Total number of unique classifications for all questions – note this is larger than $N_{\rm class}$ as each volunteer is asked a number of questions, (7) Total number of 'smooth' (A0) responses to the 'smooth or features' question (T00), (8) Fraction of the raw votes that responded 'smooth' (A0) to the 'smooth or features' question (T00), (9) Debiased vote fraction, (10) Flag for a given feature – flag = 1 means that the debiased vote fraction to a given question ≥ 0.8.

DR7 ID	RA	Dec	gz2_class	N_class	N_votes	wt_count	wt_fraction	debiased	flag
588017704028406071	15:44:20.31	+08:17:57.3	Sc?t	44	250	12	0.273	0.179	0
587736812059230542	15:27:47.42	+09:37:29.7	Ei	38	126	31	0.832	0.818	1
587728905564061741	07:59:47.02	+35:31:11.8	Ei	59	191	54	0.915	0.864	1
587745404153757824	10:07:27.51	+15:45:21.9	Sb?t	40	290	7	0.175	0.026	0
587739380448952526	14:14:05.56	+31:07:09.1	SBb?t	33	185	11	0.333	0.123	0
587745402529382865	08:03:41.70	+07:33:21.0	SBd?t(m)	38	284	4	0.109	0.098	0
587739158721462480	08:54:58.92	+26:29:24.2	SBb2m(r)	44	346	3	0.068	0.022	0
587739506079170741	12:05:11.01	+32:47:08.3	Sc3t	36	269	2	0.056	0	0
587739382595453056	14:05:53.53	+33:10:15.1	Er	41	129	39	0.951	0.905	1
587729652884439063	16:26:24.95	+42:07:23.1	Ei	43	156	33	0.767	0.74	0
587732470919856500	07:59:53.83	+26:47:20.6	SBc?t	47	296	12	0.255	0.104	0
587738197189984364	08:02:03.96	+55:51:03.2	Ei	45	157	38	0.863	0.818	1
587738066730680717	07:58:26.06	+52:50:04.6	SBb2l(u)	31	177	7	0.226	0.047	0
587732590104019128	11:52:18.78	+59:12:08.3	SBb2m	36	215	11	0.288	0.333	0
588017702394265643	12:06:21.21	+11:26:19.9	SBc2m	50	325	11	0.22	0.282	0
587729777446420748	14:37:43.25	-02:08:25.7	Sb?t	44	264	14	0.318	0.036	0

This has the effect of making each of these samples more complete with redshift, and increasing their respective overall vote fractions. However, in the $m = 5+$ arms case, the sample is still somewhat incomplete, as the overall fraction of galaxies that are assigned to this category decreases with redshift. The vote fractions for $m = 5+$ fall to 0 far more quickly with redshift than any of the other categories, as can be seen from the dashed line in the bottom panel of Fig. 3.8, making the modelling of this redshift bias difficult. Despite this, the fraction of galaxies that make up the $m = 5+$ category are still significantly improved compared to the sample sizes that would be defined using either the raw or previously debiased vote fractions.

Examples of some securely classified spiral galaxies are shown in Fig. 3.9, where each galaxy has a dominant vote fraction of $p_m > 0.8$. The samples of galaxies assigned to each of the different m-values are referred to as the *arm number samples*. As a comparison, a less securely selected sample with $p_m > 0.5$ is also shown in Fig. 3.10. Running from left to right, the galaxies are binned in redshift, and running down the page the galaxies are separated from low to high spiral arm numbers. The main result of this debiasing is that galaxies with low vote fractions for the many-armed answers are included in the many-armed categories when they were not before. As a consequence, the population of $m = 2$ galaxies is less contaminated by galaxies that actually have 3, 4 or 5+ spiral arms. This effect is illustrated in Fig. 3.10, where a selection of spiral galaxies with $0.5 < p_m \leq 0.6$ are shown. It can be seen that the $m = 4$ and $m = 5+$ spiral samples at higher redshift include spiral galaxies that initially had much lower overall vote fractions. As an example, if one were to use the raw vote fractions to select 'secure' galaxy samples with $p_m > 0.5$, then the galaxy in Fig. 3.10y would be unclassified, as its highest value of p_m would only be 0.27 (which is actually for the $m = 4$ response). Using my debiased values, it has a modal value of $p_m = 0.55$ for the $m = 5+$ armed response, so would be in the $m = 5+$ sample. Even in the case of the less secure samples of Fig. 3.10, the galaxies classified as $m = 4$ or $m = 5+$ clearly have more spiral arms than those in the $m = 2$ category.

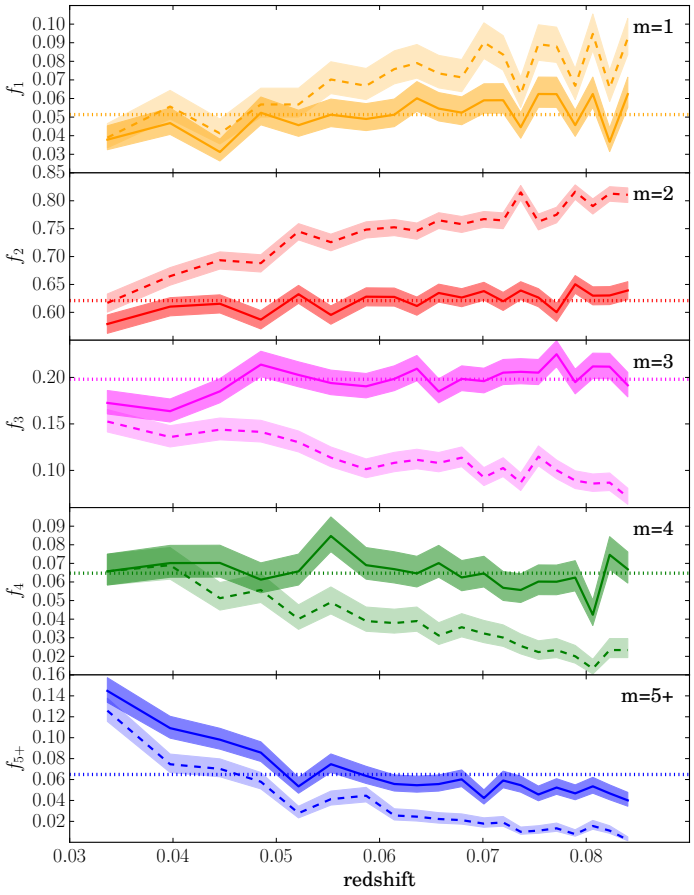

Figure 3.8: Fraction of galaxies in the *luminosity-limited spiral sample* defined in section 4.1.1 classified as having 1, 2, 3, 4, or 5+ spiral arms as a function of redshift. The solid lines indicate the fractions from the debiased values in this chapter, and the dashed line indicates the same fractions using the raw vote fractions. Errors are calculated using the method described in Cameron (2011). The horizontal dotted lines show the mean fractions using the debiased values averaged over all of the bins.

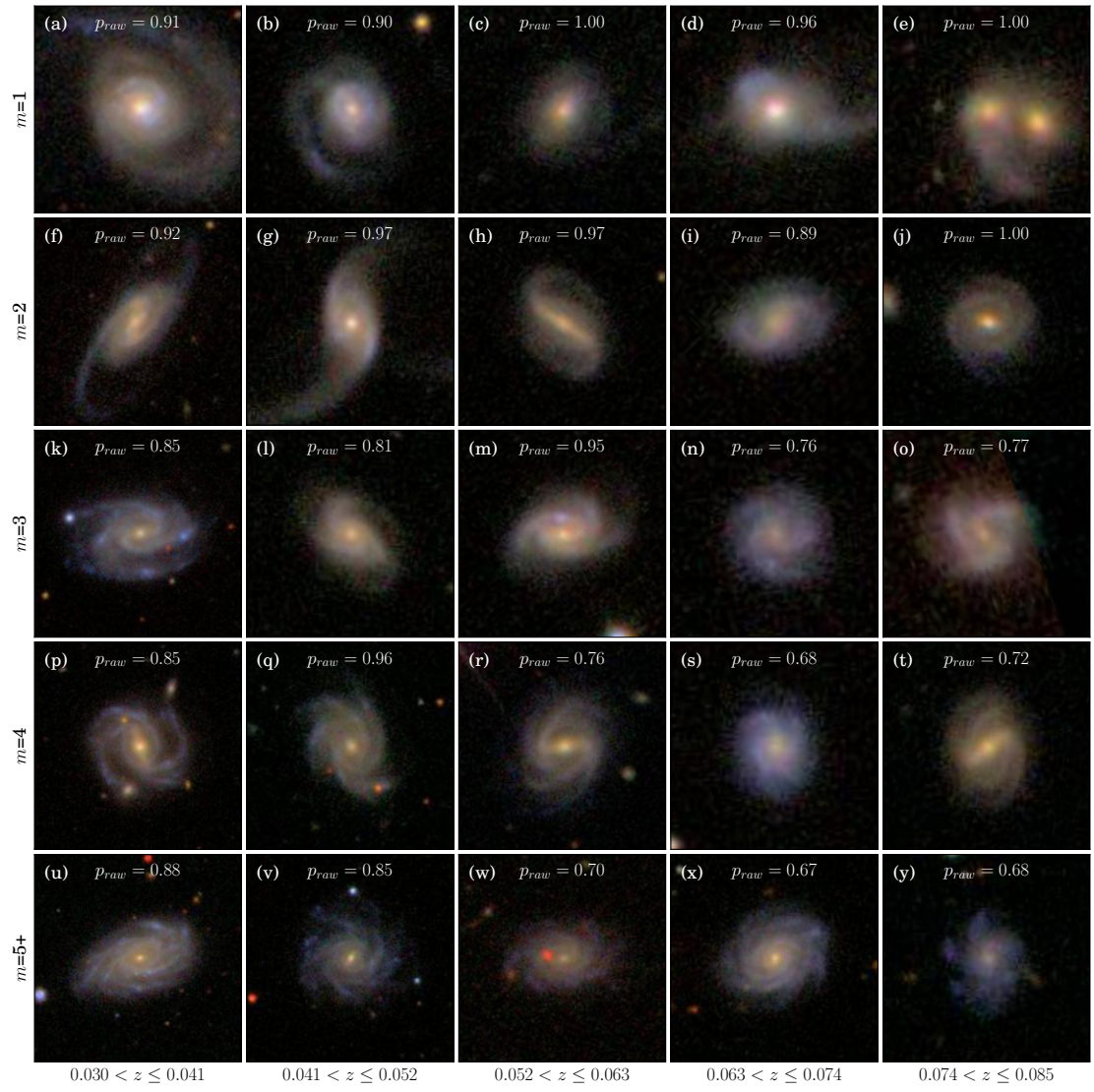

Figure 3.9: A securely classified ($p_m > 0.8$) sample of galaxies classified with $m = 1$, 2, 3, 4 or 5+ spiral arms as a function of redshift. Galaxies are taken from the *luminosity-limited spiral sample* defined in section 4.1.1, are all in the stellar mass range $10.0 < \log(M_*/M_\odot) \leq 11.0$ and are binned by redshift. Each galaxy has a debiased modal arm number vote fraction $p_m > 0.8$.

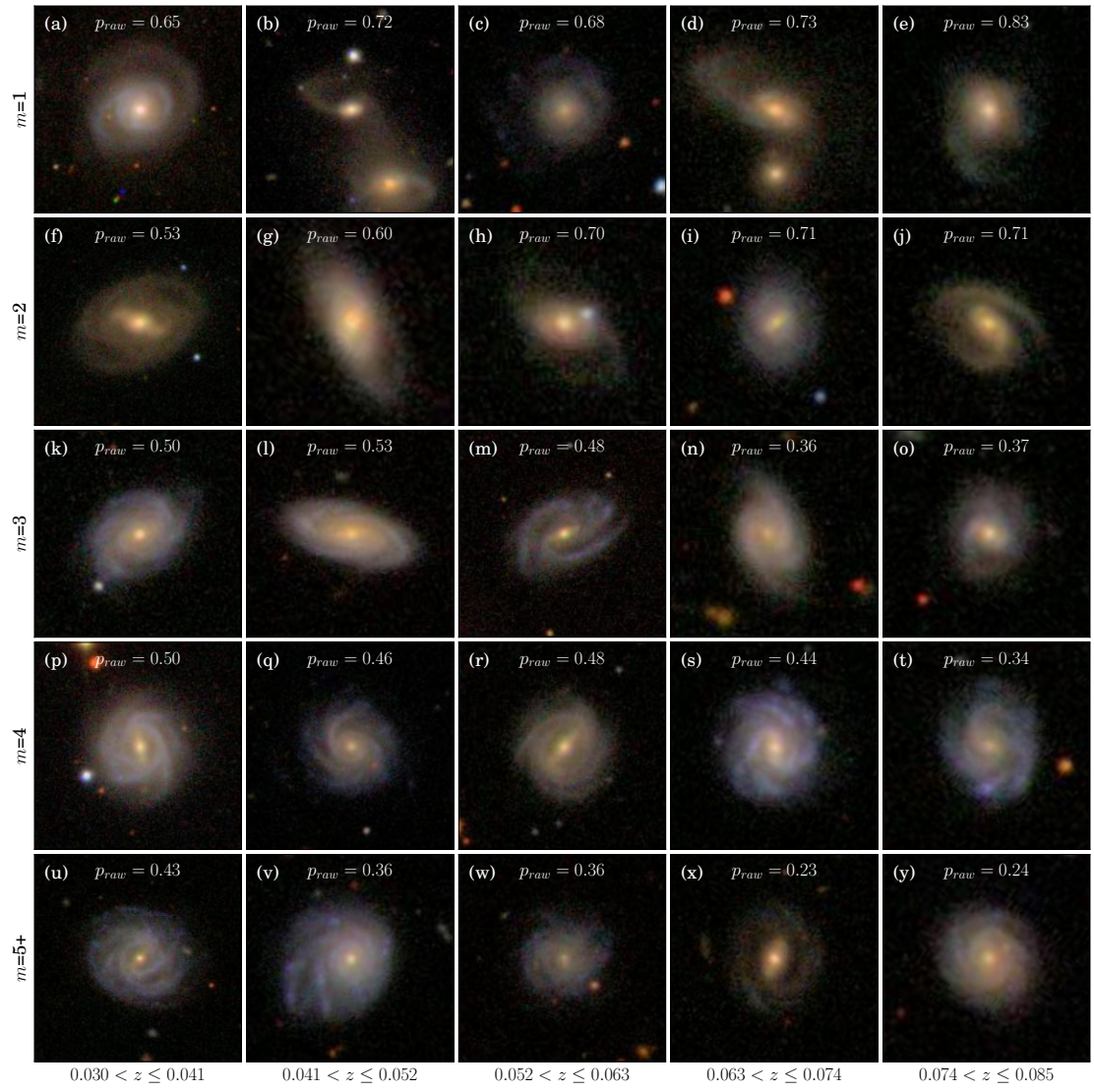

Figure 3.10: A less securely classified ($p_m > 0.5$) sample of galaxies classified with $m = 1$, 2, 3, 4 or 5+ spiral arms as a function of redshift. Galaxies are taken from the *luminosity-limited spiral sample* defined in section 4.1.1, are all in the stellar mass range $10.6 < \log(M_*/M_\odot) \leq 11.0$ and are binned by redshift. Each galaxy has a debiased modal arm number vote fraction of $p_m > 0.5$.

3.3 Measuring spiral arm pitch angles

In order to further quantify the spiral structure in SDSS spiral galaxies, a reliable measure of spiral arm pitch angle is required. In GZ2, the only data available is the response to the 'arm tightness' question (T09 in Fig. 2.2). However, these data cannot be converted to a quantitative measure of spiral arm pitch angle easily, given there are only three qualitative responses to that question. Despite the advances that Galaxy Zoo has made in terms of the study of galaxy morphology in large samples of low-redshift galaxies, measures of spiral arm pitch angles for such large samples remain elusive. Automated methods offer an interesting prospect for measuring pitch angles in large galaxy samples. Although they still cannot measure overall morphological parameters to the same level as human inspection, they do give an opportunity to study spiral arm geometries in more detail (e.g. Considere & Athanassoula 1988; Puerari & Dottori 1992; Saraiva Schroeder *et al.* 1994; Rix & Zaritsky 1995; Davis *et al.* 2012).

I use a machine-based algorithm to measure spiral arm pitch angle. Spiral arcs for all of the galaxies were measured using the automated method from SPARCFIRE (Davis & Hayes, 2014). Given an input image, SPARCFIRE automatically draws isophotal ellipses to deproject the galaxy to be face-on, and make all galaxies the same size. SPARCFIRE then identifies and fits logarithmic spiral arc structures. The code was run on a set of SDSS r-band images. The r-band was chosen as it has the greatest integrated filter response of all of the SDSS $ugriz$ bands. The outputs include several arcs that have been deemed to be a set of spiral arc features in a galaxy. Realistically, only some of the arcs were true spiral arms. An example of this can be seen in Fig. 3.11. Two arcs (1 and 2) clearly map the spiral structure very well, whereas the other two arcs (3 and 4) are instead spurious structures that do not trace a clear spiral arm. In order to use SPARCFIRE, a method was required to distinguish between the two, so that only the real spiral arms contribute to the measured pitch angle.

3.3.1 The training dataset

Previously, Davis & Hayes (2014) used the GZ2 data to decide on how best to select true spiral arms in the SPARCFIRE outputs. They concluded that to match the spiral arm number in GZ2, a length cut of 75 pixels was appropriate. In this thesis, I developed a new technique to identify real spiral arms, which takes into account a number of parameters, rather than simply the length of spiral arms. For this, a visually inspected 'true' dataset was required. With this aim, a subsample of spiral galaxies from the *stellar mass-limited sample* described in section 5.2 was presented to volunteers in an interface called SPIRALSPOTTER,[2] created using the ZOONIVERSE project builder.[3] Volunteers were presented with an image of a spiral galaxy, with the identified arcs from SPARCFIRE overlaid. An example of one of these images is shown in Fig. 3.11. In total, 252 galaxies and 640 arcs had three or more unique visual inspections (i.e. at least three different people classified the galaxy/arm). The volunteers were asked about each SPARCFIRE-identified arc, with six possible responses. They could indicate that arcs were good matches to real spiral arms (good), poor matches to real arms (poor), matches to weak spiral arms (weak), extensions of previously identified arms

[2] www.zooniverse.org/projects/uon/spiral-spotter
[3] www.zooniverse.org/lab

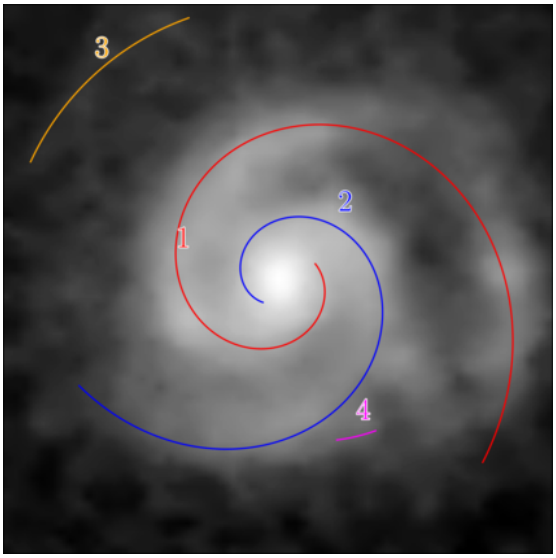

Figure 3.11: An example of a galaxy image presented to volunteers in SPIRALSPOTTER. The grey scale image is the SDSS r-band image of the galaxy deprojected to face-on in SPARCFIRE (see Davis & Hayes 2014 for details of this process). The coloured curves indicate where SPARCFIRE identified arcs in the image, each of which are assigned a number. Each arc was assigned a unique colour and number for volunteer classification.

Table 3.2: Summary of the SPARCFIRE-identified arc statistics identified by SPIRALSPOTTER. People were asked whether arcs were good, poor, weak, extensions, junk or missing. The total number of classifications for each of these classes are shown in the second column. The third column shows the number of spiral arcs classed as one of these categories, using the category which had the greatest fraction of the votes.

class	$N_{\rm clicks}$	$N_{\rm arcs}$
good	1088 (16.4 per cent)	244 (15.1 per cent)
poor	298 (4.5 per cent)	17 (1.1 per cent)
weak	713 (10.8 per cent)	85 (5.3 per cent)
extension	669 (10.1 per cent)	104 (6.4 per cent)
junk	1175 (17.8 per cent)	190 (11.8 per cent)
missing	2673 (40.4 per cent)	678 (41.9 per cent)

(extension), fits to features that were not spiral arms (junk) or not present in the image (missing). The $N_{\rm clicks}$ column of Table 3.2 shows how the total number of votes were distributed for all arcs. Each arc is identified as one of the six categories, depending on which response received the greatest number of votes. The number of arcs in each category was shown in column $N_{\rm arcs}$ of the table (any arcs where the majority vote was split between multiple categories were excluded). It is notable from this table that most of the arcs that SPARCFIRE identified were not good matches to real spiral arcs: only 15 per cent of arcs were classified as 'good'. It was therefore imperative that a technique was developed that removes the poorly matched spiral arcs in SPARCFIRE to obtain accurate spiral arm pitch angles, which I discuss in the section 3.3.3.

3.3.2 Demographics of true spiral arms

Given the statistics from SPIRALSPOTTER, the overall characteristics of good arms are assessed. We select good arcs as those where more than half of the votes were 'good' ($p_{\rm good} \geq 0.5$), with the rest being poor arcs. The resulting distributions are shown in Fig. 3.12. From these distributions, true spiral arms can be identified by the following characteristics:

1. L (arc length): this is the primary way in which true spiral arcs have been distinguished from noise in Davis & Hayes (2014). Generally, it is expected that longer arcs are more likely to be real objects. The SPIRALSPOTTER analysis shows that this is indeed the case.

2. Δr (radial arm range): generally, true spiral arcs are more likely to cover a wider range of the galaxy's radius.

3. $\psi_{\rm arc}$ (arc pitch angle): true spiral arcs seem to preferentially occupy the range $10 < \psi_{\rm arc} < 40°$. This is similar to the range observed in other samples of nearby galaxies (e.g. Seigar *et al.* 2008).

4. $r_{\rm start}$ (initial arc radius): generally, true spiral arcs are more likely to emanate from closer to the centre of galaxies.

5. $r_{\rm end}$ (end arc radius): this parameter appears to have little influence, but true spiral arcs tend to end at $\sim$100 pixels. SPARCFIRE scales all images using an isophotal ellipse fitting routine, so these distances are similar relative to the galaxy size in all galaxies.

6. $\Delta\theta$ (angular extent of the arms): true spiral arms have longer $\Delta\theta$ values, meaning that they wrap further around the centre of the host galaxy.

7. $N_{\rm pixels}$ (number of pixels that the SPARCFIRE arc mask comprises): true spiral arms are drawn through regions made up of more pixels.

These data can be used to identify the overall characteristics of true spiral arms. The data does, however, form a high-dimensional space, meaning a complex model was required to best define true spiral arms and spurious detections.

3.3.3 Identifying true spiral arms

From the SPIRALSPOTTER statistics, good arcs were selected as those where the majority of volunteers indicated that they were good matches to true spiral arms in galaxy images. Thus, each arc had a label of whether it visually corresponded to a real spiral arm or not. I trained two models with the aim of selecting only the spiral arcs from SPARCFIRE that correspond to real arm features. The first model simply aimed to identify a suitable length cut to select only the longest arcs (as in Davis & Hayes 2014). The second model used a more sophisticated support vector machine approach (SVM) trained upon more of the properties associated with each arc.

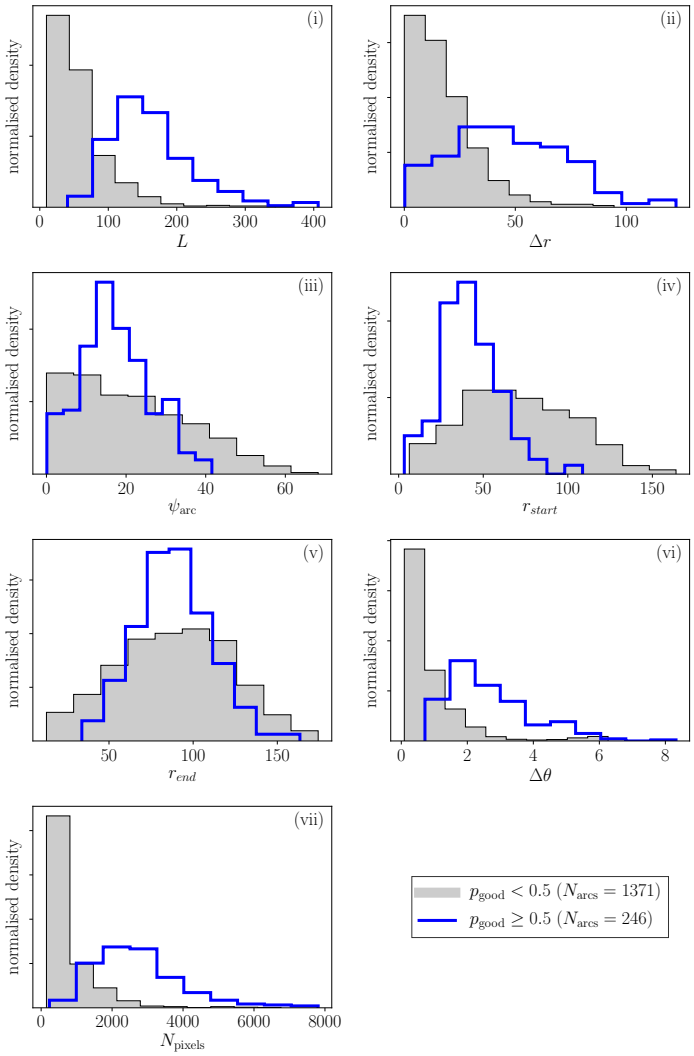

Figure 3.12: Distributions of the demographics of real and spurious spiral arms. This includes distributions of the seven parameters listed in section 3.3.2 for arcs that have been visually identified as poor arcs ($p_{\rm good} < 0.5$, grey filled histograms) and good fits to real spiral arms ($p_{\rm good} \geq 0.5$, blue stepped histograms).

In order to assess how well a classifier is performing, I used two statistics, completeness and contamination. The completeness is given by

$$\text{completeness} = \frac{tp}{tp + fn}, \tag{3.4}$$

and the contamination is given by

$$\text{contamination} = \frac{fp}{tp + fp}. \tag{3.5}$$

The parameters are given by:

- tp: true positive, an arc which was deemed to be good by inspection, and was classified as good by the SVM.
- fp: false positive, an arc which was deemed as poor by inspection, but was classified as good by the SVM.

- tn: true negative, an arc which was deemed as poor by inspection and was classified as poor by the SVM.
- fn: false negative, an arc which was deemed to be good by inspection, but was classified as poor by the SVM.

In theory, there are two ways in which a classifier can be tested – either the completeness can be maximised or the contamination minimised. There is a trade-off between these statistics, in that including more positives in a sample will generally improve the completeness, but also increase the level of contamination. One can also define the accuracy with:

$$\text{accuracy} = \frac{tp + tn}{tp + fp + tn + fn}. \tag{3.6}$$

This is the fraction of arcs which were correctly classified (either negative or positive). A useful piece of information that I also used to identify real arc features is galaxy chirality (whether arcs wind clockwise or counter-clockwise), assuming that all of the arms in a single spiral galaxy must wind the same way. Any galaxies where the chirality between spiral arms did not agree were instead likely to be disturbed systems, rather than normal star-forming spirals which are the focus of the work presented in this thesis. With SPARCFIRE, there are a number of statistics that one can use to quantify the dominant chirality in a galaxy – one can choose to use the chirality of the longest arc, the most common chirality amongst all of the arcs within a single galaxy, or the most common chirality weighted by arc length. In order to select the best statistic, I used the GZ1 statistics – each galaxy was inspected by volunteers, and not only was the presence of spiral arms noted, but also the arm chirality. From the galaxies in the *stellar mass-complete sample*, 4801 were fit in SPARCFIRE (fit state = 'OK'), of which 4779 (99.5 per cent) were visually classified by $\geq$5 people in Galaxy Zoo 1 (GZ1; Lintott *et al.* 2011).

The SPARCFIRE suggested statistic that best agreed with the GZ1 measured chiralities was the 'weighted pitch angle sum'. The sum of all pitch angles was calculated (with clockwise arcs given positive values and counter-clockwise arcs given negative values), and weighted by the arc length. If the sum was positive, then a galaxy is deemed to have clockwise dominant chirality, and if it is negative, the dominant chirality was deemed to be counter-clockwise. There was strong agreement between the SPARCFIRE and GZ1 measured chiralities, with 4112/4779 (85.8 per cent) galaxies in agreement, or 3676/3967 (92.5 per cent) when considering only galaxies where $\geq$ 80 per cent of GZ1 classifiers agreed. I therefore had the option to remove any arcs which do not agree with dominant chirality of the galaxy as measured by SPARCFIRE, if I wished to clean the sample further.

3.3.3.1 Support Vector Machine classification

In order to improve on the simple length cut, a technique was developed to fold in all of the parameters listed in section 3.3.2. The high dimensionality (including seven separate parameters with potential correlations between them) means that defining cuts in the parameters can become complicated. Instead, a machine learning classifier was trained upon the input characteristics defined in section 3.3.2. After evaluating all possibilities, we elected to use a support vector machine or SVM, using the SVM.SVC package from SCIKIT-LEARN (Pedregosa *et al.*, 2011).

A Support Vector Machine (SVM) is a discriminative classifier for separating a hyperplane. Given a set of input parameters, and a labelled input dataset, it computes an optimal boundary or hyperplane between the differently labelled training data (Ivezić *et al.*, 2014). The hyperplane is optimised to maximise the distance between distinct classes or uniquely labelled points. In the case regarded here, the classes or labels were defined as 'true' or 'false' arcs and the space in which the hyperplane was computed was the space defined by the seven input parameters detailed in section 3.3.2. The SVM includes a number of tunable parameters to optimise the fitting, which affect how the vectors are penalised. We set the choice of kernel to be a radial basis function kernel (RBF). There were two tunable parameters of note that needed to be optimised. The first was C, which smoothed the decision boundary between true and false spiral arcs (a lower C value meant that the plane had a simpler form) and the second was gamma, which weighted points by how far away they were from the fitted plane. With little information about which of these parameters would be best, optimal parameters were selected using three-fold cross-validation on the input dataset. To select the ideal set of parameters for the SVM, the accuracy parameter introduced in section 3.3.3 was maximised.

From SPIRALSPOTTER, there were 252 galaxies where each of the arcs were visually inspected (see section 3.3.1). Training the SVM required a training set and an independent test set to check its results. The training set was a randomly selected set of 200 galaxies and the test set was made up of the remaining 52 galaxies (an approximately 80:20 split). The test set was kept separate from the training set and the SVM was trained on four subsamples, including 50, 100, 150 and 200 galaxies respectively, to check its performance as more data was included. The completeness and contamination for the SVM trained on each of the subsamples are shown in Fig. 3.13. Including more galaxies delivers a marginal improvement in terms of completeness, and the contamination stays relatively constant. The SVM was therefore trained on these 200 galaxies, as adding in more galaxies does little to improve the performance of the SVM classifier. This trained SVM was then applied to the full sample of galaxies discussed in section 3.3.1 to identify reliable logarithmic arcs in galaxies.

3.3.4 Results from spiral arm classification

3.3.4.1 Comparison to length thresholding

Using a simple threshold to measure arcs, Davis & Hayes (2014) suggested that 75 pixels is the best length for finding a good agreement between *arc number* and *arm number* as measured by GZ2. Applying this threshold to the 252 galaxies in the SPIRALSPOTTER subset achieved a completeness of 0.97 (0.92 only selecting arcs which agree with the dominant chirality) and a contamination of 0.57 (0.51). Using the trained SVM method, the model achieved a completeness of 0.75 (0.73 only selecting the dominant chirality) and contamination of 0.19 (0.19). For comparison, a length cut of 125 pixels achieved a similar level of completeness of 0.74 (0.72), but suffered from a greater level of contamination, with values of 0.34 (0.28).

Given the statistics listed above, the trained SVM method was preferred as it minimised the level of contamination better than the simple length cut. Any arcs which did not agree with the dominant galaxy chirality were also removed for the reasons discussed in section 3.3.3. In total, 3028/6222 of the spiral galaxies from the *stellar*

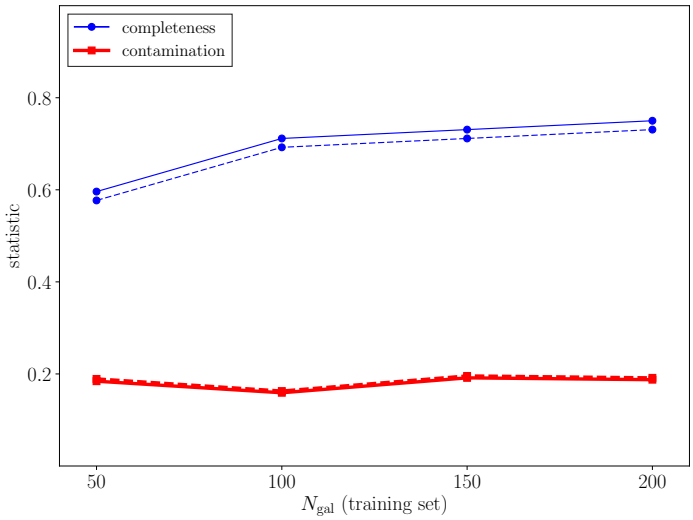

Figure 3.13: Completeness (thin blue line) and contamination (thick red line) of the test set of galaxies, for the SVM trained on samples of different sizes. The solid lines indicate the the statistics when all spiral arcs are considered, and the dashed line shows the same statistics when only arcs with agreement with the dominant galaxy chirality (discussed in section 3.3.3) are considered.

mass-complete sample had one or more reliably identified spiral arc. For the entire sample of arcs in the SPIRALSPOTTER set, there were 163 true positives (SPIRALSPOTTER = good arc, SVM = good arc), 39 false positives (SPIRALSPOTTER = poor arc, SVM = good arc), 83 false negatives (SPIRALSPOTTER = good arc, SVM = poor arc) and 1332 true negatives (SPIRALSPOTTER = poor arc, SVM = poor arc). Some examples of the SPIRALSPOTTER galaxy images with their SPARCFIRE identified spiral arcs are shown in Fig. 3.14.

3.3.4.2 Checking for redshift dependent bias

In GZ2, the effects of redshift-dependent *classification bias* were carefully considered. In section 3.2 a new technique was developed for modelling and removing biases due to resolution and signal-to-noise effects, building on the work of Bamford *et al.* (2009) and W13. This ensured that the GZ2 classifications were stable with redshift. However, such biases are not unique to visual classifications. The fraction of galaxies for which SPARCFIRE finds at least one 'reliably identified' arc (as defined in section 3.3.3.1) is plotted as a function of redshift in Fig. 3.15a. A luminosity-limited sample is used for this analysis, complete for all galaxies in the redshift range $0.02 < z \leq 0.055$ brighter than $M_r = -19.95$. There are 9275 galaxies in this sample. Fewer galaxies have arcs detected by SPARCFIRE at higher redshift: 59 ± 3 per cent of the sample have one or more arcs in the lowest redshift bin at $z \approx 0.02$, whereas only 41 ± 2 per cent have detected arcs at the high redshift limit of the sample at $z \approx 0.055$. SPARCFIRE rarely detects all of the spiral arms in a galaxy, as can be seen in Fig. 3.14, and is less likely to reliably detect spiral arms in lower resolution images, resulting in greater incompleteness at higher redshift.

To address this incompleteness, in section 5.3.2 an alternative method of determining spiral galaxy pitch angle using the GZ2 statistics alone was developed, which can be applied to all the spiral galaxies in the sample. As a further check of whether redshift-dependent incompleteness or measurement issues could bias the results (e.g. if galaxies with looser or tighter arms are more or less likely to be lost), the measured

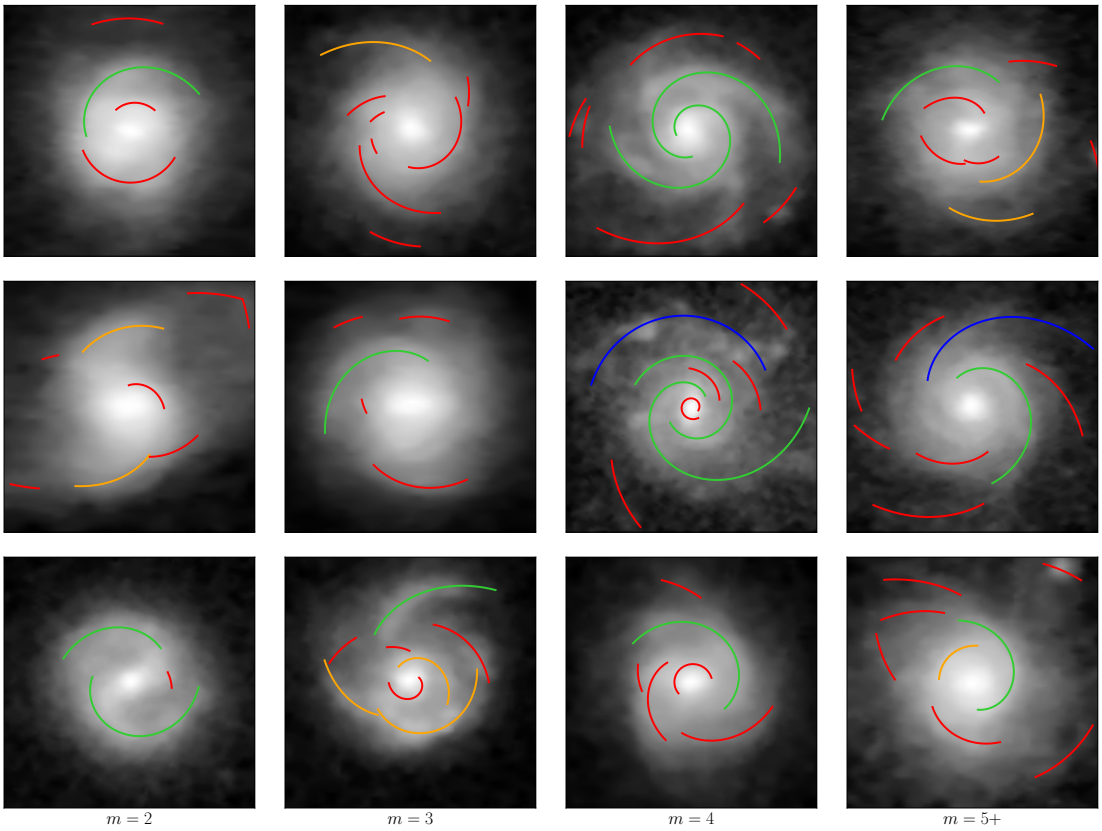

Figure 3.14: Examples of true positive, false positive, false negative and true negative arcs identified by SPIRALSPOTTER. Galaxies were a randomly selected subsample of galaxies from the SPIRALSPOTTER sample with $m = 2$, 3, 4 or 5+ spiral arms as identified by GZ2. Arcs are coloured by their status as true positive (SPIRALSPOTTER = good arc, SVM = good arc, lime green arcs), false positive (SPIRALSPOTTER = poor arc, SVM = good arc, blue), false negative (SPIRALSPOTTER = good arc, SVM = poor arc, orange) and true negative (SPIRALSPOTTER = poor arc, SVM = poor arc, red).

pitch angles are compared vs. redshift in Fig. 3.15b. There is no significant redshift trend in either the SPARCFIRE or GZ2-derived pitch angles. These checks, along with the GZ2 calibrated measurements, ensure that the results are robust to the details of the pitch angle measurements.

3.3.4.3 Completeness vs. spiral arm pitch angle

An artefact of using the SVM classifier may be that our level of completeness and contamination may show residual dependencies on other arc properties. Of most concern is spiral arm pitch angle: we may be p mis-classifying spiral arcs with certain properties. In order to check this, I compared the completeness and contamination of the 252 galaxies from the training dataset (see section 3.3.1) in bins of ψ, the spiral arc pitch angle. The level of contamination remains steady at ≈ 0.2 for all spiral arm pitch angles. The level of completeness is constant in the range $10° \lesssim \psi \lesssim 40°$, at ≈ 0.8. We do see a slight drop off at the extrema of $\psi < 10°$ and $\psi > 40°$ to completenesses of ≈ 0.4. However, these affect only the very edges of the range of pitch angles we see, and are rare cases of true spiral arms as can be seen from Fig. 3.12.

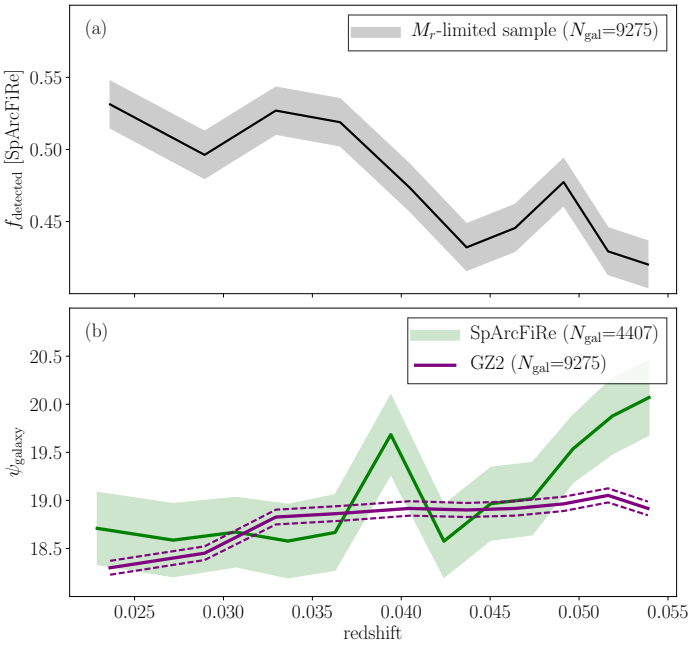

Figure 3.15: (a) Fraction of galaxies with at least one good arc as a function of redshift. The solid line indicates the fraction in each bin, and the shaded region shows the error as calculated from the method described in Cameron (2011). Fewer galaxies have detected arcs in SPARCFIRE at higher redshift. (b) Average pitch angle as a function of redshift for SPARCFIRE measured pitch angles (green line with filled errors) and GZ2 measured pitch angles discussed in section 5.3.2 (purple line with dashed errors). The lines show the mean for each bin, and the errors indicate one standard error on the mean.

3.4 Matching in stellar mass

It is often desirable to compare the properties of samples irrespective of their stellar mass. For this reason, we often like to select galaxies so that their stellar mass distributions match. A technique I employed in section 4.1 was to bin the galaxies in terms of stellar mass, and select the appropriate number of galaxies from each bin to match the distributions. Although this does an adequate job, it relies on a user-defined bin size. If the bins are too large, then any subtle features in the stellar mass distributions will not be seen; if the bins are too fine, then we may overfit the noise in the distribution. This is often described as a trade-off between *variance* and *bias*. For the work described in chapter 5, I developed a new method, with the aim of removing any user input and matching distributions automatically.

To mass-match, I used a method that we call KDE-matching.[4] This process matches two distributions by a given statistic, which I call the *reference sample* and the *match sample*. In the example of chapter 5, the *reference sample* is the $m = 4$ subsample, and the *match sample* is each of the other subsamples in turn. We convolve each distribution with a kernel density estimate (KDE) using the KERNELDENSITY package from SKLEARN. In a KDE, each point is represented by a kernel with a given bandwidth, rather than an individual point.

KDEs of the *reference sample* and the *match sample* are produced, using Gaussian kernels with the ideal bandwidth selected via five-fold cross validation, balancing bias (underfitting caused by selecting a too wide kernel that washes out subtleties in a distri-

[4]The source code for this method is publicly available at http://doi.org/10.5281/zenodo.815850

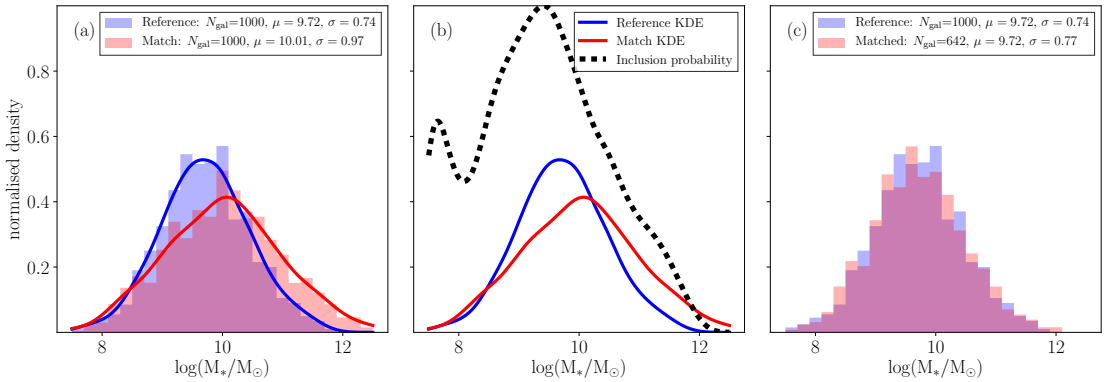

Figure 3.16: Example of the KDE-matching process. (a) Distributions of two Gaussian stellar mass distributions. The filled histograms show the distributions, and the solid lines indicate the KDE of the distributions. (b) KDEs for the reference and match distributions (thinner solid lines) and the resulting probability of inclusion as a function of stellar mass is shown by the thicker dotted black line. (c) Resulting distributions following matching.

bution) and variance (selecting a too narrow kernel that overfits causing a noisy distribution). The *match* KDE is then divided by the *reference* KDE, and each galaxy in the *match sample* now has an associated probability. These probabilities are normalised so that the 95th percentile of all of the *match* probabilities equals one. All galaxies in the top 5th percentile are set to probability $p = 1$ and all other galaxies have probabilities $0 < p < 1$. Galaxies are then sampled from the *match sample*, with probability, p of being included in the final *matched sample*.

This process is shown in Fig. 3.16. Two example samples are created, each with 1000 galaxies. The first is centred on 9.75 with spread 0.75, the second centred on 10.00, with spread 1.00. In Fig. 3.16a, we model each distribution with a KDE: critically, this requires no input from the user, and the optimum distribution is automatically calculated. In Fig. 3.16b, we show the result of dividing the match distribution by the reference distribution – there is an excess of massive galaxies in the match distribution, so we sample so that these galaxies are less likely to be included in the final matched sample. Sampling from the match sample with the probability given in Fig. 3.16b gives the final distributions in Fig. 3.16c: the mass bias has been effectively removed.

Chapter 4

Demographics and star formation properties of spiral galaxies by arm number

The analysis and results in this chapter have been previously presented in Hart *et al.* (2016) and Hart *et al.* (2017a). The work makes use of the debiased statistics first presented in Hart *et al.* (2016) and chapter 3 of this thesis to study the overall demographics of spiral galaxies with respect to their arm number (Hart *et al.*, 2016) and to understand the star formation properties of spiral galaxies with varying numbers of spiral arms (Hart *et al.*, 2017a). The work was undertaken by the author of this thesis, with advice from Steven Bamford and the co-authors of the aforementioned papers.

4.1 The demographics of spiral galaxies with respect to spiral arm number

Spiral galaxies are the most common type of massive galaxy observed in the local Universe (Nair & Abraham 2010; Lintott *et al.* 2011; W13; Kelvin *et al.* 2014a). However, the term 'spiral' encompasses a large range of galaxies with different visual morphologies. Of principal concern in this chapter is how galaxy demographics depend on spiral arm number. Overall correlations with morphology exist in the local galaxy population, with earlier type galaxies being redder (and thus less star-forming, Holmberg (1958); Roberts & Haynes (1994)), more luminous (and thus more massive, Binggeli, Sandage & Tammann (1985, 1988)) and more common in higher density environments (Dressler, 1980; Postman & Geller, 1984; Whitmore & Gilmore, 1991; Whitmore, Gilmore & Jones, 1993) than later type spiral galaxies. The main aim of this chapter is to look for similar trends looking exclusively at spiral arm number in galaxies. Of particular interest is the difference between two-arm 'grand design' and many-arm spiral galaxies.

4.1.1 Sample selection

For the work presented in this chapter, stellar masses are taken from the Baldry *et al.* (2006) calibrations. The work also draws upon the SDSS DR7 rest-frame $ugriz$ pho-

tometry discussed in chapter 2.

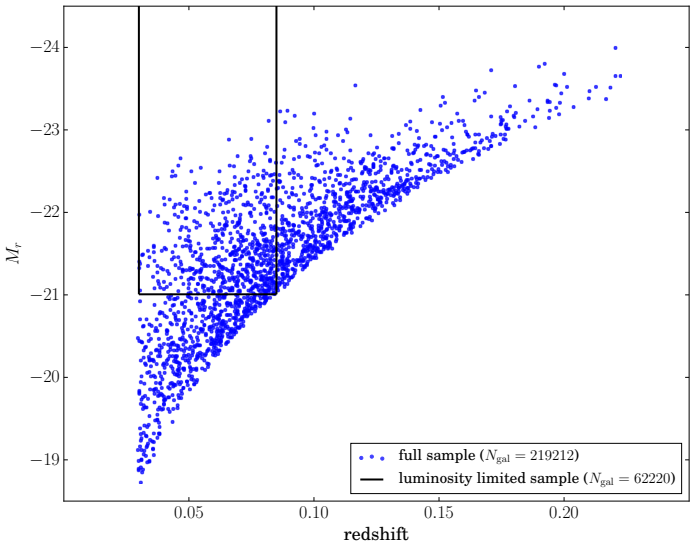

Figure 4.1: Limits of the *Luminosity-limited* sample for studying spiral arm demographics. The r-band luminosity vs. redshift distribution of the *full sample* is shown by the blue points, with the region enclosing the $0.03 < z < 0.085$, $M_r \leq -21$ *luminosity-limited sample* indicated by black lines.

In order to study galaxy properties in a representative manner in this chapter, I define a *luminosity-limited sample*, complete within a given redshift range and above a certain luminosity. The upper redshift limit is effectively a trade-off between sample size and sample reliability. A larger upper redshift limit means that more galaxies are included in the sample, yet morphologies are less likely to be reliable at higher redshift (see section 3.2.2 for a description of these issues). A higher upper redshift limit also introduces incompleteness issues – only the brightest galaxies are luminous enough to be included in the sample at higher redshift. For this work, an upper redshift limit of 0.085 was selected, which is complete for galaxies brighter than $M_r = -21.0$. These limits approximately maximize the sample size, given the $m_r \leq 17$ limit on the *full sample*. The luminosity versus redshift distribution of the *full sample*, and the limits of the *luminosity-limited sample*, are shown in Fig. 4.1. The lower redshift limit avoids a small number of galaxies with very large angular sizes, and hence accompanying morphological, photometric and spectroscopic complications. The upper redshift limit also corresponds to that for which there is reliable galaxy environmental density data from Baldry *et al.* (2006), which will be used in section 4.1.4

The *luminosity-limited sample* is incomplete for the reddest galaxies at $\log(M_*/M_\odot) < 10.6$ (calculated using the method in Bamford *et al.* 2009). With this in mind, a *stellar mass-limited sample* of 41,801 galaxies is also considered, created by applying a limit of $\log(M_*/M_\odot) \geq 10.6$ to the *luminosity-limited sample*.

Galaxies were selected as spiral using the debiased GZ2 statistics, by selecting galaxies with $p_{\rm features} \cdot p_{\rm not\,edge-ok} \cdot p_{\rm spiral} > 0.5$ and $N_{\rm spiral} - N_{\rm can't\,tell} \geq 0.5$ as described in section 3.2.5.1. The spiral arm number was defined as the response to the 'arm number' question which had the greatest fraction of the debiased votes. The overall numbers of galaxies with different arm numbers, and their relative fractions, stellar masses, colours and environmental densities are shown in Table. 4.1.

Table 4.1: Overall properties of galaxy populations with different numbers of spiral arms. The number of galaxies with 1, 2, 3, 4 and 5+ arms are shown for both the *luminosity-limited* and *stellar mass-limited spiral samples*. Mean stellar masses, colours and local densities are shown for each of the populations, with 1σ standard deviations indicated in parentheses. Errors on the mean ($\sigma/\sqrt{N_{\rm debiased}}$) are all of order < 0.01.

m	$N_{\rm raw}$	$f_{\rm raw}$	$N_{\rm W13}$	$f_{\rm W13}$	$N_{\rm debiased}$	$f_{\rm debiased}$	$M_*(\log(M/M_\odot))$	$g-i$	$\Sigma(\mathrm{Mpc}^{-2})$
Luminosity-limited	12554	1.00	14297	1.00	17957	1.00	10.62 (0.25)	0.82 (0.17)	-0.24 (0.56)
1	563	0.04	670	0.05	926	0.05	10.63 (0.28)	0.83 (0.19)	-0.25 (0.54)
2	9044	0.72	10073	0.7	11157	0.62	10.63 (0.24)	0.86 (0.17)	-0.21 (0.57)
3	1778	0.14	2158	0.15	3552	0.2	10.59 (0.26)	0.75 (0.15)	-0.28 (0.53)
4	615	0.05	751	0.05	1162	0.06	10.60 (0.26)	0.74 (0.15)	-0.30 (0.51)
5+	554	0.04	645	0.05	1160	0.06	10.65 (0.27)	0.75 (0.16)	-0.30 (0.53)
Stellar mass-limited	6683	1.00	7226	1.00	9413	1.00	10.81 (0.16)	0.91 (0.14)	-0.18 (0.57)
1	290	0.04	331	0.05	500	0.05	10.84 (0.16)	0.94 (0.14)	-0.19 (0.53)
2	4852	0.73	5191	0.72	6059	0.64	10.80 (0.15)	0.94 (0.13)	-0.15 (0.59)
3	886	0.13	991	0.14	1654	0.18	10.82 (0.16)	0.83 (0.12)	-0.23 (0.53)
4	335	0.05	366	0.05	565	0.06	10.82 (0.16)	0.82 (0.12)	-0.25 (0.53)
5+	320	0.05	347	0.05	635	0.07	10.85 (0.18)	0.82 (0.13)	-0.26 (0.53)

4.1.2 Fraction of galaxies with different arm numbers

Generally, spiral arm multiplicity is not usually studied with respect to a specific arm number, with Elmegreen-type classifications usually preferred as discussed in section 1.2. Spiral arm multiplicity does not map exactly to a specific Elmegreen-type for two reasons. Firstly, the arm number itself does not give any indication of the prominence of spiral arms, so cannot be used to distinguish between a galaxy with many well-defined arms and one with more flocculent spiral structure, which are usually defined differently (Elmegreen & Elmegreen, 1982, 1987a). The second issue is that arm structure may not necessarily be consistent at all radii (Grosbøl, Patsis & Pompei, 2004) or at all wavelengths (Block & Wainscoat, 1991; Block *et al.*, 1994; Thornley, 1996) within a galaxy disc, meaning that assigning a single m-value of arm number may not give a complete picture of the overall spiral arm structure. The most 'easy-to-map' categories are the $m = 2$ population and galaxies classified as grand design in the literature, as grand design structure is usually associated with two well-defined arms across the entire disc (Elmegreen & Elmegreen, 1982). In the *luminosity-limited spiral sample*, 62.1 ± 0.4 per cent of the galaxies with $10.0 < \log(M_*/M_\odot) < 11.5$ show two-armed spiral structure. This result is consistent with optical visual classifications (Elmegreen & Elmegreen, 1982) and IR classifications (Grosbøl, Patsis & Pompei, 2004), which suggest that ~ 60 per cent of local spiral galaxies exhibit grand design spiral structure.

4.1.3 Comparison of stellar masses

Galaxy stellar mass is known to correlate with galaxy morphology (Bamford *et al.*, 2009; Kelvin *et al.*, 2014b), and spiral galaxy Hubble type (Muñoz-Mateos *et al.*, 2015). It has been demonstrated that the *central* mass of spiral galaxies can play a role in the type of spiral structure exhibited in spiral galaxies. In particular, the pitch angle of spiral arms is related to both the SFR in spiral galaxies (Seigar, 2005), and the central mass concentration of the spiral galaxies (Seigar *et al.*, 2006, 2014). Total galaxy stellar mass has also been found to correlate with observed spiral structure, with the strength of the $m = 2$ mode in spiral galaxies being stronger in galaxies with greater physical size (Elmegreen & Elmegreen, 1987a) and stellar mass (Kendall, Clarke & Kennicutt, 2015). In this section, any stellar mass differences between galaxies with different spiral arm numbers in a complete, low-redshift *luminosity-limited sample* are investigated.

The method for measuring stellar mass, described in Baldry *et al.* (2006), uses the $u-r$ and M_r values from the SDSS. To avoid contamination of galaxies with uncertain stellar masses due to poor flux detection in these bands, only galaxies with $F/\delta F > 5$ (where F is the flux in a given band, and δF is the equivalent error on the flux) in both u and r are included in this analysis.

The distributions of stellar mass for each of the *arm number samples* are shown in Fig. 4.2a. The overall distributions for each of the galaxy samples show that there is little evidence for a dependence of spiral arm number with respect to host galaxy stellar mass; each of the samples contains galaxies across the entire range of stellar mass from $10.0 \lesssim \log(M_*/M_\odot) \lesssim 11.5$. A slight excess of low stellar mass galaxies is found in the $m = 3$ and $m = 4$ samples, as well as an excess of high stellar mass spiral galaxies for the $m = 5+$ sample.

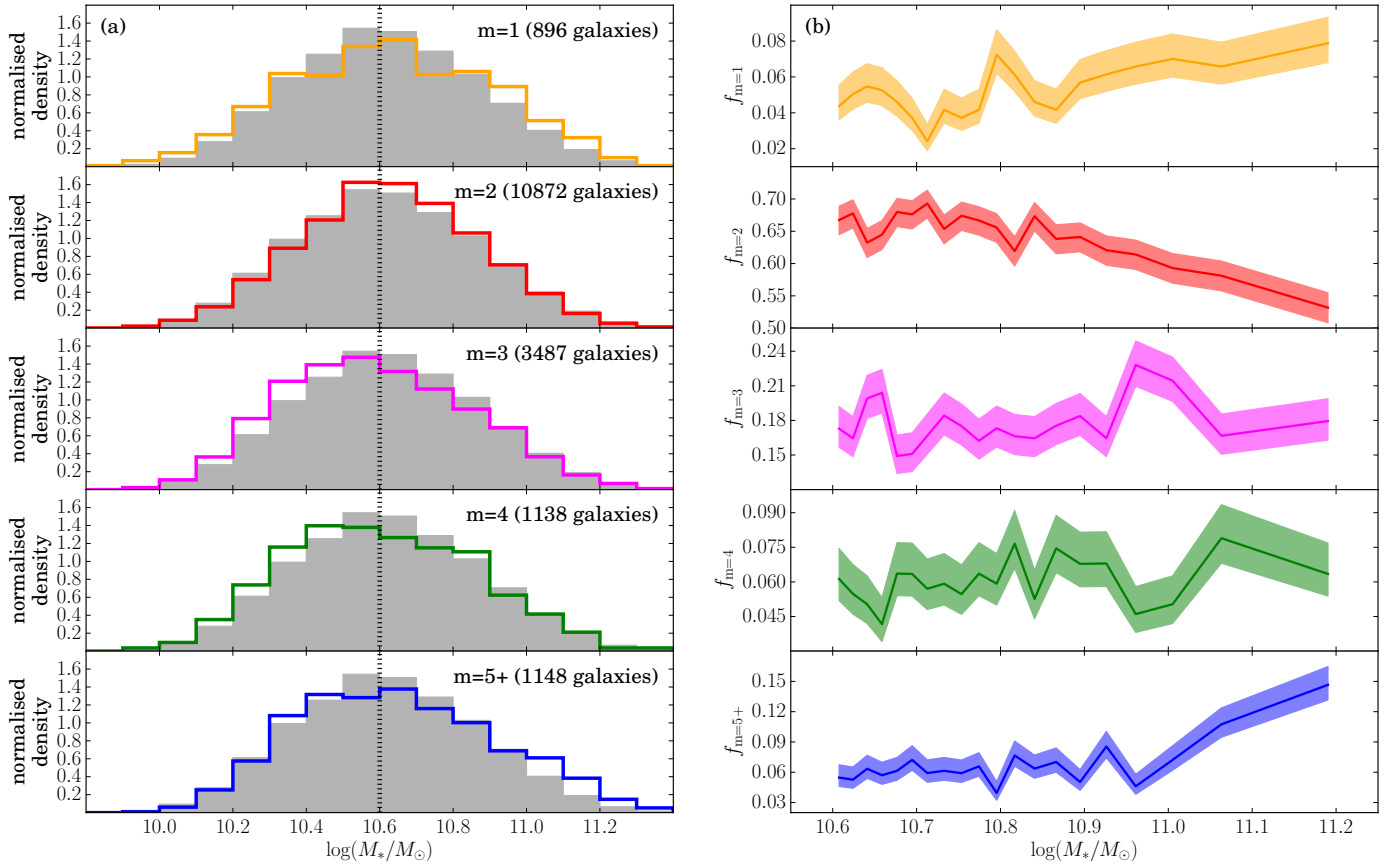

Figure 4.2: Stellar mass dependences with respect to spiral arm number. Left: distributions of stellar mass for the *luminosity-limited spiral sample*. The solid lines indicate the distributions for each of the *arm number samples*. The grey filled histograms show the equivalent distribution for all of the spiral galaxies for reference. The black dotted line indicates the stellar mass values above which the sample is complete in stellar mass. Right: fraction of the *stellar mass-limited spiral sample* classified as having each spiral arm number, in 20 bins of stellar mass. The shaded regions indicate the 1σ standard error on the mean calculated using the method described in Cameron (2011).

The distributions of Fig. 4.2a show the distributions from the *luminosity-limited spiral sample*, so are therefore incomplete for galaxies with stellar masses lower than $M_* \lesssim 10^{10.6} M_\odot$ (see section 4.1.1), indicated by the black dotted line. As we shall see in section 4.1.5, lower mass galaxies are bluer, and hence more luminous for a given stellar mass. They are thus over-represented at low mass in a luminosity-limited sample. To look for trends in terms of stellar mass, the overall fraction of the *stellar mass-limited spiral sample* is shown in Fig. 4.2b. Now, it can be seen that there do appear to be some trends between spiral arm number and host galaxy stellar mass. A significant increase in the fraction of galaxies with 5+ spiral arms is observed from the overall mean value of 0.068 ± 0.002 to 0.15 ± 0.02 for the highest stellar mass bin of $\log(M_*/M_\odot) = 11.2 \pm 0.1$. Here the $\pm$ denotes one standard error on the mean. The $m = 3$ and $m = 4$ samples hint at similar, but much weaker trends. Conversely, the fraction of galaxies with two spiral arms decreases from 0.642 ± 0.004 for the total population to 0.53 ± 0.02 in the highest stellar mass bin.

One possibility why higher mass spirals may exhibit more spiral arms is that this could purely be an effect from the visual classifications. It has already been identified that the many-armed spiral features are the most difficult to detect, so may be more easily identifiable in the largest, brightest spiral galaxies. Spiral arms are already known to have greater amplitudes (i.e. be more prominent) in galaxies with larger stellar masses (Kendall, Clarke & Kennicutt, 2015). It has already been demonstrated in section 3.2.5.1 that the $m = 5+$ sample is the most incomplete of the samples divided by spiral arm number. Thus, galaxies with greater stellar mass, that are therefore larger and brighter, may be preferentially put in this category, even after debiasing.

Another interesting scenario may be that the population of galaxies with the highest stellar mass are a population of unquenched spiral galaxies as in Ogle *et al.* (2016). Such galaxies still have their discs intact, so have no signatures of tidal interactions. As galaxy-galaxy interactions have been linked to both the inducement of two-armed spiral structure (Dobbs *et al.*, 2010; Semczuk, Łokas & del Pino, 2017), and the depletion of gas and therefore quenching (Di Matteo *et al.*, 2007; Li *et al.*, 2008), then one may conclude that the discs of these galaxies have not been disturbed. A possible explanation for this is that lower-mass galaxies are more susceptible to environment effects (Bamford *et al.*, 2009), so high mass discs are undisturbed, star-forming, many-arm galaxies.

4.1.4 Local environment

It is already well established that there is a clear dependence of the type of spiral structure that galaxies exhibit with respect to their local environment. Observational evidence from comparison of visually classified galaxies has found that grand design galaxies are more prominent in high density group environments and in binary systems where a close companion galaxy is present (Elmegreen, Elmegreen & Dressler, 1982; Elmegreen & Elmegreen, 1987b; Seigar, Chorney & James, 2003; Elmegreen, 2011). These results suggest that a mechanism is responsible for the transformation of spiral structure as galaxies enter the highest density environments, with a plausible explanation being that two-armed spiral structure is the result of a recent gravitational interaction. N-body modelling of galaxies has shown that two-armed spiral structure can occur as a result of galaxy-galaxy interactions (Sundelius *et al.*, 1987; Dobbs *et al.*,

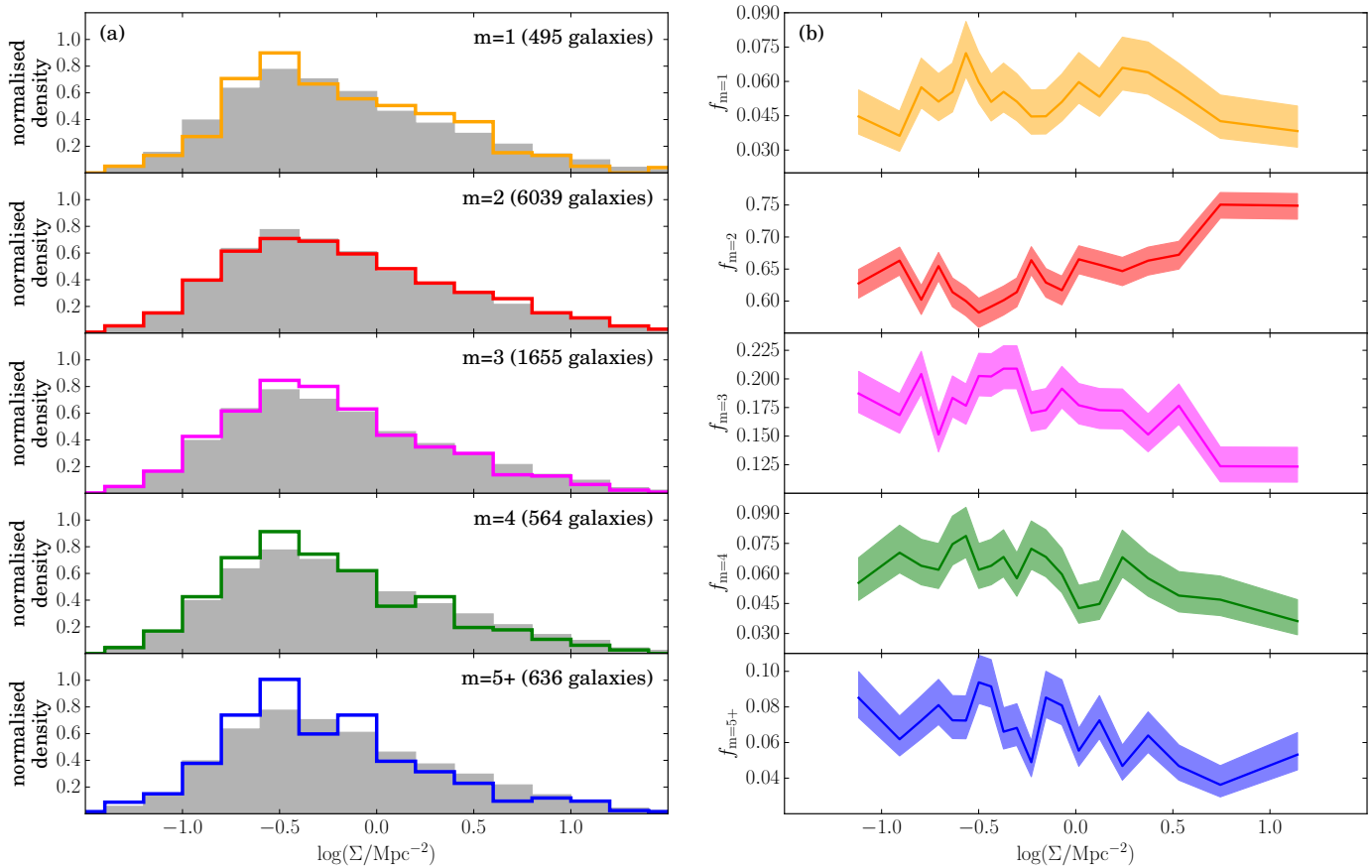

Figure 4.3: Dependence of spiral arm number on local environmental density. Left: distributions of local density (Σ) for the *stellar mass-limited spiral sample*. The solid lines indicate the distributions for each of the *arm number samples* for each of arm numbers. The grey filled histograms show the equivalent distribution for all of the spiral galaxies for reference. Right: fraction of the *stellar mass-limited spiral sample* classified as having each spiral arm number, in 20 bins of Σ. The shaded regions indicate the 1σ standard error on the mean calculated using the method described in Cameron (2011).

2010). However, the timescales of the persistence of such structures are thought to be relatively short-lived (Oh *et al.*, 2008; Dobbs *et al.*, 2010), meaning that an enhancement in the fraction of grand design galaxies is only observed in the highest density environments where interactions can happen on a frequent enough basis to sustain such structures (Elmegreen & Elmegreen, 1987a).

To compare spiral arm structure as a function of environment, we use a mean of Σ_4 and Σ_5 as an estimate of local density, as in Baldry *et al.* (2006) and Bamford *et al.* (2009), denoted as Σ. This Σ is calculated as the mean of the density enclosed within the projected distance to the 4th and 5th neighbour and is hence an adaptive scale that probes both large scales outside groups and local scales within groups.

The distributions of galaxy local densities for each of the *arm number samples* are shown in Fig. 4.3a. Here, the *stellar mass-limited spiral sample* is used to define the total population, as stellar mass and density are closely related (Baldry *et al.*, 2006), so any biases in terms of the stellar mass distributions may have an effect on the completeness of the galaxy sample in terms of environment. The distributions show a modest dependence of spiral arm number with local density. However, as was the case for stellar mass, each of the arm number samples spans the entire range of local density defined by Σ.

The fraction of spiral galaxies which exhibit each of the spiral arm numbers as a function of $\log \Sigma$ are shown in Fig. 4.3b. A clear trend is observed, with the number of two-armed spiral galaxies increasing for the highest values of local density from 64.3 ± 0.5 per cent for the overall population to 75 ± 2 per cent for the highest density bin of $\log \Sigma = 1.1 \pm 0.2$. Conversely, all of the many-armed samples with $m = 3$, 4 or 5+ all show the opposite trends, with their respective fractions decreasing with Σ. These results therefore seem to be in qualitative agreement with Elmegreen, Elmegreen & Dressler (1982) and Ann (2014), in which the fraction of galaxies displaying grand design spiral structure increases in the highest density environments. As the increase seems to be most distinct in the very highest densities, this could be indicative that two-armed spiral structure is a short-lived phase induced by galaxy-galaxy interactions, as described in Elmegreen & Elmegreen (1983). Interestingly, there is no clear enhancement in the fraction of galaxies with a single spiral arm at the highest densities, as found in Casteels *et al.* (2013). However, Casteels *et al.* (2013) found the most significant enhancements in $m = 1$ galaxies when galaxies have a close companion, which is not probed by this measure of environment. A more complete analysis of spiral structure with local environment, accounting for both interaction probabilities and local density will need to be considered to look for more significant trends of spiral arm structure with environment. This is discussed fully in section 7.2.2.

4.1.5 Galaxy colours

Colours primarily indicate stellar population ages in galaxies, although dust extinction can also have an effect. Star formation properties have been hypothesised to correlate with spiral arm properties, where galaxies with more prominent spiral arms show enhanced star formation (Seigar & James, 2002; Kendall, Clarke & Kennicutt, 2015). The presence of a density wave in a galaxy disc has been proposed as a method of inducing star formation, but the lack of evidence for a clear enhancement of star formation in grand design spiral galaxies (Elmegreen & Elmegreen, 1986; Foyle *et al.*,

2010; Willett *et al.*, 2015) or a clear age gradient within spiral arms (Foyle *et al.*, 2011; Dobbs & Baba, 2014; Choi *et al.*, 2015) suggests that this is not the case.

Galaxy colour is already known to relate to stellar mass (e.g. Kauffmann *et al.* 2004; Baldry *et al.* 2006), environment (e.g. Kauffmann *et al.* 2004; Baldry *et al.* 2004) and overall galaxy morphology (e.g. Aaronson 1978; Glass 1984; Bamford *et al.* 2009). As spiral arms are associated with recent star formation, and also the presence of dust (Grosbøl & Dottori, 2012), it is expected that their properties will also correlate with colour. Thus, galaxy colour correlates with the presence of spiral arms, with spiral galaxies being bluer in colour than ellipticals (Bamford *et al.*, 2009; Schawinski *et al.*, 2014). The colour distributions are now compared to look for any trends with recent SFH in Fig. 4.4a. The colours that are plotted here are the SDSS $g-i$ optical colours, which should probe recent star formation in galaxies. To avoid contamination from poor detections, only the galaxies with $F/\delta F > 5$ in both g and i are included. Unlike the distributions of local density and stellar mass, a strong trend is found between colour and arm multiplicity. The two-armed spiral galaxies show the reddest overall colours, with mean $g-i$ of 0.94 and a standard deviation of 0.13 in the *stellar mass-limited spiral sample*. The $m = 3$, 4 and 5+ armed samples have corresponding colours of 0.83, 0.82 and 0.82, with corresponding standard deviations of 0.12, 0.12 and 0.13. Thus, each of the many-armed spiral samples is ≈ 1 standard deviation bluer than the two armed spiral galaxy population. A population of barred red spirals in Galaxy Zoo have been found before in Masters *et al.* (2010a). As grand design spiral structure is associated with two spiral arms (Elmegreen & Elmegreen, 1982), this red spiral galaxy population may be composed of strongly barred, grand design spiral galaxies.

To further compare the overall galaxy colours, the fraction of the *stellar mass-limited spiral sample* with each of the spiral arm numbers with respect to $g-i$ is shown in Fig. 4.4b. Here, a clear trend is observed with the fraction of galaxies displaying two spiral arms with respect to colour. In the bluest bin ($g-i = 0.67 \pm 0.07$), only 32 ± 2 per cent of galaxies have two spiral arms; in the reddest bin ($g-i = 1.17 \pm 0.05$), 84 ± 2 per cent have two spiral arms.

As described above, a strong dependence of colour with stellar mass is well-known (e.g. Baldry *et al.* 2006). However, as described in section 4.1.3, the samples only show very weak trends with stellar mass. As further proof that galaxy colours are not driven by any stellar mass differences between the samples, the different arm number samples are matched in terms of total stellar mass. The samples are matched to the $m = 4$ sample, as this is the sample with the fewest number of galaxies other than the $m = 1$ sample, which are known to be a unique case usually associated with galaxy mergers (Casteels *et al.*, 2013). The arrows in Fig. 4.4a show how the mean and standard deviation change for the samples matched in stellar mass – a strong dependence on galaxy colour is still present, irrespective of the stellar mass differences between the samples.

To further test whether any of the colour differences between the samples can be attributed to differences in stellar mass, $g-i$ colour is plotted against stellar mass in Fig. 4.5. The results show that the colour differences cannot be explained by the stellar mass differences between the *arm number samples*: for a given stellar mass, the many-armed spiral galaxies are much bluer in the $g-i$ band. The samples were also matched in terms of stellar mass, and the mean and standard deviations are indicated by the arrows in Fig. 4.4. The colour differences are still ≈ 1 standard deviation bluer in the

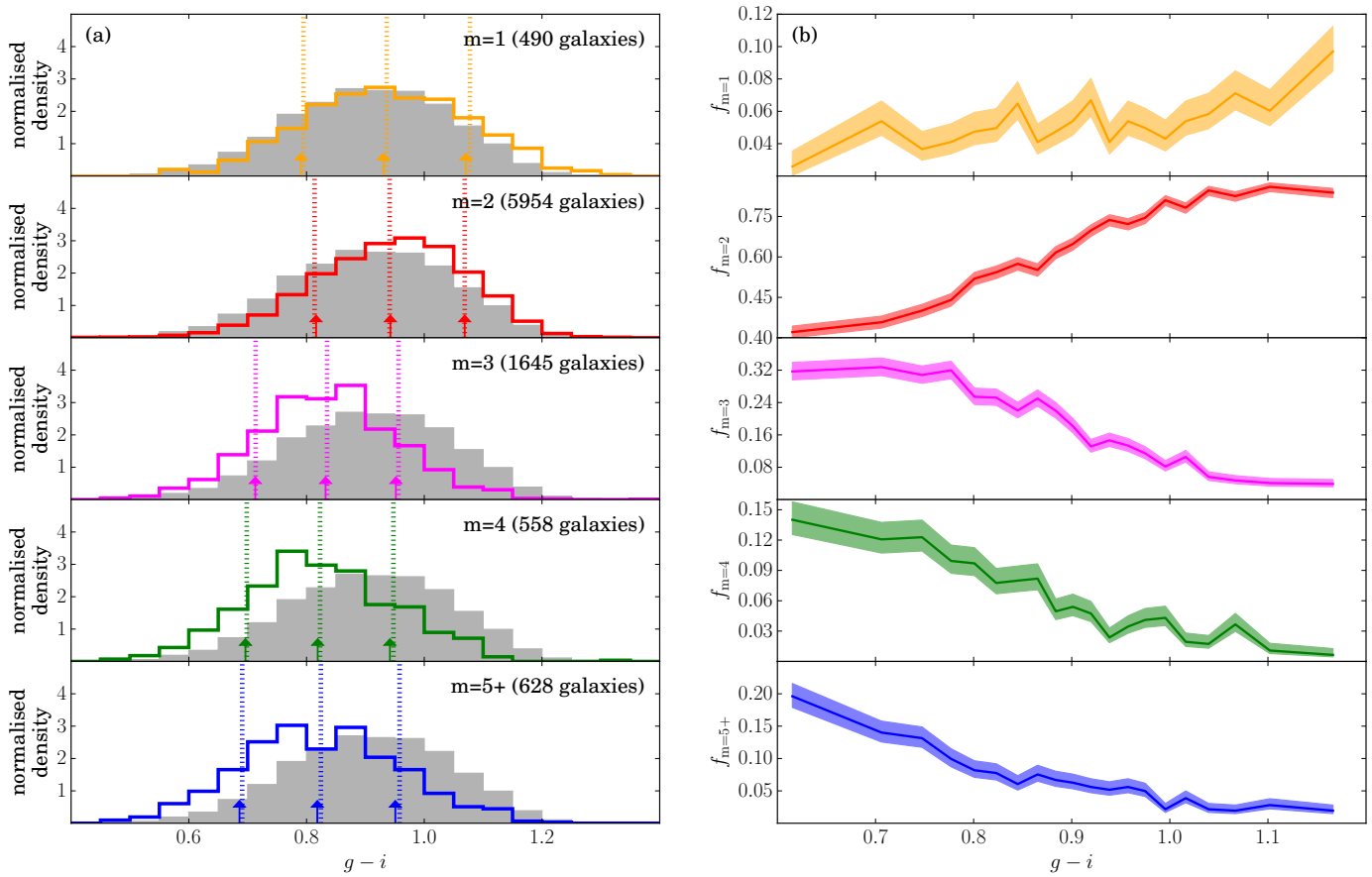

Figure 4.4: SDSS $g-i$ colours with respect to spiral arm number. Left: distributions of $g-i$ colour for the *stellar mass-limited spiral sample*. The solid lines indicate the distributions for each of the *arm number samples* for each of arm numbers. The grey filled histograms show the equivalent distribution for all of the spiral galaxies for reference. Right: fraction of the *stellar mass-limited spiral sample* classified as having each spiral arm number, in 20 bins of $g-i$. The shaded regions indicate the 1σ standard error on the mean calculated using the method described in Cameron (2011). The arrows indicate the mean and 1 standard deviation scatter for samples matched in stellar mass.

many-armed spirals compared to the two-armed spirals, after matching the samples by stellar mass.

4.1.6 Star formation histories

Using a single colour only gives a broad indication as to how the star formation properties of galaxies differ. To try to gain a more detailed understanding of the star formation in each of the *arm number samples* the $u-r$ and $r-z$ bands are compared for each of the different arm numbers, and the results are plotted in Fig. 4.6. Similar cuts in $F/\delta F$ to the u, r and z bands as described in section 4.1.3 are used to define the samples, this time applied to the u, r and z bands. It can be seen that the differences are stronger in $r-z$ than in $u-r$. The most significant differences are observed between the $m=2$ and $m=5+$ samples, where there is a significant offset in $r-z$ for a given $u-r$.
In order to gain an insight into how star formation can have affected the galaxy colours, the $m=2$ and $m=5+$ $u-r$ vs. $r-z$ distributions are plotted in Fig. 4.7, with τ-model SFHs for reference. Spectral energy distributions (SEDs) are derived from Bruzual & Charlot (2003), for a range of ages and SFHs using the initial mass function from Chabrier (2003).
In principle, the colour differences in our galaxy samples could be caused by significant metallicity variations in spiral populations with different arm numbers. It has long been established that the colours of red giant branch stars depend on the stellar population metallicity, where larger metal content causes stars to be cooler and have later spectral types (Hoyle & Schwarzschild, 1955; Sandage & Smith, 1966). Line blanketing also reddens observed colours of stellar populations, where metals in stellar atmospheres preferentially absorb blue light (Melbourne, 1960; Krishna Swamy, 1968). Both of these effects act to make stellar populations appear bluer. On galactic scales, a strong relationship exists between stellar mass and metallicity, often called the mass-metallicity or MZ relation (Tremonti *et al.*, 2004). The cause of this correlation has been interpreted as a selective loss of metals from galaxies in low mass galaxies with shallow potential wells (Larson, 1974; Tremonti *et al.*, 2004). From Fig. 4.2, we see that there is no strong stellar mass dependence with respect to spiral arm number. We therefore expect the metallicities of our stellar populations to be consistent, suggesting that this is not a significant reason for the colour differences we observe. For star-forming galaxies in the SDSS, the mean stellar metallicity varies from $Z \approx 0.7 Z_{\odot}$ for $M \approx 10^{10.6} M_{\odot}$ (the lower limit of the stellar mass-limited sample) to $Z \approx Z_{\odot}$ for $M \approx 10^{11} M_{\odot}$ (Peng, Maiolino & Cochrane, 2015). Most spirals are blue star-forming galaxies (e.g. Bamford *et al.* 2009), so the metallicity adopted is $Z = Z_{\odot}$. Two dust extinction magnitudes of $A_V = 0$ (dustless) and $A_V = 0.4$ (dusty) are considered, using the Calzetti *et al.* (2000) dust extinction prescription. The dust extinction curve can vary from galaxy to galaxy and also in individual regions in a galaxy. The Calzetti *et al.* (2000) law may therefore not include the level of complexity of the dust obscuration in the galaxies, but serves as an overall indication of the total dust extinction. A more complete analysis of dust and star formation is presented in section 4.2. Equivalent colours for each of the star formation and dust extinction models are calculated for each of the SDSS $ugriz$ filters (Doi *et al.*, 2010). The SFH models are for a quenching galaxy, defined with two parameters, t and τ, where t is the time of quenching onset and τ is the quenching timescale (a shorter τ means a faster quenching). For each

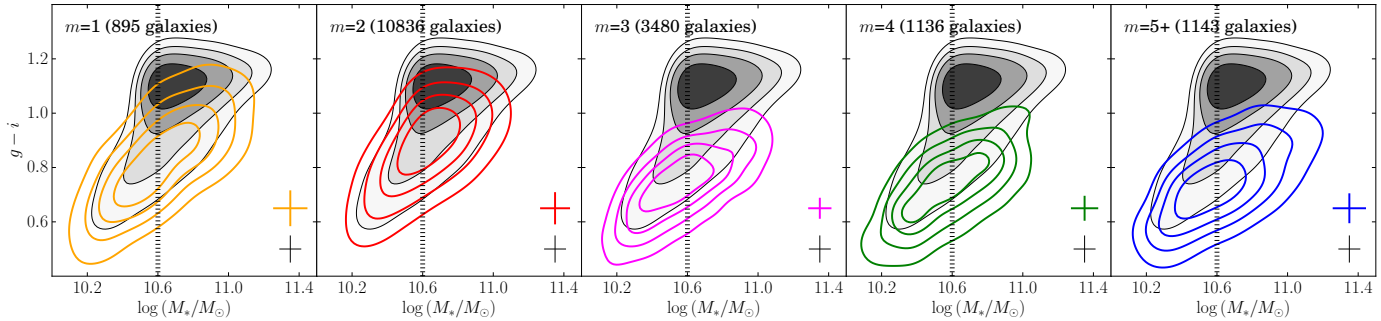

Figure 4.5: Stellar mass vs. $g - i$ colour for galaxy samples classified by spiral arm number in the *luminosity-limited sample*. The black dotted line indicates where the sample is incomplete in terms of stellar mass. The grey scale shaded contours show the total *stellar mass-limited sample* for all morphologies, whereas the solid lines show the distributions for each *arm number sample*. The contours are plotted with a kernel density estimate, with bandwidth optimised using five-fold cross validation, and the selected bandwidths are displayed in the bottom-right corner of each plot. The contour levels show the regions enclosing 20 per cent, 40 per cent, 60 per cent, and 80 per cent of the points.

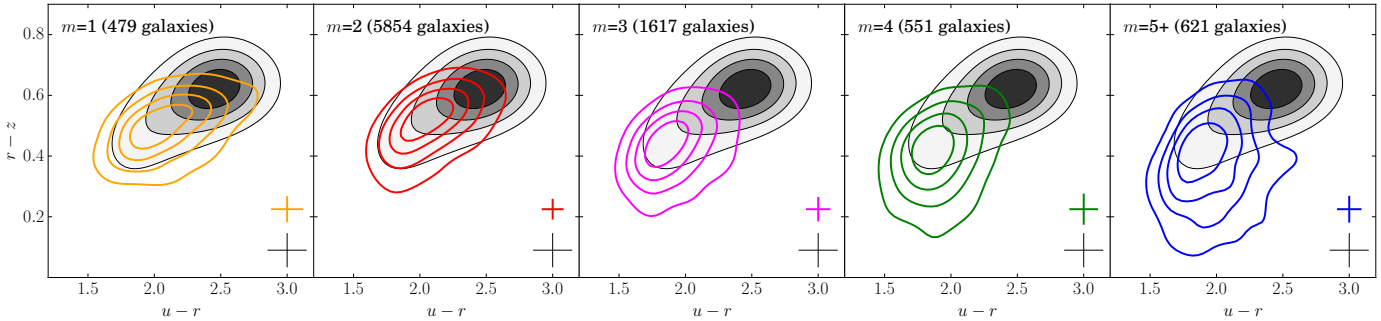

Figure 4.6: $u - r$ vs. $r - z$ colours for each of the *arm number samples* taken from the *stellar mass limited spiral sample*. The greyscale shaded contours show the entire *stellar mass-limited sample*, irrespective of morphology, whereas the solid lines indicate the same distribution for each *arm number sample*. Contours are plotted using a kernel density estimate,with bandwidths optimised using five-fold cross validation. The selected bandwidths are displayed in the bottom-right corner of each plot. The contour levels show the regions enclosing 20 per cent, 40 per cent, 60 per cent, and 80 per cent of the data for each sample.

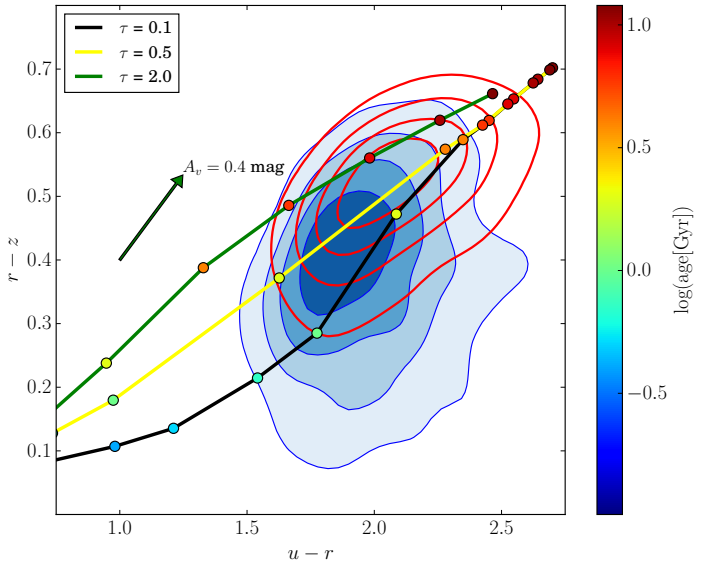

Figure 4.7: $u-r$ vs. $r-z$ for the $m=2$ and $m=5+$ samples, with different SFHs and dust attenuations overlaid. Contour plots are for the $m=2$ (red solid contours) and $m=5+$ (blue filled contours) samples as in Fig. 4.6. Three evolutionary tracks for Bruzual & Charlot (2003) stellar population models with different quenching timescales (τ) are plotted in black, yellow and green lines, indicated in the plot legend. Each point is coloured by the relative age of the SFH models (t), indicated in the colourbar. The green arrow indicates how the evolutionary curves would change colour with dust extinction A_V.

of the three timescales, the dust extinction A_V is set to zero. Full details of how the models are derived can be found in Duncan *et al.* (2014).

In Fig. 4.7, the $u-r$ vs. $r-z$ colours are plotted for the $m=2$ and $m=5+$ samples, which showed clear colour differences in Fig. 4.6. Overlaid are three SFHs with different quenching timescales ($\tau=0.1$, 0.5 and 2.0 Gyr). The plot indicates that both populations are consistent with SFH model colours, but that the quenching process is much longer in the $m=2$ population (indicated by a longer τ) than in the $m=5+$ population. The $m=5+$ population has therefore undergone a shorter, more recent phase of star formation. There is also a significant population of galaxies that are red in $u-r$ and blue in $r-z$, which cannot be explained by a τ-model, even with a quickly declining SFR. A model with a recent, short burst superimposed on a longer, smoother SFH may be more suitable.

The role of dust must also be considered. A reference dust attenuation of $A_V=0.4$ is shown by the green arrow of Fig. 4.7. The arrow indicates that extinction by dust could account for the some of differences in the colours of the galaxies if the attenuation is higher in the $m=2$ population than the $m=5+$ population. However, such a scenario would seem unlikely, as dust opacity is greater within spiral arms (Holwerda *et al.*, 2005). Therefore, one would expect that the spiral galaxies with more spiral arms to have a greater level of dust attenuation overall. Galaxies with greater levels of dust attenuation are also expected to have higher SFR (Garn & Best, 2010), with the most passive spiral galaxies being the most dust deficient (Rowlands *et al.*, 2012). In order to check whether dust is indeed the dominant factor, a more detailed analysis is presented in section 4.2.

4.2 Star formation vs. spiral arm number

In the low-redshift Universe, overall SFRs follow scaling relations with respect to galaxy stellar mass (Brinchmann *et al.*, 2004; Salim *et al.*, 2007) and gas density (Kennicutt, 1998), with the former known as the 'star formation main sequence' (SFMS). The tightness of the relationship between total SFR and stellar mass indicates that the processes responsible for star formation are regulated (Bouché *et al.*, 2010; Lilly *et al.*, 2013; Hopkins *et al.*, 2014), and apply to all galaxies, irrespective of morphology. Further scaling relations between SFR density and gas density within individual galaxies (Kennicutt, 1998; Leroy *et al.*, 2008; Bigiel *et al.*, 2008) and of SFR with total gas mass (Saintonge *et al.*, 2016) indicate that the current SFR of low-redshift galaxies is tied to the availability of gas to form new stars (Saintonge *et al.*, 2013; Genzel *et al.*, 2015), and that star formation efficiency varies little within or between galaxies (Kennicutt, 1998; Saintonge *et al.*, 2011).

In this section, the link between total SFRs and gas densities are explored with respect to the spiral arm number. Spiral arms can theoretically arise in many different ways, which affect the star formation properties of galaxies. Strong spiral density waves are a candidate mechanism for the formation of two-armed spiral structure, and were suggested to trigger star formation in the neighbourhoods of individual arms (Lindblad, 1963; Lin & Shu, 1964; Roberts, 1969). However, there is little evidence for the triggering of star formation globally in galaxies by spiral arms (Romanishin, 1985; Elmegreen & Elmegreen, 1986; Stark, Elmegreen & Chance, 1987), or within the arms of individual local galaxies (Foyle *et al.*, 2011; Dobbs, Burkert & Pringle, 2011; Eden *et al.*, 2012; Choi *et al.*, 2015). Alternatively, grand design spiral patterns could arise when the Toomre Q value in discs reaches ~ 1, and be subject to swing amplification (Toomre, 1964, 1981), be remnants of recent tidal interactions (Sundelius *et al.*, 1987; Dobbs *et al.*, 2010), or form via bar instabilities (Kormendy & Norman, 1979). Many-armed or flocculent spiral patterns, however, form via different mechanisms, and it has been proposed that they are more transient, short-lived structures in gas rich discs (e.g., Sellwood & Carlberg 1984; Baba, Saitoh & Wada 2013; D'Onghia, Vogelsberger & Hernquist 2013). Given the little evidence for triggering of star formation by any of these mechanisms, spiral arms appear to concentrate the star-forming material into the arm regions. Star formation reflects the distribution of gas, but the arms do not affect the overall star formation in the host galaxy (Vogel, Kulkarni & Scoville, 1988; Elmegreen, 2002; Moore *et al.*, 2012).

4.2.1 Sample selection

In this section, all galaxy morphological data once again uses the debiased GZ2 statistics outlined in section 3.2. Rest-frame absolute SDSS $ugriz$ and GALEX FUV (far-UV) and NUV (near-UV) photometry are obtained from the NASA Sloan Atlas (Blanton *et al.*, 2011). WISE photometry is obtained from Chang *et al.* (2015). More details on these data are included in section 2.2. Galaxy stellar masses are obtained from the SDSS-WISE SED fitting of Chang *et al.* (2015) for all galaxies in the *full sample*. The consistency of these stellar mass estimates with respect to the other mass estimates used in this thesis are outlined in section 2.4.1. In total, there are 62,903 NSA galaxies in the redshift range $0.02 \leq z \leq 0.055$ which were visually classified in GZ2. With the restrictions applied in section 2.2, 45,192 (71.8 per cent) of the NSA galaxies with

measured morphologies have unambiguous WISE matches with reliable photometry. For the remainder of this chapter, I refer to this selection as the *full sample*. To investigate the gas properties of the galaxies in the *full sample*, measured gas masses from the $\alpha 70$ data release of the ALFALFA survey (Giovanelli *et al.*, 2005; Haynes *et al.*, 2011) are used. These are described in more detail in section 2.4.3. Due to the restrictions on the $\alpha 70$-SDSS footprint and the imposed limiting redshift of $z \leq 0.05$, 20,024 galaxies from the *full sample* are targeted by ALFALFA and 5,570 of those galaxies have reliable HI fluxes.

As was the case in section 4.1.1, the aim is to study a complete sample of galaxies in a representative manner. The NASA Sloan Atlas reduces the upper redshift limit to $z = 0.055$. For a complete *luminosity-limited sample*, this corresponds to a limiting absolute magnitude of $M_r < -19.95$ for the SDSS completeness limit of $m_r = 17.0$. The stellar mass completeness is given by:

$$\log(M_{*,\mathrm{lim}}) = 2.17 \log(z) + 12.74 \ , \tag{4.1}$$

which is indicated by the curved line of Fig. 4.8b. The corresponding stellar mass completeness limit at the upper redshift limit is $\log(M_*) = 10.0 \log(M_\odot)$. The sample is still incomplete for the reddest galaxies at $\log(M_*/M_\odot) < 10.0$. Therefore, a *stellar mass-limited sample* is selected for this analysis, selecting all galaxies brighter than $M_r = -19.95$ and more massive than $10^{10.0} M_\odot$. The limits of the sample are indicated by the red box region in Fig. 4.8b, and it includes 25,063 galaxies in total.

Similar completeness limits apply to the ALFALFA data: at a given redshift, the sample is incomplete for the least luminous HI sources. For a source of profile width 200 kms^{-1} ALFALFA has a 5σ completeness limit of $S_{\mathrm{lim}} \geq 0.72$ (Giovanelli *et al.*, 2005), where S is the HI flux density. ALFALFA fluxes are converted to gas masses using Eq. 2.1 and the estimated completeness limit at a given distance can therefore be described by:

$$\log(M_{\mathrm{HI,lim}}) = 0.72 \times (2.356 \times 10^5 D^2_{\mathrm{Mpc}}) \ . \tag{4.2}$$

The limiting HI mass with redshift is shown by the curved green line of Fig. 4.8c. As many of the galaxies in $\alpha 70$ are targeted, yet undetected, an HI upper limit can be measured for a galaxy at a given distance using Eq. 4.2.

Having defined the galaxy samples, a set of spiral galaxies are selected using the visual statistics of GZ2. Galaxies with $p_{\mathrm{features}} \cdot p_{\mathrm{not\,edge\,on}} \cdot p_{\mathrm{spiral}} > 0.5$ and $N_{\mathrm{spiral}} \geq 5$ are selected in accordance with section 4.1. It is desirable to study galaxies with respect to spiral arm number only in this section, rather than other morphological differences. To this end, strongly barred galaxies are excluded from the sample, which have $p_{\mathrm{bar}} > 0.5$. This cut has been used in the past to select strongly barred galaxies from GZ2 (Masters *et al.*, 2010a).

As galaxy SFR is related to total stellar mass (e.g., Brinchmann *et al.* 2004; Salim *et al.* 2007; Guo, Zheng & Fu 2013), samples must be consistent in total stellar mass to ensure that any differences in star formation properties are due to the morphological properties studied in this chapter. A boxplot for each of the stellar mass distributions is shown in Fig. 4.9. Here we note that the derived stellar masses are those from Chang *et al.* (2015), different from those used in section 4.1 (see section 2.4.1 for details). For the stellar mass range considered in this chapter, the stellar mass distributions are consistent with spiral arm number. The $m = 2$ sample has median stellar mass of $10^{10.50} M_\odot$, whereas the $m = 3, 4$ and $5+$ samples have medians of $10^{10.46} M_\odot$,

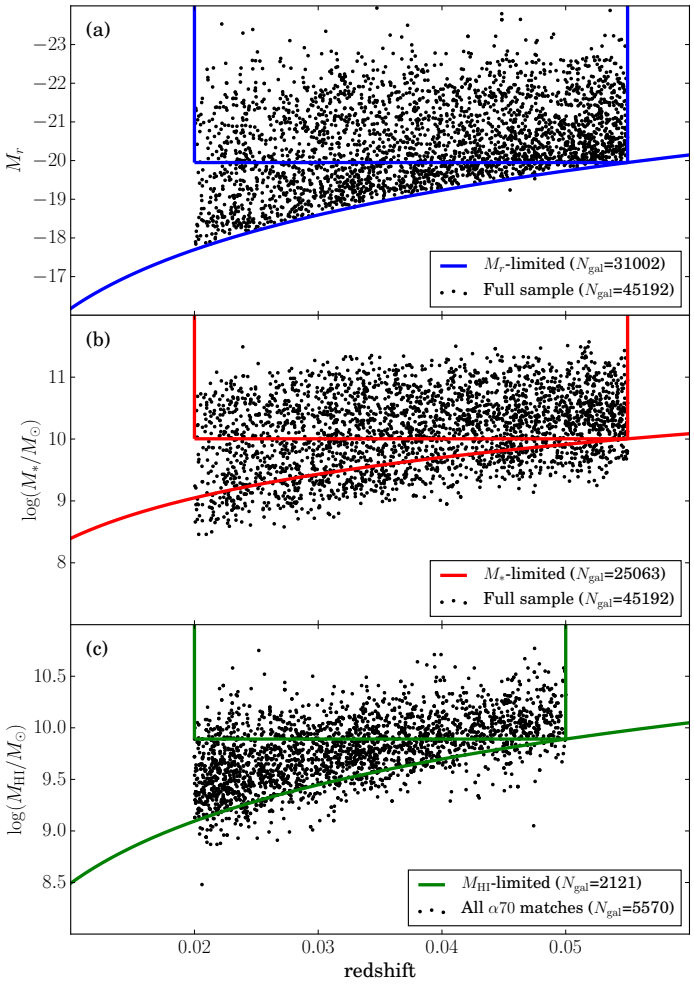

Figure 4.8: Sample selection for the star formation analysis. (a) Plot of absolute magnitude vs. redshift for the *full sample* of galaxies. The curved blue line indicates the luminosity limit as a function of redshift. Galaxies enclosed within the blue box make up the *luminosity-limited sample*. (b) Stellar mass distribution of the *full sample* vs. redshift. The curved line shows the calculated stellar mass completeness limit. Galaxies in the red boxed region are included in the *stellar mass-limited sample*. (c) Gas mass vs. redshift for all galaxies matched in α70 to the *full sample*. The curved line shows the calculated HI mass completeness limit and galaxies. Galaxies in the green boxed region are included in the *HI mass-limited sample*.

$10^{10.44} M_\odot$ and $10^{10.49} M_\odot$. The only sample with a significantly higher median stellar mass is the $m = 1$ sample, where the corresponding value is $10^{10.60} M_\odot$. However, this is the sample with the fewest galaxies (224), and the difference is still much less than the overall spread in the data (the 84th–16th percentile range for all galaxies in the *stellar mass-limited sample* is ~ 0.7 dex). For these reasons, all galaxies in the *stellar mass-limited sample* of spirals are kept for this analysis, as there is no significant stellar mass dependence on spiral arm number. The overall numbers of galaxies included in the *stellar mass-limited sample* with each spiral arm number, and the numbers with ALFALFA detections, are listed in Table. 4.2.

4.2.2 Inclination dependence on morphological classification

Another issue that may affect the results is the galaxy inclination – more inclined galaxies may have much greater levels of dust extinction (Masters *et al.*, 2010b). More

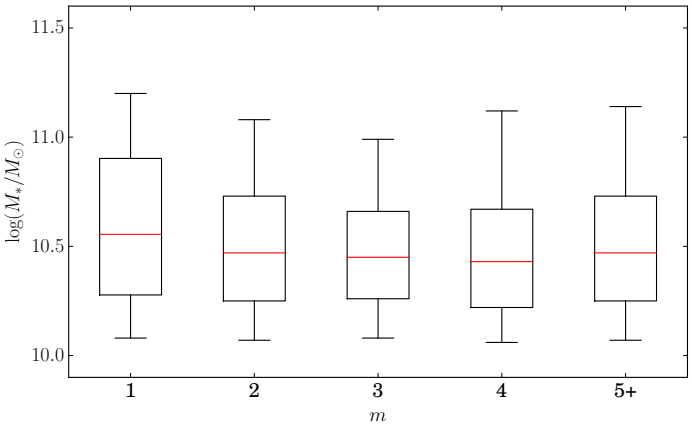

Figure 4.9: Stellar mass distributions (using the measurements of Chang *et al.* 2015) for each of the *arm number subsamples* from the *stellar mass limited sample*. The boxes show the 25th quartile, 75th quartile and the median, and the vertical lines indicate the extent of the 5th and 95th percentiles.

Table 4.2: Sample sizes for each of the samples in the star formation analysis. The columns are (1) Sample morphology from GZ2 (2) Number of galaxies in $0.02 < z \leq 0.055$ (3) Number of galaxies in the *stellar mass-limited sample* (4) Number of galaxies with an ALFALFA detection in the *stellar mass-limited sample*.

Morphology	Full sample	M_*-limited	$\alpha 70$ detected
All	45192	25063	5570
Spiral	6333	3889	1792
$m = 1$	482	224	106
$m = 2$	3298	1953	859
$m = 3$	1263	805	391
$m = 4$	534	357	165
$m = 5+$	756	550	271

inclined galaxies may also be more likely to be classified in a certain way; the aim here is to select an inclination threshold above which the morphological classifications are consistent. Any galaxies with loose spiral arms are excluded, by removing any galaxies where the debiased fraction for the 'loose' response (A2 in Fig. 2.2) to the 'arm winding' question (T10) was greater than 0.2. These are likely merger driven, which may alter the intrinsic isophotal shape of the galaxy (Casteels *et al.*, 2013). The SDSS DR7 isophotal axis measurements were used to quantify the inclination, as was used in Masters *et al.* (2010b). In Fig. 4.10, the axial ratio distribution, $(b/a)_g$, of galaxies classified as spiral for the is shown, separated by spiral arm number. All galaxies from the *luminosity-limited sample* which have measured axial ratios in SDSS DR7 and are classified as spiral are included. The number of galaxies that are classified as spiral falls drastically when considering more inclined galaxies, as the majority of these galaxies are classified as 'edge-on' further up the question tree. We also see that there are more $m = 2$ galaxies when the axial ratio is smaller (i.e. the galaxy is more inclined). In Fig. 4.11, the fraction of the votes for $m = 2$ is shown as a function of galaxy inclination – the distribution is relatively flat until $(b/a)_g \approx 0.4$. This corresponds to an inclination $i < 70°$ for disc thickness $q = 0.22$, (e.g. Unterborn & Ryden 2008). For galaxies more inclined than this, the vote fraction starts to increase for galaxies having two spiral arms as the arm structure becomes more difficult to see.

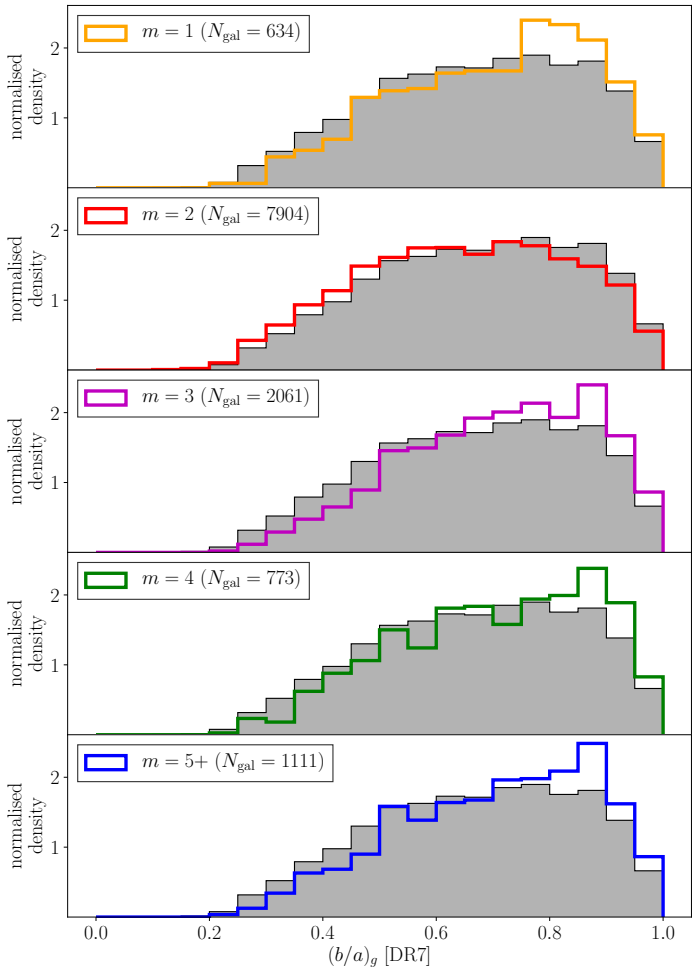

Figure 4.10: Distributions of galaxy axial ratios separated by spiral arm number from the *luminosity-limited sample*. The coloured histograms show the distributions for each spiral arm number, and the grey histograms show the distributions for all spiral galaxies regardless of spiral arm number for comparison. Galaxies with smaller axial ratios are more likely to be classified with two spiral arms.

For this reason, a threshold of $(b/a)_g \geq 0.4$ is used for selecting spiral galaxies for the rest of the work in this chapter. This is the same threshold that Masters *et al.* (2010a) found for reliably identifying bars in galaxies.

4.2.3 Measuring star formation rates

In principle, there are a number of ways to measure the total SFR in galaxies. The most commonly used SFRs in the SDSS are from the MPA-JHU catalogue (Brinchmann *et al.*, 2004): these SFRs were used in Willett *et al.* (2015) to confirm that there was no spiral arm number dependence on total SFR. Hα derived SFRs are obtained from MPA-JHU measurements of SDSS spectra (Brinchmann *et al.*, 2004; Salim *et al.*, 2007), corrected for absorption using the Balmer decrement and for aperture effects using estimates derived from photometric galaxy colour gradients. Reliable Hα measurements rely on spectra averaged across entire galaxies, which are not available from SDSS data alone (the SDSS fibre size is 3 arcsec in diameter; the median r-band Petrosian aperture diameter of galaxies in the *stellar mass-limited sample* is 7.6 arcsec). In order to account for this, the MPA-JHU catalogue applies a correction to the fibre

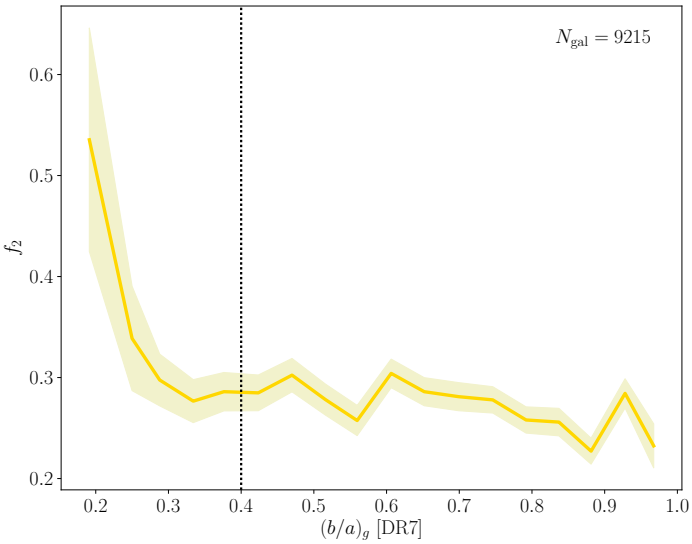

Figure 4.11: Fraction of votes for $m = 2$ vs. axial ratio. Galaxies with $(b/a)_g \lesssim 0.4$ have more votes for $m = 2$. The black dotted vertical line indicates the cut we employ to reliably select spiral galaxies.

measured Hα flux using photometry measured outside the fibre (Salim *et al.*, 2007), and thus provide reliable total SFRs of star-forming galaxies (Salim *et al.*, 2016).

Alternatively, one can measure the SFRs of galaxies using galaxy photometry rather than spectra. The UV and the MIR are usually the wavelength ranges of choice, as they are both dominated by emission from bright, young stars. The UV continuum is almost completely flat (Kennicutt, 1998), and arises from the direct photometric emission of the youngest stellar population. There are several published conversion factors to convert from UV flux to SFR; I used the conversion factor of Buat *et al.* (2008, 2011) to measure unobscured SFRs:

$$SFR_{\rm FUV} = 10^{-9.69}(L_{\rm FUV}/L_{\odot}) \ . \tag{4.3}$$

In order to get a reliable measure of SFR, however, the amount of UV emission that is obscured by dust must be corrected for. As dust absorbs UV photons and re-emits the energy at longer wavelengths, then one can also measure the SFR using the MIR emission. Again there are several published conversion factors; I used the following prescription from Jarrett *et al.* (2013):

$$SFR_{22} = (1-\eta)10^{-9.125}(L_{22}/L_{\odot}) \ , \tag{4.4}$$

where L_{22} is the luminosity measured in the WISE $22\,\mu$m band, and η is the fraction of MIR emission that originates from the absorption of radiation from the older stellar population. Here, I used $\eta = 0.17$ measured in Buat *et al.* (2011). This conversion is for a Kroupa (2001) IMF, which is converted to a Chabrier (2003) IMF by adjusting the SFR by -0.03 dex as suggested in Zahid *et al.* (2012) and Speagle *et al.* (2014). To reliably measure the total SFR, the $22\,\mu$m-derived SFR is then be added to the unobscured FUV measured SFR (e.g., Wang & Heckman 1996; Heckman *et al.* 1998; Hao *et al.* 2011; Jarrett *et al.* 2013; Clark *et al.* 2015):

$$SFR_{\rm total} = SFR_{\rm FUV} + SFR_{22} \ . \tag{4.5}$$

The specific SFR is given by $sSFR = SFR_{\rm total}/M_*$.

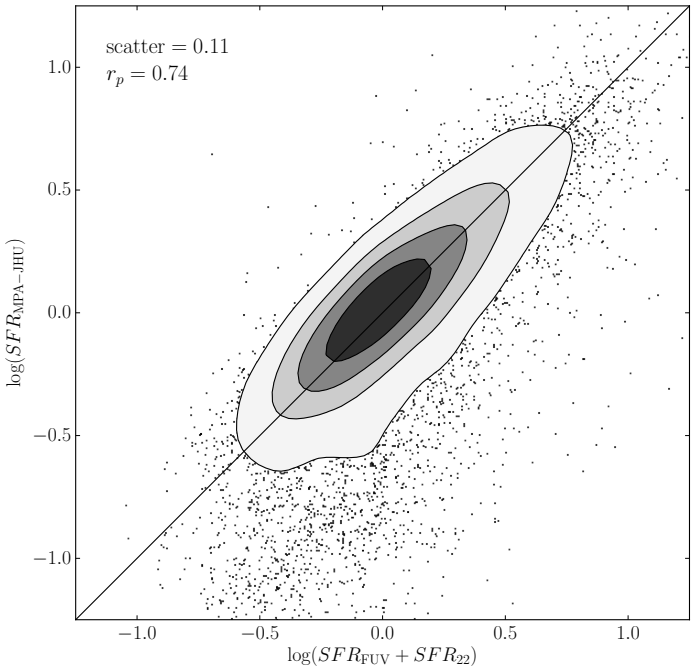

Figure 4.12: SFRs from Eq. 4.5 compared to the values measured from the MPA-JHU catalogue (Brinchmann *et al.*, 2004) for galaxies in the redshift range $0.02 < z \leq 0.055$ with $\mathrm{SNR} > 2$ in the GALEX FUV and WISE 22 μm bands. The shaded grey contours show the regions enclosing 20, 40, 60 and 80 per cent of the data points, and the thinner black line shows the expected one-to-one relationship.

To check the reliability of the SFRs obtained from this measure and to ensure the results are consistent with Willett *et al.* (2015), I compare the SFRs from Eq. 4.5 with the MPA-JHU Hα estimates in Fig. 4.12. The plot shows all galaxies in the redshift range $0.02 < z \leq 0.055$ which have $\mathrm{SNR} \geq 2$ in both the GALEX FUV and the WISE 22 μm. The GALEX FUV band is complete for galaxies with $L_{\rm FUV} \geq 10^{8.5} L_{\odot}$ at $z = 0.02$ and $L_{\rm FUV} \geq 10^{8.9} L_{\odot}$ at $z = 0.055$. The WISE 22 μm band is complete for galaxies with $L_{\rm FUV} \geq 10^{7.5} L_{\odot}$ at $z = 0.02$ and $L_{\rm FUV} \geq 10^{8.4} L_{\odot}$ at $z = 0.055$. There is good agreement between the FUV+MIR derived SFRs and those inferred from the Balmer lines, with Pearson's r coefficient of 0.74, indicative of a strong linear correlation between the variables. The scatter is 0.11 dex. There is also no significant offset between the measurements (the median difference is < 0.01 dex), suggesting that these SFR measurements are indeed comparable. However, there is a slight tendency for galaxies at the lower end of $SFR_{\rm MPA-JHU}$ to have higher SFRs measured from Eq. 4.5. Salim *et al.* (2016) attributes galaxies with higher SFRs measured in Chang *et al.* (2015) to galaxies with low measured fluxes in WISE being overestimated. However, this effect is unlikely to dominate as there is strong agreement between the SFR indicators using a single value of $\eta = 0.17$ from Buat *et al.* (2008), with the only differences observed for galaxies with low SFRs ($\lesssim 0.5\,\mathrm{M_{\odot} yr^{-1}}$). This issue affects only a small fraction of galaxies in the sample, with < 10 per cent of galaxies having more than 0.5 dex disagreement between the two SFR measures. All galaxies with $\mathrm{SNR} \geq 2$ in both the GALEX FUV and the WISE 22 μm are therefore kept in the in the sample as galaxies with reliably measured total SFRs.

4.2.4 The star formation main sequence

The SFMS describes the SFR of the galaxy population as a function of stellar mass. In the low-redshift Universe, this correlation has been shown to be very tight for normal star-forming galaxies (Brinchmann *et al.*, 2004; Salim *et al.*, 2007; Chang *et al.*, 2015). Galaxies with significantly enhanced star formation are usually associated with merging or interacting systems (Sanders & Mirabel, 1996; Veilleux, Kim & Sanders, 2002; Engel *et al.*, 2010; Kaviraj, 2014; Willett *et al.*, 2015), with the rest of the difference across the main sequence attributable to differences in the gas content and star formation efficiency of galaxies (Saintonge *et al.*, 2011, 2016).

In order to test whether the morphology of the galaxies affects the total SFR, the SFMS is plotted using the definition of sSFR defined in section 4.2.3. Specific SFR (sSFR) is plotted rather than SFR, as this more clearly demonstrates how efficiently stars are formed in star-forming galaxies with respect to stellar mass, M_*. Galaxies at low-redshift can be considered bimodal in terms of their colour and SFR properties (Baldry *et al.*, 2006; Schawinski *et al.*, 2014; Morselli *et al.*, 2016). To plot the SFMS, a set of star-forming galaxies must therefore be selected. I choose to use the definition of Chang *et al.* (2015), who define star-forming galaxies using SDSS *ugriz* photometry. Using this definition, galaxies with $(u-r)_{\rm rest} < 2.1$ or $(u-r)_{\rm rest} < 1.6(r-z)_{\rm rest}+1.1$ are selected as star-forming. The majority of spiral galaxies (78.3 per cent) are found to be star-forming using this method. The resulting plot of $\log(M_*)$ vs. $\log(sSFR)$ is shown in Fig. 4.13. As expected, there is a tight relationship, as galaxies with greater stellar masses have lower sSFRs. The best-fit linear model to the data is given by:

$$\log(sSFR_{\rm expected}) = -0.49\log(M_*/M_\odot) - 5.06\ , \tag{4.6}$$

and the scatter is 0.19 dex. This relationship can now be used to assess whether galaxies have systematically high or low sSFRs for their stellar mass, by defining the best-fit line as the *expected* sSFR for a galaxy of a given stellar mass. Given this information, the $sSFR_{\rm residual}$ is described by:

$$\log(sSFR_{\rm residual}) = \log(sSFR_{\rm total}) - \log(sSFR_{\rm expected})\ , \tag{4.7}$$

where $\log(sSFR_{\rm expected})$ is given in Eq. 4.6. If a given galaxy lies above the $sSFR_{\rm expected}$ line, it has a higher sSFR for its stellar mass compared to the total star-forming galaxy population, and a positive value for $sSFR_{\rm residual}$. Conversely, galaxies below the line can be considered as being deficient in sSFR, and have a negative value for $sSFR_{\rm residual}$.

Using Eq. 4.6 and 4.7, the effect that spiral galaxy morphology has on the total sSFRs of galaxies is now considered. For this analysis, the spiral galaxies are divided into *arm number subsamples* as described in section 4.2.1 for galaxies in the *stellar mass-limited sample*.

As discussed in section 4.2.3, cuts are imposed in SNR to ensure that we have flux measurements that are not dominated by noise to get a reliable estimate of SFR in both the FUV and the MIR. It is therefore important to first check the completeness of each of the samples that I compare. The fraction of galaxies that meet the minimum $\mathrm{SNR} \geq 2$ threshold in the GALEX FUV filter, the WISE $22\,\mu\mathrm{m}$ filter, and both filters, are shown in Fig. 4.14. The overall completeness of each of the samples is similar, with $\sim 70-80$ per cent of galaxies having a detection in both filters. Many-armed

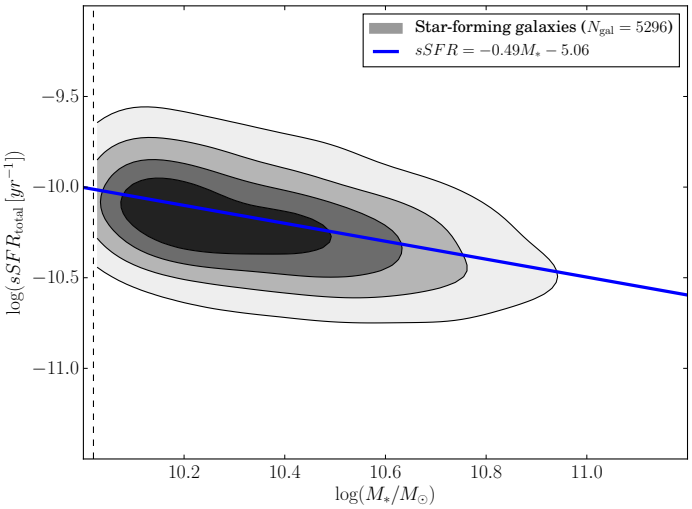

Figure 4.13: Stellar mass vs. sSFR for star-forming galaxies in the redshift range $0.02 < z \leq 0.05$. The grey contours show regions enclosing 20, 40, 60 and 80 per cent of the points. The blue line indicates the linear best fit line to the data. The black dashed vertical line indicates the lower stellar mass limit of this sample.

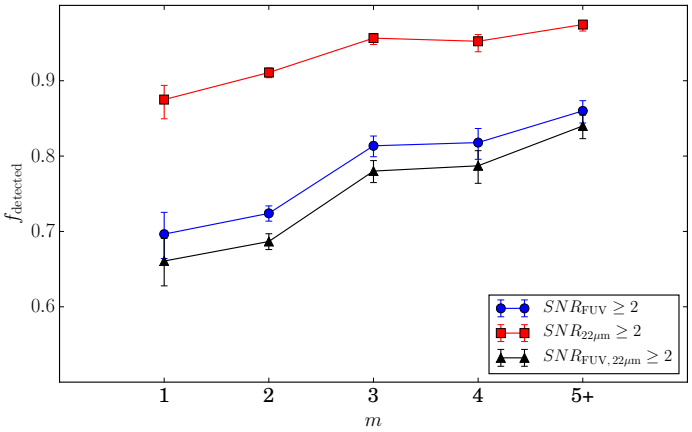

Figure 4.14: Fraction of galaxies with SNR $\geq$ 2 detection in the GALEX FUV (blue circles), WISE 22 μm (red squares), and both (black triangles), for each of the *arm number subsamples* taken from the *stellar mass-limited* sample of spiral galaxies. The error bars show the 1σ errors, calculated using the method of Cameron (2011).

samples ($m = 3$, 4 or 5+) have a greater fraction of galaxies with reliable fluxes in both the 22 μm and the GALEX FUV than the $m = 1$ and $m = 2$ samples, however. Thus, galaxies with one or two spiral arms are more likely to have undetectable MIR or FUV emission and thus low SFRs.

The resulting distributions of $sSFR_{\rm residual}$ for each of the *arm number subsamples* are shown in Fig. 4.15. Here I plot all spiral galaxies, and make no cuts on selecting only star-forming galaxies. It is immediately apparent that there is no strong dependence of $sSFR_{\rm residual}$ on spiral arm number – the median of the $m = 2$ distribution compared with the $m = 3$, 4 and 5+ distributions shift by $\lesssim 0.05$ dex, which is much smaller than the scatter in the SFMS of 0.19 dex. This result is perhaps surprising, given that in section 4.1.5, it was shown that the many-armed samples are much bluer in colour compared to their two-armed counterparts, an effect which was suggested to be related to the star formation properties of the galaxies. The $m = 1$ sample of spiral galaxies has the highest median value of $sSFR_{\rm residual}$ of 0.02 ± 0.05, and is the only sam-

ple which lies above the defined SFMS, although this is the *arm number subsample* with the lowest number of galaxies with reliable FUV and 22μm measurements (148 galaxies). These high sSFRs are likely because GZ2 classified $m = 1$ spiral galaxies are associated with tidally induced features (Casteels *et al.*, 2013), which are in turn associated with enhanced star formation (Sanders & Mirabel, 1996; Veilleux, Kim & Sanders, 2002; Engel *et al.*, 2010). This result is consistent with Willett *et al.* (2015), who showed that spiral arm number does not affect the position of the SFMS, albeit using the spectroscopic SFRs of Brinchmann *et al.* (2004). Merger systems, on the other hand, did show SFRs above the SFMS in the Willett *et al.* (2015) study. It should also be noted that each of the galaxy distributions lie very close to the SFMS. In this comparison of spirals, no cuts are employed to only select star-forming galaxies, yet the medians of each of the spiral galaxy subsamples are within $\lesssim 0.1$ dex of the SFMS, where we specifically selected star-forming galaxies. The majority of spiral galaxies are observed to be 'passively' star-forming (i.e. either lie on the SFMS, or show blue optical colours), but a significant population of passive red spirals also exists (Masters *et al.*, 2010a; Fraser-McKelvie *et al.*, 2016; Kuchner *et al.*, 2017). Masters *et al.* (2010a) measures that ≈ 6 per cent of spirals are red and passive. From our results, this population cannot be attributed to galaxies of a specific spiral arm number – the majority of galaxies with *any* spiral arm number are actively star-forming.

4.2.5 Comparing obscured and unobscured star formation

As discussed in section 4.2.3, the different SFR indicators in Eq. 4.5 correspond to the combination of emission from the youngest, hottest stars (measured in the UV), and emission originating from the radiation absorbed by interstellar dust and re-emitted at longer wavelengths (the MIR). Although both sources of emission arise from young stars of order ~ 10 Myr in age (Hao *et al.*, 2011; Rieke *et al.*, 2009), their relative contributions actually trace different phases in the molecular gas clouds from which they form. Calzetti *et al.* (2005) noted that the MIR emission from galaxies traces the Hα emission, which itself originates from absorption of photons of the youngest stars (< 10 Myr in age), suggesting that warm dust emission is attributable to the star-forming regions of galaxies. UV emitting populations are instead visibly offset from the most active star-forming regions (Calzetti *et al.*, 2005). The processes via which the UV population become exposed take some time, and are highly dependent on the gas and star formation conditions of the molecular clouds from which stars form (Parravano, Hollenbach & McKee, 2003).

To give an insight into the relative fractions of obscured and unobscured star formation in the galaxy samples, the FUV and MIR contributions to $sSFR_{\rm total}$ are compared in Fig. 4.16. Each of the *arm number subsample* populations lie close to the SFMS, even with no cuts on only selecting star-forming galaxies, so the expectation is that they are dominated by normal star-forming galaxies with little contribution from starburst populations. The amount of unobscured FUV star formation relative to the amount of obscured MIR measured star formation is shown in Fig. 4.16 for each of the *arm number subsamples*. Here, a clear trend is observed – many-armed spiral galaxies have less obscured star formation than the $m = 2$ sample of spiral galaxies. The $m = 1$ sample has the lowest median $\log(SFR_{\rm FUV}/SFR_{22})$ value of -0.28 ± 0.05, corresponding to a mean of 34 ± 1 per cent of the $SFR_{\rm total}$ being measured by the young stars unobscured by dust in the FUV. The $m = 2$, 3, 4 and 5+ values for

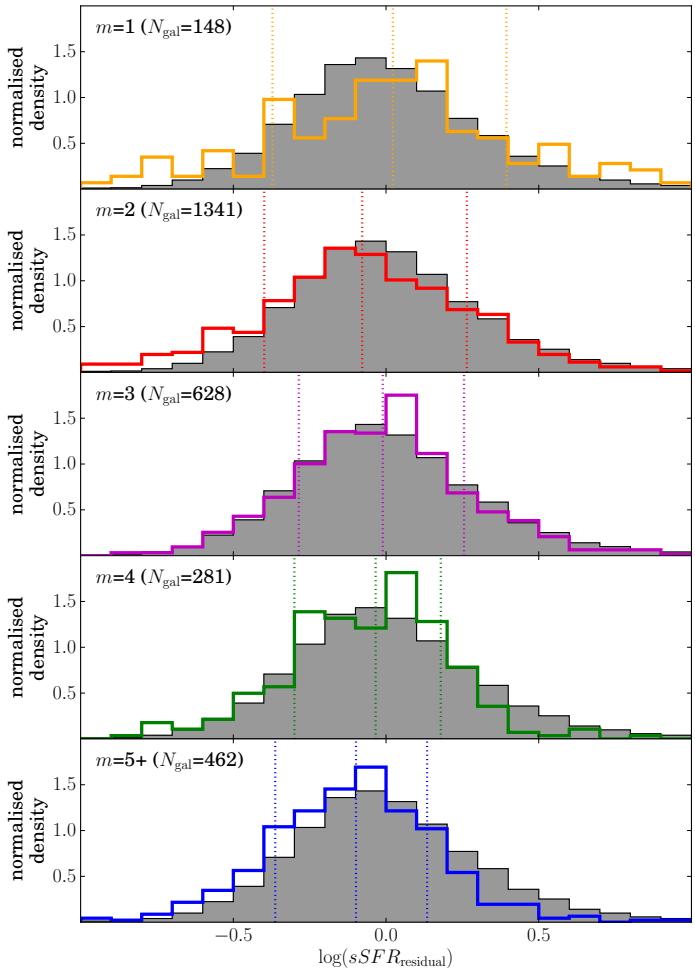

Figure 4.15: Residual sSFRs for each of the *arm number subsamples* taken from the *stellar mass-limited sample*, calculated using Eq. 4.6 and 4.7. All spiral galaxies are included, with no cuts made to only select star-forming galaxies. The solid histograms show the distributions for each subsample, and the filled grey histograms indicate the same distributions for the entire sample of *star-forming* galaxies for reference. The vertical dotted lines indicate the 16th, 50th and 84th percentiles.

$\log(SFR_{\rm FUV}/SFR_{22})$ are -0.15 ± 0.01, -0.13 ± 0.01, -0.03 ± 0.02 and 0.04 ± 0.02, corresponding to 40 ± 1, 42 ± 1, 47 ± 1 and 51 ± 1 per cent of the total star formation being measured in the FUV. All of the many-armed spiral galaxy subsamples have significantly higher fractions of their total SFR measured in the FUV – the KS p-values are $\sim10^{-3}$, $\sim10^{-7}$ and $\sim10^{-26}$ between the $m=2$ sample and the $m=3$, 4 and 5+ samples, respectively. The many-armed spiral samples have less obscured star formation than the two-armed sample, with a greater fraction of the SFR measured from young stars unattenuated by dust in the FUV.

4.2.5.1 The IRX-β relation

A common parametrisation of the amount of dust obscuration in star-forming galaxies is through the IRX-β relation (Calzetti, Kinney & Storchi-Bergmann, 1994; Meurer, Heckman & Calzetti, 1999; Calzetti *et al.*, 2000). The quantity IRX refers to the infrared excess, and corresponds to the ratio of MIR emission originating from warm dust to the UV emission from exposed young stars. The quantity IRX is defined by

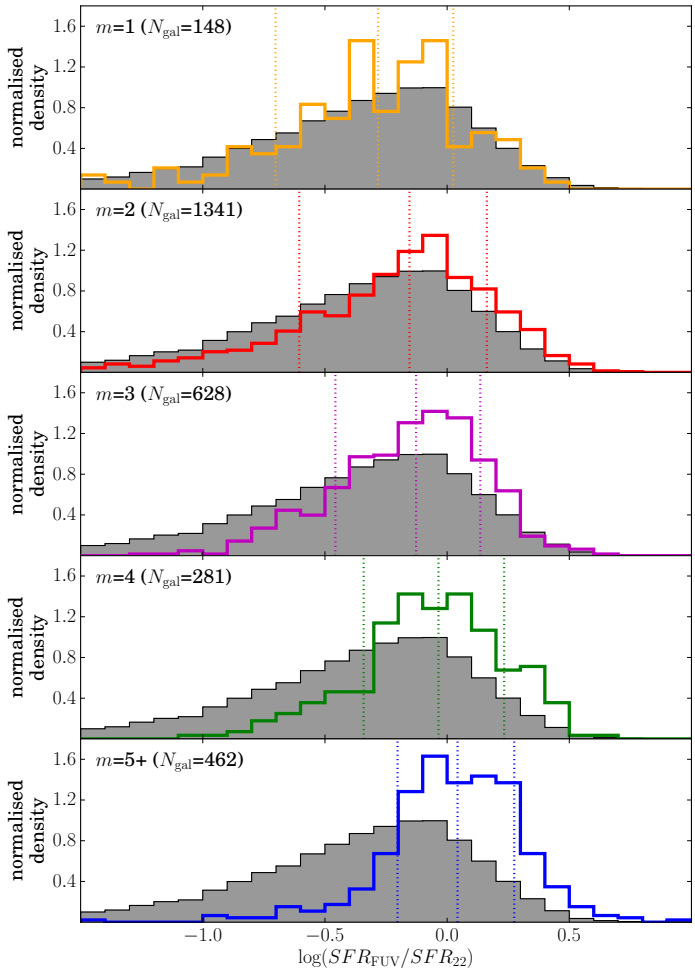

Figure 4.16: Ratio of FUV and MIR measured SFRs for spirals from the *stellar mass-limited samples*. The grey filled histogram shows the same distribution for all galaxies in the *stellar mass-limited sample*, irrespective of morphology. The vertical lines show the median, 16th and 84th percentiles for each of the *arm number subsamples*.

Boquien *et al.* (2012) as:

$$\mathrm{IRX} = \log(L_{\mathrm{dust}}/L_{\mathrm{FUV}}) \; . \tag{4.8}$$

The quantity β measures the slope in the UV continuum of galaxies, which depends on both the intrinsic UV slope, β_0, and the UV slope induced by dust reddening, and is defined in Boquien *et al.* (2012):

$$\beta = \frac{M_{\mathrm{FUV}} - M_{\mathrm{NUV}}}{2.5 \log(\lambda_{\mathrm{FUV}}/\lambda_{\mathrm{NUV}})} - 2 \; . \tag{4.9}$$

For starburst galaxies, the relationship between IRX and β has been shown to be very tight, with galaxies with greater IRX having a greater UV slope (Meurer, Heckman & Calzetti, 1999; Kong *et al.*, 2004; Overzier *et al.*, 2011). Quiescently star-forming galaxies, however, lie below the IRX-β law for starburst galaxies, and show significantly more scatter. Contributions to both the MIR and the UV from ageing stellar populations, variations in the dust extinction properties or variations in SFHs of star-forming regions have all been hypothesised as reasons why star-forming galaxies show this scatter (Bell, 2002; Kong *et al.*, 2004; Boquien *et al.*, 2009, 2012).

The y-axis of the IRX-β relation is the *total* dust emission divided by the UV flux. The total dust emission, L_{dust}, is taken from the catalogue of Chang *et al.* (2015), which fit

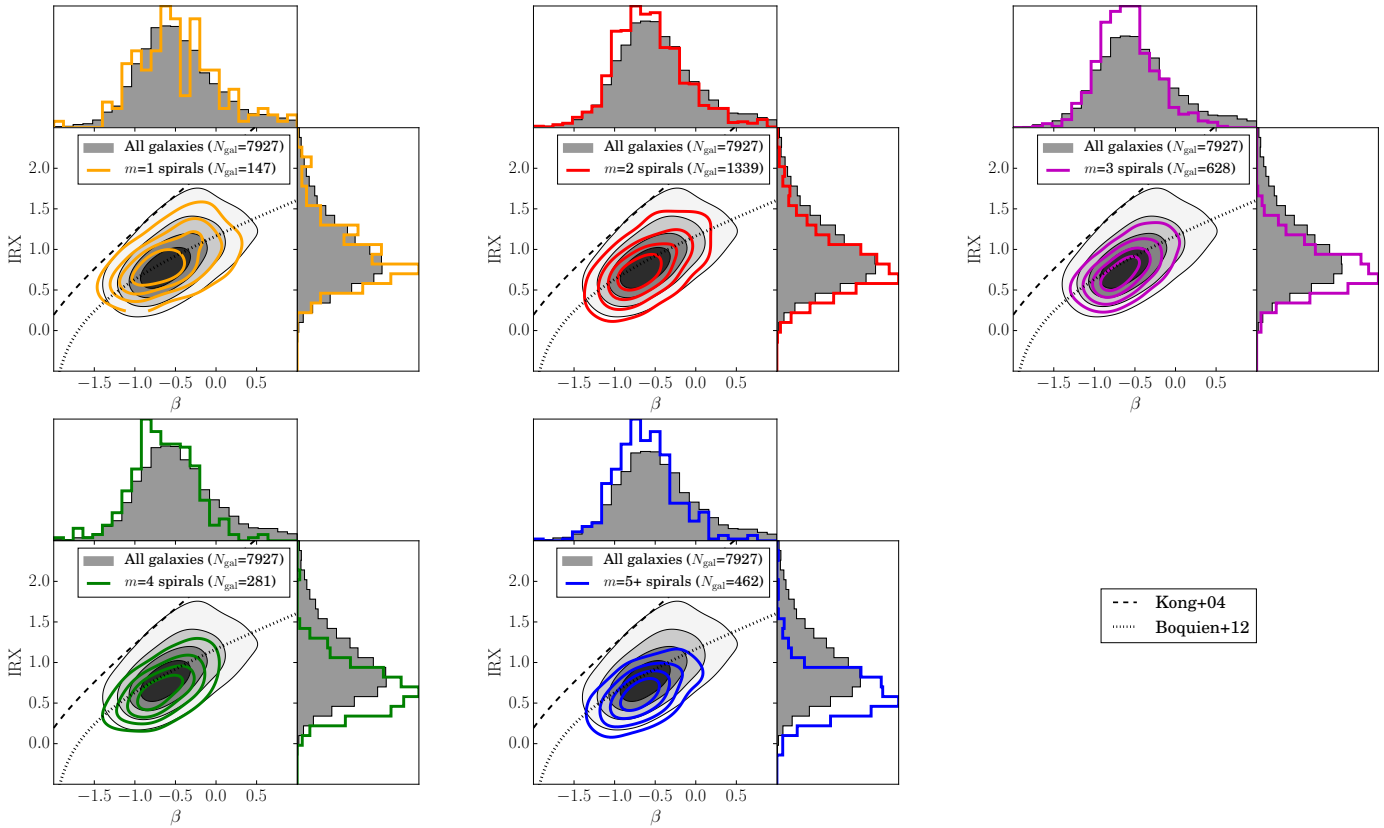

Figure 4.17: IRX (from Eq. 4.8) vs. β (from Eq. 4.9), for each spiral arm number. The underlying grey contours show the same distribution for all galaxies in the *stellar mass-limited sample* with detections in the GALEX FUV and the WISE 22 μm, regardless of morphology. The solid lines show the same values for the *stellar mass-limited spiral sample*, split by spiral arm number. The black dashed line shows the IRX-β relation measured for starburst galaxies (Kong *et al.*, 2004) and the black dotted line shows the relationship for low-redshift star-forming galaxies (Boquien *et al.*, 2012).

stellar and dust emission curves to SDSS+WISE photometry for each of the galaxies. Only galaxies with $\mathrm{SNR} \geq 2$ in the WISE 12 and 22μm bands are included in this analysis, in order to ensure a good constraint on the total dust emission. The resulting IRX-β relations for the *arm number subsamples* are shown in Fig. 4.17.

All of the spiral galaxy populations lie below the starburst IRX-β relation from Kong *et al.* (2004), with no significantly enhanced starburst-like formation. In order to measure how closely each of the samples lie to the expected quiescent IRX-β relation of Boquien *et al.* (2012) (the dotted lines in Fig. 4.17), the median offset from the relation for a given β is calculated: if a galaxy population lies below the relation, it has a negative offset, and if it lies above the line, the offset is positive. For reference, the full sample of galaxies irrespective of morphology (shown by the filled grey contours in Fig 4.17) has a median offset of -0.01 ± 0.01, indicating that this population is representative of a normal star-forming galaxy population that follows the IRX-β relation of Boquien *et al.* (2012). The corresponding offsets for each of the *arm number subsamples* are -0.01 ± 0.04, -0.05 ± 0.05, -0.09 ± 0.01, -0.14 ± 0.02 and -0.20 ± 0.01. Each of the spiral galaxy populations actually lie below the IRX-β relation, indicating that they are less luminous in the MIR than expected for their β. There is also a clear trend with spiral arm number – the $m = 1$ and $m = 2$ populations lie much closer to the IRX-β relation for normal star-forming galaxies, whereas galaxies with more spiral arms lie further below the relation, indicating that they have more UV emission relative to MIR emission than expected for their measured β. This will be discussed further in section 4.3.1

4.2.6 Gas properties of spiral galaxies

The amount of gas that galaxies contain is usually related to both the current star formation activity (Huang *et al.*, 2012; Saintonge *et al.*, 2011, 2013, 2016) and galaxy morphology (Helmboldt *et al.*, 2004, 2005; Saintonge *et al.*, 2012; Masters *et al.*, 2012). However, the amount of gas in galaxy discs has little dependence on the presence of spiral structure or its type, with spiral structure instead believed to rearrange the star-forming material in galaxies (Vogel, Kulkarni & Scoville, 1988; Elmegreen, 2002; Dobbs, Burkert & Pringle, 2011; Moore *et al.*, 2012). By using the atomic gas mass measurements of ALFALFA (Giovanelli *et al.*, 2005; Haynes *et al.*, 2011), I consider whether spiral structure has any link to an excess or deficiency of gas in the spiral samples. The HI fraction, $f_{\mathrm{HI}} = M_{\mathrm{HI}}/M_{\odot}$ exhibits a strong dependence on stellar mass, with more massive galaxies having lower gas fractions (Haynes & Giovanelli, 1984; Cortese *et al.*, 2011; Saintonge *et al.*, 2016). It is therefore useful to define the *expected* gas fraction as a function of stellar mass, in order to define whether a galaxy is deficient in HI for its stellar mass. The value for $\log(M_{\mathrm{HI}}/M_{\odot})_{\mathrm{expected}}$ can be calculated in a similar way to $sSFR_{\mathrm{expected}}$ in section 4.2.4, by fitting a line to the plot of $\log(M_*)$ vs. $\log(M_{\mathrm{HI}}/M_*)$. The parent sample for this comparison comprises galaxies in the *stellar mass-limited sample*, including all galaxies with an HI detection, regardless of morphology. In order to probe the entire range of gas fractions, all galaxies from the *stellar mass-limited sample* with a reliable HI detection are used, giving 2,434 galaxies in total. Galaxies that fall below the HI completeness limit with $M_{\mathrm{HI}} < 10^{9.89} M_{\odot}$ are weighted by $1/V_{\mathrm{max}}$. The plot of gas fraction vs. stellar mass for this sample is shown in Fig. 4.18. The best fit line to the data, with each point weighted by $1/V_{\mathrm{max}}$, yields

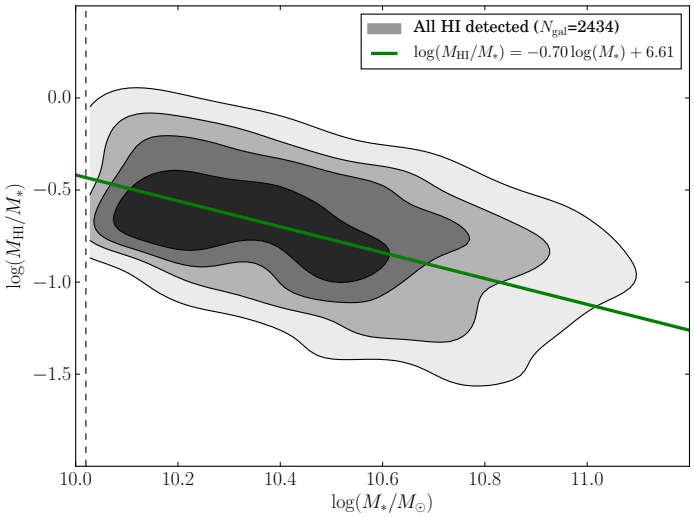

Figure 4.18: Gas fraction as a function of stellar mass for all galaxies in the *stellar mass-limited sample* with an HI detection. The filled grey contours show where 20, 40, 60 and 80 per cent of the galaxies lie, weighted by each galaxy's $1/V_{\rm max}$-value. The green line shows the best fit line to the data, with each point again weighted by $1/V_{\rm max}$. The dashed black line indicates the lower stellar mass limit of the dataset.

the following relationship:

$$\log(M_{\rm HI}/M_*)_{\rm expected} = -0.70\log(M_*/M_\odot) + 6.61\ . \tag{4.10}$$

The scatter in this relationship is 0.26 dex. One can now measure the HI deficiency using (Masters *et al.*, 2012):

$$\log(M_{\rm HI}/M_*)_{\rm deficiency} = \log(M_{\rm HI}/M_*)_{\rm expected} - \log(M_{\rm HI}/M_*)\ , \tag{4.11}$$

where $\log(M_{\rm HI}/M_*)_{\rm expected}$ is given in Eq. 4.10. Galaxies with higher gas fractions than expected for their stellar mass have negative HI deficiency, and galaxies with low HI fractions have positive HI deficiency.

As in section 4.2.4, the first comparison is for the completeness of the *arm number subsamples*. The fraction of the *stellar mass-limited sample* of ALFALFA targeted spiral galaxies with a single detection in the α70 catalogue as a function of arm number is shown in Fig. 4.19. As was the case in for the FUV and MIR fluxes, there is a preference for more of the many-armed galaxies to have measured HI fluxes. However, as in section 4.2.4, the overall completeness is similar, with each of the samples having detection fractions of ∼70–80 per cent.

To compare whether the spiral galaxy samples are deficient in gas for their stellar mass, the measured gas fractions for the *stellar mass-limited* sample of spirals are compared, and the distributions are plotted in Fig. 4.20. Only galaxies with ALFALFA detections are included, giving 1,066 spiral galaxies in total. To ensure that a full range of gas masses is probed, all α70 detections are included and a $V_{\rm max}$ weighting to the HI detections that fall below the HI complete mass of $\log(M_{\rm HI}) = 9.89\log(M_\odot)$ is applied. The resulting HI deficiency distributions are plotted in Fig. 4.20. The median HI deficiencies are -0.15 ± 0.08, -0.05 ± 0.02, -0.10 ± 0.03, -0.18 ± 0.05 and -0.24 ± 0.04 for $m = 1$, 2, 3, 4 and 5+ respectively. There is a trend that many-armed spiral galaxy samples are more HI rich than $m = 2$ galaxy samples. Although the null hypothesis that the $m = 3$ sample is from the same parent distribution as the $m = 2$

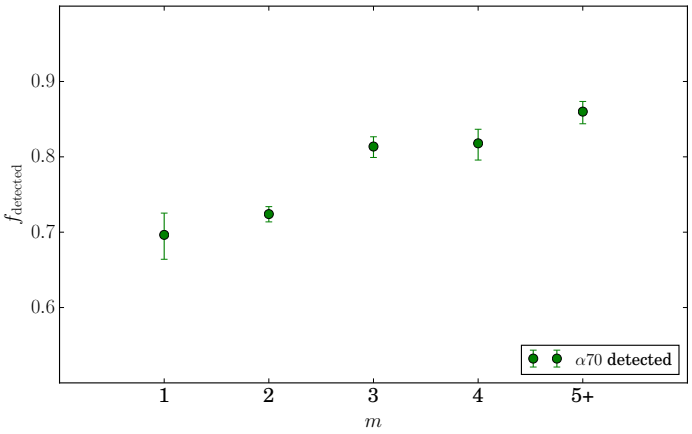

Figure 4.19: Fraction of galaxies in the α70-SDSS footprint with a reliably detected HI flux, in accordance with Haynes *et al.* (2011) as a function of spiral arm number. The error bars show the 1σ error calculated in accordance with Cameron (2011).

sample cannot be ruled out, as the KS p-value is 0.31, it is unlikely that this is the case for the $m = 4$ and $m = 5+$ *arm number subsamples* with respect to the $m = 2$ sample, where the corresponding p-values are $\sim 10^{-2}$ and $\sim 10^{-4}$.

4.2.7 The role of bars

One of the key features via which a grand design spiral pattern may emerge is via a bar instability (Kormendy & Norman, 1979). The exact nature of the dependence of grand design spiral structure on the presence of a bar in a galaxy disc is not fully understood, since many-armed spiral galaxies can still exist in the presence of a bar, and not all grand design spiral galaxies host strong bars (this was discussed in detail in section 1.3.4). Nonetheless, bars are more common in grand design spiral galaxies (Elmegreen & Elmegreen, 1982, 1987b). Bars can affect the gas and star formation properties of their host galaxies (Athanassoula, 1992; Oh, Oh & Yi, 2012; Masters *et al.*, 2012). Previously, *strong* bars were removed from the analysis. Given the dependences found in the earlier parts of this chapter, the final piece of analysis is to assess the potential impact of bars in driving these dependencies. To assess the impact that the presence of bars have on spiral galaxies and understand whether the differences in the galaxy populations are driven by the presence of bars with spiral structure, the properties of barred and unbarred galaxies are now compared.

GZ2 has been used to define galaxies with and without bars. I use the same prescription of Masters *et al.* (2011) by selecting galaxies with $p_{\rm bar} > 0.5$ as barred. The fraction of galaxies with bars is significantly higher for the $m = 2$ sample, with 50 ± 1 per cent of galaxies having bars, compared to $16 - 25$ per cent for each of the many-armed samples. This confirms the results of previous studies (e.g., Elmegreen & Elmegreen 1982, 1987b) for my sample: two-armed grand design spiral galaxies are more likely to host a bar than many-armed spiral galaxies.

Each of the many-armed samples comprise fewer galaxies than the two-armed galaxy sample, and only a small number of those have bars. In order to compare the properties of barred and unbarred samples of galaxies with different arm numbers with good number statistics, the 3, 4, and 5+ armed spiral galaxies are grouped into a single, 'many-arm' category. I deem this to be reasonable, since any trends seen in each of the many-armed spiral galaxy samples have been shown to be similar, and contrast with the

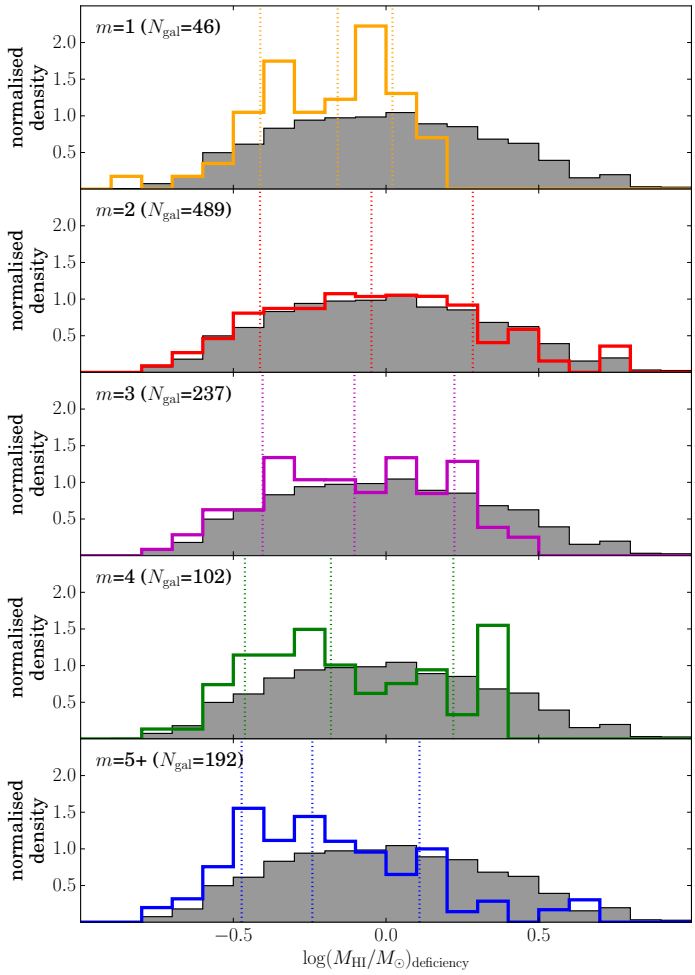

Figure 4.20: HI deficiency, calculated using Eq. 4.10 and 4.11, for each of the *arm number sub-samples*. The underlying grey histograms show the distributions for all galaxies with detected HI, irrespective of morphology and the solid lines show the same distributions for all galaxies split by spiral arm number. Each HI detection is weighted by $1/V_{\rm max}$. The dotted vertical lines show the median, 16th and 84th percentiles of each of the distributions.

$m = 2$ sample. In this analysis, all galaxies classified as spiral are included, retaining those with $p_{\rm bar} > 0.5$, which were removed for the earlier results. As was the case in sections 4.2.4 and 4.2.6, the first stage is to compare the completeness fractions. They are shown in Fig. 4.21. The overall completeness of each of these measures decreases for strongly barred galaxies, yet the detection fractions are still consistently higher for many-armed spirals irrespective of $p_{\rm bar}$.

In order to check whether the presence of bars in the galaxy *arm number samples* affect the IRX-β trends in section 4.2.5.1, the samples are divided into four bins of bar strength, defined using the GZ2 $p_{\rm bar}$ statistic. The resulting IRX-β relations for the $m = 2$ and the $m > 2$ samples are shown in Fig. 4.22. The median offsets from the Boquien *et al.* (2012) relation are -0.06 ± 0.01, -0.02 ± 0.02, 0.00 ± 0.02 and 0.00 ± 0.02 for each of the bar strength bins for two-armed spirals. The corresponding offsets for the many-armed spirals are -0.15 ± 0.01, -0.10 ± 0.02, -0.11 ± 0.02 and -0.17 ± 0.03. These results therefore show that with or without the presence of a bar, many-armed spirals are more UV luminous than expected for normal star-forming galaxies than two-armed spiral galaxies.

It is evident from the top row of Fig. 4.22 that bars affect both IRX and β in two-armed

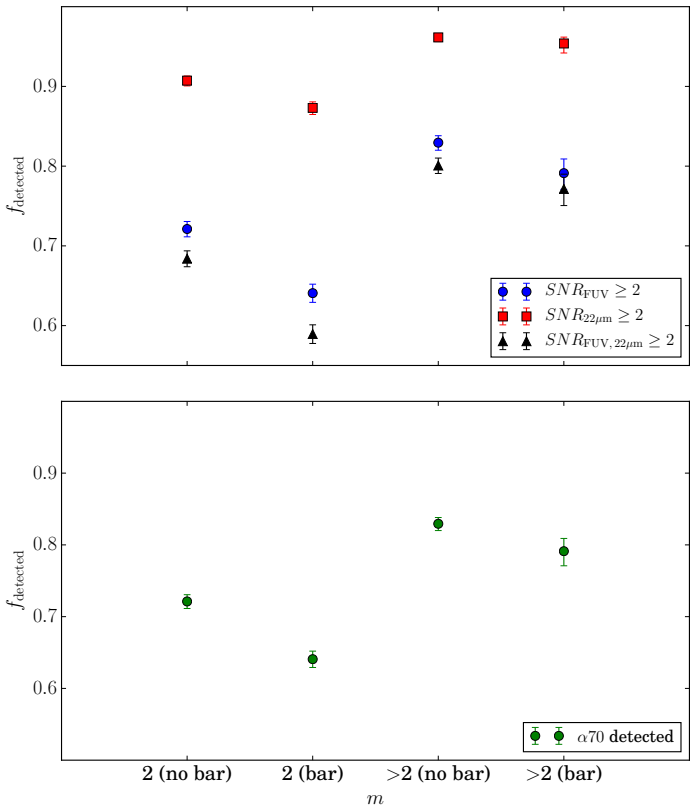

Figure 4.21: GALEX FUV, WISE 22μm and ALFALFA HI detection fractions for barred and unbarred galaxies. Top panel: fraction of galaxies with GALEX FUV and WISE 22 μm detections for each of the barred and unbarred spiral samples. Bottom panel: fraction of the galaxies in the α70 survey region with a reliable detection. The error bars show the $\pm 1\sigma$ errors, calculated according using the method of Cameron (2011).

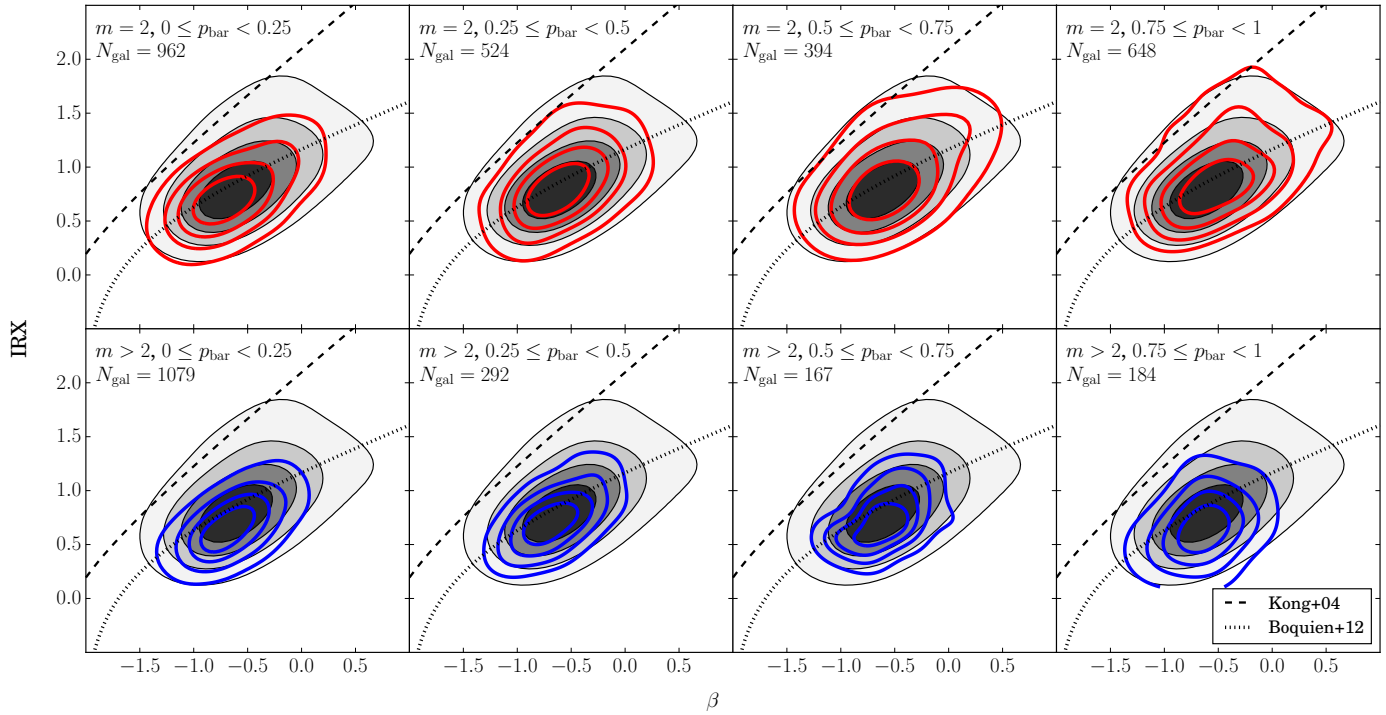

Figure 4.22: IRX-β for $m = 2$ and $m > 2$ spiral galaxies divided into bar strength bins. The filled grey contour shows the distribution for all galaxies from the *stellar mass-limited sample*, including galaxies of all morphologies. Four bins of GZ2 $p_{\rm bar}$ run from left to right for $m = 2$ galaxies (top row) and $m > 2$ galaxies (bottom row), and their respective points are indicated by the solid contours. The contours indicate the regions enclosing 20, 40, 60 and 80 per cent of the points for each sample. The measured IRX-β relations for normal star-forming galaxies (Boquien *et al.*, 2012) and starburst galaxies (Kong *et al.*, 2004) are shown for reference.

spirals, without causing any significant deviation away from the IRX-β relation for normal star-forming galaxies.

4.3 Discussion

In this chapter, the overall demographics of spiral galaxies were first considered. The total stellar masses of spiral galaxies are consistent, irrespective of the spiral arm number. This result is unsurprising if one considers swing amplification theory (Toomre, 1981). This suggests that it is not the overall size and mass of a galaxy that determines the spiral arm number. Instead, the galaxy bulge, disc and halo relative sizes and masses determine the overall spiral arm number, following a relation strongly dependent on the disc fraction, $f_{\rm d}$ (Carlberg & Freedman, 1985; Bottema, 2003; Fujii *et al.*, 2011; D'Onghia, Vogelsberger & Hernquist, 2013). In this brief analysis, the overall bulge and disc masses have not been considered in any detail. A weak trend was found that two-arm spiral galaxies are more common in higher density environments, which may be related to tidally induced spirals (Chamberlin, 1901; Toomre & Toomre, 1972b,a; Tully, 1974; Oh *et al.*, 2008). The strongest result was observed in the overall galaxy colours. Given that we expect metallicity does not play a significant role (see section 4.1.6), there are two ways in which the colours of galaxies can be changed – either the recent SFHs can differ, or a larger dust fraction may be present. The relative roles that each of these play are discussed below.

4.3.1 Total SFRs

In section 4.2.4, overall SFRs with respect to spiral arm numbers were compared. There were only marginal differences between the samples. I note that galaxies with different spiral arm numbers occupy similar ranges of stellar mass (see Fig. 4.2 and 4.9) and find no enhancement in the measured SFR of the two-armed spirals relative to the many-armed spirals. On the other hand, galaxies with more spiral arms have slightly higher detection fractions (and hence less likelihood of very low SFR) in both the UV and MIR. For galaxies with secure measurements, 3- and 4-armed galaxies have marginally higher average sSFRs than those in the two-armed sample.

Many-armed spiral patterns occur readily in simulations of undisturbed discs, and tend to be transient in nature (Bottema, 2003; Baba *et al.*, 2009; Grand, Kawata & Cropper, 2012b; Baba, Saitoh & Wada, 2013; D'Onghia, Vogelsberger & Hernquist, 2013; Roca-Fàbrega *et al.*, 2013). In contrast, stable two-armed spiral patterns usually require some form of perturbation (Sellwood, 2011), in the form of a tidal interaction, bar instability or density wave. An enhancement in the current SFR would be expected if strong density waves were responsible for the triggering of star formation (Roberts, 1969), bars were triggering star formation in the galaxy centre (Athanassoula, 1992) or if there were ongoing tidal interactions (Barton, Geller & Kenyon, 2000; Ellison *et al.*, 2008) in two-armed galaxies. Such mechanisms should not be evident in many-armed galaxies. My results show no strong evidence for any SFR enhancement in two-armed spiral galaxies. These results therefore support those of Elmegreen & Elmegreen (1986), Stark, Elmegreen & Chance (1987) and Willett *et al.* (2015), where it was found that different forms of spiral structure do not lead to a deviation from the total SFR relations of local galaxies. They are also consistent with Foyle

et al. (2011) and Choi *et al.* (2015), where there was no conclusive evidence for the triggering of star formation by grand design spiral arms themselves. Instead, my results favour a scenario where spiral arms simply reflect the arrangement of star-forming material in galaxies, without being directly responsible for the triggering of star formation (Vogel, Kulkarni & Scoville, 1988; Elmegreen, 2002; Moore *et al.*, 2012).

4.3.2 Obscured vs. unobscured star formation

In section 4.2.5 it was shown that although the *total* SFRs are consistent with spiral arm number, the fraction of the young stars that are obscured by dust differs significantly. At a given SFR, two-armed spirals display more MIR dust emission, indicating that a greater proportion (~ 10 per cent) of their young stellar population resides in heavily obscured regions. This is likely due to different relative distributions of star formation and dust in galaxies with different numbers of spiral arms.

Considering the IRX-β diagram, (unbarred) galaxies with all numbers of arms have similar β distributions, indicating that the amount of extinction affecting the *observed* UV light does not vary substantially with spiral structure. On the other hand, IRX varies substantially, indicating more extinction for two-armed spirals. In order to avoid modifying β, this additional extinction must be in the form of heavily obscured regions, from which almost no UV escapes. Therefore, it is the relative distribution of young stars and regions of high extinction which varies with arm number.

However, regions of very high dust extinction are the same places in which stars form, and so their distributions are closely related. A number of possibilities seem to be admitted by my results. Consider a single star-forming molecular cloud within a galaxy spiral arm. The fraction of young stars which are heavily obscured could depend on the covering fraction of surrounding, but otherwise unrelated, molecular clouds. Alternatively, it may depend on the degree to which the young stars have escaped their own birth cloud. In the first case, the obscured fraction is determined primarily by geometry: by the relative spatial distribution (and perhaps sizes) of star-forming regions. In the second scenario, the obscured fraction is related to the time since the region commenced star formation, and perhaps other physical properties of the molecular cloud.

Grand design spiral arms are typically better defined and higher-contrast than many-arm structures (Elmegreen, 2011). I have also seen that, despite having fewer arms, they have similar total SFRs. These observations imply that two-arm spirals have more, or larger, star formation regions in a given volume of spiral arm. This could result from mechanisms associated with grand design spiral structure, such as a strong density wave, that act to gather more gas and dust into spiral arm regions. For example, simulations suggest that the presence of density waves leads to the formation of more massive molecular clouds (Dobbs, Burkert & Pringle, 2011; Dobbs, Pringle & Burkert, 2012). Since the molecular clouds present a larger local cross section, a greater fraction of young stars are obscured by dust. The ratio of MIR to UV emission (i.e. IRX) is therefore higher.

Alternatively, the obscured fraction may be related to the recent SFH. If this is more bursty in nature, then more of the resulting luminosity is emitted in the MIR than in the UV: the IRX-β relation is displaced upwards (Meurer, Heckman & Calzetti, 1999; Kong *et al.*, 2004). If star formation in grand design spirals is driven by a triggering mechanism – such as a tidal interaction with a companion galaxy (Sundelius *et al.*,

1987; Dobbs *et al.*, 2010) or a density wave (Seigar & James, 2002; Kendall, Clarke & Kennicutt, 2015) – while many-armed spirals are not subject to the same mechanisms, then one would expect their recent SFHs to differ. Boquien *et al.* (2012) show that the scatter in IRX-β for star-forming galaxies is attributable to the intrinsic UV slope β_0, which is sensitive to the recent SFH. Kong *et al.* (2004) suggests that for a period of ~ 1 Gyr *following* a starburst, galaxies will occupy a lower position in the IRX-β plane: as the new stars escape their molecular birth clouds the galaxy becomes UV bright, and the declining MIR emission is not replaced by further star formation. As many-armed spirals lie lower in the IRX-β plane, it is possible they are associated with a (mild) post-starburst state. In Fig. 4.7, it was shown that a recent, rapid decline in SFR was required to produce the observed optical colours for many-armed spirals, which would be consistent with these observations.

A further possibility is that the dispersal time of molecular clouds varies with spiral arm number. Although both UV and MIR emission are associated with recent star formation (e.g., Hao *et al.* 2011; Kennicutt & Evans 2012), they actually probe different timescales in the evolution of star-forming regions. In nearby galaxies, UV emission is displaced from the Hα emission that traces the most recent star formation, whereas MIR emission arises from regions much closer to the brightest Hα knots (Helou *et al.*, 2004; Calzetti *et al.*, 2005; Crocker *et al.*, 2015). To observe UV emission, the parental molecular cloud must be dispersed, a process that takes ~ 7 Myr in local spirals (Grosbøl & Dottori, 2012). However, more massive molecular clouds may take longer to disperse. The dispersion of molecular clouds may thus be a more rapid process in many-armed galaxies, with weaker spiral structure, meaning that the UV emitting population emerges more quickly.

The radial geometry of the star formation in spiral galaxies may also be affected by the presence of differing forms of spiral structure. Since the level of dust obscuration is greater towards the centre of galaxies (e.g., Boissier *et al.* 2004; Roussel *et al.* 2005; Boissier *et al.* 2007) these results could imply that star formation occurs more centrally in two-armed spiral galaxies, which is proposed to be the case for barred spirals (e.g., Athanassoula 1992; Oh, Oh & Yi 2012). Given that bars are also associated with two-armed spiral structure (Kormendy & Norman, 1979), this may have a strong influence on the observed properties of galaxies. However, in section 4.2.7 the influence that the presence of strong bars has on the IRX-β diagram was investigated, and I found that the presence of bars in the galaxies led to no differences in the offset from the IRX-β relation. This suggests that the spiral structure itself is responsible for the observed offsets from the normal IRX-β relation, rather than bars and the radial geometry of star formation.

Discerning between the possibilities outlined above will require a more careful consideration of the distribution, properties and evolution of molecular clouds within individual galaxies. However, with further synthesis of empirical results and sophisticated modelling, further progress in understanding how spiral arms relate to star formation seems promising. I discuss future possibilities for further analysis of these results in section 7.2.2.

4.3.3 HI fractions

Gas plays a critical role in sustaining spiral structure in discs. Gas in discs contributes to the growth of spiral perturbations via swing amplification in both grand design and many-armed spirals (Jog, 1992, 1993). The accretion of cool gas onto galaxy discs can also help sustain many-armed patterns. The role that the amount of gas plays in galaxies with different spiral arm numbers was considered in section 4.2.6. Given that gas could potentially amplify or sustain both two-armed (Ghosh & Jog, 2015, 2016) and many-armed spiral structure (Jog, 1993), then it is expected that all of the galaxy samples should contain significant quantities of HI. I found that many-armed spiral galaxies are the most gas rich, whereas two-armed spirals are the most gas deficient. Given that the total SFRs are similar for all of the samples, this implies that HI is converted to stars more efficiently in two-armed spirals than in many-armed spirals. As swing amplification (theoretically) acts to amplify all types of spiral structure, it is unclear why different spiral arm patterns would be more or less gas rich. It is perhaps the case that a higher gas fraction is required to sustain a many-armed spiral pattern in galaxy discs.

Another factor to be considered is the presence of bars in the spiral galaxies. In this analysis, I remove all strongly barred galaxies, yet still see a trend for two-armed galaxies, which are usually associated with bar instabilities, to be the most gas poor (Davoust & Contini, 2004; Masters *et al.*, 2012). Therefore, variation in the gas fraction must also relate directly to differences in spiral arm structure or to the presence of weak bars.

Chapter 5

The demographics of galaxies with respect to spiral arm pitch angle

In this chapter, I present the results that were first presented in Hart *et al.* (2017b). All of the work undertaken in this chapter was performed by the author, with advice from Steven Bamford and the other co-authors listed in Hart *et al.* (2017b).

5.1 Overview

In general, spiral arms can be described by two quantities – the spiral arm number, and the spiral arm pitch angle (Dobbs & Baba, 2014). The latter quantity is a measure of how tightly wound spiral arms are, and is the main focus of this chapter. Spiral arms can usually be described by one of two equations. The first is the logarithmic spiral, given by (eg. Seigar & James 1998b; Davis *et al.* 2012)

$$r = r_0 e^{\tan(\psi)\theta}, \tag{5.1}$$

in circular polar co-ordinates. The second is the hyperbolic spiral function, given by

$$r = r_0/\theta. \tag{5.2}$$

A hyperbolic spiral can be thought of as a log spiral with a varying pitch angle which tightens towards the centre. This effect is shown in Fig. 5.1a. The quantity r_0 scales the size of the spiral structure. The second quantity in Eq. 5.1, ψ is called the spiral arm pitch angle and affects how tightly wound the spiral arms are: smaller pitch angles mean tighter spiral arms. The effect of varying the pitch angle is shown in Fig. 5.1b. In the extreme case of $\psi = 0°$, the spiral pattern is a circle of radius r_0; when $\psi = 90°$, it is a straight line emanating from the centre of the circle. The form of the equation describing the path of a spiral arm offers information on the underlying processes that are responsible for the spiral arm. Logarithmic spiral arms are usually indicative of density waves, including kinematic density waves from swing amplified mechanisms, whereas material arms can usually be described by a hyperbolic function. The latter function is directly proportional to the galaxy rotation velocity if the rotation curve is flat, as material arms rotate rigidly with the galaxy disc (Kennicutt, 1981). It has been demonstrated that most spiral arms can be well described by log spiral arcs (Rots & Shane, 1974, 1975; Boeshaar & Hodge, 1977; Kennicutt & Hodge, 1982; Davis &

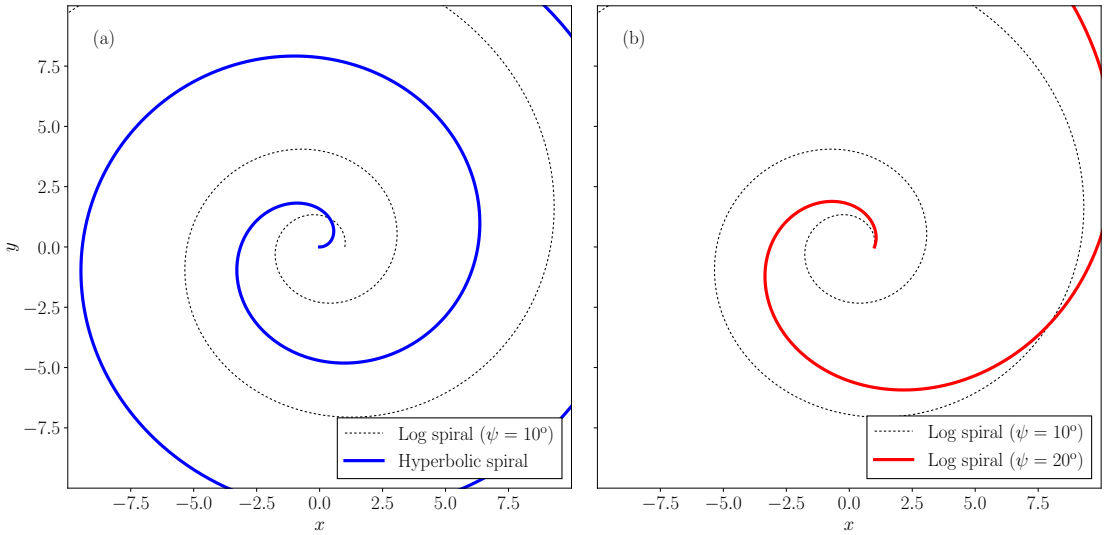

Figure 5.1: Diagrams of logarithmic and hyperbolic spiral patterns. In each panel, a logarithmic spiral with $\psi = 10°$ is shown for reference. (a) Comparison with a hyperbolic spiral. (b) The effect of changing the pitch angle. $r_0 = 1$ in all cases.

Hayes, 2014), which in turn suggests that spiral arms are density enhancements due to the presence of density waves or other similar mechanisms, and are not material in nature (Seigar & James, 1998a,b; D'Onghia, Vogelsberger & Hernquist, 2013).

Given the difficulties in measuring pitch angle in large samples of galaxies, small samples with typically $\lesssim 100$ galaxies have been used to study how it varies with other galaxy properties (e.g. Seigar 2005; Seigar *et al.* 2006; Martínez-García 2012; Savchenko & Reshetnikov 2013). These studies of local galaxies reveal interesting trends relating spiral arm geometry with fundamental galaxy properties. It has been established that spiral arm pitch angle is strongly correlated with the rotation properties of galaxies: galaxies with higher rotation velocities have more loosely wound spiral arms (Kennicutt, 1981), and pitch angles are even more closely correlated with the central mass concentration which alters the rate of shear in galaxies (Seigar, 2005; Seigar *et al.*, 2006). These results imply that the underlying mass distribution of galaxies directly affects the shapes of spiral arms (Seigar *et al.*, 2008, 2014; Berrier *et al.*, 2013), explaining why galaxies with more tightly wound arms are often associated with greater central mass concentrations (Hubble, 1926b). Although this link has been clearly established, it has only been observed in small samples of nearby grand design spirals. Galaxies which display different types of spiral structure could have a different explanation.

Simulations show that many-arm structures should have larger pitch angles (D'Onghia, Vogelsberger & Hernquist, 2013; Grand, Kawata & Cropper, 2013) and there is evidence that weaker, multi-arm spiral patterns are looser (Puerari & Dottori, 1992). In these simulated galaxies, spiral arms wind up, becoming tighter over time, meaning that pitch angle may also indicate the age of the arm feature (Pérez-Villegas *et al.*, 2012; Grand, Kawata & Cropper, 2013). Strong bars can also influence the pitch angles of spiral galaxies (Athanassoula, Romero-Gómez & Masdemont, 2009; Martínez-García, 2012; Baba, 2015). If a bar is strong enough and its corotation radius extends beyond the disc, the nature of spiral arms could change completely, from density waves to material arms amplified at the end of the bar (Roca-Fàbrega *et al.*, 2013). Another factor to consider is galaxy-galaxy interactions – such interactions can morphologically

disturb galaxies (e.g. Ellison *et al.* 2010; Kaviraj 2014; Patton *et al.* 2016), leading to looser arms in galaxy-galaxy separations $\lesssim 100$ kpc (Casteels *et al.*, 2013). Testing the effects that the aforementioned processes have on the structure of spiral arms requires statistically complete samples of spiral galaxies with measured arm pitch angles.

In this chapter, I use the pitch angle measurements as described in chapter 3 to measure pitch angles in a large sample of low-redshift galaxies. Using these data, I look at how various morphological features affect spiral arm pitch angle, including spiral arm number, the presence of bars, and central mass concentrations.

5.2 Sample selection

Spiral galaxies are selected using the same criteria of chapter 4, by selecting galaxies with $p_{\rm features} \cdot p_{\rm not\,edge\,on} \cdot p_{\rm spiral} \geq 0.5$ and $N_{\rm spiral} \geq 5$. I also limit my sample to galaxies with redshift $0.02 < z \leq 0.055$ to select the most reliably identified spiral galaxies, and to ensure the greatest reliability in the Mendel *et al.* (2014) bulge-disc mass measurements. I ensure all of our galaxies are relatively face-on by using a cut of $(b/a)_g > 0.4$, where a and b are the isophotal semi-major and minor axes in the g-band. The reasoning behind the selection of this cut was discussed in section 4.2.2. Galaxy Zoo statistics can reliably identify bars (Masters *et al.*, 2011) and spiral arms (section 4.2.2) for galaxies more face-on than this threshold. Galaxies were also subdivided into barred, weakly barred and unbarred subsamples using the GZ2 statistics. The presence of bars in our galaxies is measured using the response to the 'is there a bar?' question in GZ2. A continuous statistic for this purpose is the quantity $p_{\rm bar}$, defined as the fraction of responses that said a bar was present in a galaxy. The bar question has been shown to be an effective method for measuring not only the presence of bars, but also the strength of bars in galaxies (Skibba *et al.*, 2012). In some of our analysis, we will compare galaxy properties irrespective of the presence of bars. I therefore use cuts of $p_{\rm bar} > 0.5$ to define a subsample of strongly barred galaxies, $0.2 < p_{\rm bar} \leq 0.5$ to define weakly barred galaxies and $p_{\rm bar} \leq 0.2$ to define unbarred galaxies in the spiral sample (Masters *et al.*, 2011; Skibba *et al.*, 2012). The numbers of galaxies in subsamples made using these cuts are detailed in Table 5.1.

In order to study galaxy properties in a representative manner, I define a sample of spiral galaxies complete in stellar mass. The Mendel *et al.* (2014) catalogue contains galaxies with $14 < m_r \leq 17.77$. In GZ2, a faint magnitude limit of $m_r \leq 17$ is also applied. All galaxies with $0.02 < z \leq 0.055$ with magnitudes $14 < m_r \leq 17$ are included in the *luminosity-complete sample*. The thin blue line in Fig. 5.2a shows the faint magnitude limit as a function of redshift, and the thicker red line shows the bright end limit imposed in Mendel *et al.* (2014). In total, there are 9570 spiral galaxies with $0.02 < z \leq 0.055$ in the *luminosity-complete sample*.

In order to define a sample complete in stellar mass, the stellar mass completeness limits are computed with redshift. In this chapter, I used the bulge+disc stellar masses from Mendel *et al.* (2014), assuming that all galaxies have a bulge and disc component. I followed the method of Pozzetti *et al.* (2010), later used in a low-redshift SDSS sample in Weigel, Schawinski & Bruderer (2016), to define the stellar mass completeness and the steps are outlined below. Spiral galaxies were binned by redshift in bins of Δz=0.0025. Each galaxy in a bin was then assigned a limiting mass, $M_{*,\rm lim}$, defined as the mass the galaxy would have if its luminosity was that of the faint luminosity-limit

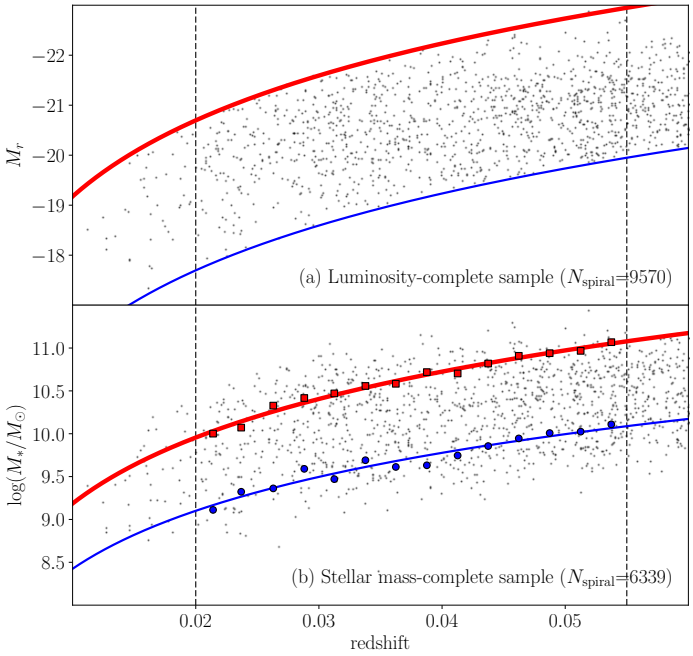

Figure 5.2: Galaxy magnitude and stellar mass completeness for the study of pitch angles. (a) Galaxy redshift vs. absolute r-band magnitude. The black points show individual galaxies. The thinner blue line indicates the faint magnitude limit (m_r=17), and the thicker red line shows the bright magnitude limit ($m_r = 14$). (b) Galaxy redshift vs. total galaxy stellar mass (Mendel *et al.*, 2014). The black points show individual galaxies. The red squares show the upper mass limits in bins of Δz=0.0025, and the blue circles show the lower mass limits. The vertical dashed black lines show the redshift limits of $0.02 < z \leq 0.055$. The best fit lines to the red squares is shown by the thicker red line, and the best fit to the blue circles is shown by the thinner blue line. In both panels, a subset of 4,000 galaxies are shown for clarity.

of the survey at the galaxy's redshift, given its own mass-to-light ratio, M_*/L_r. I then selected the faintest 20 per cent of galaxies in the bin. The stellar mass completeness limit, $M_{*,\rm lower}$, was measured as the mass below which lay 95 per cent of the $M_{*,\rm lim}$ values of this faintest 20 per cent subsample. This was computed for each bin in turn, and they are shown by the blue circles in Fig. 5.2b. As the sample also includes a bright magnitude limit, I computed the upper mass limit, $M_{*,\rm upper}$, by calculating the maximum mass galaxies could have, $M_{*,\rm lim\,max}$, and measuring the mass above which 95 per cent of the limiting masses of the 20 per cent brightest galaxies in each bin lay. These are shown by the red squares in Fig. 5.2b. The limiting masses with redshift were then measured by fitting a log curve to the upper and lower mass limits, and they take the form

$$\log(M_{*,\rm lower}/M_\odot) = 2.07(\pm0.15)\log(z) + 12.64(\pm0.21), \tag{5.3}$$

and

$$\log(M_{*,\rm upper}/M_\odot) = 2.45(\pm0.08)\log(z) + 14.05(\pm0.12). \tag{5.4}$$

The $\pm$ values indicate the error in each fitted parameter, obtained from the covariance matrix. These lower and upper mass limits are shown by the thin blue line and thicker red line in Fig. 5.2b. In total there are 6339 galaxies in the *stellar mass-complete sample* between these limits.

In order to sample fairly for all stellar masses, a volume correction was applied. This means the *stellar mass-complete sample* can mimic a *stellar mass-limited sample*. For

each galaxy, the maximum volume is calculated using the upper and lower redshift bounds where a galaxy with its stellar mass could fall within the stellar mass completeness limits defined above. Each galaxy is then assigned a $1/V_{\rm max}$ weighting. I removed any galaxies that lie in a very small volume, and thus having large $1/V_{\rm max}$ corrections, by only selecting galaxies in $9.45 < \log(M_*/M_\odot) \leq 11.05$ (corresponding to $1/V_{\rm max} \leq 10$). In total, 117 (1.8 per cent) of the galaxies were removed for this reason, leaving a final *stellar mass-complete sample* of 6222 spiral galaxies. These samples are further subdivided into spiral galaxies with different arm numbers and bar probabilities. The number of spiral galaxies in each subsample of the *stellar mass-complete sample* is given in $N_{\rm gal}$ of Table 5.1, and the median, 16th and 84th percentile stellar masses is given in the $\log(M_*/M_\odot)$ column of Table 5.1.

In Table 5.1, it can be seen that there is a small residual dependence of stellar mass on galaxy morphology, with galaxies with more spiral arms and stronger bars having greater stellar masses. In this chapter, we wish to study properties of galaxies with respect to galaxy morphology only, with none of our results dependent on stellar mass. For this reason, I chose to match all of the subsamples in stellar mass to ensure there are no residual dependencies driving our results in later sections. The four-arm unbarred subsample is selected as the sample to match to (denoted by a * in Table 5.1) as it is the one with the fewest galaxies. I note that there are actually fewer one-arm spirals, but these are a special case of galaxy, usually associated with mergers (Casteels *et al.*, 2013), so contribute little to our analysis later in the paper. I used the KDE-matching method described in section 3.4 to match up the samples in stellar mass to the $m = 4$ sample. The number of galaxies, and their associated stellar masses, for each *mass-matched subsample* are given in the columns $N_{\rm gal}$ (M_*-matched) and $\log[M_*/M_\odot]$ (M_*-matched) of Table 5.1.

5.3 Assessing the reliability of pitch angle measurements

In this section, I assess how reliable the spiral arm pitch angles derived from section 3.3 are. In section 5.3.1, I consider how reasonable the pitch angle distributions are, and in section 5.3.2 I look at how they compare directly to another measure of pitch angle.

5.3.1 Pitch angle distributions

Using the arcs identified in section 3.3, the overall pitch angles of the spiral galaxies are compared. I use two statistics to define pitch angles. The quantity $\psi_{\rm arc}$ is the pitch angle assigned to each arc. To define a galaxy-level pitch angle, $\psi_{\rm galaxy}$, I use the same length-weighted average pitch angle as Davis & Hayes (2014), this time restricted to the arcs which I deemed reliable thanks to the work described in section 3.3. The statistic is defined by

$$\psi_{\rm galaxy} = \sum_{n=1}^{N_{\rm arcs}} \frac{L_n \psi_n}{L_{\rm total}}, \tag{5.5}$$

where $N_{\rm arcs}$ is the total number of well-identified arcs, L_n is the length of each individual arc, ψ_n is the pitch angle of each detected arc and $L_{\rm total}$ is the sum of all of the arc lengths. In order to compare the distributions of pitch angles covering all of the broad morphological characteristics identified in GZ2, the *stellar mass-complete* sample is

Table 5.1: Galaxy sample parameters for all of the samples of galaxies in this chapter. For the N columns, the first number indicates the total number of galaxies, and the bracketed number indicates the fraction of those galaxies with at least one good spiral arm in SPARCFIRE (see section 3.3). In the stellar mass columns, the first number indicates the median stellar mass, and the bracketed values are the 16th and 84th percentiles. The * next to the $m = 4$ (spiral) sample indicates that it is the sample that was used as the reference sample for matching in stellar mass.

subsample	N (all)	$\log[M_*/M_\odot]$ (all)	N (M_*-matched)	$\log[M_*/M_\odot]$ (M_*-matched)
spiral (all)	6222 (48.7 per cent)	10.27 (9.89, 10.64)	4908 (48.2 per cent)	10.26 (9.92, 10.58)
$m = 1$ (all)	243 (25.9 per cent)	10.18 (9.78, 10.57)	151 (20.5 per cent)	10.25 (9.92, 10.56)
$m = 2$ (all)	4014 (46.6 per cent)	10.26 (9.88, 10.63)	3208 (45.6 per cent)	10.26 (9.93, 10.58)
$m = 3$ (all)	1108 (56.9 per cent)	10.32 (9.93, 10.66)	876 (57.5 per cent)	10.25 (9.91, 10.56)
$m = 4$ (all)	405 (54.6 per cent)	10.31 (9.93, 10.67)	337 (55.5 per cent)	10.26 (9.92, 10.56)
$m = 5+$ (all)	452 (53.8 per cent)	10.27 (9.88, 10.62)	336 (53.3 per cent)	10.24 (9.93, 10.57)
spiral ($p_{\rm bar} \leq 0.2$)	2237 (48.4 per cent)	10.23 (9.89, 10.56)	1920 (47.6 per cent)	10.26 (9.92, 10.57)
$m = 1$ ($p_{\rm bar} \leq 0.2$)	135 (20.7 per cent)	10.18 (9.76, 10.54)	93 (16.1 per cent)	10.3 (9.98, 10.58)
$m = 2$ ($p_{\rm bar} \leq 0.2$)	1034 (46.9 per cent)	10.19 (9.87, 10.53)	879 (44.7 per cent)	10.25 (9.91, 10.57)
$m = 3$ ($p_{\rm bar} \leq 0.2$)	570 (53.5 per cent)	10.27 (9.93, 10.58)	514 (54.1 per cent)	10.26 (9.93, 10.57)
$m = 4$ ($p_{\rm bar} \leq 0.2$)*	221 (52.0 per cent)	10.26 (9.93, 10.59)	221 (52.0 per cent)	10.26 (9.93, 10.59)
$m = 5+$ ($p_{\rm bar} \leq 0.2$)	277 (53.8 per cent)	10.25 (9.88, 10.58)	213 (53.1 per cent)	10.27 (9.93, 10.58)
spiral ($0.2 < p_{\rm bar} \leq 0.5$)	1858 (50.4 per cent)	10.25 (9.89, 10.61)	1554 (50.3 per cent)	10.25 (9.93, 10.56)
$m = 1$ ($0.2 < p_{\rm bar} \leq 0.5$)	79 (27.8 per cent)	10.24 (9.81, 10.6)	43 (27.9 per cent)	10.24 (9.87, 10.5)
$m = 2$ ($0.2 < p_{\rm bar} \leq 0.5$)	1226 (48.2 per cent)	10.23 (9.89, 10.57)	1081 (47.5 per cent)	10.26 (9.94, 10.57)
$m = 3$ ($0.2 < p_{\rm bar} \leq 0.5$)	330 (60.0 per cent)	10.34 (9.94, 10.65)	256 (60.2 per cent)	10.27 (9.89, 10.56)
$m = 4$ ($0.2 < p_{\rm bar} \leq 0.5$)	115 (59.1 per cent)	10.32 (9.9, 10.66)	88 (61.4 per cent)	10.26 (9.91, 10.51)
$m = 5+$ ($0.2 < p_{\rm bar} \leq 0.5$)	108 (53.7 per cent)	10.27 (9.91, 10.61)	86 (54.7 per cent)	10.21 (9.92, 10.52)
spiral ($p_{\rm bar} > 0.5$)	2127 (47.4 per cent)	10.35 (9.89, 10.72)	1434 (46.7 per cent)	10.26 (9.92, 10.6)
$m = 1$ ($p_{\rm bar} > 0.5$)	29 (44.8 per cent)	10.17 (9.83, 10.82)	15 (26.7 per cent)	10.08 (9.89, 10.43)
$m = 2$ ($p_{\rm bar} > 0.5$)	1754 (45.3 per cent)	10.33 (9.88, 10.69)	1248 (44.6 per cent)	10.27 (9.93, 10.6)
$m = 3$ ($p_{\rm bar} > 0.5$)	208 (61.1 per cent)	10.51 (9.99, 10.8)	106 (67.9 per cent)	10.2 (9.9, 10.54)
$m = 4$ ($p_{\rm bar} > 0.5$)	69 (55.1 per cent)	10.6 (9.96, 10.81)	28 (64.3 per cent)	10.18 (9.87, 10.51)
$m = 5+$ ($p_{\rm bar} > 0.5$)	67 (53.7 per cent)	10.38 (9.85, 10.75)	37 (51.4 per cent)	10.24 (9.92, 10.66)

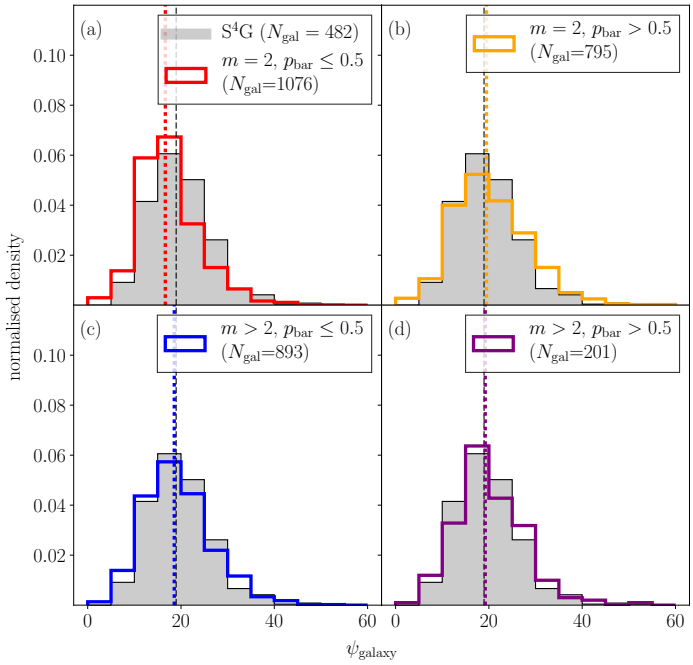

Figure 5.3: Distributions of SPARCFIRE derived galaxy pitch angles ($\psi_{\rm galaxy}$) for four samples of spiral galaxies: (a) two-arm weakly barred/unbarred, (b) two-arm barred, (c) many-arm weakly barred/unbarred and (d) many-arm barred. The grey histogram in each panel show the distributions for the S^{4}G sample of low-redshift galaxies. The vertical dashed black lines show the median pitch angle of the S^{4}G sample, and the dotted vertical coloured lines show the median for each of the subsamples.

divided into four categories: two-arm weakly barred/unbarred ($m = 2$ and $p_{\rm bar} < 0.5$), two-arm barred ($m = 2$ and $p_{\rm bar} \geq 0.5$), many-arm weakly barred/unbarred ($m > 2$ and $p_{\rm bar} < 0.5$) and many-arm barred ($m > 2$ and $p_{\rm bar} \geq 0.5$), and the distributions of $\psi_{\rm galaxy}$ are shown in Fig. 5.3. The mean pitch angle is 18.0° with 16th and 84th percentiles of 12.2° and 26.1° for the entire sample of spirals. For comparison, the Herrera-Endoqui *et al.* (2015) S^{4}G sample is shown. As there is no additional information about arm length here, I measure $\psi_{\rm galaxy}$ as the mean pitch angle of all of the arcs in each galaxy. For this comparison sample, the mean pitch angle is 19.0°, with 16th and 84th percentiles of 13.5° and 25.7°. The overall distributions match well with observed spiral arms in S^{4}G, with the peak pitch angles at $\sim 15 - 20°$ in all cases and KS p-value $> 10^{-2}$ in all but the GZ2 two-arm unbarred subsample, where the distribution is clearly offset to smaller pitch angles. I note that we also see very few galaxies with $\psi_{\rm galaxy} < 10°$ and $\psi_{\rm galaxy} > 40°$, as expected from observations of nearby galaxies (Seigar *et al.*, 2008).

5.3.2 Comparing SPARCFIRE and GZ2 derived pitch angles

In order to check the reliability of our pitch angle measurements, we wish to compare our pitch angles to independently derived pitch angle measurements. In GZ2, there are two characteristics of the spiral structure that have been classified by eye: the number of spiral arms and how tightly wound the spiral arms are. The latter gives a qualitative measure of pitch angle in galaxies. In GZ2, volunteers were asked whether the arms they saw were 'tight', 'medium' or 'loose'. Here, it should be expected that galaxies classified with 'loose' arms have larger galaxy pitch angles.

To measure how tightly wound the spiral structure is in GZ2, I defined two statistics. The first is w, which is defined as the response to the arm winding question which had the highest debiased vote fraction, and can take the values 't', 'm' or 'l' (tight, medium or loose). The second statistic I defined was the average winding score, $w_{\rm avg}$. This is defined as

$$w_{\rm avg} = \sum_{w=1}^{3} w p_w. \tag{5.6}$$

If a galaxy has perfect agreement and all classifiers said the spiral arms were tightly wound, $w_{\rm avg} = 1$, and if everyone classified the arms as loose, then $w_{\rm avg} = 3$. It is sometimes desirable to define a more continuous statistic for measuring arm number, which does not have discrete values. We therefore define $m_{\rm avg}$, which is the average of all of the arm number responses, given by

$$m_{\rm avg} = \sum_{m=1}^{5} m p_{\rm m}, \tag{5.7}$$

where m is the value assigned to each response in turn (1, 2, 3, 4 or 5+) and p_m is the fraction of votes for that response. The statistic can take any value in the range 1–5, where $m_{\rm avg} = 1$ means all volunteers said a galaxy had one spiral arm, and $m_{\rm avg} = 5$ means all classifiers said a galaxy had 5+ spiral arms.

In Fig. 5.4, the winding scores from GZ2 are compared with the directly measured pitch angles, $\psi_{\rm galaxy}$, derived from SPARCFIRE. The black lines in each of the panels of Fig. 5.4 represent the entire population of 3190 galaxies from the *stellar mass-complete sample* with reliable arcs identified by SPARCFIRE, with no cuts made in arm number or bar probability. A clear correlation does exist between the two statistics (Spearman rank statistics $r_s = 0.30$, $p < 10^{-3}$). Such a result is expected if both measurements are reliable methods for measuring spiral arm pitch angle. To check whether this relation holds for all types of spiral structure, I subdivide this full sample into the same four broad spiral morphological subsamples as in section 5.3.1. The winding score vs. pitch angle relation is plotted for each of these subsamples in Fig. 5.4. The correlation between these two measures still exist ($r_s = 0.35$, 0.30, 0.26 and 0.25, $p < 10^{-3}$), no matter which type of spiral structure is present in the galaxy disc. These results therefore offer encouragement that the SPARCFIRE derived pitch angles are physically meaningful. It is also interesting to note that pitch angle estimates are also obtainable from the GZ2 data alone, given the tight relationship between the GZ2 and SPARCFIRE measured statistics. One can do this using a fit to the GZ2 data. A linear best fit yields

$$\psi_{\rm GZ2} = 6.37 w_{\rm avg} + 1.30 m_{\rm avg} + 4.34. \tag{5.8}$$

This calibration depends on both the GZ2 arm winding score and the arm number. As can be seen from Fig. 5.4a and 5.4c, there is an offset from the black line for all galaxies that depends on spiral arm number. Arm number was therefore included in the fit to avoid a systematic uncertainty with arm number. From the distributions of $\psi_{\rm galaxy}$ vs. $\psi_{\rm GZ2}$, I find that the RMS scatter between the two galaxy pitch angle measurements is $\pm 7°$. Given that this covers a significant range of true observed pitch angles (see Fig. 5.3), I advise that these pitch angle measurements should not be used for small samples of galaxies. However, using Eq. 5.8 on large samples of galaxies should give accurate measurements of galaxy pitch angle across the population, which

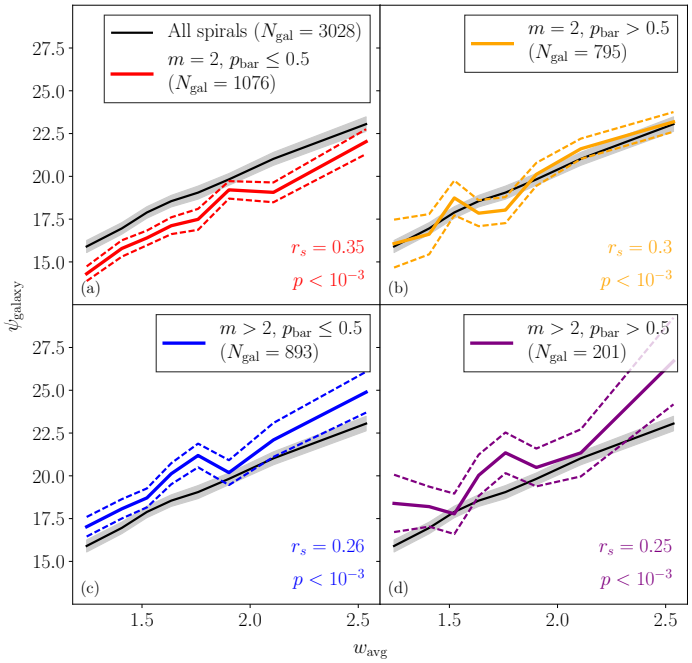

Figure 5.4: GZ2 measured arm tightness ($w_{\rm avg}$) vs. SPARCFIRE measured galaxy pitch angle ($\psi_{\rm galaxy}$) for the *stellar mass-complete sample* of spirals. The lines indicate the mean value for each bin, and the errors indicate 1 standard error on the mean. The black line with grey-filled errors represent the full *stellar mass-limited spiral sample*, and the thicker coloured lines with dashed errors show the same values for four subsamples (a) two-arm weakly barred/unbarred, (b) two-arm barred, (c) many-arm weakly barred/unbarred and (d) many-arm barred. A strong correlation is observed between the GZ2 arm winding statistic and the measured pitch angle in all cases.

can be seen from the tightness of the standard error on the mean in the black lines in Fig. 5.4.

5.4 Pitch angle vs. galaxy structural parameters

In this section, galaxy structural properties and their relation to spiral arm pitch angles are investigated. Of particular note are two statistics that have been derived from the GZ2 classifications of our galaxies: the number of spiral arms and the presence of bars in galaxy discs. Other galaxy structural properties, including galaxy bulge and disc massses as well as SFRs, are also considered here.

5.4.1 Spiral arm number

Simulations of modal spiral arms predict many-arm structures will have looser spiral arms than spirals with fewer arms (Grand, Kawata & Cropper, 2013). On the other hand, given that some two-arm structures are associated with galaxy-galaxy interactions, which are in turn associated with loose structures (Casteels *et al.*, 2013), the two-arm population may include galaxies with looser arms.

In Fig. 5.5a, I plot spiral arm number, m, vs. pitch angle for all of our spiral galaxies. The *stellar mass-matched sample* is used for this, as galaxy stellar mass properties influence the pitch angles of spiral galaxies (e.g. Seigar *et al.* 2006, 2014). Spiral galaxies with one spiral arm are removed from this analysis, as there are only 31 one-arm spirals with reliable arms in the *stellar mass-matched sample*. There is a weak

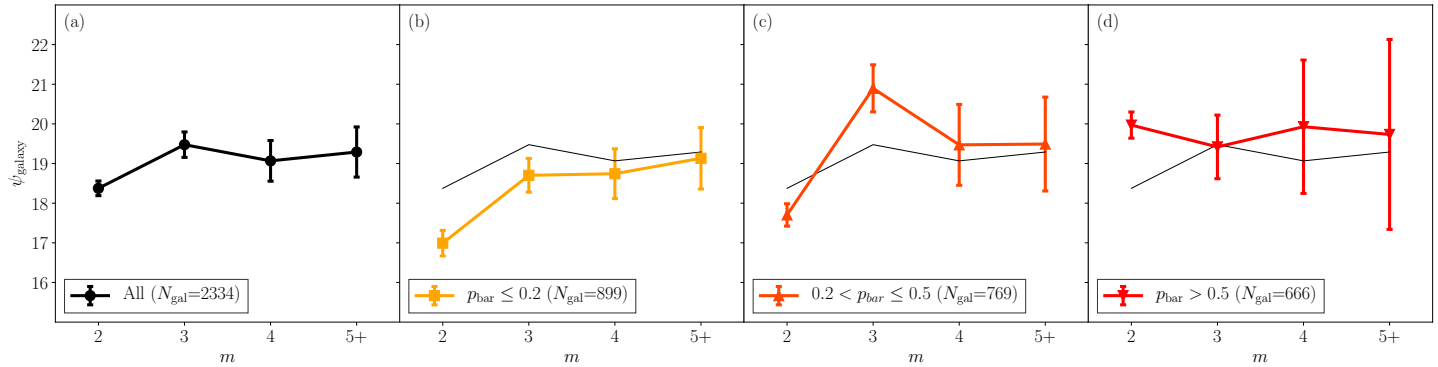

Figure 5.5: Spiral arm number, m, vs. pitch angle, $\psi_{\rm galaxy}$ for the *stellar mass-matched spiral sample* with reliable SpArcFiRe arcs for (a) all, (b) unbarred, (c) weakly barred and (d) strongly barred galaxies. The coloured markers show the mean for each arm number, and the error bars indicate one standard error on the mean. The black line in each plot shows the relationship for all spiral galaxies, irrespective of bar presence for reference. Two-arm galaxies have tighter spiral arms than many-armed galaxies for unbarred and weakly barred galaxies.

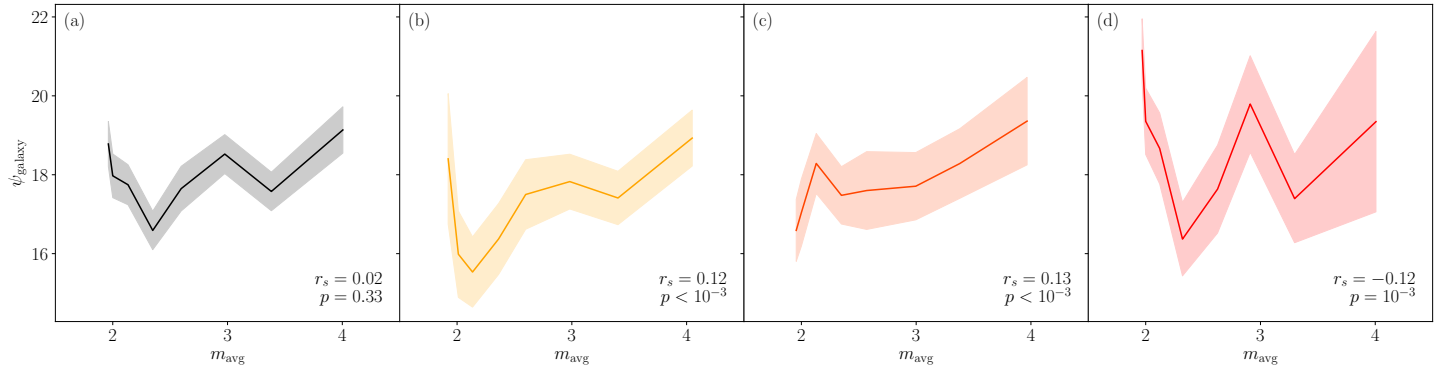

Figure 5.6: Average arm number, $m_{\rm avg}$ vs. pitch angle, ψ, for the *stellar mass-matched spiral sample* with reliable SpArcFiRe arcs for (a) all, (b) unbarred, (c) weakly barred and (d) strongly barred galaxies. The data is divided into eight bins in each panel, and the line shows the mean for each bin. The shaded error region shows one standard error on the mean. The arms of fewer-armed galaxies are tighter for both the unbarred and weakly barred subsamples.

trend that galaxies with more spiral arms have looser spiral structures – two-arm spirals have mean pitch angle $18.6 \pm 0.2°$, whereas the corresponding values for each of the many-arm categories are 19.2 ± 0.3, 19.2 ± 0.5, $19.4 \pm 0.6°$ for $m = 3$, 4 and 5+ respectively. The $\pm$ values denote one standard error on the mean.

Bars could potentially influence the pitch angles of spiral arms, and are more common in grand design, two-arm spiral galaxies (e.g. Elmegreen & Elmegreen 1982; Elmegreen *et al.* 2011). I investigate the role of bars in more detail in section 5.4.2. In this section, I still control for the bar influence on our arm number comparisons by using cuts on the GZ2 $p_{\rm bar}$ statistic described in section 5.2. In Fig. 5.5b-d, I show the arm number vs. pitch angle relationship for unbarred, weakly barred and strongly barred galaxies separately. Removing barred galaxies has little effect on the spiral arm pitch angle of many-arm galaxies: for three arm galaxies, the mean pitch angles are $18.7 \pm 0.4°$, $20.9 \pm 0.6°$ and $19.4 \pm 0.8°$ for unbarred, weakly-barred and strongly-barred galaxies. For four-armed galaxies, the mean pitch angles are $18.7 \pm 0.6°$, $19.5 \pm 1.0°$ and $19.9 \pm 1.7°$, and for five or more armed galaxies they are $19.1 \pm 0.8°$, $19.5 \pm 1.2°$ and $19.7 \pm 2.4°$ respectively. However, the galaxy pitch angle does depend on bar strength in two-arm galaxies: the mean pitch angles are $17.0 \pm 0.3°$, $17.7 \pm 0.3°$ and $20.0 \pm 0.3°$. From Fig. 5.5, it can be seen that unbarred two-arm galaxies are between $1.7°$ and $2.1°$ tighter than each of the many-arm subsamples.

In Fig. 5.6a-d, the spiral arm number vs. pitch angle relation is investigated, this time using the average arm number $m_{\rm avg}$, rather than the absolute arm number. Similar results are observed, where galaxies with more spiral arms have a tendency to have looser arms. As was the case in Fig. 5.5a, a weak correlation is observed when I include all spiral galaxies in Fig. 5.6a ($r_s = 0.02$, $p = 0.33$). However, a clear trend is observed where the arms of many-arm spirals are looser than in two-arm spirals for unbarred ($r_s = 0.12$, $p < 10^{-3}$) and weakly barred galaxies ($r_s = 0.13$, $p < 10^{-3}$) in Fig. 5.6b-c. The trend disappears when one considers strongly barred galaxies and galaxies with fewer arms actually have looser pitch angles ($r_s = -0.12$, $p = 10^{-3}$).

5.4.2 The influence of bars

Bars can affect the types of spiral structures observed in galaxies. In Fig. 5.7, I plot the GZ2 measured bar fraction, $p_{\rm bar}$ for two subsamples of galaxies with measured pitch angles from SPARCFIRE. The thin orange line with filled errors shows how the galaxy pitch angle depends on the GZ2 bar probability for all galaxies in the *stellar mass-complete spiral sample*, irrespective of spiral arm number. Here there is a correlation, where galaxies with stronger bars tend to have looser arms ($r_s = 0.12$). If one instead focuses on only the galaxies with two spiral arms, indicated by the thicker blue line in Fig. 5.7, then a stronger correlation emerges ($r_s = 0.20$). For all spiral galaxies, the mean pitch angle varies from $17.9 \pm 0.4°$ for the bin with the lowest bar fraction to $22.1 \pm 0.7°$ for the bin with the highest bar fraction, a difference of $4.1°$. In the two-arm case, it varies between $16.2 \pm 0.5°$ and $22.1 \pm 0.8°$, a significant difference of $5.9°$.

Here, there are two competing effects which affect the galaxy pitch angle. In section 5.4.1, respect to arm number was only observed in weakly barred or unbarred galaxies. Although two-arm spirals generally have tighter pitch angles, bars are also more common in these galaxies. When considering unbarred spirals, there is a popula-

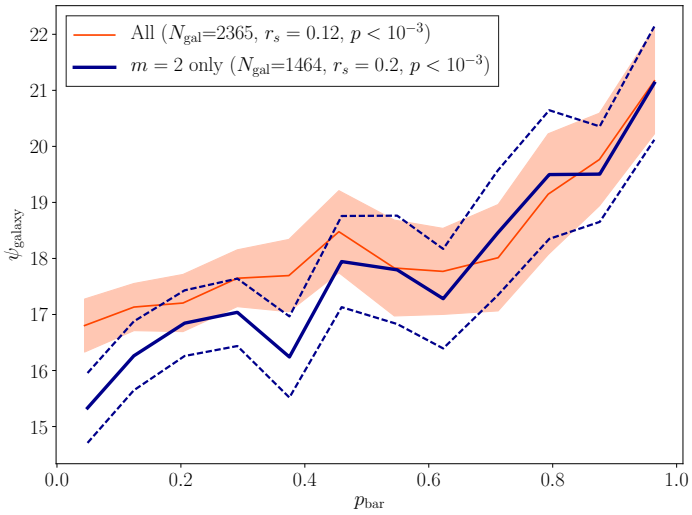

Figure 5.7: GZ2 bar fraction, $p_{\rm bar}$ vs. pitch angle, $\psi_{\rm galaxy}$. The orange line with filled errors indicates the relation for all spiral galaxies in the *stellar mass-limited sample*. The thicker blue line with dashed errors show the same relation for only galaxies with two spiral arms in GZ2 ($m = 2$). The lines indicate the mean for each of the bins, and the errors show one standard error on the mean. Galaxies with stronger bars have looser spiral arms.

tion of two-arm spirals with arms with tight pitch angles, and a many-arm population with arms with looser pitch angles. Adding barred galaxies introduces a population of galaxies with looser arms, which preferentially have two spiral arms. This means the two-arm population has only slightly tighter spiral arms when one considers the overall population including barred galaxies.

5.4.3 Galaxy stellar mass properties

There is evidence that the central mass concentration affects the shear in galaxy discs, which in turn directly influences the spiral arm pitch angle, both in grand design spirals (Seigar *et al.*, 2006, 2014) and in modal many-arm structures (Grand, Kawata & Cropper, 2013). Using the stellar mass properties of galaxies from Mendel *et al.* (2014), I investigate any correlations between central mass concentration and spiral arm structure.

Some of the spiral galaxies in our sample include bars, which often require a separate component to be fit (Gadotti, 2009; Kruk *et al.*, 2017), potentially affecting the accuracy of bulge and disc mass measurements. For this reason, any strongly barred galaxies are removed from this analysis (removing galaxies with $p_{\rm bar} \geq 0.5$). Since all of the galaxies are visually classified spirals, then it is expected that they should be bulge-disc systems, with two distinct components. Therefore, all galaxies in the *stellar mass-complete sample* which have a bulge and disc component fit are used. This leaves a sample of 4095 unbarred spirals, 2019 of which have spiral arm measurements from SpArcFiRe. The spiral arm number is compared for four mass characteristics of our *stellar mass-complete* spiral sample: the bulge mass ($\log[M_{\rm B}]$), disc mass ($\log[M_{\rm D}]$), the total mass ($\log[M_{\rm total}] = \log[M_{\rm B} + M_{\rm D}]$) and the bulge-to-total ratio ($M_{\rm B}/M_{\rm total}$). These quantities are compared to the average arm number in Fig. 5.8a-d. A clear trend is observed in Fig. 5.8, where galaxy mass concentration does seem to have a connection to spiral arm number: galaxies with greater bulge fractions tend to have fewer spiral arms ($r_s = -0.10$, $p < 10^{-3}$). There is also a weak trend that more massive

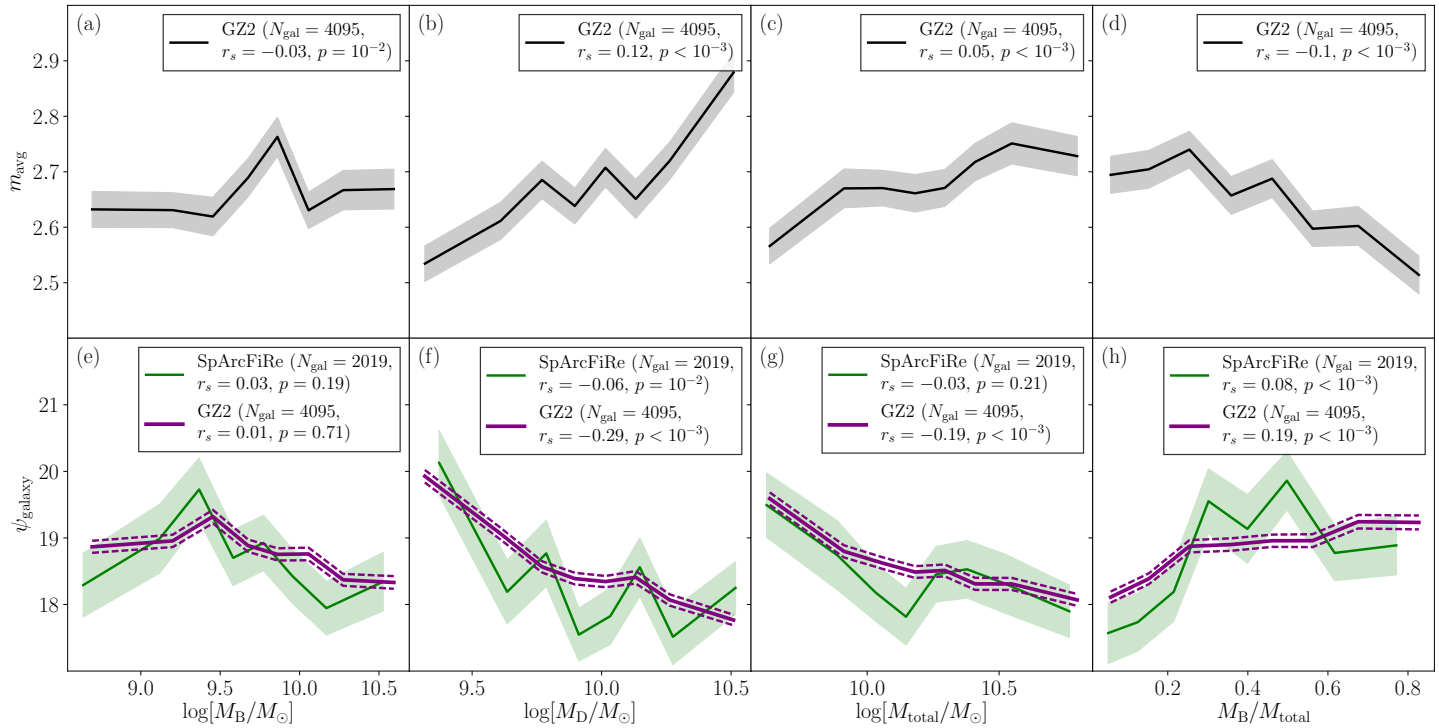

Figure 5.8: Bulge, disc and total stellar mass vs. average spiral arm number and pitch angle. (a)-(d) Galaxy mass parameters vs. average arm number ($m_{\rm avg}$) for the *stellar mass-complete sample*. Left to right: galaxy bulge mass, galaxy disc mass, galaxy total mass, galaxy bulge fraction. The black line shows the mean and the shaded black region indicates one standard error on the mean. Each galaxy is weighted by $1/V_{\rm max}$. (e)-(h) Galaxy mass parameters vs. pitch angle for the *stellar mass-complete sample*. The thinner green line with shaded errors show the pitch angles derived from SpArcFiRe, and the thicker purple line with dashed errors show pitch angles measured from the GZ2 calibration. The strongest trends I observe are that galaxies with more massive discs have more spiral arms and tighter pitch angles.

galaxies also tend to have more spiral arms ($r_s = 0.05$, $p = 10^{-3}$), a result first observed in chapter 4, albeit with a different stellar mass indicator. From Fig. 5.8a-b, these results appear to be driven by differences in disc mass, rather than bulge mass – there is a stronger positive trend that galaxies with more massive discs have more spiral arms ($r_s = 0.12$, $p < 10^{-3}$) and a much weaker trend that galaxies with less massive bulges have fewer spiral arms ($r_s = -0.03$, $p = 10^{-2}$). Galaxy mass properties do seem to affect the spiral arm number of galaxies but these differences are mainly due to galaxy disc mass variations, rather than any variations in bulge mass.

In Fig. 5.8e-h, the same four mass characteristics are plotted against the two measures of spiral arm pitch angle defined in sections 5.3.1 and 5.3.2. The first, $\psi_{\rm galaxy}$ from SPARCFIRE is a directly measured quantity, but is only available for the 2019 galaxies with measured good arms in SPARCFIRE. The alternative GZ2 derived pitch angle (see section 5.3.2) is available for all 4095 spiral galaxies. As was the case with respect to spiral arm number, there are some correlations with respect to stellar mass. There is a weak positive trend that galaxies with greater bulge fractions tend to have looser spiral arms ($r_s = 0.08$ for SPARCFIRE, 0.19 for GZ2; $p < 10^{-3}$ in both cases). There are also weak negative correlations that galaxies with greater total stellar mass have tighter arms ($r_s = -0.03$ and -0.19, $p = 0.21$ and $< 10^{-3}$). Comparing Fig. 5.8e-f shows that it is the galaxy disc mass that is responsible for these trends, as was the case for the dependence of spiral arm number on stellar mass. There is a negative correlation between disc mass and pitch angle ($r_s = -0.06$ and -0.29, $p = 10^{-2}$, $< 10^{-3}$), but there is little or no correlation between bulge mass and galaxy pitch angle ($r_s = 0.03$ and 0.01, $p = 0.19$ and 0.71).

It is interesting to note that these trends are the opposite to what one would expect if pitch angle differences were driven purely by spiral arm number. In Fig. 5.5 and Fig. 5.6 it was shown that galaxies with more spiral arms had looser structures, so one would expect galaxies with more massive discs to have looser spiral arms. Galaxy central mass concentration does seem to affect both arm number and pitch angle, but the disc mass is the main reason for the observed differences, rather than the bulge mass.

5.4.4 Star formation rates

The star formation properties of galaxies have been shown to correlate with the properties of the spiral arms. For example, in section 4.2, it was shown that galaxies with fewer spiral arms have a greater level of dust obscured star formation. Studies of grand design spirals also show that SFR is lower in galaxies with high shear (Seigar, 2005), which in turn means that spirals with the tightest arms have lower SFRs. The star formation properties of spiral galaxies are now compared with respect to both the spiral arm number and the spiral arm pitch angle in galaxies.

There are two photometrically derived SFRs used in this chapter. The first is the FUV measured SFR, $SFR_{\rm FUV}$, which measures the amount of unobscured star formation in galaxies. The second is the MIR measured SFR, SFR_{22}, which measures the amount of dust obscured star formation. Full details of these SFRs are described in section 4.2.3. These measures can be added to measure the total SFR, $SFR_{\rm total}$, and the ratios of these indicators describe the fraction of the star formation that is dust obscured. In the left hand side of Fig. 5.9, four measures of SFR are presented as a

function of average arm number, $m_{\rm avg}$. They are $SFR_{\rm FUV}$, SFR_{22}, $SFR_{\rm total}$, and the fraction of the SFR which is obscured ($SFR_{22}/SFR_{\rm total}$) vs. average arm number. The *stellar mass-matched sample* of $m = 1$, 2, 3, 4 and 5+ arm galaxies was used for this analysis, as there is a stellar mass dependence on total SFR which I wish to control for (e.g. Brinchmann *et al.* 2004; Salim *et al.* 2007). Fig. 5.9a-d show the already established correlation seen in chapter 4, this time using a continuous statistic to measure arm number. Galaxies with fewer spiral arms have more MIR star formation ($r_s = -0.14$, $p < 10^{-3}$) and less FUV star formation ($r_s = -0.21$, $p < 10^{-3}$). The total SFRs remain consistent, with a sharp upturn below $m_{\rm avg} = 2$. One-arm spirals are associated with galaxy-galaxy interactions (Casteels *et al.*, 2013), which explains this trend.

In Fig. 5.9e-l, I plot the same four SFR quantities vs. spiral arm pitch angle, rather than arm number. I again use two measures of spiral arm pitch angle: Fig. 5.9e-h show the SPARCFIRE derived pitch angles Fig. 5.9i-l show the GZ2 derived pitch angles. There are no strong correlations that SFR varies in galaxies with different pitch angles, measured from both GZ2 and SPARCFIRE. Although spiral arm number has a strong influence on the amount of dust obscured star formation in galaxies, galaxies with different pitch angles all show consistent SFRs and fractions of obscured star formation.

5.4.5 Pitch angle variations within individual galaxies

If many-arm spirals are caused by multiple swing-amplified features, and two-arm spirals are caused by a single dominant long-lived mode, then we may find clues to this in the spiral arm pitch angles. If single modes are responsible for two-arm structures then we would expect the pitch angles of spiral arms in individual galaxies to be the same; this would not necessarily be the case for many-arm structures. In order to test this, I isolate galaxies with two or more arcs identified by SPARCFIRE from the *stellar mass-complete sample* of unbarred galaxies. From this sample, 555/2237 (24.8 per cent) have two or more arcs with measured pitch angles. This is the case for 256/1034 of $m = 2$ galaxies (24.8 per cent) and 291/1068 of galaxies with $m > 2$ (27.2 per cent). Note here that the $m = 1$ galaxies have been excluded. We can now compare the pitch angle of the dominant arc (the longest arc) with each of the other identified arcs in each galaxy. This quantity is denoted by the value $\Delta\psi$. For the $m = 2$ spirals, the distribution of $\Delta\psi$ is centred on 0.6° and the 84th–16th percentile range is 18.3°. For the $m > 2$ case, the distribution of $\Delta\psi$ is centred on 0.0° and the 84th–16th percentile range is 25.6°, 7° broader than the $m = 2$ case. Therefore, the spread in pitch angles within individual galaxies is broader in many-arm spirals. This could be preliminary evidence that two-arm spirals are more likely to be single, long-lived modes in discs. However, we cannot rule out other possibilities: the arms of many-arm galaxies are likely to be weaker, making accurate pitch angles more difficult to determine. This would lead to a greater error in the measurement of the pitch angle for each individual spiral arm, broadening the $\Delta\psi$ distribution.

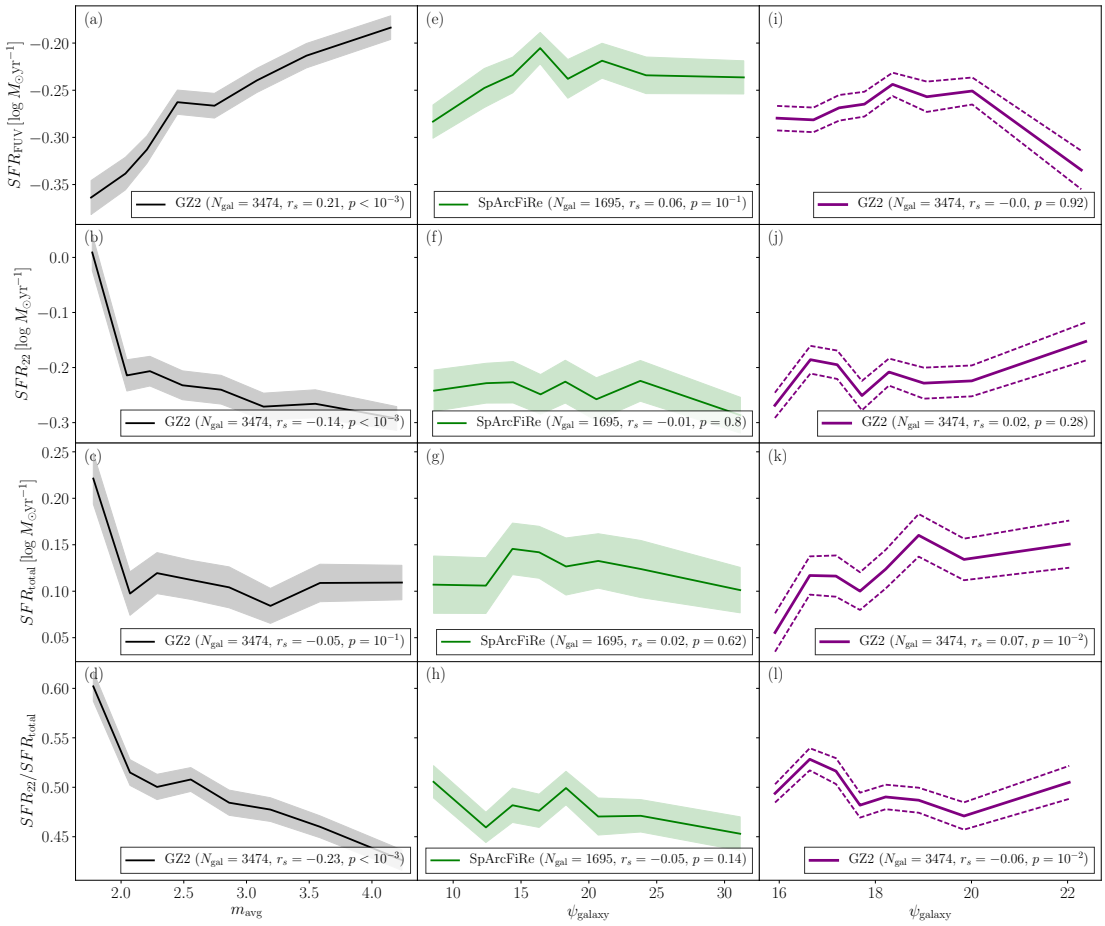

Figure 5.9: (a)-(d) Spiral arm number vs. galaxy SFR properties for the *stellar mass-matched sample* of spirals. From top to bottom, the properties are FUV SFR, MIR SFR, total SFR and MIR SFR fraction. The same four quantities are plotted vs. SpArcFiRe derived pitch angles in (e)-(h) and GZ2 derived pitch angles in (i)-(l). The solid line in each subplot shows the mean, and the errors indicate one standard error on the mean. Although SFR properties vary with spiral arm number, there is no clear correlation with pitch angle.

5.5 Discussion

5.5.1 SpArcFiRe derived spiral arms

In section 5.3.1, the overall spiral arm pitch angle distributions were compared to those from Herrera-Endoqui *et al.* (2015). Using the raw SpArcFiRe output combined with our by-eye classified galaxies, it was shown that the range of spiral arms that our SVM deems reasonable agrees well with this independent survey of spiral arm pitch angle. Given that S^{4}G (Sheth *et al.*, 2010) is a volume-limited local survey with no cuts on galaxy morphology and Herrera-Endoqui *et al.* (2015) fitted their sample of 482 spirals by eye, this should provide a set of reliable arc measurements for a representative sample of local spirals. This means that the spiral arms being detected by SpArcFiRe do seem to have the same range of pitch angles as those observed using other methods. There are very few galaxies with $\psi_{\rm galaxy} < 10°$ (7.5 per cent of galaxies) or $\psi_{\rm galaxy} > 40°$ (1.1 per cent of galaxies). This agrees remarkably well with both the most open spiral structure of $40 - 45°$ (Seigar & James, 1998b; Block & Puerari, 1999; Seigar, 2005), and the tightest of $7 - 10°$ (Block & Puerari, 1999; Seigar, 2005) observed in other studies of nearby spirals. Seigar *et al.* (2008) attributed these

limits to the range of the shear in spiral galaxies – the shear in the discs of galaxies is closely related to the central mass concentration and galaxies with little or no bulge have $\psi \approx 10°$. Conversely, the loosest observed pitch angles correspond to the smallest central mass concentrations observed in galaxies. Our distributions of spiral arm pitch angles imply that these naturally occurring limits do exist in a statistically complete sample of spiral galaxies in the local Universe, and that these limits extend to all types of spiral structure, rather than just grand design spirals.

5.5.2 Pitch angle and galaxy structure

In section 5.4, the spiral arm pitch angles were compared for a number of different galaxy structural parameters. The first measure that was compared was the spiral arm number of the host galaxy, measured using the GZ2 visual morphologies. Many-armed galaxies generally have looser spiral arms than their two-armed counterparts, irrespective of host galaxy stellar mass. Studies of local grand design spiral galaxies such as M51 show us that many two-arm structures are genuine density waves (Colombo *et al.*, 2014; Schinnerer *et al.*, 2017). Many-arm structures are instead usually considered to be modal structures arising in gas rich discs (Carlberg & Freedman, 1985; Baba, Saitoh & Wada, 2013). Arm number vs. pitch angle correlations have been noted before, where a dependence of pitch angle on Elmegreen spiral arm class has been observed. Garcia Gomez & Athanassoula (1993) noted that there is a correlation, where many-arm and flocculent spiral arms are looser than two-arm structures. Our results confirm the correlation of Garcia Gomez & Athanassoula (1993) for a large statistically complete sample of spiral galaxies, with two-arm grand design spirals having tighter spiral arms than each of the many-arm categories, which we expect to include both many-arm and flocculent Elmegreen-type spirals.

A potential explanation for the differences in spiral arm pitch angles in different galaxy structures is due to the varying timescales over which spiral arms exist. Simulations of many-arm structures show that the pitch angle of individual spiral modes wind up over time (e.g. Wada, Baba & Saitoh 2011; Grand, Kawata & Cropper 2012a,b; Baba, Saitoh & Wada 2013). Many simulations also predict that these structures are usually short-lived phenomena and are usually broken or merged into other structures after ~ 100 Myr (Baba, Saitoh & Wada, 2013; D'Onghia, Vogelsberger & Hernquist, 2013), where spiral arms with $\psi > 20°$ likely to be more transient features (Pérez-Villegas *et al.*, 2012) than those with $\psi \leq 20°$. However, the mechanisms responsible for two-arm structures are different from those in many-arm galaxies. The timescale over which two-arm structures can exist is still debatable, with some studies suggesting they are also transient phenomena (Merrifield, Rand & Meidt, 2006) but can potentially persist for longer when considering the gas component of galaxy discs (Ghosh & Jog, 2015, 2016). Two arm structures can also be tidally induced and wind up and decay over ~ 1 Gyr (Oh *et al.*, 2008; Struck, Dobbs & Hwang, 2011). It may therefore be the case that the tightly wound unbarred spirals are the remnants of long-lived internal structures or the later stages of tidal features.

Another reason for the observed differences in pitch angle with spiral arm number may be related to the rotation curves of galaxies. Seigar (2005) demonstrated that spiral arm pitch angles can be directly related to the shear in the discs of galaxies: discs with falling rotation curves have tighter spiral arms than discs with rising rotation curves.

Some tentative evidence that many-arm galaxies have steeper, rising rotation curves has been found before (Biviano *et al.*, 1991), so these results may also indicate that many-arm structures arise in discs with lower shear rates (with rising rotation curves). However, galaxy shear rates are closely related to the central mass concentrations in galaxies (Seigar, 2005), which are in turn related to spiral arm pitch angles (Seigar *et al.*, 2008). We see no trend for galaxies with greater central mass concentrations having tighter spiral arm pitch angles. We instead observe a weak trend opposite to this, where galaxies with greater central mass concentrations actually have looser spiral arms. This suggests that these differences are not driven by differences in the central mass concentrations.

5.5.2.1 The role of bars

In section 5.4.2, the SPARCFIRE measured spiral arm pitch angles were related to the presence of bars in the discs of galaxies, finding that galaxies with bars have looser spiral arms. This trend is particularly apparent when considering the two-arm population of spirals. Since grand design, two-arm structures are usually linked with both bars and companions (Kormendy & Norman, 1979; Seigar & James, 1998a; Kendall, Kennicutt & Clarke, 2011), and bars can be tidally induced (Semczuk, Łokas & del Pino, 2017), one possibility is that loose spiral arms in barred galaxies can potentially be the result of a galaxy-galaxy interaction disturbing the structure. Spiral arms formed in this way would form from the remnants of tidal tails and bridges, and therefore be either material in nature or kinematic density waves (see section 1.3.4). Although bars are more common in higher density environments (Skibba *et al.*, 2012; Smethurst *et al.*, 2017), GZ2 statistics from Casteels *et al.* (2013) suggest that the combination of loose arms and bars are not due to pair interactions. Casteels *et al.* (2013) showed that bars are suppressed, but the frequency of two-arm structures and loose spiral arms actually increases in close galaxy pairs. We therefore do not favour this scenario where pair interactions cause both bars and loose spiral arms.

A second possibility is that the presence of bars may have a strong influence on the dynamics within the discs of galaxies. Of particular interest is the 'invariant manifold theory' discussed in section 1.3.4. (Romero-Gómez *et al.*, 2006, 2007; Athanassoula, Romero-Gómez & Masdemont, 2009; Athanassoula *et al.*, 2009, 2010). A key prediction of this theory is that galaxies with stronger bars will have looser spiral arms than those with weak bars. Interpreting the GZ2 p_{bar} statistic as a relative measure of bar strength, the result presented in section 5.4.2 would be in direct agreement with this prediction. I do, however, note that this evidence is somewhat tentative, as there are also other possibilities related to the dynamics of spiral galaxies that could give rise to this result. For example, Baba (2015) shows a full hydrodynamical simulation of a barred grand design spiral galaxy. Fig. 4 of Baba (2015) shows that the spiral arm amplitude is out of phase with the spiral arm pitch angle. They suggest that spiral arms are more strongly amplified as they come closer to the bar, and this amplification is stronger at larger pitch angles. We may be seeing this effect in our results, with bars causing an amplification of looser spiral arm modes. Another possibility is that the dynamics of spiral arms are altered when the bar becomes prominent (Roca-Fàbrega *et al.*, 2013). In this case, it has been suggested that the arms are better fit with a rigidly rotating disc, which would lead to arms which have hyperbolic rather than logarithmic patterns (Seiden & Gerola, 1979; Kennicutt, 1981), potentially closing to ring-like fea-

tures which cannot be described by a spiral equation with a single pitch angle (Buta, 1986, 2017). In this set of SPARCFIRE models, only logarithmic spirals are used to measure arms, so in principle the differences in pitch angle could arise as an artefact of mis-fitting the arms with a function that does not represent the spiral arm. If the logarithmic spiral equation was not the correct equation to fit, one would expect fewer galaxies to have detected arms. However, there is no difference in the number of galaxies with detected spiral arms with respect to $p_{\rm bar}$, meaning that spiral arms in barred galaxies are log spiral arcs, disfavouring the possibility that they are rigidly rotating arms.

5.5.2.2 Galaxy mass concentrations

In section 5.4.3, the mass properties of unbarred galaxies were compared with respect to their spiral arm morphologies. Galaxies with more massive discs have more spiral arms, which in turn means that galaxies with lower bulge-to-total ratios have more spiral arms. However, there is no trend with respect to bulge mass. Given that pitch angle correlates with arm number, one naively would expect a positive correlation between pitch angle and disc mass. Instead, there is a weak negative trend that galaxies with more massive discs and lower bulge-to-total ratios have tighter spiral arms. This result is perhaps surprising when considering simulations of modal spiral arms, which suggest that when galaxies have more massive bulges, higher order modes (more spiral arms) will dominate (Grand, Kawata & Cropper, 2013; D'Onghia, 2015). These models usually consider isolated galaxies and some assumed dark matter halo profile. The dominant spiral arm mode will actually depend on the scale and mass of the dark matter halo as well as the mass of the disc and bulge, requiring a more complex analysis. Our first impression suggests that the spiral arms in galaxies are not modal in nature, but driven by other processes, such as density waves or galaxy interactions. However, a more complete analysis of these models, including all of the relevant parameters is required to confirm this result – these are considered in chapter 6.

That greater central mass concentrations lead to looser spiral arms would also appear to contradict the idea that galaxies with greater levels of shear have more tightly wound spiral arms (Seigar, 2005; Seigar *et al.*, 2008). These studies are usually done on small samples of nearby galaxies, with clear, unbarred grand design spiral arms. My result that bulge mass has no influence on arm pitch angle suggests that this relation does not hold for the entire spiral galaxy population, and that spiral arm pitch angle is more heavily influenced by other properties, such as disc mass, arm number and the potential presence of a bar, rather than just the central mass concentration.

5.5.3 Star formation rates

Galaxies with more spiral arms tend to have more UV and less MIR emission, indicating that the SFR is less obscured by dust in many-armed galaxies, but that the overall SFRs are similar in all types of spiral galaxies. The reasons for these trends are discussed in more detail in chapter 4, and can be related to the geometry of star formation and molecular clouds in galaxies. In this chapter, I also found that SFRs are consistent in spiral galaxies irrespective of arm number, other than when the number of spiral arms was less than two. In this case there is an increase in both the MIR and total SFR. Given that one-arm galaxies in GZ2 have been associated with merger remnants (Cas-

teels *et al.*, 2013), this would suggest that high SFRs are triggered by galaxy-galaxy interactions (Barton, Geller & Kenyon, 2000; Ellison *et al.*, 2008; Willett *et al.*, 2015). Despite the strong, clear trends with spiral arm number, I found no differences in the SFRs with spiral arm pitch angle.

In grand design spiral galaxies, shear rates are related to spiral arm pitch angles (Seigar *et al.*, 2008, 2014). If the shear is too high, galaxies have been shown to have lower total SFRs (Seigar, 2005). One would therefore expect galaxies with tighter spiral arms to have lower total SFRs if shear was responsible for the differences in spiral galaxy pitch angle. Given that I find no relation between SFR and pitch angle, this would suggest that shear is not responsible for pitch angle differences between galaxies. I also find no enhancements in the SFRs of spirals with looser arms, meaning that the loosest arm spirals are not likely to be dominated SFR-promoting interactions, unlike one-arm spirals.

Chapter 6

Testing predictions of swing amplification theory

The analysis and results in this chapter are presented in Hart *et al.* (2018). The work looks at number of analytic predictions, which have been verified by disc simulations, for the spiral arm number and pitch angle as a function of the properties of the bulge, disc and halo. I test the validity of these models with a sample of SDSS galaxies. All work was performed by the author, with advice from the co-authors of the above paper.

6.1 Overview

In section 1.3.2, I introduced a swing amplified mechanism for spiral arm formation. In this scenario, spiral arms form due to unstable regions where self gravity dominates, but are eventually broken up by the disc shear. Despite the transient nature of individual arms, a long-lived mode can exist in galaxy discs (Grand, Kawata & Cropper, 2012a; D'Onghia, Vogelsberger & Hernquist, 2013; Sellwood & Carlberg, 2014). Simulations predict that although spiral arms can be broken and remade, the average total spiral arm number, or dominant mode, will exist beyond the lifetime of a single spiral arm. The nature of these long-lived modes are related directly to the underlying mass distribution of these galaxy discs – the mathematics of swing amplification predict an expected spiral arm number (D'Onghia, Vogelsberger & Hernquist, 2013; D'Onghia, 2015) and pitch angle (Baba, Saitoh & Wada, 2013; Michikoshi & Kokubo, 2014, 2016), given the mass distribution in a galaxy.

A key issue for any simulation is directly reproducing observable properties of spiral galaxies. There is still much conflict, with disc simulations usually predicting dominant many-arm modes in galaxy discs. Observations instead suggest that even in unbarred galaxies, two-arm spirals are the most common type of spiral structure (Elmegreen & Elmegreen, 1982) which do not arise as readily in the simulations (D'Onghia, 2015). Therefore, there may be a number of mechanisms responsible for the different spiral arm structures we observe, and all spiral galaxies may not be governed by a dominant swing amplified mode.

The aims of this chapter are twofold. We first carefully obtain predictions from swing amplification for samples of real galaxies. These predictions are then compared to observed spiral arm properties, in order to evaluate the performance of the swing amplification model. Swing amplification predicts both the spiral arm number and the

pitch angle in galaxies with respect to the relative masses and sizes of the dark matter halo, disc and bulge in galaxies. I combine measurements of bulge and disc masses and sizes with published dark matter halo scaling relations to predict the arm properties of galaxies (these are discussed fully in section 6.2). I utilise a large sample of spirals from the SDSS (York *et al.*, 2000) and a smaller sample of S^4G (Sheth *et al.*, 2010) spiral galaxies. Using these data, predicted spiral arm numbers and pitch angles are compared to the same observed quantities.

6.2 Data

The model I employ in this chapter has three main components – a galaxy bulge, disc and dark matter halo. Measurements and models for these components are outlined in the rest of this section.

6.2.1 Sample selection and visual morphologies

6.2.1.1 SDSS

The main galaxy sample is taken from the GZ2 SDSS sample outlined in section 2.3. I employ an upper redshift limit of $z = 0.085$ in accordance with Willett *et al.* (2015), a general limit to which classifications remain reliable. In this chapter, I am only concerned with how the relative sizes and masses of components affect the overall galaxy spiral arm morphology. For this reason, I make no further completeness cuts to the sample, selecting all galaxies in the redshift range $0.02 < z \leq 0.085$ brighter than $m_r = 17.0$.

Galaxy morphological data are obtained from GZ2. I use the debiased statistics from section 3.2 to ensure the results are free of resolution-dependent redshift bias. I apply a cut of $p_{\rm spiral} \geq 0.5$ to select a reliable sample of spiral galaxies (see section 3.2.5.1 for examples of spiral galaxies selected in this way). An inclination cut of $(b/a)_g > 0.4$ is also used to ensure we only select face-on spirals with reliable spiral morphology estimates (see section 4.2.2). The principal concern of this chapter is spiral structure, without the influence of bars, so I also define a clean, unbarred sample of galaxies, with $p_{\rm bar} \leq 0.2$. This cut has been used in GZ2 papers before to select unbarred galaxies (Galloway *et al.*, 2015; Kruk *et al.*, 2018).

Spiral arm numbers are obtained from the GZ2 catalogue, depending on the fractional responses to the 'how many spiral arms are there?' question. I make use of two arm number statistics in this chapter. The first is m, the response which had the greatest debiased vote fraction. The second is $m_{\rm avg}$, the average arm number from the classifications, which was introduced in section 5.3.2.

Given the lack of directly measured pitch angles in GZ2, I use the SPARCFIRE method, introduced in section 3.3, to measure spiral arm pitch angles, ψ. Any galaxies which had no reliable spiral arms detected are removed from further analysis of spiral arm pitch angle. I define the spiral arm pitch angle for each galaxy as the arc-length weighted average pitch angle, $\psi_{\rm avg}$, introduced in section 5.3.1.

6.2.1.2 S4G

In order to check the GZ2 obtained results with an independent dataset, I also include a sample of spiral galaxies from the S^{4}G sample (Sheth *et al.*, 2010; Muñoz-Mateos *et al.*, 2013; Querejeta *et al.*, 2015). This is a low-redshift, volume-limited sample complete for galaxies closer than $D = 40$ Mpc, brighter than $m_B = 15.5$ and diameter larger than $D_{25} = 1$ arcmin. Unlike the SDSS sample, this sample is observed in the NIR, specifically the Spitzer 3.6μm and 4.5μm bands. The visual morphologies are from the classifications of Buta *et al.* (2015). These statistics include an F value, with greater F meaning a galaxy has a stronger bar. I select galaxies with $F < 0.25$ for the unbarred spiral sample. The spiral arm structure is also listed in this catalogue, with galaxies listed as either grand design (G), many-arm (M) or flocculent (F). Spiral arm pitch angles are obtained from Herrera-Endoqui *et al.* (2015). All of the galaxies in S^{4}G were visually inspected, and logarithmic spiral arms were drawn and fit to the galaxies. Given that we expect all features to be real spiral arms in these galaxies, the galaxy pitch angle is given by the mean pitch angle of all of the measured spiral arms in each galaxy.

6.2.2 Baryonic masses and sizes

Galaxy stellar masses and sizes for the SDSS sample are obtained from the photometric decompositions of Simard *et al.* (2011) and Mendel *et al.* (2014). These were introduced in section 2.4.1. The Mendel *et al.* (2014) catalogue gives an estimate of the the total stellar mass content of the SDSS galaxies in the bulge and disc components. To avoid any spuriously fit galaxies, only galaxies where Mendel *et al.* (2014) deemed the fit to be either a disc system (type = 2) or a bulge+disc system (type = 3) were included in any samples used later in this chapter. Using the bulge+disc fits assumes that all galaxies have two distinct components, but this is not always the case (Simmons *et al.*, 2013; Simmons, Smethurst & Lintott, 2017). With this in mind, for galaxies where the F-test statistic for a two-component fit is ≤ 0.32, the disc-only fit is used, and the bulge mass component is set to 0 – motivation for this cut is given in section 6.2.2.1.

Relative sizes of the bulge and disc components are taken from the Simard *et al.* (2011) fits to the r-band of galaxies. Simard *et al.* (2011) provides measurements of scale length for the disc and half light radius for the bulge. For the Hernquist bulge, scale lengths are measured by dividing the half light radius by a factor of $1+\sqrt{2}$, as described by Eq. 4 of Hernquist (1990). I note that the r-band does not directly trace the overall stellar mass, with light dominated by younger stars. I therefore correct the sizes of the bulge and disc components by dividing by a factor of 1.5$\pm$0.2, given that the NIR is usually $\sim$1.5 times smaller than the optical component in galaxies (Vulcani *et al.*, 2014).

For the S^{4}G sample, photometric bulge+disc decompositions are again used to determine the masses and sizes of the stellar component of galaxies. Bulge and disc photometry are obtained from the fits to the 3.6μm band from Salo *et al.* (2015). I select only galaxies where either a single disc component or a disc and bulge component are well-fit (quality = 5). Given that the NIR component follows the underlying stellar mass distributions of galaxies closely, I use the 3.6μm fits directly, without a scaling like that used for the SDSS sample (Eskew, Zaritsky & Meidt, 2012; Meidt

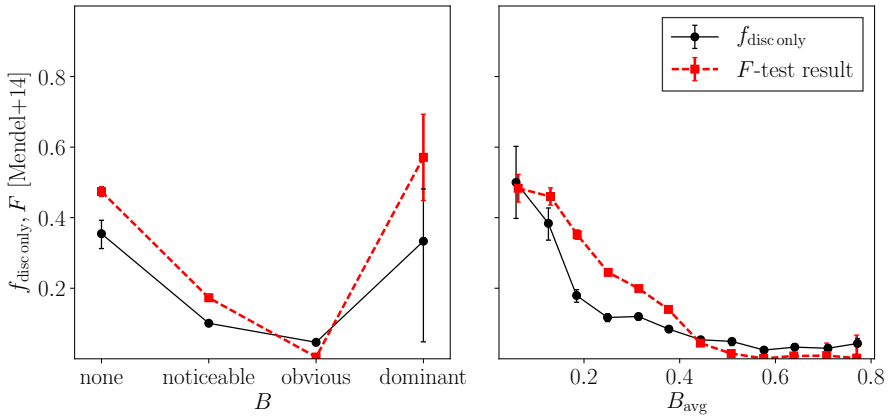

Figure 6.1: (a) Modal value of response to the bulge prominence question in GZ2, B, vs. fraction of discs classified with only a disc (black circle points with a thin black line) and median F-test value (red squares with a thicker dashed line). (b) As in (a), but using the continuous average bulge prominence statistic, $B_{\rm avg}$. We see a strong correlation that galaxies with less prominent bulges in GZ2 are more likely to be fit with a single bulge component.

et al., 2012). The fraction of the mass in the bulge and disc component is simply the fraction of the 3.6μm light in each component from Salo *et al.* (2015), and the sizes of each of the components are simply the sizes of the components measured at 3.6μm.

6.2.2.1 The use of one or two component fits

I use already derived bulge and disc mass estimates from Simard *et al.* (2011) and Mendel *et al.* (2014) as parameters in the galaxy model. The Mendel *et al.* (2014) catalogue usually fits galaxies with two components, but also includes single fit models. The catalogue provides a statistic, the F-test statistic, to determine which model is more appropriate. The paper also advises that this statistic is not perfect, and arguments from what is expected from the physical properties of galaxies should instead be used if possible. I do, however, want to avoid the fitting of a bulge+disc to a system where the galaxy has little or no bulge. The reliability of galaxy bulge size measurements have already been shown to correlate well with a visually characterised bulge prominence statistic in GZ2 (Masters *et al.*, in prep). In order to check whether the F-test statistic can reliably identify bulge-less systems, I use the same visual statistic. I define the bulge prominence using the 'is there any sign of a bulge?' question in GZ2. I define $B_{\rm avg}$ in the same way as Masters *et al.* (in prep):

$$B_{\rm avg} = 0.0 p_{\rm no\,bulge} + 0.2 \cdot p_{\rm noticeable} + 0.8 \cdot p_{\rm obvious} + 1.0 \cdot p_{\rm dominant}, \qquad (6.1)$$

and the statistic B which corresponds to which response to the bulge prominence question got the most votes. In Fig. 6.1, I check how both the median F-test statistic and the fraction of galaxies with $F < 0.32$, $f_{\rm disc\,only}$ changes with GZ2 bulge prominence. Here there is a strong correlation ($r_s(B_{\rm avg}, f_{\rm disc\,only}) = -0.41$) between the two statistics, meaning that galaxies with a higher probability of having no bulge from the GZ2 statistics are much more likely to require the single component model. I therefore use the F-test statistic to define whether we use a bulge+disc or disc only model for the SDSS galaxies.

6.2.2.2 HI masses and sizes

For the SDSS sample, a set of HI measurements of galaxies is also available. This can help address any missing baryonic mass in galaxies, given that a fraction of the mass in galaxy discs is gaseous rather than stellar. For a fraction of the SDSS sample, there are HI masses available from ALFALFA survey measurements of the HI 21cm line. These masses are obtained from the $\alpha 70$ data release of the ALFALFA survey (Giovanelli *et al.*, 2005; Haynes *et al.*, 2011), and were first introduced in section 2.4.3. For the galaxies with no direct measurement, I use HI masses estimated from other galaxy properties. Teimoorinia, Ellison & Patton (2017) fitted an artificial neural network (ANN) to 15 input galaxy parameters to estimate HI masses. These estimates do not rely on a single parameter such as stellar mass or colour, which have been shown to vary systematically with spiral arm number (e.g. chapter 4), meaning they should be valid estimates for all galaxies. Different HI estimates have different uncertainties, described by the quantity $C_{\rm fgas}$ in Teimoorinia, Ellison & Patton (2017). I therefore select reliable estimates as galaxies with $C_{\rm fgas} \geq 0.5$ and including an uncertainty of 0.22 dex, in accordance with Teimoorinia, Ellison & Patton (2017).

HI disc size estimates are obtained from the following scaling relation between HI size and galaxy disc size from Lelli, McGaugh & Schombert (2016):

$$\log(R_{\rm HI}) = (0.86 \pm 0.04)\log(R_{\rm d}) + (0.68 \pm 0.03), \tag{6.2}$$

where $R_{\rm HI}$ is the radius at which the HI surface density falls to 1 $\mathrm{M_{\odot}pc^{-2}}$. It has also been demonstrated that the HI scale length, $r_{\rm s,HI}$, is closely related to $R_{\rm HI}$ – I therefore use a further scaling relation to equate the two quantities from Wang *et al.* (2014):

$$r_{\rm s,HI} = (0.19 \pm 0.03)R_{\rm HI}. \tag{6.3}$$

Using these relations, we can create exponential stellar + HI discs. The total disc mass is given by adding the HI mass to the stellar disc mass, and the disc scale length is given by the scale length of the best fitting exponential profile to the stellar plus gas disc systems. Discs created in this way are referred to as SDSS+HI samples for the rest of this chapter.

6.2.3 Dark matter haloes

The final component that requires consideration is the dark matter halo, the only component in the model that is not observable. I use published scaling relations between the galaxy dark matter halo mass and galaxy stellar mass to estimate the dark matter halo mass for each galaxy. I use the relation of Dutton *et al.* (2010), which combined abundance matching studies and various observational studies of dark matter haloes from satellite kinematics and weak lensing. The best fit line to observational studies from Mandelbaum *et al.* (2006), Conroy, Ho & White (2007) and More *et al.* (2011) for late-type galaxies yielded the following scaling relation:

$$y = y_0\left(\frac{x}{x_0}\right)^{\alpha}\left[\frac{1}{2} + \frac{1}{2}\left(\frac{x}{x_0}\right)^{\gamma}\right]^{(\beta-\alpha)/\gamma}. \tag{6.4}$$

The quantity x is the galaxy total stellar mass, $\mathrm{M_{star}}$, and the quantity y is the halo-to-galaxy mass, $y = \mathrm{M_{200}/M_{*}}$. For late-type galaxies, the parameters are $\alpha = -0.50^{+0.025}_{-0.075}$,

$\beta = 0.0$, $\log(x_0) = 10.4$, $\log(y_0) = 1.89^{+0.14}_{-0.12}$ and $\gamma = 1.0$. I calculate the total halo mass for each of our galaxies using Eq. 6.4 and the total galaxy stellar mass defined in section 6.2.2. These are then converted to virial radii, R_{200}, with (e.g. Huang *et al.* 2017):

$$R_{200} = \left[\frac{3\mathrm{M}_{200}}{4\pi \cdot 200\rho_{\mathrm{crit}}}\right]^{1/3}, \tag{6.5}$$

where ρ_{crit} is the critical density of the Universe at $z = 0$. The $\pm$ values here denote the scatter in this relation, so are the expected errors on any dark matter halo estimate for a single galaxy. To convert this to a halo scale radius, a_{h}, I use the relation

$$R_{200} = c_{200} a_{\mathrm{h}}. \tag{6.6}$$

In order to measure a scale radius, one requires knowledge of the halo concentration. I again rely on a published scaling relation, this time from N-body simulations which form NFW profiles. The halo concentration is related to the halo mass using the abundance matching equation of Dutton & Macciò (2014):

$$\log(c_{200}) = 0.905 - 0.101 \log(\mathrm{M}_{200}/[10^{12} h^{-1} \mathrm{M}_{\odot}]). \tag{6.7}$$

From these scaling relations, I compute the total halo mass, M_{200}, and the scale length, a_{h}, for each of our galaxies.

6.2.3.1 Halo profiles

For mathematical simplicity, I consider two dark matter profiles in this analysis. The first is the Hernquist (1990) dark matter halo, referred to as 'Hernquist' hereafter. This halo has the desirable quality that it closely matches the cusped NFW dark matter haloes (Navarro, Frenk & White, 1996) in the inner regions. In the outer regions, the dark matter halo begins to deviate from that of the NFW dark matter profile. As it is the inner dark matter profile that is most critical to influencing spiral arm morphology in galaxy discs (D'Onghia, 2015), I choose to match the inner regions closely by matching to the dark matter density at a_{h}. The shape of the Hernquist halo for a galaxy with parameters from the Milky Way measured in Bovy & Rix (2013) is shown by the orange dashed line in Fig. 6.2a.

In order to understand the influence on the slope of the dark matter profile, I adopt a Burkert (1995) dark matter profile for comparison, described as a 'Burkert' profile in the rest of this chapter. The Burkert profile has a number of characteristics that make it ideal for comparison to the Hernquist profile. It follows a similar shape to the much used NFW profile in the outer regions, which is useful given that the scaling relations I employ in this chapter are based upon NFW profiles. However, its centre has a 'core' rather than a 'cusp', unlike the Hernquist and NFW profiles. In Fig. 6.2a, the blue line indicates the Burkert dark matter halo profile for the Milky Way model. Together, these allow us to compare the spiral arm properties of 'cusped' and 'cored' profiles. The use of the two different dark matter halo profiles also allows us to interpolate between them, a property which is used later in this chapter. We can define the quantity α to interpolate between a cusped and cored profile. The quantity α is used to give the following dark matter halo profiles:

$$\begin{aligned} \rho(r) &= (1+\alpha)\rho_{\mathrm{b}}(r) && (\alpha < 0) \\ \rho(r) &= (1-\alpha)\rho_{\mathrm{b}}(r) + \alpha\rho_{\mathrm{h}}(r) && (0 \leq \alpha \leq 1) \\ \rho(r) &= \alpha\rho_{\mathrm{h}}(r) && (\alpha > 1), \end{aligned} \tag{6.8}$$

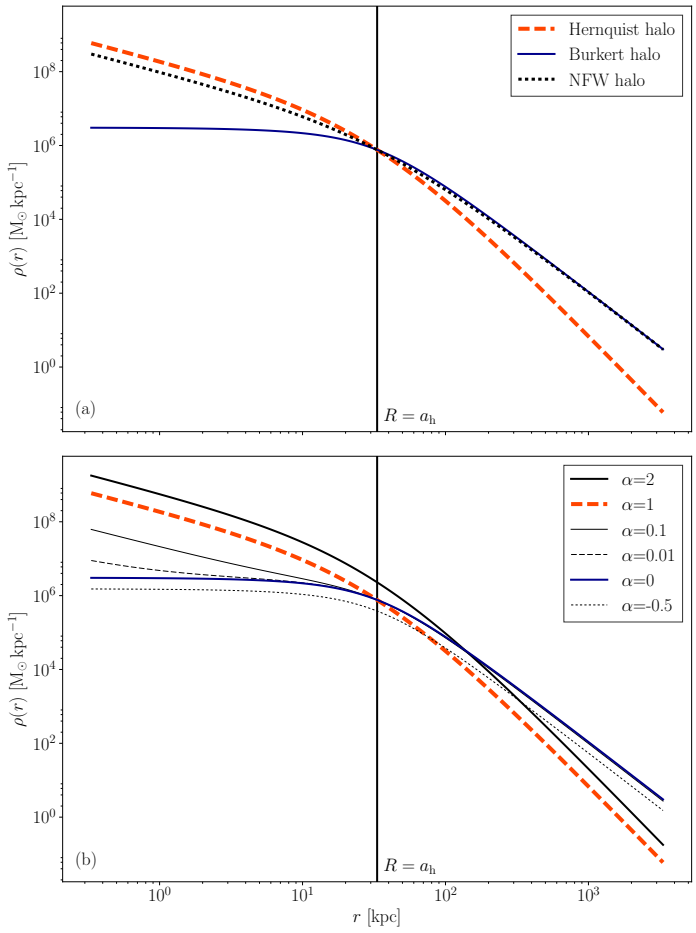

Figure 6.2: (a) Comparison of NFW (black dotted line), Hernquist (orange dashed line) and Burkert (blue line) halo shapes for the Milky Way. The Hernquist halo follows the cuspy shape of the NFW profile, and the Burkert profile is instead cored. (b) Comparison of various values of α. When $0 \leq \alpha \leq 1$, the halo changes between more cored or more cusped. When $\alpha < 0$, the cored shape is retained, but the halo is less massive. When $\alpha > 1$, the cusped profile is retained, but the halo is more massive.

where $\rho_{\rm h}(r)$ and $\rho_{\rm b}(r)$ are the densities of the Hernquist and Burkert dark matter profiles at a radius r. The influence that the quantity α has on the dark matter halo is shown in Fig. 6.2b. A value of $\alpha = 1$ means that the dark matter halo is a cusped Hernquist halo and $\alpha = 0$ means that the dark matter halo is a cored Burkert halo. Interpolating between the two means that the halo is more or less like the Hernquist and Burkert profiles. To allow for sensible behaviour outside $0 \leq \alpha \leq 1$, we can extrapolate as follows. For values of $\alpha < 1$, the halo shape does not change from that of the Burkert profile, but the total halo mass in the inner regions is reduced. For $\alpha > 1$, the halo stays cusped, but is more massive in the inner regions.

6.2.4 Overall galaxy properties

Only galaxies with measurements of bulge+disc or disc masses are included in these final samples. The overall numbers of galaxies in each of these samples are listed in the second column of Table. 6.1. Only some of the galaxies have reliably identified spiral arms from which the pitch angle, ψ can be measured – the number of galaxies with measured ψ values are shown in the third column of Table. 6.1. The final column shows

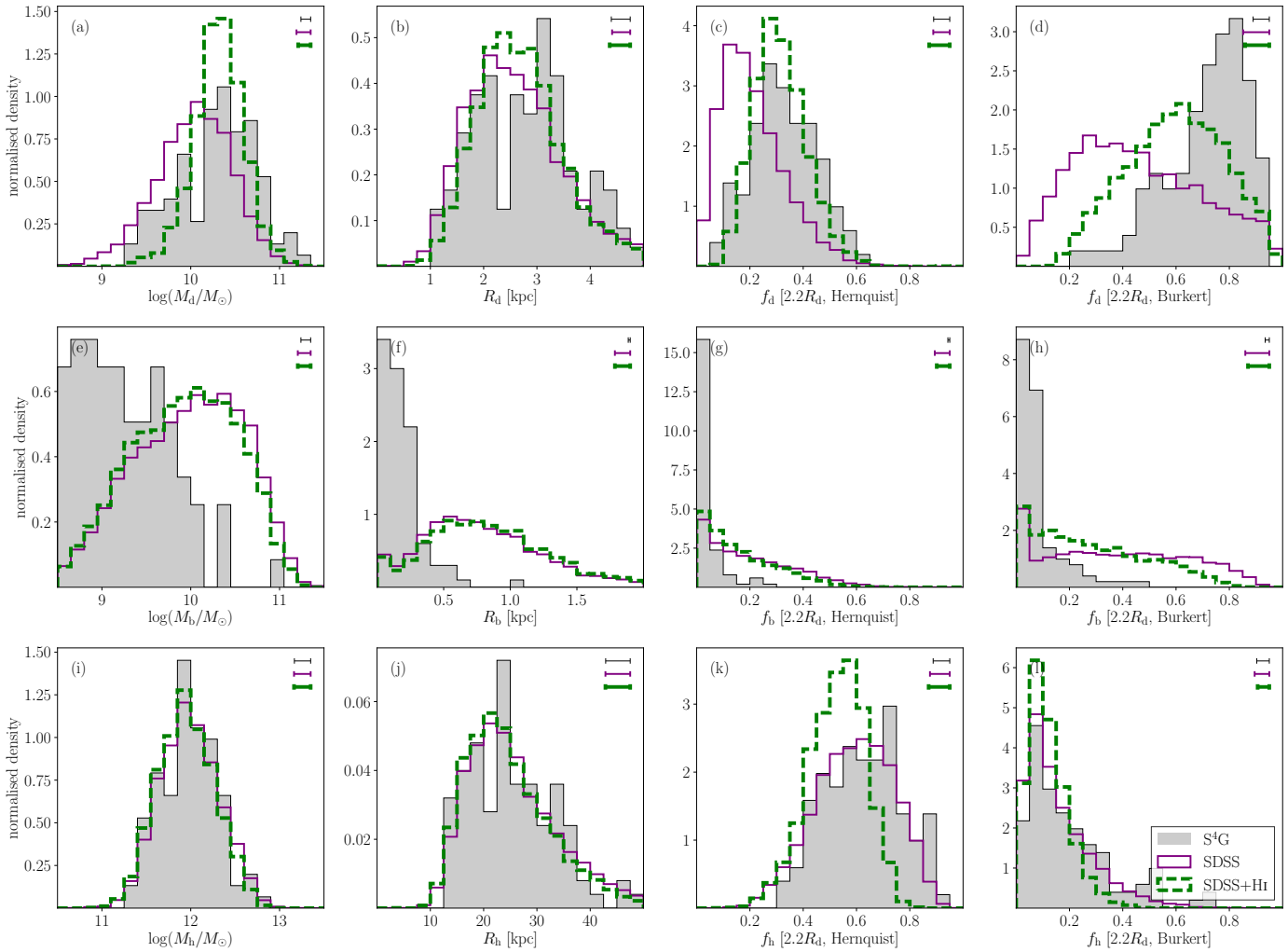

Figure 6.3: Distributions of galaxy stellar mass, scale radius and mass fractions for our galaxy samples. The top row shows the distributions of (a) disc total stellar mass, (b) radius, (c) fraction of the total galaxy mass within $2.2R_d$ for the Hernquist halo and (d) the same fraction with a Burkert halo. The same four parameters are shown for the galaxy bulge (middle row, e-h) and the galaxy halo (bottom row, i-l). The distributions are shown for the three distributions utilised in this chapter (see section 6.2): the S^{4}G sample is shown by the grey filled histograms, the SDSS is shown by the purple stepped histograms and the SDSS+HI is shown by the thicker dashed green histograms. The median error the parameters are indicated by the error bar in the upper right of each sub figure.

Table 6.1: Number of galaxies in each of the three samples used in this chapter. The first column shows the name of each sample. The second column indicates the total number of galaxies in each sample, and the third column indicates how many of these galaxies have measured pitch angles. The final column shows the median, 16th and 84th percentiles of stellar mass for each sample.

Sample	$N_{\rm gal}$	$N_{\rm gal}$ (with measured ψ)	$\log(\mathrm{M}/\mathrm{M}_\odot)$
S^{4}G	101	77	$10.4(9.8, 10.8)$
SDSS	7611	2661	$10.4(9.9, 10.8)$
SDSS+HI	5696	2241	$10.3(9.8, 10.7)$

the median, 16th and 84th percentiles of the stellar mass of all galaxies in each sample. Despite the different sample selections employed in each of the samples, all of the samples have similar stellar mass distributions with median $\log(\mathrm{M}_*) \sim 10.4\log(\mathrm{M}_\odot)$. The overall population stellar mass and size characteristics are shown in Fig. 6.3. The low-redshift galaxies occupy a range of bulge, disc and halo masses. The first column shows the bulge, disc and halo stellar masses for the S^{4}G sample (grey filled histograms), the SDSS sample (purple stepped histograms) and the SDSS+HI sample (green stepped histograms with dashed lines). The first attribute to note is the change in the disc mass and scale length when the HI is included in the disc fit, shown in Fig. 6.3a. The median disc mass is $10.06^{+0.46}_{-0.39}$ $\log(\mathrm{M}_\odot)$ for the pure stellar disc and increases to $10.32^{+0.27}_{-0.26}$ $\log(\mathrm{M}_\odot)$. The $\pm$ values denote the 16th and 84th percentiles of the distributions. The disc radius is also increased from $2.53^{+0.82}_{-1.07}$ to $2.62^{+0.73}_{-0.90}$ kpc. These differences lead to differences in the disc fractions, $f_{\rm d}$, in Fig. 6.3c-d, where the inclusion of HI in the discs leads to the discs being more maximal. The disc fraction is defined as the fraction of the total mass inside a given radius that is in the baryonic disc component, $\mathrm{M_d}(r)/[\mathrm{M_b}(r) + \mathrm{M_d}(r) + \mathrm{M_h}(r)]$. The inclusion of HI has a strong influence on the disc properties, which may in turn affect the properties of spiral arms, which will be explored in section 6.4.

The next item to note is the clear difference in the bulge properties of galaxies selected for the SDSS and S^{4}G samples. From Fig. 6.3a-b, we see that the disc properties are consistent in these samples, despite the differing selection criteria. The bulges of the SDSS galaxies have median stellar mass of $9.88^{+1.07}_{-0.69}$ $\log(\mathrm{M}_\odot)$ (or $9.83^{+0.91}_{-0.67}$ $\log(\mathrm{M}_\odot)$ for the SDSS+HI sample) and median radius of $0.74^{+0.38}_{-0.51}$ kpc (or $0.80^{+0.40}_{-0.50}$ kpc for the SDSS+HI sample). However, bulges in the S^{4}G sample are systematically smaller in both mass (Fig. 6.3e) and size (Fig. 6.3f), with median values of $8.99^{+0.64}_{-0.76}$ $\log(\mathrm{M}_\odot)$ and $0.15^{+0.07}_{-0.14}$ kpc. These offsets could be due to two reasons. The first is sample selection: the SDSS galaxy sample should include all galaxies with spiral morphology, regardless of bulge mass; the selection of late-type galaxies in the Buta *et al.* (2015) classifications may instead have introduced an unintended bias towards later type galaxies with smaller, less massive bulges. The other is that the techniques used to measure bulge mass differ, mainly in the wavelength selected. The SDSS bulge+disc masses are derived from fits to the stellar population of the galaxies using the optical *ugriz* bands. The S^{4}G sample instead uses information from the near infrared, which directly traces the older stellar population and thus the underlying stellar mass distribution. Investigating the true cause of this offset is beyond the scope of this thesis, but does highlight the importance of using two complementary datasets to investigate and confirm any results.

6.3 The galaxy model

In this section, I draw upon a number of measured parameters of spiral galaxies to model spiral galaxies and predict their properties with a swing amplified model.[1] Wherever there are no directly measurable quantities in galaxies, I use well-defined scaling relations to predict expected properties in galaxies.

6.3.1 Swing amplification derived quantities

I adopt the model of D'Onghia, Vogelsberger & Hernquist (2013) and D'Onghia (2015) for our spiral galaxies. In D'Onghia (2015), an equation was derived from arguments of swing amplification and disc stability, and verified by N-body simulations of isolated discs. The equation describing the dominant spiral arm mode at a given galaxy radius R is given by:

$$\begin{aligned} m = \frac{e^{2y}}{X}\Big(& \Big[\frac{\mathrm{M_b}}{\mathrm{M_d}}\frac{2y+3a_\mathrm{b}/R_\mathrm{d}}{(2y+a_\mathrm{b}/R_\mathrm{d})^3}\Big] \\ & + \Big[\frac{\mathrm{M_h}}{\mathrm{M_d}}\frac{2y+3a_\mathrm{h}/R_\mathrm{d}}{(2y+a_\mathrm{h}/R_\mathrm{d})^3}\Big] \\ & + y^2(3I_0K_0 - 3I_0K_1 + I_1K_2 - I_2K_1) \\ & + 4y(I_0K_0 - I_1K_1)\Big). \end{aligned} \tag{6.9}$$

The quantity $y = R/2R_\mathrm{d}$, meaning that the predicted spiral arm number varies with galaxy radius. This equation follows from classic models of swing amplification, first outlined in Toomre (1981). A useful property of this equation is that it can be split into three main components, each contributing to the expected spiral arm number: the bulge term, the halo term and the disc term. The bulge term, m_b, is given by the first line to the right of the equality in Eq. 6.9, and depends on the bulge mass ($\mathrm{M_b}$), disc mass ($\mathrm{M_d}$), bulge scale length (a_b) and disc scale length (R_d). The simplicity of this term's form is due to the adoption of a Hernquist profile to model the bulge mass distribution, compared to, for example, a de Vaucoleurs profile (de Vaucouleurs, 1948). Generally, galaxies with greater bulge-to-disc mass ratios and galaxies with smaller bulge-to-disc size ratios for a given bulge mass are predicted to have more spiral arms.

The second line to the right of the equality in Eq. 6.9 gives a similar term which I call m_h, this time with the bulge mass and size replaced by halo mass and size ($\mathrm{M_h}$ and a_h). This term is very similar to the one for the the bulge, as D'Onghia (2015) model the halo with a Hernquist profile. However, there is evidence that galaxy dark matter haloes may be less cuspy than a Hernquist profile (e.g. Flores & Primack 1994; van den Bosch *et al.* 2000). I therefore derive an alternative form of the halo term for a Burkert dark matter profile in section 6.3.1.1. Either way, there is a clear expected dependence on the dark matter halo and disc properties – galaxies with greater halo-to-disc mass ratios and galaxies with smaller halo-to-disc sizes are predicted to have more spiral arms.

The final two lines of the Eq. 6.9 form the disc term, m_d. The mathematical formulation is given in more detail in D'Onghia, Vogelsberger & Hernquist (2013). The

[1]The code used to model the galaxies described in this section is publicly available at https://zenodo.org/record/1164581

quantities I_0 and K_0 are Bessel functions of the first kind with respect to y.
From Eq. 6.9 and 6.20, spiral arm numbers can be predicted for the swing amplified model. I measure spiral arm numbers at 2 disc scale lengths in the rest of this chapter, as a radius well into the disc, but not too far so that the spiral arms are too faint to measure.
Another property of spiral galaxies we can use to quantify the spiral arm is the pitch angle, ψ. The rate of shear has a direct influence on the pitch angle of the spiral arms one expects to measure (Fuchs, 2001; Seigar *et al.*, 2006, 2008; Baba, Saitoh & Wada, 2013). The shear is given by (e.g. Julian & Toomre 1966; Michikoshi & Kokubo 2016):

$$\Gamma = 2 - \frac{\kappa^2}{2\Omega^2}. \tag{6.10}$$

The quantity κ is the epicycle frequency, and Ω is the angular frequency of the system. A falling rotation curve has $\Gamma > 1$, and a rising rotation curve has $\Gamma < 1$. Various relations exist between the rate of shear and pitch angle. Some are based upon observational studies of nearby galaxies (Seigar *et al.*, 2006), others from the analysis of the mathematics of swing amplification (Fuchs, 2001) and others are directly from simulations of galaxy discs (Baba, Saitoh & Wada, 2013; Michikoshi & Kokubo, 2014). I assume the pitch angles of our spirals to satisfy the following relation from Michikoshi & Kokubo (2014), taken from simulations. These predictions match up to analytical predictions from Fuchs (2001) for $\Gamma < 1$, with the advantage that they cover the entire range of Γ from $0 - 2$. The predicted pitch angle is given by:

$$\psi = \frac{2}{7}\frac{\sqrt{4 - 2\Gamma}}{\Gamma}. \tag{6.11}$$

The value Γ uses Ω and κ defined in Eq. 4 of D'Onghia (2015) and Eq. 6 of D'Onghia, Vogelsberger & Hernquist (2013) for the Hernquist profile and Eq. 6.16 and Eq. 6.18 of this chapter for the Burkert profile. Using this equation, predicted pitch angles in the rest of this chapter are measured at 2 disc scale radii.

6.3.1.1 The Burkert dark matter profile

In section 6.2.3, a Burkert dark matter halo was discussed to model the dark matter halo of spiral galaxies. The Burkert profile (Burkert, 1995) is characterised by the following function:

$$\rho = \rho_0 \frac{r_0^3}{(r + r_0)(r^2 + r_0^2)}, \tag{6.12}$$

where ρ_0 is the central density of the dark matter halo, r_0 is the scale length and r is the radius. We can define the following quantity to make the equations appear a little simpler:

$$\phi(r, r_0) = \ln\left(\frac{r + r_0}{r_0}\right) + \frac{1}{2}\ln\left(\frac{r^2 + r_0^2}{r_0^2}\right) - \arctan\left(\frac{r}{r_0}\right). \tag{6.13}$$

The mass enclosed within a sphere of radius r is given by

$$\mathrm{M}(r) = 2\pi\rho_0 r_0^3 \phi(r, r_0). \tag{6.14}$$

The central density, ρ_0, can be calculated from the mass of the halo at r_{200}, where r_{200} is the radius where the halo density falls to 200 times the critical density of the

Universe. By rearranging Eq. 6.14, the central density is

$$\rho_0 = \frac{\mathrm{M}_{200}}{2\pi r_0^3 \phi(r_{200}, r)}, \tag{6.15}$$

where M_{200} is the halo mass at r_{200}. The angular frequency of the halo is

$$\Omega^2(r) = 2\pi G \rho_0 r_0^3 \frac{\phi(r, r_0)}{r^3}. \tag{6.16}$$

The spiral arm number is given by Eq. 1 of D'Onghia (2015):

$$m = \frac{\kappa^2}{2\pi G \Sigma} \frac{R}{X}, \tag{6.17}$$

where Σ is the surface density of the stellar disc and X is a factor introduced in Toomre (1981) which is most effective at $X = 1.5 - 2$ (D'Onghia, Vogelsberger & Hernquist, 2013). κ^2 is given by

$$\kappa^2 = r\frac{d\Omega^2}{dr} + 4\Omega^2. \tag{6.18}$$

For the Burkert profile, this becomes

$$\kappa^2 = \frac{2\pi G \rho_0 r_0^3}{r^3}\left[\frac{r^2}{r^2 + r_0^2} - \frac{r}{r_0(r^2/r_0^2 + 1)} + \frac{r}{r + r_0} + \phi(r, r_0)\right]. \tag{6.19}$$

Putting together Eq. 6.17 and Eq. 6.19 yields the following relation for spiral arm number with respect to the dark matter halo:

$$m_{\mathrm{h}} = \frac{e^{2y}}{X}\frac{\pi \rho_0 r_0^3}{\mathrm{M_d}}\frac{y^2}{2}\left[\frac{r^2}{r^2 + r_0^2} - \frac{r}{r_0(r^2/r_0^2 + 1)} + \frac{r}{r + r_0} + \phi(r, r_0)\right]. \tag{6.20}$$

This now replaces the halo term in Eq. 6.9 so that m can be calculated for the Burkert dark matter halo.

6.3.1.2 Predicted arm numbers for typical spirals

The differences in halo profiles can have a strong influence on the expected spiral arm numbers in galaxies. In Fig. 6.4, the spiral arm number predicted from the galaxy model described in section 6.3 are shown for typical spiral galaxies from the S^{4}G and SDSS samples used in this chapter. For reference, I also compute the halo properties of the Milky Way using the structural parameters of Bovy & Rix (2013). Their measured stellar mass value of $5.9 \pm 0.5 \times 10^{10}\mathrm{M}_\odot$ predicts a halo of mass $\mathrm{M}_{200} = 2.14 \pm 0.83 \times 10^{12}\mathrm{M}_\odot$ and scale radius $a_{\mathrm{h}} = 34.5 \pm 4.5$ kpc. The predicted number of arms for the Milky Way for this halo mass, disc mass and a galaxy bulge of mass $4 \times 10^9\mathrm{M}_\odot$ and scale radius 0.6 kpc (as used in D'Onghia 2015) are shown in Fig. 6.4a. We see a small offset in that the model predicts more spiral arms than the D'Onghia (2015) Milky Way model – this difference is due to the differences in the halo mass and size, with our predicted halo being larger in mass and than the one used in D'Onghia (2015).
In Fig. 6.4b-d, I plot the same radius vs. predicted arm number trend for galaxies typical of the S^{4}G, SDSS and SDSS+HI samples. I use the median values for disc, bulge and halo masses and sizes, and median error values for each sample. The variations in

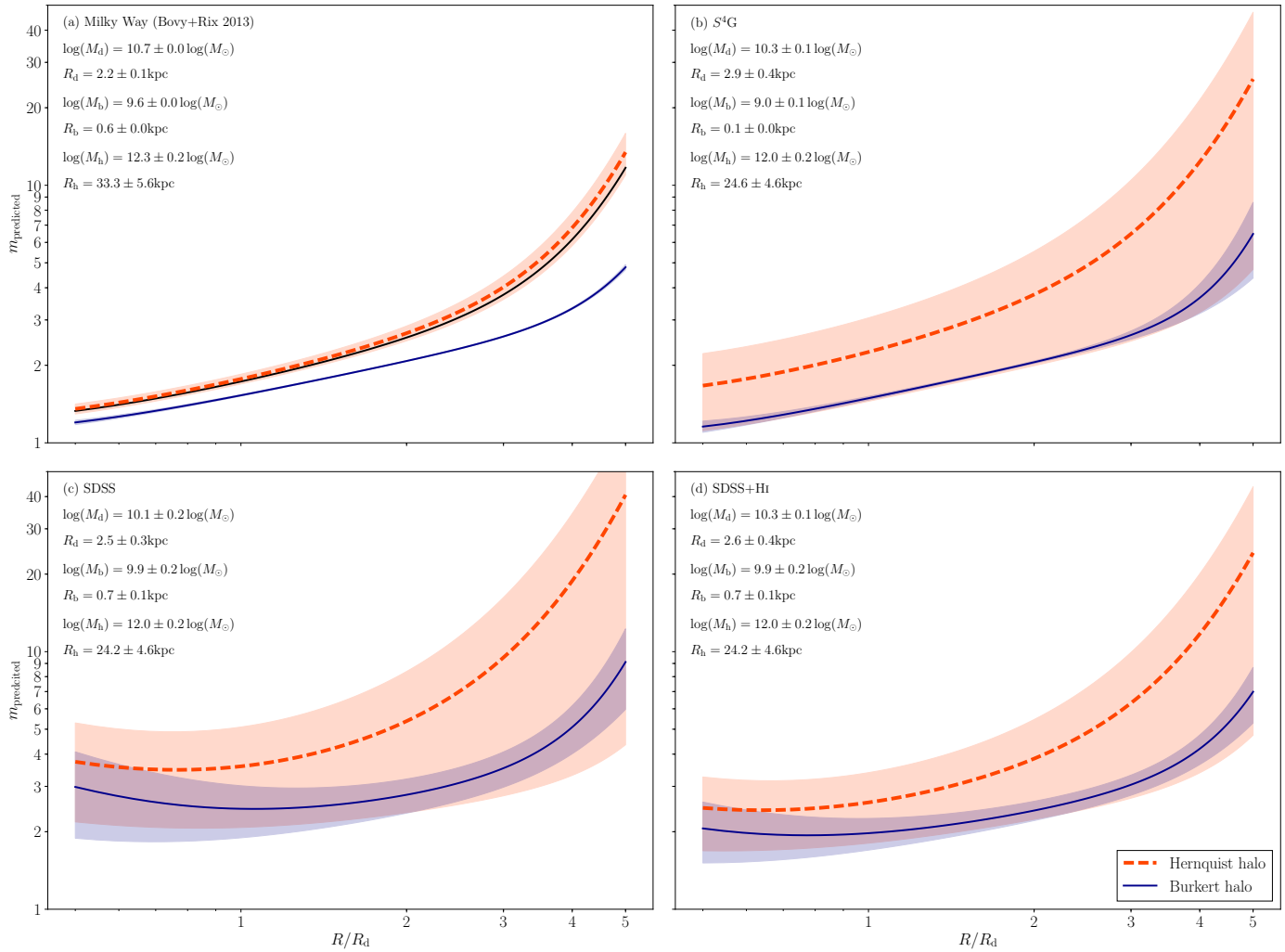

Figure 6.4: Spiral arm number vs. radius for four typical spiral galaxies: (a) the Milky Way (Bovy & Rix, 2013); (b) a galaxy with median properties for the S^{4}G sample; (c) a galaxy with median properties from the SDSS sample and (d) a galaxy with median properties from the SDSS+HI sample. The orange dashed lines show the expected spiral arm numbers for the cusped Hernquist dark matter profile, and the thinner, solid blue lines show the expected arm number for the cored Burkert profile. Both galaxy properties and halo shape have a strong influence on the expected spiral arm number in galaxies. The disc, bulge and halo parameters are listed in the top-left corner of each plot. In the model, we propagate through all of the errors from the disc, bulge and halo mass and size estimates. The shaded region indicates one standard error in the predicted spiral arm number for each example galaxy.

the galaxy parameters discussed in section 6.2.4 lead to changes in the expected spiral arm morphology. The median S^4G galaxy follows the trend of the Milky Way fairly closely, albeit with a larger error in the expected spiral arm number, owing to greater uncertainty in the measured bulge and disc parameters. A galaxy typical of the SDSS sample predicts more spiral arms, owing to the fact that the bulge is more prominent for this model – this leads to an increase in the size of the bulge term in Eq. 6.9, which in turn increases the predicted spiral arm number. Including the HI component in the SDSS model makes the disc more dominant, which leads to a suppression of the expected spiral arm number, which can be seen comparing Fig. 6.4c and d. We also see the direct influence that the dark matter profile shape has on the spiral arm numbers predicted for our galaxy model. The Hernquist profile is strongly cusped in the centre, whereas the Burkert profile is almost flat. The Burkert halo therefore has less influence on the spiral arm number in the baryon-dominated centre of galaxies, leading to systems being more disc dominated and therefore having fewer spiral arms. The predicted spiral arm number is also distinctly flatter in the inner regions, which is particularly apparent for the SDSS and SDSS+HI samples in Fig. 6.4c-d. From these plots we can conclude that there are a number of factors that influence the spiral arm number in the model: more disc dominated systems should have fewer spiral arms, and systems with flatter dark matter halo profiles should also have systematically fewer spiral arms.

The models outlined in this section give directly predictable arm numbers and pitch angles. All of the predictions are taken from direct analytical calculations of swing amplification theory and disc stability, and further verified by simulations. This simple galaxy model, with arm morphology predictions from only a bulge, disc and dark matter halo can now be tested with respect to observed visual galaxy morphology.

6.4 Comparing model predictions with observations

In this section, I compare the predictions of swing amplification with outlined in section 6.3 with observed morphologies of spiral galaxies. I begin by looking at the predicted arm number and pitch angle distributions from the Burkert and Hernquist haloes, in order to check whether they match the overall distributions we observe in real galaxies. I then look at how well the model can predict spiral arm numbers on a galaxy by galaxy basis, looking in more detail at the properties the dark matter halo requires for the model to work.

6.4.1 Spiral arm number distributions

Spiral arm numbers pose an interesting challenge to both observers and modellers of disc galaxies. From observations, we know that low arm numbers are preferred, with two-arm structures being particularly prevalent in the low-redshift Universe (Elmegreen & Elmegreen, 1982; Grosbøl, Patsis & Pompei, 2004). However, simulations often try to predict spiral arm numbers in the absence of bars. In this case, simulated spiral patterns are typically dominated by higher-order modes i.e. many-arm patterns (see Dobbs & Baba 2014 and references therein).

I plot the distributions of spiral arm numbers for our samples of spiral galaxies in Fig. 6.5. The observed GZ2 $m_{\rm avg}$ arm number distribution of the SDSS sample is plotted for reference in each panel. Additional histograms show the arm number dis-

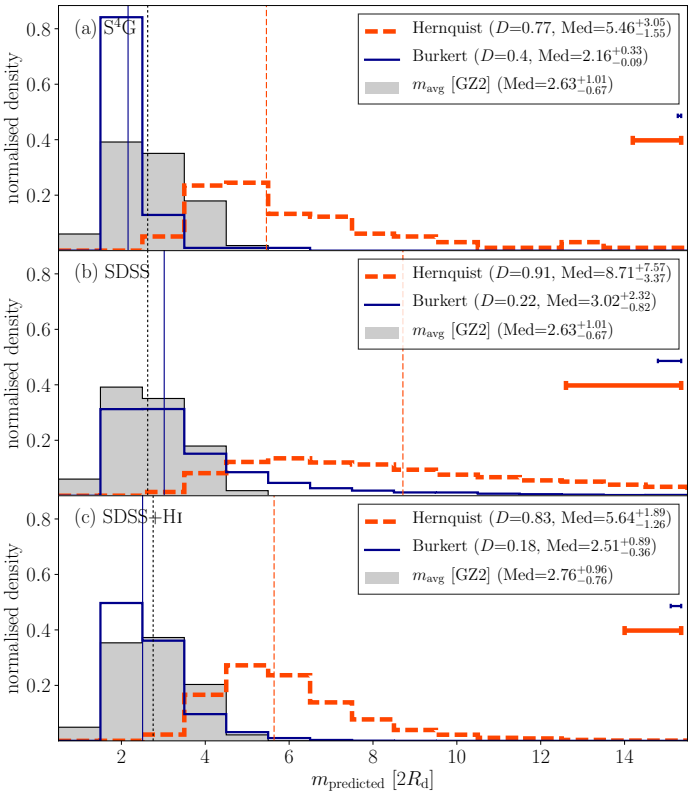

Figure 6.5: Distributions of predicted spiral arm number for (a) S^{4}G, (b) SDSS and (c) SDSS+HI galaxy samples. The grey histograms show the distributions of average arm number, $m_{\rm avg}$ for the SDSS galaxy sample in a-b and the SDSS+HI sample in c, and the vertical dotted black line shows their corresponding median values. The orange dashed histograms show the expected distribution for the Hernquist halo model, and the blue line shows the same distribution for the Burkert halo model. The error bars show the median error on the predicted m-value for each sample.

tributions predicted by our model for each halo type and sample. Fig. 6.5a shows the S^{4}G sample, Fig. 6.5b shows the SDSS sample and Fig. 6.5c shows the SDSS+HI sample. In Fig. 6.5a, there are no direct arm number measurements for the S^{4}G sample; the SDSS sample is used for comparison, given its similarity in total stellar mass. From the observed spiral arm numbers, we see the familiar trend that disc galaxies tend to prefer lower order spiral modes, with the two-arm mode being particularly prevalent – the modal bin is centred on $m_{\rm avg} = 2$, and the median arm number is $2.63^{+1.01}_{-0.67}$, where the $\pm$ values denote the 16th and 84th percentiles. For SDSS+HI, the modal bin is centred on 2.5 and the distribution has median arm number $2.76^{+0.96}_{-0.76}$. The galaxy model with the Hernquist halo clearly produces too many spiral arms, with median arm number $5.46^{+23.05}_{-1.55}$ for the S^{4}G sample, $8.71^{+7.57}_{-3.37}$ for the SDSS sample and $5.65^{+1.89}_{-1.27}$ for the SDSS+HI sample. The reasons for these differences between the samples were discussed in section 6.3.1.2. We can quantify how closely related these distributions are using the KS D-statistic.[2] The D-statistic is very large for the Hernquist halo model, with value $\sim 0.8 - 0.9$ for each of the samples in Fig. 6.5. If one instead models the distributions with cored Burkert dark matter halo (thinner blue lines), we see that the distributions of spiral arm number match a realistic spiral arm number distribution more closely, with median $m_{\rm avg}$-values of $3.02^{+2.32}_{-0.82}$ for the pure stellar sample and $2.51^{+0.89}_{-0.36}$ and much lower D-statistics of 0.22 and 0.18 respectively. The result for the

[2]Our simplified model is unlikely to recover the range of morphologies exactly, so the KS p-value is likely to converge to close to 0 in all cases, making it unsuitable for distinguishing any differences.

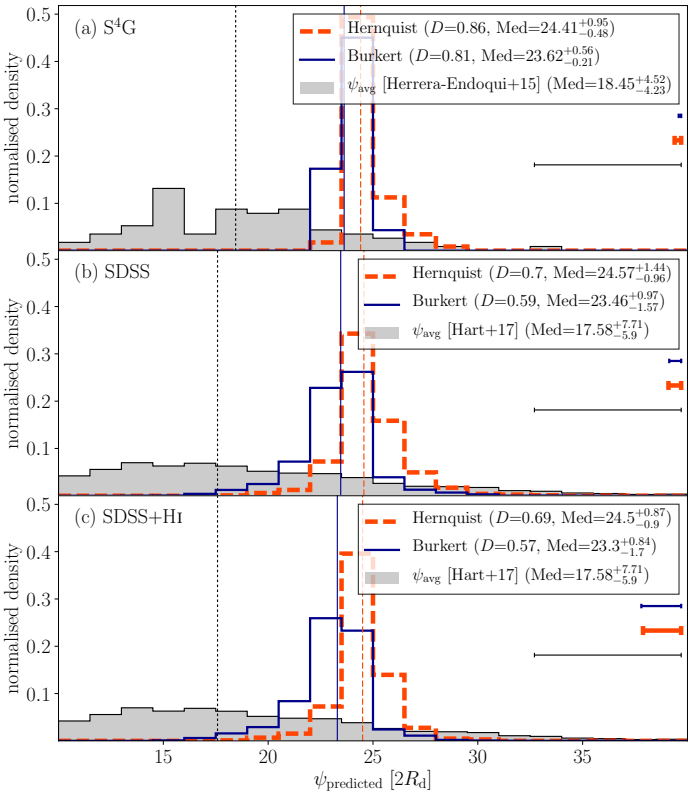

Figure 6.6: Distributions of predicted pitch angle for (a) S^{4}G, (b) SDSS and (c) SDSS+HI galaxy samples. The grey filled histograms show the measured spiral arm pitch angle distributions for each sample from Herrera-Endoqui *et al.* (2015) for S^{4}G and section 3.3 for the SDSS and SDSS+HI samples. The orange dashed histograms show the expected distribution for swing amplified arms, assuming the Hernquist halo model, and the blue line shows the same distribution for the Burkert halo model. The median error in each measurement is shown by the error bar in each panel and the black error bar shows the estimated observational error from section 5.3.2.

S^{4}G sample in Fig. 6.5a is that we produce too many two-arm galaxies. I note, however, that the comparison is less certain, given the different sample selections for S^{4}G and SDSS, and the potential discrepancies discussed in section 6.2.4.

6.4.2 Spiral arm pitch angle distributions

The spiral arm pitch angle measures how tightly wound spiral arms are. The expected pitch angle in spiral galaxies depends on the underlying mass distribution, with more centrally concentrated masses leading to tighter spiral arms. This is usually predicted to be the case, no matter which mechanism is responsible for producing the arms (Fuchs, 2001; Seigar *et al.*, 2008). However, other properties such as the age of the spiral arm (Grand, Kawata & Cropper, 2012a) and the number of arms (chapter 5) can affect pitch angles. From the simulations of Michikoshi & Kokubo (2014), we can directly predict the pitch angle given the rate of shear in the disc of a galaxy (see section 6.3). I plot the expected distributions of spiral arm pitch angle in Fig. 6.6. The grey distributions show the observed spiral arm pitch angles measured for the S^{4}G sample and the SDSS samples from Herrera-Endoqui *et al.* (2015) and section 3.3 respectively. If the model perfectly fit the spiral galaxy population as a whole, one would expect a distribution of pitch angles centred on $\sim 19°$ and 16th–84th percentile range of $\sim 12 - 15°$ for each sample. Instead, for each dark matter halo profile, we observe

a narrow range of pitch angles with looser spiral arms (larger pitch angles).

The Burkert profile leads to spiral arms which are tighter than those in the Hernquist profile, and also leads to distributions which are peaked at $\sim 24°$. Fig. 6.7 shows the distributions of the shear, Γ. Both the Hernquist and the Burkert halo in our galaxy model predict $\Gamma \sim 1$. The Hernquist profile has distributions of lower Γ values, but neither model gives distributions of $\Gamma > 1$ required to produce the distributions of tighter spiral arms observed in real spiral galaxies.

One potential reason for the discrepancies in the pitch angles is measurement error. In chapter 5, I derived two alternative pitch angle measurements, and saw a scatter of $\approx 7°$. Convolving the predicted pitch angle distributions with a random Gaussian error of 7° leads to the widening of the distributions – the 16th–84th percentile range is $\approx 12°$ for the S^{4}G sample and $\approx 15°$ for the SDSS samples in this case. This can account for the discrepancy between the measured and observed pitch angle distribution widths. However, the peaks of the predicted pitch angle distributions are still too loose compared to those observed.

In Fig. 6.8, I show the cumulative distributions of spiral arm pitch angles for the model compared with the observations, with the predictions convolved with 7° errors. The picture which emerges is interesting – the maximum pitch angle seems to be the same between the observations and predictions. The 99.7th percentile ($\approx 3\sigma$) is $\psi = 44.3°$ in the observations; the equivalent values are 43.3, 44.8, 45.0 and 43.0° for the SDSS with the Hernquist halo, SDSS with the Burkert halo, SDSS+HI with the Hernquist halo and the SDSS+HI with the Burkert halo respectively. However, the model deviates from the observed distributions for tighter spiral arms. Swing amplified arms are, however, kinematic in nature, and do wind up over time. Grand, Kawata & Cropper (2013) demonstrated that spiral arms exist for ≈ 100 Myr, and wind up by approximately 10° over the course of their lifetime. The dotted lines in Fig. 6.8 show the same galaxies, with a random winding of $0 - 10°$ applied to each galaxy (each galaxy is randomly $0 - 10°$ tighter than the model prediction). In this case, we see the model is much more consistent with the observations. This is particularly the case for the Burkert dark matter profile, where the KS D-statistic has been reduced to ≤ 0.1 in both the SDSS and SDSS+HI cases. In order to match the distributions correctly, the winding up of spiral arms must also be taken into account.

These results show that spiral arm number is the better diagnostic tool for finding swing amplified spiral modes. The model inputs that I employ cannot reproduce the subtle differences in Γ that are required to produce the variety of pitch angles in galaxies. The errors on the measured pitch angles are also relatively large, of order 7°. This makes any model difficult to constrain due to a large scatter introduced by the errors in the measurements. Additionally, the age of the spiral arms appears to have an effect – if spiral arms do wind up over time, as the evidence here suggests, then this will introduce an unwanted and difficult to quantify scatter in the true pitch angles of spiral galaxies.

6.4.3 The disc fraction-arm number relation

From the formalism described in section 6.3, the predicted spiral arm number is expected to have a strong dependence on the relative sizes and masses of haloes, bulges and discs. Of particular note is the relation with the disc fraction: many simulations

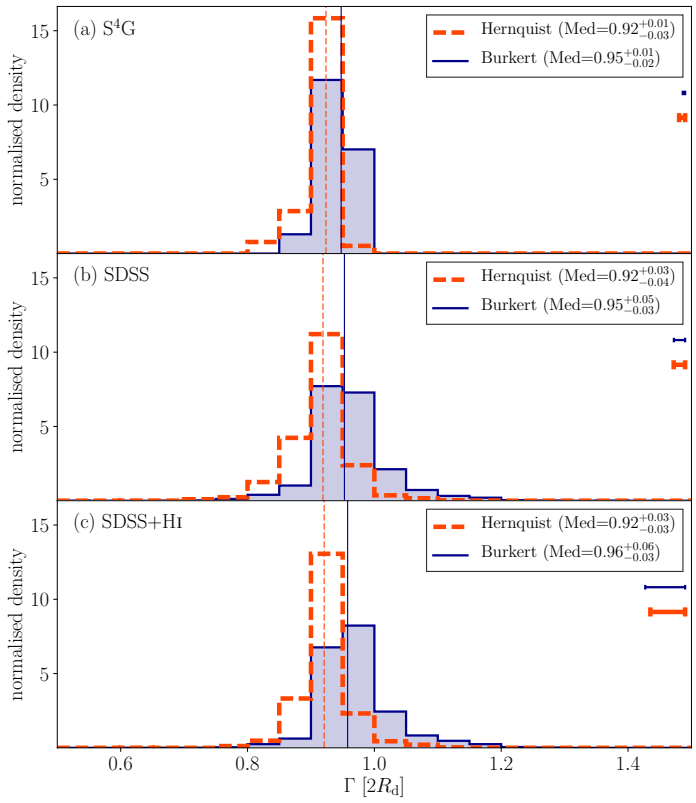

Figure 6.7: Distributions of predicted values for shear, Γ, for (a) S^{4}G, (b) SDSS and (c) SDSS+HI galaxy samples. The filled blue histograms show the values with a Burkert halo, and the dashed orange histograms show the histograms with a Hernquist halo. The median error in each measurement is shown by the error bar in each panel.

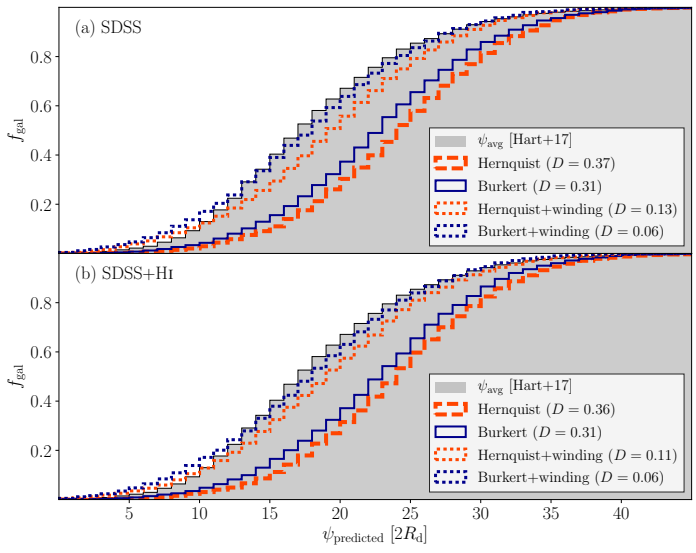

Figure 6.8: Cumulative fractions of observed (grey filled histograms) and predicted spiral arm pitch angles (stepped histograms) for (a) the SDSS sample and (b) the SDSS+HI sample. The dashed orange line and the solid blue line show the distributions of pitch angles from the model using Hernquist and Burkert dark matter profiles respectively, convolved with a Gaussian error of 7°. The dotted orange and blue lines indicate the same distributions, with a random scatter downwards of 0-10°. This scatter makes the predicted pitch angles match the real distribution more closely.

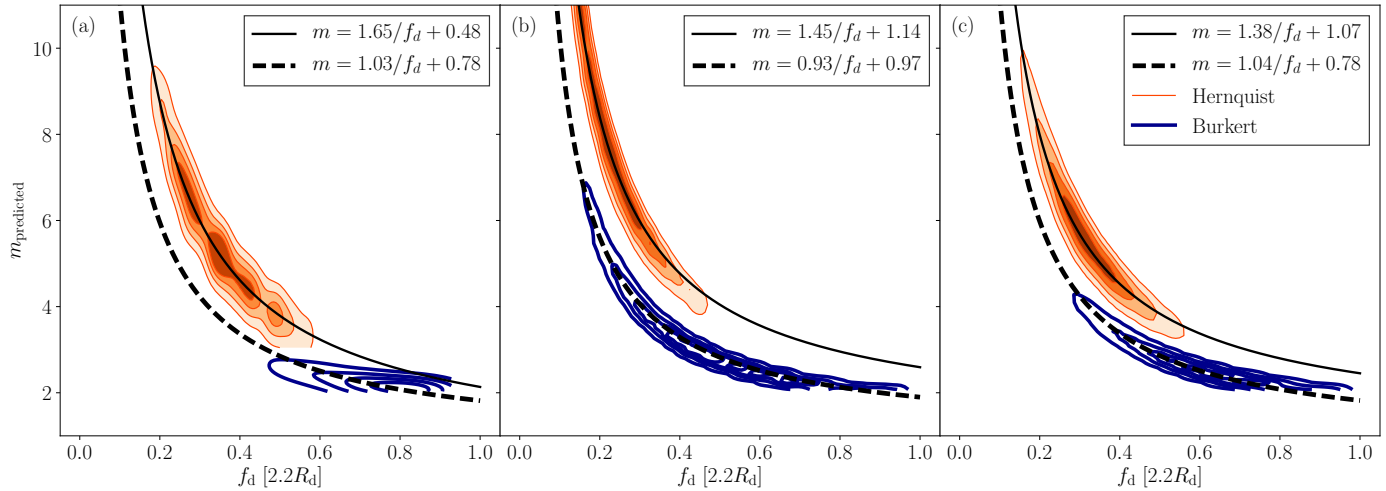

Figure 6.9: Disc fraction, $f_{\rm d}$ vs. predicted spiral arm number, $m_{\rm predicted}$ for (a) the S^{4}G sample, (b) the SDSS sample and (c) the SDSS+HI sample. The orange filled contours show the predictions for the Hernquist halo and the blue lined contours show the predictions for the Burkert halo. The contour lines show where 20, 40, 60 and 80 per cent of the data lie for each sample. The flatter inner profile leads to fewer predicted arms for a given disc fraction.

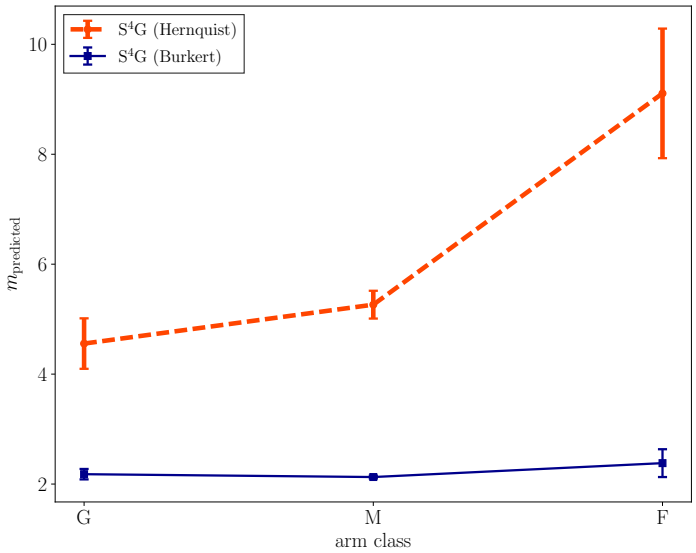

Figure 6.10: Predicted spiral arm numbers for S^{4}G grand design (G), many-arm (M) and flocculent (F) spirals. The orange dashed line shows the median spiral arm number for the Hernquist dark matter halo, and the solid blue line shows the same value for the Burkert dark matter halo. The error bars indicate one standard error on the median for each sub sample.

predict a strong correlation of $m \propto f_{\rm d}^{-1}$, where $f_{\rm d}$ is the disc fraction within 2.2 times the disc scale length (Carlberg & Freedman, 1985; Bottema, 2003; Fujii *et al.*, 2011; D'Onghia, Vogelsberger & Hernquist, 2013). Such a relation is unsurprising, given the functional form of Eq. 6.9. The equation has terms predicting $m \propto {\rm M_b/M_d}$ and $m \propto {\rm M_h/M_d}$; the only complications are the other dependencies on the relative sizes of the components. In Fig. 6.9, the relations for each of the subsamples are shown. Here we see the expected relationship of $m_{\rm predicted} \propto f_{\rm d}^{-1}$. The scatter is very small, meaning the relationship is dominated by the mass fractions, rather than the relative sizes of the components. We also see another trend that the relationship depends not only on $f_{\rm d}$, but the shape of the dark matter profile also plays a role: the Burkert profile, which has a flat inner profile, leads to a lower predicted spiral arm number for a given disc fraction as well as larger disc fractions.

6.4.4 Predicting spiral arm numbers in galaxies

Given that the modal spiral arm theory does seem able to predict reasonable spiral arm number distributions, given a cored dark matter profile, we will now investigate how well the theory predicts spiral arm numbers in individual galaxies. If the modal theory is indeed accurate, we expect to see a strong correlation between the observed spiral arm numbers and those predicted by Eq. 6.9.

As a first test, I check the predicted spiral arm numbers for the S^{4}G sample. This sample is observed in the NIR, so the spiral arms we see here should correspond to the underlying mass distributions of the galaxies. In the S^{4}G sample, we do not have a direct measurement of spiral arm number in the way we have for SDSS. Instead, galaxies are classified by their Elmegreen arm-type, as either grand design, many-arm or flocculent. Grand design spiral galaxies are characterised by their strong two-arm structure, whereas many-arm spirals instead have more than two spiral arms, and flocculent spiral galaxies have more, broken, patchy spiral arms than many-arm galaxies (see section 1.2.2). From these arguments, we expect the grand design spiral galax-

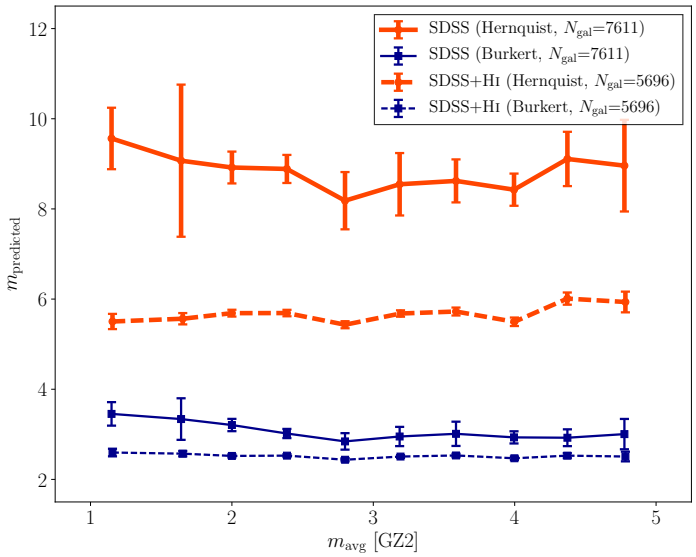

Figure 6.11: Spiral arm number measured from GZ2, $m_{\rm avg}$, vs. spiral arm number predicted from the galaxy model. The orange lines show the model with a Hernquist dark matter halo, and the blue lines show the models with a Burkert dark matter halo profile. The solid lines show the SDSS samples, and the dashed lines show the SDSS+HI samples. The points show the median and the error bars indicate one standard error on the median. There is no clear correlation to confirm that the model can predict spiral arm numbers accurately with either a universally cusped or cored halo.

ies to have the fewest predicted spiral arms, and the flocculent galaxies to have the most predicted spiral arms. In Fig. 6.10, the median predicted spiral arm number is shown for each of the spiral arm subcategories. There is a weak trend for exactly what we expect: the flocculent spirals do have the most predicted spiral arms, with $m_{\rm predicted} = 9.1 \pm 1.2$. There is, however, little difference between the grand design and many-arm spiral categories with $m_{\rm predicted} = 4.6 \pm 0.5$ and 5.3 ± 0.3. The $\pm$ values here denote one standard error on the median. We also see evidence that a cored Burkert dark matter halo profile cannot reproduce the variability in spiral structure between spiral galaxies – in all cases, the predicted spiral arm number is ≈ 2.

For the SDSS sample, we have direct measurements of spiral arm numbers from the GZ2 classifications of spiral galaxies. Rather than asking questions to describe the spiral arm type, Galaxy Zoo volunteers instead classified the number of spiral arms they could observe in the optical image. I use the average arm number $m_{\rm avg}$, to describe the spiral arm number for each galaxy. The number of spiral arms observed for the SDSS and SDSS+HI vs. the number of spiral arms predicted for those same galaxies are shown in Fig. 6.11. Here, there is no evidence that the optically classified spiral arm number has any relation to the number of spiral arms predicted. This is the case for the cusped Hernquist and cored Burkert profiles, with and without the disc gas mass being included in the prediction. We observe no strong correlation between the predicted and observed spiral arm numbers, with $|r_s| \leq 0.1$ in each case.

6.4.5 Varying the dark matter halo

In the above sections, it was discovered that the dark matter halo shape has a profound influence on the number of spiral arms one would expect a galaxy to have if swing amplification was at play. However, neither a cored or cusped halo could produce the variety of spiral arm morphologies in local galaxies from grand design to many-arm

structures. This does not necessarily mean spiral arms are not swing amplified modes; instead, the dark matter halo may exhibit strong differences from galaxy to galaxy. In fact, the radial profiles of dark matter haloes have been shown to vary greatly from galaxy to galaxy, with earlier type massive ellipticals having cuspier profiles (Dutton *et al.*, 2013; Dutton & Macciò, 2014; Sonnenfeld *et al.*, 2015), and later type, low surface brightness systems having flatter inner profiles (de Blok *et al.*, 2001; Swaters *et al.*, 2003; Goerdt *et al.*, 2006), with some level of interpolation in between (Dutton *et al.*, 2016).

With the mathematics formulated in sections 6.2.3 and 6.3.1, we can interpolate between the Burkert (cored) and Hernquist (cusped) dark matter profiles. Models of dark matter haloes usually describe the profile shape in terms of halo contraction. Contracted haloes have less mass in their inner regions, and more in their outer regions, with star formation feedback often cited as the cause of such a change (Navarro, Frenk & White, 1996; Oh *et al.*, 2011; Katz *et al.*, 2017). In our model, we are principally concerned with the inner region of the halo. We can mimic the halo contraction in the inner region by varying the shape of the halo as described in section 6.2.3.1.

In order to address the issue of whether an interpolated halo can reproduce the predictions of swing amplified spiral arms, we can ask the question of what value of α (a proxy for the contraction in the inner regions) our haloes need to be in order for a model to match perfectly. That Eq. 6.9 can be split into multiple parts allows for easy manipulation when we consider our superimposed hybrid dark matter haloes described in section 6.2.3.1. The equations become:

$$\begin{aligned} m(r) &= m_{\rm b}(r) + m_{\rm d}(r) + (1+\alpha)m_{\rm h,B}(r) && (\alpha < 0) \\ m(r) &= m_{\rm b}(r) + m_{\rm d}(r) + (1-\alpha)m_{\rm h,B}(r) + \alpha m_{\rm h,H}(r) && (0 \leq \alpha \leq 1) \\ m(r) &= m_{\rm b}(r) + m_{\rm d}(r) + \alpha m_{\rm h,H}(r) && (\alpha < 0), \end{aligned} \tag{6.21}$$

where $m_{\rm h,H}$ and $m_{\rm h,B}$ are the Hernquist and Burkert halo arm numbers. We now have a set of inferred dark matter halo profile shapes, α, based on each galaxy's measured bulge and disc properties, observed spiral arm number, and the assumption of the swing amplification model. Dark matter halo expansion is often quantified as the mass of the halo inside a given radius when baryonic processes have been taken into account divided by the mass the halo would have if only dark matter were present (e.g. Dutton *et al.* 2016). To this end, we define the following to estimate the same quantity:

$$\epsilon_{\rm halo} = \log(\mathrm{M}_{\rm halo}[0.01R_{200}]/\mathrm{M}_{\rm hernquist}[0.01R_{200}]), \tag{6.22}$$

where $\mathrm{M}_{\rm halo}$ is the mass of a given halo constructed from the superposition of the Hernquist and Burkert profile as described in section 6.2.3.1, and $\mathrm{M}_{\rm hernquist}$ is the mass of the Hernquist halo of the same mass and size. The Hernquist halo should approximate a dark matter only halo, given that dark matter simulations predict cuspy NFW-like haloes (Navarro, Frenk & White, 1996, 1997).

For each galaxy, I calculate the mass of the modified halo that gives the correct arm number vs. the mass of the halo one would expect if there were no baryonic processes affecting the halo. The distributions of the required $\epsilon_{\rm halo}$ values are shown in Fig. 6.12. Only galaxies with physical dark matter haloes are included in this distribution – these are galaxies with $\alpha > -1$, and make up 3157/7611 of the SDSS galaxies (41.5 per cent) and 2489/5696 of the SDSS+HI galaxies (43.7 per cent). For the remaining ~ 60 per cent of the galaxies, the spiral arm number from the disc and bulge is greater

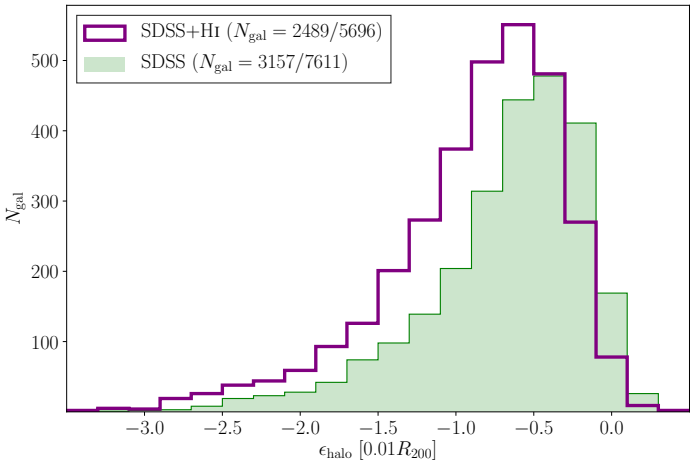

Figure 6.12: Values of halo expansion parameter required to reproduce the spiral arm numbers from GZ2. The green filled histogram shows the SDSS+HI sample and the purple stepped histogram shows the SDSS sample. A significant fraction of both populations cannot be explained by swing amplification, even with a dark matter halo set to M_h=0.

then the observed spiral arm number; even in the extreme case where there is no dark matter halo contribution, the predictions cannot match the observations. Their origin is therefore unlikely to be swing amplification. These are usually galaxies with low spiral arm numbers: 71.3 per cent of these galaxies have spiral arm numbers of $m = 1$ or $m = 2$ according to GZ2. For the galaxies that may have swing amplified arms ($\alpha > -1$), this value is just 25.2 per cent.

To test whether these α parameters derived directly from observed quantities are reasonable, I compare them to results from simulations. The dark matter only halo mass, M_{DMO}, is taken as simply the mass of the Hernquist halo. The mass of the halo required, $M_{h,req}$, is the mass of the interpolated halo. Recent simulations have predicted that the size of the dark matter halo depends on a number of parameters related to the host galaxy (Di Cintio *et al.*, 2014b,a). Notably, Dutton *et al.* (2016) simulated a range of galaxies with the NIHAO simulation suite, finding clear correlations between galaxy star formation efficiency, stellar mass and halo mass and the dark matter halo contraction. They also published a relationship between galaxy size, halo size and the halo contraction of the following form:

$$\begin{aligned}\log(M^{0.01}_{hydro}/M^{0.01}_{DMO}) = &-0.28(\pm0.11)\\ &- 1.52(\pm0.42)(\log(R_{1/2}/R_{200}) + 1.68),\end{aligned} \tag{6.23}$$

where M_{hydro} is the mass of the dark matter halo simulated with baryonic processes and $R_{1/2}$ is the galaxy half mass radius. The superscripts 0.01 denote the mass within $0.01R_{200}$, the central part of the halo where there is significant baryonic mass content: the term $\log(M^{0.01}_{hydro}/M^{0.01}_{DMO})$ is therefore directly replaceable with our ϵ_{halo} term. This correlation is used as a direct comparison for the data in this chapter. The calculated dark matter halo contraction parameters vs. galaxy half light radius for both the SDSS and the SDSS+HI samples are shown in Fig. 6.13. The dashed line defined by Eq. 6.23 is also shown for reference. The majority of the galaxies lie to the right of $R_{1/2}/R_{200} = 2$, which is where the efficiently star-forming NIHAO disc galaxies lie, which is expected given that we consider star-forming spiral galaxies in this thesis (this was shown in section 4.2.4). Here, an interesting result emerges – galaxies which have physical α values ($\alpha > -1$) require dark matter haloes very similar to the ones which

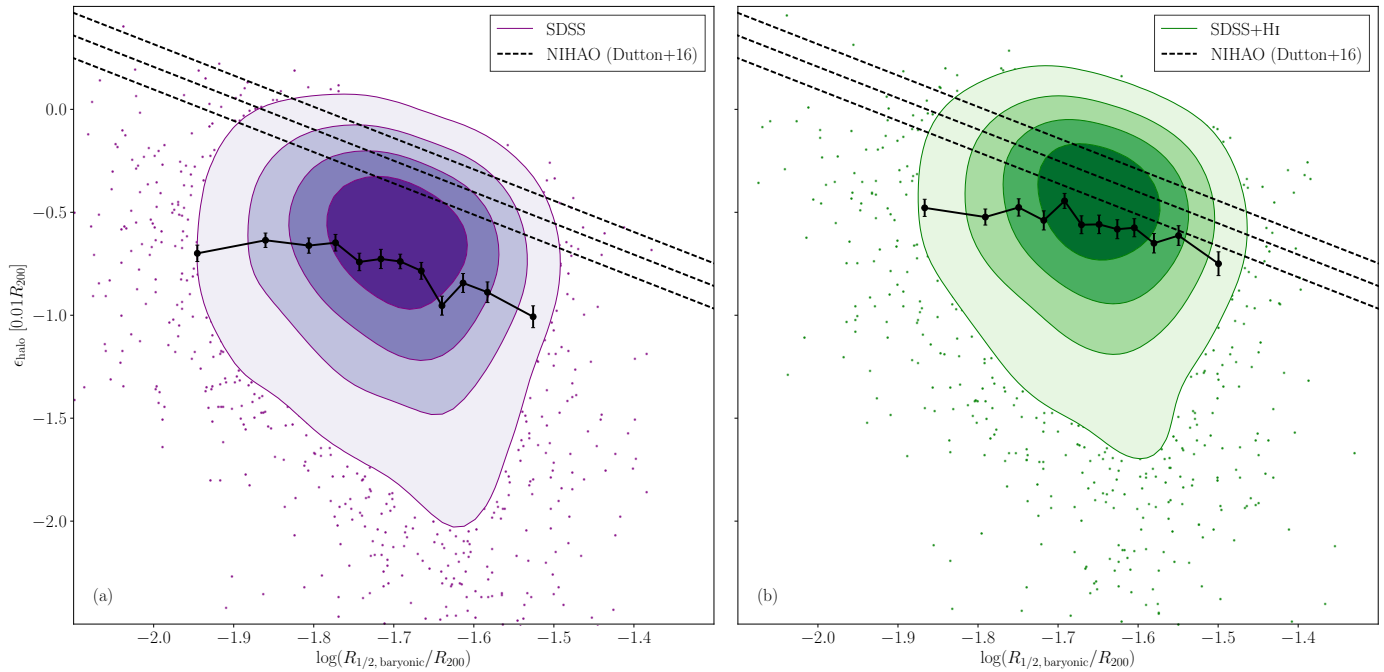

Figure 6.13: Mass of the halo calculated from the swing amplification model divided by the mass of a cuspy Hernquist dark matter halo inside $0.01R_{200}$. (a) shows the SDSS sample and (b) shows the SDSS+HI samples. The contours enclose 20, 40, 60 and 80 per cent of the data points in each panel. Galaxies with physical ($\alpha > -1$) haloes lie in the region where one would expect to observe them if their spiral arms are swing amplified modes. The dashed lines show the prediction for the halo expansion/contraction from NIHAO (Dutton *et al.*, 2016). The solid black lines show the median line and the error bars indicate one standard error on the median.

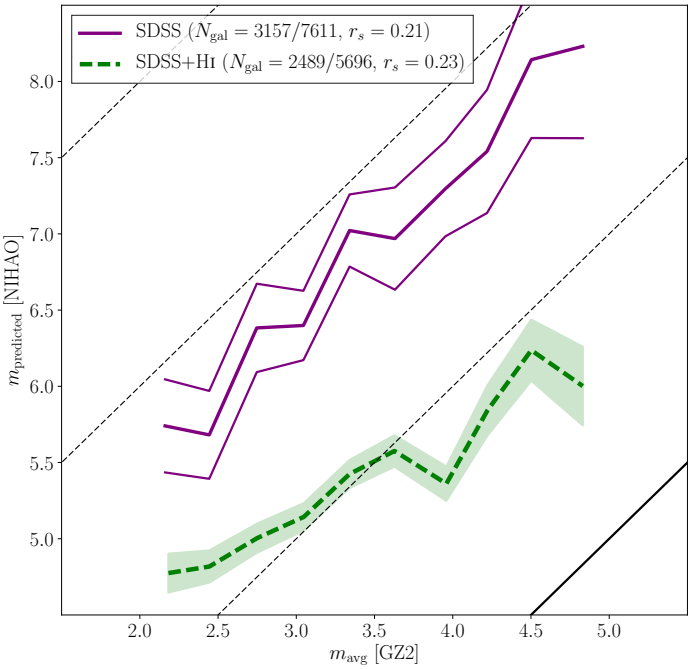

Figure 6.14: Observed spiral arm number from GZ2 ($m_{\rm avg}$) vs. predicted spiral arm number for the SDSS and SDSS+HI samples with haloes contracted or extended according to Eq. 6.23. The thick black line indicates the expected one-to-one correlation, and the dashed black lines show the same correlation offset by two spiral arms. Using this prescription for the dark matter halo, a key prediction from swing amplification emerges, suggesting that a fraction of the galaxies with realistic α values are swing amplified.

the Dutton *et al.* (2016) simulations predict. The inclusion of a gas component also appears to bring the overall distributions closer to where one would expect the spiral galaxy sample in this chapter to lie. There also appears to be a negative correlation between halo expansion and baryonic-to-halo size in both cases, as indicated by the solid black line in each panel, in agreement with the NIHAO simulation.

Given that these galaxies lie so close to the line defined by the NIHAO simulation, I test whether this relationship between galaxy size and flattened profile can produce arm numbers that one would expect if swing amplification was responsible for spiral arms. For all of the galaxies with physical α values, I contract or expand the haloes to match the prescription of Eq. 6.23. From these haloes, I again calculate the expected spiral arm number for the SDSS and the SDSS+HI samples. The plot comparing predicted vs. observed spiral arm number is shown in Fig. 6.14. From the resulting plot, we see a remarkable correlation: galaxies where one would expect to see more spiral arms do indeed have more arms. If the model were to work perfectly, then these galaxies would lie on the one-to-one line shown by the solid black line of Fig. 6.14. Instead, the SDSS sample lies ≈ 3 spiral arm numbers too high, but with a strong correlation of $r_s = 0.21$. If we include the HI component in the disc, the model predicts spiral arm numbers more accurately, with the systematic offset reduced to ≈ 2 spiral arms, with a similar strength of correlation with $r_s = 0.23$. The swing amplified model can predict a key observable, albeit with a systematic offset. The source or sources of this offset are discussed in more detail in section 6.5.

6.5 Discussion

By drawing on a number of observational measurements and models for dark matter halo, I have investigated whether predictions of swing amplification theory can predict morphological characteristics of spiral arms in galaxies. Neither universal cusped or cored haloes can predict the spiral arm numbers or pitch angles in galaxies accurately. However, by invoking a halo which is contracted or expanded by an amount dependent on the relative size of its baryonic content, there is a population of galaxies for which the predicted spiral arm numbers correlate strongly with those observed.

6.5.1 Can the model produce realistic spiral arms?

In the local Universe, the varieties of spiral structure and their relative fractions are well constrained. The majority of spirals tend to have grand design arms – both IR and optical studies show that ~ 60 per cent of unbarred, low-redshift spirals with stellar mass $\log(\mathrm{M}_*) \gtrsim 10\log(\mathrm{M}_\odot)$ have two-arm or grand design spiral structure (Elmegreen & Elmegreen, 1982; Grosbøl, Patsis & Pompei, 2004). In section 6.4.1, I demonstrated a familiar problem with the simulations of swing amplified spiral galaxies. These models produced galaxies with too many spiral arms, with median arm number of ~ 10 spiral arms for the SDSS sample. The inclusion of the HI component to add to the galaxy disc mass does improve the situation somewhat, reducing the median spiral arm number to ~ 6. This picture is still unsatisfactory in terms of describing the spiral arms in our galaxy sample. Although an extra gas component can reduce the spiral arm number, it still cannot reproduce the dominant two-arm spiral population we expect to see. The other complicating factor is the role that gas plays in the disc. The swing amplified quantities described in this chapter are based on N-body simulations – the discs consist of many stellar particles, and their self-gravity form spiral arms in galaxies. The role that a gas component will play is not fully understood. The inclusion of a gas component can help to stabilise the two-arm mode (Bournaud & Combes, 2002) and make swing amplification more efficient (Jog, 1992, 1993). Gas has also been suggested as a requirement to cool the stellar system in order for it to be unstable to arm formation (Sellwood, 1985).

In order to produce a modal galaxy population which produces a reasonable number of unbarred two-arm modes, we require that the dark matter halo potential in the inner regions is significantly reduced. In section 6.4.1 I showed that the swing amplification mechanism can produce a spiral population with more prominent lower order modes if the dark matter halo is cored to the extent that it is flat within a_h. Both the SDSS and SDSS+HI models produce spiral arms representative of those at low-redshift. This does, however, produce its own complications. Of greatest concern is how stable such low-order modes are. Currently, N-body simulations cannot produce long-lived $m = 2$ spirals without quickly forming a central bar (Sellwood, 2011). Additionally, these modes do not predict a correlation between predicted and observed spiral arm numbers. Rather, the dominant mode is usually driven down to ~ 2 in almost all spiral galaxies: a cored dark matter halo cannot predict the range of spiral arm numbers observed in low-redshift galaxies.

In order to reproduce realistic spiral arms, I have found that a halo with some level of interpolation between a cored and cusped dark matter halo is required. In order for the model to match the observations, most galaxies need some level of halo ex-

pansion. Such a result should not be surprising, however – recent work suggests that low-redshift disc galaxies require strongly cored inner profiles in order to fit rotation curves (Cole & Binney, 2017; Katz *et al.*, 2017).

Examining these required halo masses leads one to the conclusion that there are two distinct populations of galaxies. Of all of the galaxies, only ~ 40 per cent of galaxies can be modelled by swing amplification with any kind of dark matter halo. Remarkably, these galaxies show a strong correlation between the spiral arm numbers expected and those observed. This leads us to conclude that swing amplification does play a dominant role in generating spiral structure in around half of unbarred disc galaxies. The secondary population is discussed in more detail in section 6.5.1.3.

Although a correlation does exist, it is offset from the one-to-one line that one would expect, overestimating the number of spiral arms by approximately three. This may be due to how mass is assigned to the bulge and disc. I used photometric decompositions of Simard *et al.* (2011) and Mendel *et al.* (2014) to assign mass to the bulge and the disc. Such a model fits a classical bulge with $n = 4$ and an exponential disc. This may cause a systematic for two reasons. Firstly, the photometric decomposition of galaxies may introduce a bias due to image resolution effects. The second issue is pseudo vs. classical bulge argument – the model we use assumes an inner classical spherical bulge; bulges instead may be pseudo bulges, which may not have a spherical shape, and profile well-described by a spherical Hernquist profile. Studying bulges and discs in detail is beyond the scope of this thesis. Another possibility is that the assumption that spiral arms are measured at $2R_{\rm d}$ may not be valid – if spiral arms were instead measured closer to the inner regions of galaxies, then this offset is negated. Unfortunately, the binary nature of visual morphological classifications, where arms either are or are not recorded, prevents further investigation of this point. Finally, there may be some spiral arms which are impossible to observe with visual morphology in the way presented in this chapter. Of particular note is the case where the model predicts very high spiral arm numbers. In this case, the spiral arms may instead be wakelets which are difficult to observe visually; our observed arm number measurements may therefore be systematically low for these galaxies. Investigating which caveat, or which combination of caveats is responsible requires higher resolution imaging of galaxies than those used in this chapter. Any study of this nature would be severely restricted in terms of sample size and completeness compared to the results I present here.

Another potential source of systematic uncertainty is the model we use to contract or expand the dark matter halo. I used a recently-published prediction from a full-hydrodynamical code in NIHAO (Wang *et al.*, 2015) to compare our model to predictions. However, there are a number of parameters that go into such a model – the expansion of dark matter cores is usually driven by gas outflows caused by feedback from stars and supernovae (Read & Gilmore, 2005; Governato *et al.*, 2010; Pontzen & Governato, 2012; Chan *et al.*, 2015). Small adjustments to the strength of this feedback would theoretically cause haloes to expand more if the other properties of galaxies were kept the same. However, testing these effects is not the purpose of this chapter, or this thesis.

6.5.1.1 A note on disc maximality

In a number of simulations, it has been shown that the spiral arm number has a dependence on the disc fraction within 2.2 disc scale radii, $2.2R_{\rm d}$, which takes the

functional form $m \propto f_{\rm d}^{-1}$ (Carlberg & Freedman, 1985; Bottema, 2003; Fujii *et al.*, 2011; D'Onghia, Vogelsberger & Hernquist, 2013). We therefore expect galaxies with greater disc fractions to have fewer spiral arms.

Maximal discs are usually defined as discs with $f_{\rm d}(2.2R_{\rm d}) > 0.7$. Disc maximality has been a subject of much debate, and often depends on the technique one uses to measure it (Bosma, 2017). Recent work based on velocity dispersion measurements of disc galaxies suggests that discs may be sub-maximal (Bottema, 1993; Kregel, van der Kruit & Freeman, 2005; Bershady *et al.*, 2011). A recent study that should be directly comparable to our work is that of Martinsson *et al.* (2013), where a set of low-redshift spiral galaxies were decomposed into bulge and disc components, meaning the disc contribution was directly measured with little or no bulge contamination. This study also found discs to be sub-maximal, with $f_{\rm d}(2.2R_{\rm d}) = 0.31 \pm 0.07$. However, other recent studies instead suggest that discs may indeed be more maximal than these kinematic studies would suggest. Velocity dispersion-based techniques rely on estimates of both the velocity dispersion and the disc scale height, which are often probed by different stellar populations (Bosma, 1999; Aniyan *et al.*, 2016; Bosma, 2017; Aniyan *et al.*, 2018). Aniyan *et al.* (2016) demonstrated that accounting for these systematic differences leads one to conclude that the Milky Way's disc is maximal, in agreement with measurements of the Milky Way's rotation curve from Bovy & Rix (2013).

Athanassoula, Bosma & Papaioannou (1987) showed that for swing amplified spiral arms to exist in a sample of nearby spirals, maximal discs are required to match the observed spiral arm numbers. We can see from Fig. 6.3 that cored inner profiles mean that discs are close to maximal in nature, particularly if one considers the HI component in the SDSS galaxies. The work presented in this chapter supports this idea that spiral arms can be maintained via a swing amplified mechanism, if the inner profiles of galaxies are cored to the extent of, or perhaps even more so than, the relation given by the NIHAO prediction of Dutton *et al.* (2016). If we assume that all of the galaxies which have realistic dark matter haloes described in section 6.4.5 exist via the swing amplified mechanism, then we obtain $f_{\rm d} = 0.48^{+0.11}_{-0.17}$ ($0.54^{+0.11}_{-0.15}$ with the inclusion of HI; the value quoted is the median, and the bounds indicate the 16th and 84th percentiles). The predictions using the NIHAO simulations, which generally give too many spiral arms, give $f_{\rm d} = 0.21^{+0.11}_{-0.19}$ ($0.25^{+0.19}_{-0.08}$). In order for our spirals to be swing amplified modes, our discs must be more maximal than the sub-maximal values measured in Martinsson *et al.* (2013).

6.5.1.2 A note on halo scaling relations

In this chapter, the dark matter component in galaxies cannot be directly measured. Instead, we relied on halo scaling relations published in Dutton *et al.* (2010) and Dutton & Macciò (2014). Dark matter halo scaling relations generally have large scatter, generally up to half an order of magnitude (e.g. Macciò *et al.* 2007; Dutton *et al.* 2010; Somerville *et al.* 2018). One may therefore find it surprising that we find any correlation between the expected and observed spiral numbers – such a large scatter may blur out any relationship. A clue to why this is the case can be found in Fig. 6.4. Here we see that the introduction of the cored Burkert profile has two significant effects on the expected spiral arm number. Firstly, it reduces the number of arms we expect. The other effect is observed in the relative errors – the sizes of the relative errors are significantly reduced for the cored profile. The reason for this is due to the relative

contributions of the disc, bulge and dark matter halo to the spiral arm number. The halo term in Eq. 6.9 is the term which has the greatest uncertainty, due to the fact that it is not a function of observable quantities. The halo term makes a smaller contribution to $m_{\rm predicted}$ when we invoke a cusped profile; it therefore adds less uncertainty to the total $m_{\rm predicted}$ value. In order to match the spiral arm numbers, we require a close to cored profile, meaning we have a relatively low uncertainty in $m_{\rm predicted}$. Thus the correlation in Fig. 6.14 still emerges.

6.5.1.3 A bimodality in the galaxy population

Given the evidence listed above, most spiral galaxies may not exist as swing amplified modes. Approximately 60 per cent of the galaxies in the sample do not fit the expected characteristics from swing amplification theory. I demonstrated that this subpopulation cannot exist with the model we use in this chapter – even if there is no massive dark matter component, the spiral arm numbers predicted are still greater than those observed. A likely scenario is that spiral arms can be triggered and exist via a multitude of mechanisms, and that the model presented in this chapter is only applicable to a select sample of galaxies.

One mechanism that can generate spiral structure is the presence of bars. However, in this chapter, I explicitly control for this by removing any galaxies with even weak bars in the various samples using visual galaxy classifications. However, I cannot rule out the other often quoted mechanisms for driving spiral arms: density wave theory and tidal interactions. Quasi-stationary density wave theory (Lin & Shu, 1964) is a mechanism via which two-arm spiral patterns can emerge, while simulations also predict that galaxy-galaxy interactions can effectively trigger the formation of two-arm patterns. A second population of spiral galaxies completely separate from the swing amplified spirals also goes a long way to explain the results of many of the simulations to date. As yet, simulations which predict long-lived, stable two-arm patterns are rare (Dobbs & Baba, 2014). As discussed in section 1.3.6, Roškar *et al.* (2012) demonstrated that discs can exist with long-lived $m = 2$ modes. However, an efficient cooling mechanism is required to sustain such a structure. That two-arm spirals form a secondary population triggered in another way would suggest that the models are correct in that they do not predict two-arm patterns, and that inclusion of other physical parameters will not affect this result in future simulations.

6.5.2 Arm number and pitch angle as tracers of swing amplification

We have the option to test the modal mechanisms of spiral structure using either pitch angle, arm number or a combination of both. I note that I expect our measured spiral arm numbers to be more certain than the measures of spiral arm pitch angle, given that they require an accurate measurement on each individual galaxy compared to simply counting arms. I therefore suggest that the spiral arm number is the best technique for testing and calibrating any models of spiral galaxies. The different effectivenesses of pitch angle and arm number as tracers of swing amplification appears to be due to what they probe in the model. From Eq. 6.9, we see that spiral arm number is a result of the relative sizes and masses of the components that make up galaxies. However, pitch

angle probes something altogether more subtle. The shear in galaxy discs probes the gradients of the mass distribution inside galaxies. With the models employed in this chapter, all galaxies tend to have flat rotation curves, consistent with observations of the overall galaxy population. Without direct measurements of the galaxy dynamics from accurate galaxy rotation curve data, one cannot model the subtle differences that lead to large variations in pitch angles.

The spiral arm pitch angle distributions of our spiral galaxy populations were compared in section 6.4.2. The galaxy model I use leads to the majority of spirals having arms centred around $\psi = 24°$. As was the case for the spiral arm number, the pitch angle is a quantity that we can constrain from observations of local galaxies. I used two complementary datasets to test how well the swing amplified predictions match the observations of local spirals. The S^{4}G sample was measured directly from NIR imaging by hand by professional astronomers; the SDSS pitch angles were instead measured automatically, a method I tested the reliability of in chapter 5. We see that both samples give distributions centred on $\sim 19°$ with spiral arms ranging from $5 - 40°$. These are both similar to the pitch angle distributions measured in other samples, indicating that these pitch angle distributions seem to be characteristic of the total galaxy population (Seigar & James, 1998b; Block & Puerari, 1999; Seigar, 2005; Seigar *et al.*, 2008). We see that neither dark matter halo can produce the correct distribution of spiral arm pitch angles: the distributions are too loose. I interpret this as evidence that spiral arm pitch angle depends on a number of different properties, rather than simply the underlying mass distribution in a swing amplification regime. The fact that the spiral arms are tighter than those predicted is also of interest, given the predictions for how spiral arms should evolve over time. Generally, spiral arms produced in a swing amplified N-body regime will tighten as the galaxy rotates (Pérez-Villegas *et al.*, 2012; Grand, Kawata & Cropper, 2013). It could potentially be the case that new spiral arms will form at $\psi = 24°$, and age to produce the tighter distribution we observe in our galaxies. For our sample, a scatter introduced by this effect resolves the differences between the distributions of observed and predicted spiral arm numbers. Accurately estimating the age of a spiral arm would, however, be very challenging. Given the above caveats, spiral arm number was a much better method for testing the predictions of swing amplification, and was thus employed for the rest of this chapter; I advise that it is the better tool for any further studies of this kind.

Chapter 7

Conclusions and future work

7.1 Conclusions

7.1.1 Measuring morphology

In this thesis, I have presented the results of a comprehensive study of spiral galaxies in the local Universe, with samples obtained from the SDSS survey. Galaxy surveys provide a challenge if we wish to study how various properties of galaxies vary with respect to their visual morphology. To this end, we developed new techniques to measure the visual morphologies in galaxies that could be applied to the large samples from SDSS, and potentially to future upcoming surveys.

To measure the first fundamental property to describe spiral galaxies, the spiral arm number, we relied upon the citizen science classifications of Galaxy Zoo 2 (GZ2). Members of the public were asked a series of simple questions to determine whether particular morphological features are present in galaxies. The work done to collect and reduce the GZ2 data was completed prior to the work in this thesis. This was described in W13, and also included an attempt to remove the redshift-dependent classification bias in galaxies. The redshift-dependent bias described in this thesis is not caused by any evolution in the galaxy population – we only focus on low-redshift galaxies, where evolution is expected to be minimal. It is instead an inherent property that affects *any* measurement of visual morphology. Simply, galaxies viewed from further away are more poorly resolved, meaning that their more detailed features are harder to discern. The previous method to adjust the morphological vote fractions described in W13 does an adequate job at first inspection, with the fractions of galaxies classified as spiral or elliptical being constant between $z = 0$ and $z = 0.25$. However, the vote fractions were not consistent for the questions further down the GZ2 question tree. The questions of most concern to us were the spiral arm number and the spiral arm tightness, examples of questions where the old debiasing method was not working. We therefore developed a completely new technique that ensured that the vote fraction distributions matched as closely as possible at all redshifts, meaning that the many-arm subsamples were more complete, and the two-arm sample was uncontaminated. The removal of these two issues was imperative to the science described in the later chapters.

We also developed a method to measure the spiral arm pitch angle in galaxies. We again relied on a method already published, called SPARCFIRE. Again, SPARCFIRE was developed prior to the work undertaken in this thesis – this was described in detail

in Davis & Hayes (2014). The principal issue here was instead that SPARCFIRE detects a number of objects in images: some are real spiral arm features, and others are not. One must discern the real spiral arms from the false detections in order to measure pitch angles accurately. In order to do this, we combined SPARCFIRE's raw outputs with human-verification and trained a support vector machine to identify the real spiral arms. Using this technique, we achieve a completeness of 75 per cent of real arcs being identified by SPARCFIRE. It also allowed for the independent measurement of pitch angles using the GZ2 vote fractions via a simple calibration.

7.1.2 Demographics with respect to spiral arm number

The distributions of environment, stellar mass and colour were compared for spiral galaxies with different numbers of arms. We found a very weak trend that the most massive galaxies are slightly more likely to have more spiral arms. As discussed in chapter 6, this is expected for swing amplified arms in the absence of bars or tidal interactions. However, the trend is very weak, and may be easily explained as a size-dependent bias in our classifications. An enhancement in the fraction of two-armed spiral galaxies was observed in the highest density environments – approximately 60 per cent of spirals in low density environments have two spiral arms, and this fraction increases to approximately 75 per cent in the highest density environments. This result was interpreted as an indication that galaxy-galaxy interactions could play a role in inducing two-armed spiral structure.

By comparing optical colours, we found that two-armed spirals are much redder in colour than their many-arm counterparts. Although the $u - r$ colour is broadly consistent with respect to arm number, the $r - z$ colours are distinctly redder in the two-armed galaxy population. In principle this could be due to two reasons. Firstly, the recent SFHs could be significantly different. Otherwise, the level of dust obscuration must be significantly higher in two-arm spirals. However, the locations of the majority of the many-arm sample in Fig. 4.7 show that a simple dust sheet model is insufficient to explain the differences. If the first reason is the cause of the significant colour distinction with respect to spiral arm number, then a recent, rapidly quenched burst of star formation ($\tau \lesssim 0.1$ Gyr) is implied in many-arm galaxies, whereas star formation must persist over much longer timescales in two-arm galaxies. To further investigate which of the above is responsible for the observed differences total SFRs were compared by combining measures of unobscured star formation from UV emission and obscured star formation from the MIR from GALEX and WISE. Many-armed spiral galaxies are less likely to have very low sSFRs and thus be undetected in the UV or MIR. However, for galaxies with reliable UV and MIR detections, sSFR has no significant dependence on spiral arm number. Despite this, we found that spirals with different numbers of arms do have different levels of dust obscuration, with many-armed spirals having more UV emission from young stars unobscured by dust. This was most evident when comparing the IRX-β relation, where IRX measures the relative fraction of MIR to UV emission, and β is the UV slope. Many-armed spirals have significantly lower IRX for a given β.

There are three possible scenarios for the variation in the IRX-β relation. Firstly, the differences could be due to the relative distribution of star-forming regions in galaxies with different spiral structure. In grand design spirals, the molecular clouds may be

more concentrated in the dense arm regions. The consequent increase in dust obscuration may lead to a reduction in UV emission compared to that in the MIR. Secondly, molecular cloud properties, e.g. mass and size distributions, may differ in discs hosting two or more spiral arms. In this case, in addition to geometrical effects, molecular clouds may take longer to disperse in two-armed galaxies. The UV emitting population would thus emerge over a longer timescale, leading to an enhanced IRX. Interestingly, simulations predict that the presence of strong density waves should lead to both two-arm structures and larger molecular clouds within the spiral arms (Dobbs, Burkert & Pringle, 2011; Dobbs, Pringle & Burkert, 2012). Thirdly, our results also appear consistent with many-armed spirals having recently experienced a rapid decline in star formation rate, with little influence from the molecular cloud properties. This would mean that very little of the star formation in many-arm galaxies is associated with the dusty birth clouds, and that all of the star formation is instead detected in the UV.

Two-armed spirals are more gas deficient than many-armed spirals which, given their similar SFRs, means that two-arm spirals are more efficient at converting gas to stars. Two-armed spirals are also more likely to host bars, with ~ 50 per cent having strong bars compared to only ~ 20 per cent of many-armed galaxies. However, we showed that bars only serve to move galaxies along the normal IRX-β relation: strongly barred galaxies have higher levels of MIR emission as well as steeper UV slopes. Spiral arm number, on the other hand, has a significant effect on how far spirals are offset perpendicular to the normal IRX-β relation.

7.1.3 Demographics with respect to spiral arm pitch angle

In the absence of bars, the arm pitch angles in many-arm spiral galaxies are on average larger than those in grand design, two-arm spirals by $\sim 2°$. We suggested a number of possible reasons for these results, including the ideas that multi-arm patterns may be short-lived or that the mechanisms that cause galaxies to have different arm numbers also influence the spiral arm pitch angles. We also found evidence that spiral arms are looser when strong bars are present in galaxies, this time by up to $\sim 6°$. This can be interpreted as evidence for bars influencing the dynamics of galaxies, such as in invariant manifold theory, or as evidence that barred galaxies are potentially triggered by interactions. We showed that many-arm structures are more prevalent in galaxies with less dominant bulges and that pitch angles are looser when the bulge is more dominant. These results imply that the shear rates in discs are not the dominant reason for variations in spiral arm pitch angle. We do, however, note that the dark matter halo also plays a significant role in shear, which was not accounted for in chapter 5; it could be the case that differences in the dark matter haloes have the dominant effect on pitch angle in galaxies.

Finally, we saw weak trends that galaxies with more MIR star formation have looser spiral arms, an effect that could be related to shear or galaxy-galaxy interactions, given that interactions can both trigger star formation with significant MIR emission, and lead to loose tidal bridges and tails.

Given that spiral arms are fundamental features seen in significant numbers of low-redshift galaxies, the results of the studies of pitch angle presented in this thesis show that their origins are still not well-understood. Given that bar and disc properties seem to be as important as central mass concentrations in influencing the pitch angles of

spiral galaxies, there are a multitude of complex mechanisms at play in galaxies that affect the pitch angles of spiral arms.

7.1.4 Testing swing amplification theory

The final, and perhaps most fundamental result presented in this thesis was the test of the predictions of swing amplification theory. Both spiral arm number and pitch angle are predicted by analytical theory of a three component system – a disc, a bulge, and a dark matter halo. Measurements of galaxy bulge+disc sizes and masses were available from two-component fits, and dark matter halo masses and sizes were obtainable from literature-derived scaling relations. Using these three components, the spiral arm numbers and pitch angles in galaxies were predicted. Using a universally cored or cusped dark matter halo does not reproduce the the observed spiral arm numbers in galaxies – the cusped NFW-like profile produced galaxies with many spiral arms, and a cored inner profile predicted that almost all galaxies should have ≈ 2 spiral arms, which are often predicted to be unstable to bar formation unless cooling occurs via the process of star-formation.

In order to make the model work, we considered the role of the dark matter halo in more detail. By including a dark matter profile with some level of expansion, as predicted by simulations due to feedback from star formation, a significant agreement emerges – approximately half of galaxies have spiral arms consistent with the model we employed in chapter 6. These display a significant correlation between predicted and observed spiral arm number. The rest of the unbarred spiral population is unlikely to be dominated by swing amplified arms.

7.1.5 Towards a complete understanding of spiral galaxies

Studies of the galaxy stellar mass function (GSMF) show that galaxies can display a multitude of morphologies. According to Kelvin *et al.* (2014a), the low mass end ($\mathrm{M}_* \lesssim 10^{9.5}\mathrm{M}_\odot$) of the GSMF is dominated by discy, irregular objects with irregular, Sd/Irr Hubble types. The massive end of the GSMF ($\mathrm{M}_* \gtrsim 10^{11}\mathrm{M}_\odot$) is dominated by early-type spheroid dominated morphologies. The majority of massive, luminous galaxies at low redshift exhibit disc like structure: ≈ 70 per cent of galaxies at $10^{9.5}\mathrm{M}_\odot \lesssim \mathrm{M}_* \lesssim 10^{11}\mathrm{M}_\odot$ have discy Hubble morphologies between S0-Sc. Further, Galaxy Zoo shows that the majority of discs have visible spiral arms when viewed face-on (W13). These galaxies make up the majority of star-forming galaxies at low-redshift, with star formation particularly associated with the spiral arms themselves (Dobbs & Baba, 2014).

Since the work presented in Elmegreen & Elmegreen (1982), there has been a distinct possibility that there may be a strong bimodality on the spiral galaxy population. Approximately 60 per cent of low-redshift spirals display two strong grand design spiral arms (Elmegreen & Elmegreen, 1982; Grosbøl, Patsis & Pompei, 2004). They are often found in high density environments and accompanied by the presence of bars in the centres of their discs. Given the work described in this thesis, a firm conclusion on their origin is yet to be confirmed. However, that a significant fraction of the grand design spiral population are caused by density waves is certainly possible given the results we showed in section 4.2. That density waves do not trigger star formation is one

constraint that we show in accordance with previous theory that arms cannot convert diffuse gas into stars any more effectively than inter-arm regions. Rather, the total SFR in grand design discs can be considered saturated (Vogel, Kulkarni & Scoville, 1988; Elmegreen, 2002). However, we do find some strong hints that density waves may indeed be present, the most notable of which being the significant enhancement in the level of dust obscuration in grand design spirals. Spiral arms are regions of enhanced gas density, and thus star formation density, but the efficiency in which gas is converted to stars is no different in the arm vs. inter-arm regions. Although spiral arms are generally regions of enhanced density, strong density waves are potentially the only mechanism strong enough to cause a significant change in the total disc GMC population. It is encouraging that the result we see is as expected from simulations, that the UV-emitting population takes some time to leave the molecular clouds if strong density waves are present. The concentration of material into arms appears to produce more massive individual molecular clouds (Dobbs, Burkert & Pringle, 2011; Colombo *et al.*, 2014). These are, in turn, capable of forming massive stars in greater numbers than would be possible for a given gas mass distributed in smaller clouds (Kroupa, 2001). These massive stars dominate local star formation feedback, both positive and negative. Furthermore, the higher SFR in arms allows star formation outflows to more effectively expel gas and result in feedback on a larger scale (Hopkins, Quataert & Murray, 2011; Hopkins *et al.*, 2014). This means that spiral arms have a significant role in the regulation of star formation.

In chapter 4, we also demonstrated the classic result that grand design spirals are more common in higher density environments. This suggests that a fraction of the grand design population form via tidal interactions. However, making a stronger statement than this was not possible, given that we did not explore galaxy environment any further. In section 7.2.2, I discuss possibilities for constraining whether grand design spirals form via tidal interactions.

The remaining 40 per cent of the spiral population is composed of many-arm spirals. Their origin has long been hinted at in simulations, where many-arm spirals form simply due to self-gravity processes in the disc (Sellwood & Carlberg, 1984; Sellwood, 1985). In chapter 6, we showed that the arm morphologies displayed by this population are consistent with the predictions of swing amplification theory. Given the number of input parameters into the model we use in chapter 6, and the relative uncertainties on all of the variables, we interpret such a strong correlation between predicted and observed spiral arm number as primary evidence for spiral arms forming due to the growth of swing amplified, locally unstable regions. We found that the number of arms displayed by spiral galaxies is sensitive to the relative density of the disc, bulge and dark matter halo. This is the first study of its kind to observationally confirm this effect.

It has been fifty years since the density wave theory was proposed (Lindblad, 1963; Lin & Shu, 1964) as the principal reason for the appearance of spiral arms in galaxies and thirty years since spiral arms have been formed in simulations (Sellwood & Carlberg, 1984). In this thesis, we provide some strong constraints on the origin of the many-arm population, and also some early evidence that the grand design population has its origin in density waves or tidal interactions. With the work presented here, we are a significant step closer to formulating the elusive complete picture of spiral arm formation. Fully constraining the origin of the grand design spiral population will be the next significant step in our goal towards a complete understanding of spiral arms

across the galaxy population.

7.2 Future work

7.2.1 The future of galaxy morphology

The immediate future for galaxy morphology is to apply the techniques utilised in chapter 3 to other datasets to be processed by Galaxy Zoo. An ongoing survey is Galaxy Zoo-GAMA, which classifies galaxies using the same tree structure as in GZ2, this time using galaxies taken from the GAMA survey (Driver *et al.*, 2011), with optical imaging provided by KiDS (de Jong *et al.*, 2015; Kuijken *et al.*, 2015). Although GAMA does not have the sky coverage of SDSS, it has a fainter limiting magnitude of $m_r < 19.8$, of order 2–3 magnitudes deeper. The required classifications have now been collected, and initial exploration of this dataset has now commenced. The debiasing procedure we developed in section 3.2.4 will be used on these data, and the code is now freely available for application by the Galaxy Zoo team. Galaxy Zoo will continue to add new datasets for classification, which are usually deeper than the SDSS imaging we used in GZ2. These include DECaLS, providing deeper images of the Northern Sloan regions, and DES providing deep imaging of the Southern hemisphere. Imaging depth could be critical to the next science results from Galaxy Zoo, as the morphologies of the faintest galaxies will be quantified, and greater depth will allow for investigation of the influence of galaxy interactions with faint companions. As is the case with all visual morphologies, quantifying morphologies with Galaxy Zoo will require some level of correction for redshift-dependent classification bias, which can be provided for all future datasets by the methods described in this thesis.

Galaxy Zoo is not the only technique that can be used to measure visual morphology in galaxy surveys. We are now entering a new era where machine-based morphology estimates are starting to be honed. Classically, one would measure morphology by a number of parameters measured directly on the input image of a galaxy. There are some cases where these techniques work well – asymmetry has often been shown to be good indicator that galaxies are merging systems at higher redshift (Conselice, 2003; Pawlik *et al.*, 2016), and Sérsic profiles have long been used to differentiate early and late-type elliptical and discy morphologies (de Vaucouleurs, 1948; Kormendy, 1977; Kennedy *et al.*, 2015). However, the formulation of a complete picture of galaxy morphology from purely machine-based measurement, including the presence of spiral arms and bars, requires more complex modelling of galaxies. Using modern machine learning algorithms to help with this task looks promising; deep learning implemented with convolutional neural networks is improving all of the time, and now claim to reproduce visual morphologies with high accuracy, albeit in the most certain test cases (Dieleman, Willett & Dambre, 2015; Domínguez Sánchez *et al.*, 2017). However, any supervised machine learning algorithm is only as good as its training dataset, meaning further exploration of new galaxy surveys with Galaxy Zoo will always have a place.

7.2.2 The future outlook for spiral structure

Given the work presented in this thesis, we can now begin to make some firm conclusions about the spiral galaxy population. There are several competing theories to

explain the origin of spiral arms, and they were outlined in some detail in chapter 1. From our results, our understanding of spiral arms is as follows. Approximately half of spiral galaxies in the Universe have spiral arms as predicted by swing amplification theory, introduced in section 1.3.2. These galaxies are usually many-arm structures ($m > 2$). The rest of the population must form in another way. In chapter 1, we introduced the two leading theories for their origin – tidally induced spiral arms and quasi-stationary density waves. Confirming whether these mechanisms are responsible for this remaining spiral galaxy population will be the next stage in our understanding of spiral structure.

The link between tidal interactions and spiral arms has long been established, since the earliest studies showed that grand design structure is more prevalent in the highest density environments (Elmegreen & Elmegreen, 1982, 1983). Observational evidence that interactions do trigger long-lived spiral patterns has yet to be confirmed. This is particularly true for studies of spiral arm strength, where there has been no conclusive evidence that strong spiral arms are triggered by interactions with companions and weaken over time (Seigar & James, 2002; Kendall, Clarke & Kennicutt, 2015). The most tantalising glimpse of interaction driven spirals was provided by Elmegreen & Elmegreen (1983), where it was demonstrated from arguments of grand design fractions as a function of group crossing time that interactions could trigger spiral arms. Providing a more up-to-date study of this effect would be the key step in constraining whether spiral galaxies can indeed be tidally triggered, what fraction of spiral galaxies are tidally triggered, and how long such structures persist after interaction.

To get a true constraint on whether or not tidal interactions are responsible for spiral structure, and how many spirals are actually formed in this way, requires one to disentangle the various environmental processes in galaxies. Major mergers are likely to disrupt a galaxy's morphology in a way that removes any type of spiral structure; spiral arms are instead more likely due to fleeting interactions between galaxies, or mergers with much less massive counterparts, with M51 being the classic example. Looking for signatures of these subtle interactions requires a level of detail beyond the Σ parameter we use in this thesis. Of particular note is the recent technique described in Patton *et al.* (2016), using the large scale statistics of surveys to disentangle the different roles of environment. They demonstrated a new method for determining and controlling for the various effects of galaxy environment in SDSS data. They used two measures of environment: N_2, the number of galaxies within 2 Mpc, and r_2, the projected distance to the nearest neighbour galaxy as two distinct measures of morphology. N_2 measures the overall nearby density, similarly to the $\Sigma_{4,5}$ statistic used in chapter 4. r_2 directly probes the influence of the interaction with the closest companion. The study showed that due to the large number statistics that the SDSS provides, one can directly control for the overall local density effect and truly measure the influence of interactions alone. This can be done by comparing galaxies directly with other galaxies which reside in the same or similar local densities (N_2) and looking for any signatures that vary with respect to r_2. In this case, one is controlling for the effects of local density. Combining this technique with the wealth of morphological data provided in this thesis is the next logical step in understanding the origin of a further subset of spiral galaxies. The inclusion of future, deeper studies in Galaxy Zoo will also mean that the influence of fainter companions can also be probed in more detail.

This leaves the most commonly cited theory of spiral structure, quasi-stationary density wave theory. Although it is the most well established theory in the literature,

testing whether quasi-stationary density waves exist in low-redshift discs without any triggering by tidal interactions is still challenging. In section 4.2, we showed that grand design spirals have heavily obscured star formation, a result which may be caused by the presence of strong density waves. Understanding whether density waves are indeed responsible for this result requires high resolution photometry or spectroscopy across the face of entire galaxies. With current instruments, it is now possible to measure spectra and more accurately constrain star formation and dust properties inside individual regions of galaxies in large surveys, thanks to surveys such as MaNGA (Bundy *et al.*, 2015) and SAMI (Bryant *et al.*, 2015). This is a task that Galaxy Zoo can already help with – Galaxy Zoo 3D has asked classifiers to measure where the spiral arms are in individual galaxies in MaNGA, allowing for arm vs. inter-arm observations. Even higher resolution, lower redshift instruments will also be able to help. Notably, SDSS-V includes plans for a Local Volume Mapper (Kollmeier *et al.*, 2017), obtaining high resolution spectra across the face of a number of local galaxies. These can help to constrain whether there are any significant signatures of density waves in spiral arms: the most commonly held theory is that an age gradient may exist across spiral arms, if density waves do trigger star formation.

In the spirit of this thesis, studies can now potentially extend to several, or even several thousand galaxies, helping to build large, statistical samples of arms in galaxies. The techniques and tools discussed here can help to explain why and how spiral arms exist across the entire population beyond the often-studied arms of M51.

Bibliography

Aaronson M., 1978. *ApJL*, **221**, L103. *The morphological distribution of bright galaxies in the UVK color plane*.

Abazajian K. N., Adelman-McCarthy J. K., Agüeros M. A., Allam S. S., Allende Prieto C., An D., Anderson K. S. J., Anderson S. F., Annis J., Bahcall N. A., et al., 2009. *ApJS*, **182**, 543. *The Seventh Data Release of the Sloan Digital Sky Survey*.

Abraham R. G., van den Bergh S., Nair P., 2003. *ApJ*, **588**, 218. *A New Approach to Galaxy Morphology. I. Analysis of the Sloan Digital Sky Survey Early Data Release*.

Aniyan S., Freeman K. C., Gerhard O. E., Arnaboldi M., Flynn C., 2016. MNRAS, **456**, 1484. *The influence of a kinematically cold young component on disc-halo decompositions in spiral galaxies: insights from solar neighbourhood K-giants*.

Aniyan S., Freeman K. C., Arnaboldi M., Gerhard O. E., Coccato L., Fabricius M., Kuijken K., Merrifield M., Ponomareva A. A., 2018. MNRAS, **476**, 1909. *Resolving the disc-halo degeneracy - I: a look at NGC 628*.

Ann H. B., 2014. *Journal of Korean Astronomical Society*, **47**, 1. *Environment Dependence of Disk Morphology of Spiral Galaxies*.

Arp H., 1966. *ApJS*, **14**, 1. *Atlas of Peculiar Galaxies*.

Athanassoula E., Bosma A., 1988. *Dynamical Evidence for Dark Matter in Individual Disk Galaxies*, In: *Large Scale Structures of the Universe*, 391, eds Audouze J., Pelletan M.-C., Szalay A., Zel'dovich Y. B., Peebles P. J. E.

Athanassoula E., Bosma A., Papaioannou S., 1987. A&A, **179**, 23. *Halo parameters of spiral galaxies*.

Athanassoula E., Romero-Gómez M., Bosma A., Masdemont J. J., 2009. MNRAS, **400**, 1706. *Rings and spirals in barred galaxies - II. Ring and spiral morphology*.

Athanassoula E., Romero-Gómez M., Bosma A., Masdemont J. J., 2010. *MNRAS*, **407**, 1433. *Rings and spirals in barred galaxies - III. Further comparisons and links to observations*.

Athanassoula E., Romero-Gómez M., Masdemont J. J., 2009. *MNRAS*, **394**, 67. *Rings and spirals in barred galaxies - I. Building blocks*.

Athanassoula E., 1992. *MNRAS*, **259**, 345. *The existence and shapes of dust lanes in galactic bars*.

Athanassoula E., 2012. MNRAS, **426**, L46. *Manifold-driven spirals in N-body barred galaxy simulations*.

Baba J., Asaki Y., Makino J., Miyoshi M., Saitoh T. R., Wada K., 2009. *ApJ*, **706**, 471. *The Origin of Large Peculiar Motions of Star-Forming Regions and Spiral Structures of Our Galaxy*.

Baba J., Saitoh T. R., Wada K., 2013. *ApJ*, **763**, 46. *Dynamics of Non-steady Spiral Arms in Disk Galaxies*.

Baba J., 2015. *MNRAS*, **454**, 2954. *Short-term dynamical evolution of grand-design spirals in barred galaxies*.

Babcock H. W., 1939. *Lick Observatory Bulletin*, **19**, 41. *The rotation of the Andromeda Nebula*.

Baldry I. K., Balogh M. L., Bower R., Glazebrook K., Nichol R. C., 2004. *Color bimodality: Implications for galaxy evolution*, In: *The New Cosmology: Conference on Strings and Cosmology*, p. 106, eds Allen R. E., Nanopoulos D. V., Pope C. N.

Baldry I. K., Balogh M. L., Bower R. G., Glazebrook K., Nichol R. C., Bamford S. P., Budavari T., 2006. *MNRAS*, **373**, 469. *Galaxy bimodality versus stellar mass and environment*.

Ball N. M., Loveday J., Fukugita M., Nakamura O., Okamura S., Brinkmann J., Brunner R. J., 2004. *MNRAS*, **348**, 1038. *Galaxy types in the Sloan Digital Sky Survey using supervised artificial neural networks*.

Bamford S. P., Nichol R. C., Baldry I. K., Land K., Lintott C. J., Schawinski K., Slosar A., Szalay A. S., Thomas D., Torki M., Andreescu D., Edmondson E. M., Miller C. J., Murray P., Raddick M. J., Vandenberg J., 2009. *MNRAS*, **393**, 1324. *Galaxy Zoo: the dependence of morphology and colour on environment*.

Barazza F. D., Jablonka P., Desai V., Jogee S., Aragón-Salamanca A., De Lucia G., Saglia R. P., Halliday C., Poggianti B. M., Dalcanton J. J., Rudnick G., Milvang-Jensen B., Noll S., Simard L., Clowe D. I., Pelló R., White S. D. M., Zaritsky D., 2009. *A&A*, **497**, 713. *Frequency and properties of bars in cluster and field galaxies at intermediate redshifts*.

Barton E. J., Geller M. J., Kenyon S. J., 2000. *ApJ*, **530**, 660. *Tidally Triggered Star Formation in Close Pairs of Galaxies*.

Bell E. F., de Jong R. S., 2001. ApJ, **550**, 212. *Stellar Mass-to-Light Ratios and the Tully-Fisher Relation*.

Bell E. F., 2002. *ApJ*, **577**, 150. *Dust-induced Systematic Errors in Ultraviolet-derived Star Formation Rates*.

Berentzen I., Shlosman I., Jogee S., 2006. ApJ, **637**, 582. *Stellar Bar Evolution in Cuspy and Flat-cored Triaxial CDM Halos*.

Berrier J. C., Davis B. L., Kennefick D., Kennefick J. D., Seigar M. S., Barrows R. S., Hartley M., Shields D., Bentz M. C., Lacy C. H. S., 2013. *ApJ*, **769**, 132. *Further Evidence for a Supermassive Black Hole Mass-Pitch Angle Relation*.

Bershady M. A., Martinsson T. P. K., Verheijen M. A. W., Westfall K. B., Andersen D. R., Swaters R. A., 2011. *ApJL*, **739**, L47. *Galaxy Disks are Submaximal*.

Bertin G., Lin C. C., 1996. *Spiral structure in galaxies a density wave theory*.

Bigiel F., Leroy A., Walter F., Brinks E., de Blok W. J. G., Madore B., Thornley M. D., 2008. *AJ*, **136**, 2846. *The Star Formation Law in Nearby Galaxies on Sub-Kpc Scales*.

Binggeli B., Sandage A., Tammann G. A., 1985. *AJ*, **90**, 1681. *Studies of the Virgo Cluster. II - A catalog of 2096 galaxies in the Virgo Cluster area.*

Binggeli B., Sandage A., Tammann G. A., 1988. *ARAA*, **26**, 509. *The luminosity function of galaxies*.

Binney J., 1977. ApJ, **215**, 483. *The physics of dissipational galaxy formation*.

Biviano A., Girardi M., Giuricin G., Mardirossian F., Mezzetti M., 1991. *ApJ*, **376**, 458. *Arm classification and velocity gradients in spiral galaxies*.

Blanton M. R., Moustakas J., 2009. ARA&A, **47**, 159. *Physical Properties and Environments of Nearby Galaxies*.

Blanton M. R., Roweis S., 2007. *AJ*, **133**, 734. *K-Corrections and Filter Transformations in the Ultraviolet, Optical, and Near-Infrared.*

Blanton M. R., Kazin E., Muna D., Weaver B. A., Price-Whelan A., 2011. *AJ*, **142**, 31. *Improved Background Subtraction for the Sloan Digital Sky Survey Images*.

Block D. L., Puerari I., 1999. *A&A*, **342**, 627. *Toward a dust penetrated classification of the evolved stellar Population II disks of galaxies*.

Block D. L., Wainscoat R. J., 1991. *Nature*, **353**, 48. *Morphological differences between optical and infrared images of the spiral galaxy NGC309*.

Block D. L., Bertin G., Stockton A., Grosbol P., Moorwood A. F. M., Peletier R. F., 1994. *A&A*, **288**. *2.1 μm images of the evolved stellar disk and the morphological classification of spiral galaxies*.

Block D. L., Buta R., Knapen J. H., Elmegreen D. M., Elmegreen B. G., Puerari I., 2004. AJ, **128**, 183. *Gravitational Bar and Spiral Arm Torques from K_s-band Observations and Implications for the Pattern Speeds*.

Boeshaar G. O., Hodge P. W., 1977. *ApJ*, **213**, 361. *H II Regions and the Spiral Structure of NGC 3631* .

Boissier S., Boselli A., Buat V., Donas J., Milliard B., 2004. *A&A*, **424**, 465. *The radial extinction profiles of late-type galaxies.*

Boissier S., Gil de Paz A., Boselli A., Madore B. F., Buat V., Cortese L., Burgarella D., Muñoz-Mateos J. C., Barlow T. A., Forster K., Friedman P. G., Martin D. C., Morrissey P., Neff S. G., Schiminovich D., Seibert M., Small T., Wyder T. K., Bianchi L., Donas J., Heckman T. M., Lee Y.-W., Milliard B., Rich R. M., Szalay A. S., Welsh B. Y., Yi S. K., 2007. *ApJS*, **173**, 524. *Radial Variation of Attenuation and Star Formation in the Largest Late-Type Disks Observed with GALEX*.

Bolatto A. D., Wong T., Utomo D., Blitz L., Vogel S. N., Sánchez S. F., Barrera-Ballesteros J., Cao Y., Colombo D., Dannerbauer H., García-Benito R., Herrera-Camus R., Husemann B., Kalinova V., Leroy A. K., Leung G., Levy R. C., Mast D., Ostriker E., Rosolowsky E., Sandstrom K. M., Teuben P., van de Ven G., Walter F., 2017. ApJ, **846**, 159. *The EDGE-CALIFA Survey: Interferometric Observations of 126 Galaxies with CARMA*.

Boquien M., Calzetti D., Kennicutt R., Dale D., Engelbracht C., Gordon K. D., Hong S., Lee J. C., Portouw J., 2009. *ApJ*, **706**, 553. *Star-Forming or Starbursting? The Ultraviolet Conundrum*.

Boquien M., Buat V., Boselli A., Baes M., Bendo G. J., Ciesla L., Cooray A., Cortese L., Eales S., Gavazzi G., Gomez H. L., Lebouteiller V., Pappalardo C., Pohlen M., Smith M. W. L., Spinoglio L., 2012. *A&A*, **539**, A145. *The IRX-β relation on sub-galactic scales in star-forming galaxies of the Herschel Reference Survey*.

Bosma A., 1999. *Dark Matter in Disk Galaxies*, In: *Galaxy Dynamics - A Rutgers Symposium*, eds Merritt D. R., Valluri M., Sellwood J. A.

Bosma A., 2017. *HI in the Outskirts of Nearby Galaxies*, In: *Outskirts of Galaxies*, 209, eds Knapen J. H., Lee J. C., Gil de Paz A.

Bottema R., 1993. *A&A*, **275**, 16. *The Stellar Kinematics of Galactic Disks*.

Bottema R., 2003. *MNRAS*, **344**, 358. *Simulations of normal spiral galaxies*.

Bouché N., Dekel A., Genzel R., Genel S., Cresci G., Förster Schreiber N. M., Shapiro K. L., Davies R. I., Tacconi L., 2010. *ApJ*, **718**, 1001. *The Impact of Cold Gas Accretion Above a Mass Floor on Galaxy Scaling Relations*.

Bournaud F., Combes F., 2002. *A&A*, **392**, 83. *Gas accretion on spiral galaxies: Bar formation and renewal*.

Bovy J., Rix H.-W., 2013. *ApJ*, **779**, 115. *A Direct Dynamical Measurement of the Milky Way's Disk Surface Density Profile, Disk Scale Length, and Dark Matter Profile at 4 kpc $<$ R $<$ 9 kpc*.

Brinchmann J., Charlot S., White S. D. M., Tremonti C., Kauffmann G., Heckman T., Brinkmann J., 2004. *MNRAS*, **351**, 1151. *The physical properties of star-forming galaxies in the low-redshift Universe*.

Bruzual G., Charlot S., 2003. *MNRAS*, **344**, 1000. *Stellar population synthesis at the resolution of 2003*.

Bryant J. J., Owers M. S., Robotham A. S. G., Croom S. M., Driver S. P., Drinkwater M. J., Lorente N. P. F., Cortese L., Scott N., Colless M., Schaefer A., Taylor E. N., Konstantopoulos I. S., Allen J. T., Baldry I., Barnes L., Bauer A. E., Bland-Hawthorn J., Bloom J. V., Brooks A. M., Brough S., Cecil G., Couch W., Croton D., Davies R., Ellis S., Fogarty L. M. R., Foster C., Glazebrook K., Goodwin M., Green A., Gunawardhana M. L., Hampton E., Ho I.-T., Hopkins A. M., Kewley L., Lawrence J. S., Leon-Saval S. G., Leslie S., McElroy R., Lewis G., Liske J., López-Sánchez Á. R., Mahajan S., Medling A. M., Metcalfe N., Meyer M., Mould J., Obreschkow D., O'Toole S., Pracy M., Richards S. N., Shanks T., Sharp R., Sweet S. M., Thomas A. D., Tonini C., Walcher C. J., 2015. *MNRAS*, **447**, 2857. *The SAMI Galaxy Survey: instrument specification and target selection*.

Buat V., Boissier S., Burgarella D., Takeuchi T. T., Le Floc'h E., Marcillac D., Huang J., Nagashima M., Enoki M., 2008. *A&A*, **483**, 107. *Star formation history of galaxies from z = 0 to z = 0.7. A backward approach to the evolution of star-forming galaxies*.

Buat V., Giovannoli E., Takeuchi T. T., Heinis S., Yuan F.-T., Burgarella D., Noll S., Iglesias-Páramo J., 2011. *A&A*, **529**, A22. *Spectral energy distributions of an AKARI-SDSS-GALEX sample of galaxies*.

Bundy K., Bershady M. A., Law D. R., Yan R., Drory N., MacDonald N., Wake D. A., Cherinka B., Sánchez-Gallego J. R., Weijmans A.-M., Thomas D., Tremonti C., Masters K., Coccato L., Diamond-Stanic A. M., Aragón-Salamanca A., Avila-Reese V., Badenes C., Falcón-Barroso J., Belfiore F., Bizyaev D., Blanc G. A., Bland-Hawthorn J., Blanton M. R., Brownstein J. R., Byler N., Cappellari M., Conroy C., Dutton A. A., Emsellem E., Etherington J., Frinchaboy P. M., Fu H., Gunn J. E., Harding P., Johnston E. J., Kauffmann G., Kinemuchi K., Klaene M. A., Knapen J. H., Leauthaud A., Li C., Lin L., Maiolino R., Malanushenko V., Malanushenko E., Mao S., Maraston C., McDermid R. M., Merrifield M. R., Nichol R. C., Oravetz D., Pan K., Parejko J. K., Sanchez S. F., Schlegel D., Simmons A., Steele O., Steinmetz M., Thanjavur K., Thompson B. A., Tinker J. L., van den Bosch R. C. E., Westfall K. B., Wilkinson D., Wright S., Xiao T., Zhang K., 2015. *ApJ*, **798**, 7. *Overview of the SDSS-IV MaNGA Survey: Mapping nearby Galaxies at Apache Point Observatory*.

Burkert A., 1995. *ApJL*, **447**, L25. *The Structure of Dark Matter Halos in Dwarf Galaxies*.

Burkhart B., Stalpes K., Collins D. C., 2017. ApJ, **834**, L1. *The Razor's Edge of Collapse: The Transition Point from Lognormal to Power-Law Distributions in Molecular Clouds*.

Buta R. J., Sheth K., Athanassoula E., Bosma A., Knapen J. H., Laurikainen E., Salo H., Elmegreen D., Ho L. C., Zaritsky D., Courtois H., Hinz J. L., Muñoz-Mateos J.-C., Kim T., Regan M. W., Gadotti D. A., Gil de Paz A., Laine J., Menéndez-Delmestre K., Comerón S., Erroz Ferrer S., Seibert M., Mizusawa T., Holwerda B., Madore B. F., 2015. *ApJS*, **217**, 32. *A Classical Morphological Analysis of Galaxies in the Spitzer Survey of Stellar Structure in Galaxies (S4G)*.

Buta R., 1986. *ApJS*, **61**, 609. *The structure and dynamics of ringed galaxies. I - The morphology of galaxy rings, and statistics of their apparent shapes, relative sizes, and apparent orientations with respect to bars.*

Buta R. J. *Galaxy Morphology*, 155. 2013.

Buta R. J., 2017. *ArXiv e-prints*. *Galactic Rings Revisited. I. CVRHS Classifications of 3962 Ringed Galaxies from the Galaxy Zoo 2 Database*.

Calzetti D., Armus L., Bohlin R. C., Kinney A. L., Koornneef J., Storchi-Bergmann T., 2000. *ApJ*, **533**, 682. *The Dust Content and Opacity of Actively Star-forming Galaxies*.

Calzetti D., Kennicutt, Jr. R. C., Bianchi L., Thilker D. A., Dale D. A., Engelbracht C. W., Leitherer C., Meyer M. J., Sosey M. L., Mutchler M., Regan M. W., Thornley M. D., Armus L., Bendo G. J., Boissier S., Boselli A., Draine B. T., Gordon K. D., Helou G., Hollenbach D. J., Kewley L., Madore B. F., Martin D. C., Murphy E. J., Rieke G. H., Rieke M. J., Roussel H., Sheth K., Smith J. D., Walter F., White B. A., Yi S., Scoville N. Z., Polletta M., Lindler D., 2005. *ApJ*, **633**, 871. *Star Formation in NGC 5194 (M51a): The Panchromatic View from GALEX to Spitzer*.

Calzetti D., Kinney A. L., Storchi-Bergmann T., 1994. *ApJ*, **429**, 582. *Dust extinction of the stellar continua in starburst galaxies: The ultraviolet and optical extinction law*.

Cameron E., 2011. *PASA*, **28**, 128. *On the Estimation of Confidence Intervals for Binomial Population Proportions in Astronomy: The Simplicity and Superiority of the Bayesian Approach*.

Cappellari M., Copin Y., 2003. *MNRAS*, **342**, 345. *Adaptive spatial binning of integral-field spectroscopic data using Voronoi tessellations*.

Cappellari M., Emsellem E., Bacon R., Bureau M., Davies R. L., de Zeeuw P. T., Falcón-Barroso J., Krajnović D., Kuntschner H., McDermid R. M., Peletier R. F., Sarzi M., van den Bosch R. C. E., van de Ven G., 2007. MNRAS, **379**, 418. *The SAURON project - X. The orbital anisotropy of elliptical and lenticular galaxies: revisiting the (V/σ, ϵ) diagram with integral-field stellar kinematics*.

Carlberg R. G., Freedman W. L., 1985. *ApJ*, **298**, 486. *Dissipative models of spiral galaxies*.

Casoli F., Combes F., 1982. A&A, **110**, 287. *Can giant molecular clouds form in spiral arms*.

Casteels K. R. V., Bamford S. P., Skibba R. A., Masters K. L., Lintott C. J., Keel W. C., Schawinski K., Nichol R. C., Smith A. M., 2013. *MNRAS*, **429**, 1051. *Galaxy Zoo: quantifying morphological indicators of galaxy interaction*.

Chabrier G., 2003. *PASP*, **115**, 763. *Galactic Stellar and Substellar Initial Mass Function*.

Chamberlin T. C., 1901. *ApJ*, **14**, 17. *On a Possible Function of Disruptive Approach in the Formation of Meteorites, Comets, and Nebulae*.

Chan T. K., Kereš D., Oñorbe J., Hopkins P. F., Muratov A. L., Faucher-Giguère C.-A., Quataert E., 2015. *MNRAS*, **454**, 2981. *The impact of baryonic physics on the structure of dark matter haloes: the view from the FIRE cosmological simulations*.

Chang Y.-Y., van der Wel A., da Cunha E., Rix H.-W., 2015. *ApJS*, **219**, 8. *Stellar Masses and Star Formation Rates for 1M Galaxies from SDSS+WISE*.

Charlot S., Fall S. M., 2000. *ApJ*, **539**, 718. *A Simple Model for the Absorption of Starlight by Dust in Galaxies*.

Cheung E., Athanassoula E., Masters K. L., Nichol R. C., Bosma A., Bell E. F., Faber S. M., Koo D. C., Lintott C., Melvin T., Schawinski K., Skibba R. A., Willett K. W., 2013. *ApJ*, **779**, 162. *Galaxy Zoo: Observing Secular Evolution through Bars*.

Choi Y., Dalcanton J. J., Williams B. F., Weisz D. R., Skillman E. D., Fouesneau M., Dolphin A. E., 2015. *ApJ*, **810**, 9. *Testing Density Wave Theory with Resolved Stellar Populations around Spiral Arms in M81*.

Clark C. J. R., Dunne L., Gomez H. L., Maddox S., De Vis P., Smith M. W. L., Eales S. A., Baes M., Bendo G. J., Bourne N., Driver S. P., Dye S., Furlanetto C., Grootes M. W., Ivison R. J., Schofield S. P., Robotham A. S. G., Rowlands K., Valiante E., Vlahakis C., van der Werf P., Wright A. H., de Zotti G., 2015. *MNRAS*, **452**, 397. *Herschel-ATLAS: the surprising diversity of dust-selected galaxies in the local sub-millimetre Universe*.

Cole D. R., Binney J., 2017. *MNRAS*, **465**, 798. *A centrally heated dark halo for our Galaxy*.

Colombo D., Meidt S. E., Schinnerer E., García-Burillo S., Hughes A., Pety J., Leroy A. K., Dobbs C. L., Dumas G., Thompson T. A., Schuster K. F., Kramer C., 2014. *ApJ*, **784**, 4. *The PdBI Arcsecond Whirlpool Survey (PAWS): Multi-phase Cold Gas Kinematic of M51*.

Combes F., Sanders R. H., 1981. A&A, **96**, 164. *Formation and properties of persisting stellar bars*.

Combes F., Young L. M., Bureau M., 2007. MNRAS, **377**, 1795. *Molecular gas and star formation in the SAURON early-type galaxies*.

Conroy C., Ho S., White M., 2007. *MNRAS*, **379**, 1491. *Constraints on the merging time-scale of luminous red galaxies, or, where do all the haloes go?*

Conselice C. J., 2003. ApJS, **147**, 1. *The Relationship between Stellar Light Distributions of Galaxies and Their Formation Histories*.

Conselice C. J., 2006. *MNRAS*, **373**, 1389. *The fundamental properties of galaxies and a new galaxy classification system*.

Considere S., Athanassoula E., 1988. *A&AS*, **76**, 365. *Analysis of spiral components in 16 galaxies*.

Corder S., Sheth K., Scoville N. Z., Koda J., Vogel S. N., Ostriker E., 2008. ApJ, **689**, 148. *Detection of Dense Molecular Gas in Interarm Spurs in M51*.

Cortese L., Catinella B., Boissier S., Boselli A., Heinis S., 2011. *MNRAS*, **415**, 1797. *The effect of the environment on the H I scaling relations*.

Crocker A. F., Chandar R., Calzetti D., Holwerda B. W., Leitherer C., Popescu C., Tuffs R. J., 2015. *ApJ*, **808**, 76. *Origin of the Diffuse, Far Ultraviolet Emission in the Interarm Regions of M101*.

da Cunha E., Charlot S., Elbaz D., 2008. *MNRAS*, **388**, 1595. *A simple model to interpret the ultraviolet, optical and infrared emission from galaxies*.

Darg D. W., Kaviraj S., Lintott C. J., Schawinski K., Sarzi M., Bamford S., Silk J., Proctor R., Andreescu D., Murray P., Nichol R. C., Raddick M. J., Slosar A., Szalay A. S., Thomas D., Vandenberg J., 2010a. *MNRAS*, **401**, 1043. *Galaxy Zoo: the fraction of merging galaxies in the SDSS and their morphologies*.

Darg D. W., Kaviraj S., Lintott C. J., Schawinski K., Sarzi M., Bamford S., Silk J., Andreescu D., Murray P., Nichol R. C., Raddick M. J., Slosar A., Szalay A. S., Thomas D., Vandenberg J., 2010b. *MNRAS*, **401**, 1552. *Galaxy Zoo: the properties of merging galaxies in the nearby Universe - local environments, colours, masses, star formation rates and AGN activity*.

Davis D. R., Hayes W. B., 2014. ApJ, **790**, 87. *SpArcFiRe: Scalable Automated Detection of Spiral Galaxy Arm Segments*.

Davis B. L., Berrier J. C., Shields D. W., Kennefick J., Kennefick D., Seigar M. S., Lacy C. H. S., Puerari I., 2012. *ApJS*, **199**, 33. *Measurement of Galactic Logarithmic Spiral Arm Pitch Angle Using Two-dimensional Fast Fourier Transform Decomposition*.

Davis B. L., Graham A. W., Seigar M. S., 2017. *MNRAS*, **471**, 2187. *Updating the (supermassive black hole mass)-(spiral arm pitch angle) relation: a strong correlation for galaxies with pseudobulges*.

Davoust E., Contini T., 2004. *A&A*, **416**, 515. *Starbursts in barred spiral galaxies. VI. HI observations and the K-band Tully-Fisher relation*.

de Blok W. J. G., McGaugh S. S., Bosma A., Rubin V. C., 2001. *ApJL*, **552**, L23. *Mass Density Profiles of Low Surface Brightness Galaxies*.

de Jong J. T. A., Verdoes Kleijn G. A., Boxhoorn D. R., Buddelmeijer H., Capaccioli M., Getman F., Grado A., Helmich E., Huang Z., Irisarri N., Kuijken K., La Barbera F., McFarland J. P., Napolitano N. R., Radovich M., Sikkema G., Valentijn E. A., Begeman K. G., Brescia M., Cavuoti S., Choi A., Cordes O.-M., Covone G., Dall'Ora M., Hildebrandt H., Longo G., Nakajima R., Paolillo M., Puddu E., Rifatto A., Tortora C., van Uitert E., Buddendiek A., Harnois-Déraps J., Erben T., Eriksen M. B., Heymans C., Hoekstra H., Joachimi B., Kitching T. D., Klaes D., Koopmans L. V. E., Köhlinger F., Roy N., Sifón C., Schneider P., Sutherland W. J., Viola M., Vriend W.-J., 2015. A&A, **582**, A62. *The first and second data releases of the Kilo-Degree Survey*.

de Vaucouleurs G., de Vaucouleurs A., Corwin, Jr. H. G., Buta R. J., Paturel G., Fouqué P., 1991. *Third Reference Catalogue of Bright Galaxies. Volume I: Explanations and references. Volume II: Data for galaxies between 0^h and 12^h. Volume III: Data for galaxies between 12^h and 24^h*.

de Vaucouleurs G., 1948. *Annales d'Astrophysique*, **11**, 247. *Recherches sur les Nebuleuses Extragalactiques*.

de Vaucouleurs G., 1959. *Handbuch der Physik*, **53**, 275. *Classification and Morphology of External Galaxies.*

de Vaucouleurs G., 1963. *ApJS*, **8**, 31. *Revised Classification of 1500 Bright Galaxies.*

Debattista V. P., Sellwood J. A., 2000. ApJ, **543**, 704. *Constraints from Dynamical Friction on the Dark Matter Content of Barred Galaxies*.

Debattista V. P., Mayer L., Carollo C. M., Moore B., Wadsley J., Quinn T., 2006. ApJ, **645**, 209. *The Secular Evolution of Disk Structural Parameters*.

Debattista V. P., Kazantzidis S., van den Bosch F. C., 2013. ApJ, **765**, 23. *Disk Assembly and the M $_{BH}$-σ_e Relation of Supermassive Black Holes*.

Debattista V. P., 2014. MNRAS, **443**, L1. *The vertical structure and kinematics of grand design spirals*.

Di Cintio A., Brook C. B., Dutton A. A., Macciò A. V., Stinson G. S., Knebe A., 2014a. *MNRAS*, **441**, 2986. *A mass-dependent density profile for dark matter haloes including the influence of galaxy formation*.

Di Cintio A., Brook C. B., Macciò A. V., Stinson G. S., Knebe A., Dutton A. A., Wadsley J., 2014b. *MNRAS*, **437**, 415. *The dependence of dark matter profiles on the stellar-to-halo mass ratio: a prediction for cusps versus cores*.

Di Matteo P., Combes F., Melchior A.-L., Semelin B., 2007. *A&A*, **468**, 61. *Star formation efficiency in galaxy interactions and mergers: a statistical study*.

Dieleman S., Willett K. W., Dambre J., 2015. *MNRAS*, **450**, 1441. *Rotation-invariant convolutional neural networks for galaxy morphology prediction*.

Dobbs C., Baba J., 2014. *PASA*, **31**, e035. *Dawes Review 4: Spiral Structures in Disc Galaxies*.

Dobbs C. L., Burkert A., Pringle J. E., 2011. *MNRAS*, **417**, 1318. *The properties of the interstellar medium in disc galaxies with stellar feedback*.

Dobbs C. L., Theis C., Pringle J. E., Bate M. R., 2010. *MNRAS*, **403**, 625. *Simulations of the grand design galaxy M51: a case study for analysing tidally induced spiral structure*.

Dobbs C. L., Pringle J. E., Burkert A., 2012. MNRAS, **425**, 2157. *Giant molecular clouds: what are they made from, and how do they get there?*

Dobbs C. L., 2008. MNRAS, **391**, 844. *GMC formation by agglomeration and self gravity*.

Doi M., Tanaka M., Fukugita M., Gunn J. E., Yasuda N., Ivezić Ž., Brinkmann J., de Haars E., Kleinman S. J., Krzesinski J., French Leger R., 2010. *AJ*, **139**, 1628. *Photometric Response Functions of the Sloan Digital Sky Survey Imager*.

Domínguez Sánchez H., Huertas-Company M., Bernardi M., Tuccillo D., Fisher J. L., 2017. *ArXiv e-prints*. *Improving galaxy morphologies for SDSS with Deep Learning*.

D'Onghia E., Vogelsberger M., Hernquist L., 2013. *ApJ*, **766**, 34. *Self-perpetuating Spiral Arms in Disk Galaxies*.

D'Onghia E., 2015. *ApJL*, **808**, L8. *Disk-stability Constraints on the Number of Arms in Spiral Galaxies*.

Donoso E., Yan L., Tsai C., Eisenhardt P., Stern D., Assef R. J., Leisawitz D., Jarrett T. H., Stanford S. A., 2012. *ApJ*, **748**, 80. *Origin of 12 μm Emission across Galaxy Populations from WISE and SDSS Surveys*.

Dressler A., 1980. *ApJ*, **236**, 351. *Galaxy morphology in rich clusters - Implications for the formation and evolution of galaxies*.

Driver S. P., Hill D. T., Kelvin L. S., Robotham A. S. G., Liske J., Norberg P., Baldry I. K., Bamford S. P., Hopkins A. M., Loveday J., Peacock J. A., Andrae E., Bland-Hawthorn J., Brough S., Brown M. J. I., Cameron E., Ching J. H. Y., Colless M., Conselice C. J., Croom S. M., Cross N. J. G., de Propris R., Dye S., Drinkwater M. J., Ellis S., Graham A. W., Grootes M. W., Gunawardhana M., Jones D. H., van Kampen E., Maraston C., Nichol R. C., Parkinson H. R., Phillipps S., Pimbblet K., Popescu C. C., Prescott M., Roseboom I. G., Sadler E. M., Sansom A. E., Sharp R. G., Smith D. J. B., Taylor E., Thomas D., Tuffs R. J., Wijesinghe D., Dunne L., Frenk C. S., Jarvis M. J., Madore B. F., Meyer M. J., Seibert M., Staveley-Smith L., Sutherland W. J., Warren S. J., 2011. MNRAS, **413**, 971. *Galaxy and Mass Assembly (GAMA): survey diagnostics and core data release*.

Duncan K., Conselice C. J., Mortlock A., Hartley W. G., Guo Y., Ferguson H. C., Davé R., Lu Y., Ownsworth J., Ashby M. L. N., Dekel A., Dickinson M., Faber S., Giavalisco M., Grogin N., Kocevski D., Koekemoer A., Somerville R. S., White C. E., 2014. *MNRAS*, **444**, 2960. *The mass evolution of the first galaxies: stellar mass functions and star formation rates at $4 \leq z \leq 7$ in the CANDELS GOODS-South field*.

Dutton A. A., Macciò A. V., 2014. MNRAS, **441**, 3359. *Cold dark matter haloes in the Planck era: evolution of structural parameters for Einasto and NFW profiles*.

Dutton A. A., Conroy C., van den Bosch F. C., Prada F., More S., 2010. *MNRAS*, **407**, 2. *The kinematic connection between galaxies and dark matter haloes*.

Dutton A. A., Macciò A. V., Mendel J. T., Simard L., 2013. *MNRAS*, **432**, 2496. *Universal IMF versus dark halo response in early-type galaxies: breaking the degeneracy with the Fundamental Plane*.

Dutton A. A., Macciò A. V., Dekel A., Wang L., Stinson G., Obreja A., Di Cintio A., Brook C., Buck T., Kang X., 2016. *MNRAS*, **461**, 2658. *NIHAO IX: the role of gas inflows and outflows in driving the contraction and expansion of cold dark matter haloes*.

Eden D. J., Moore T. J. T., Plume R., Morgan L. K., 2012. *MNRAS*, **422**, 3178. *Star formation towards the Scutum tangent region and the effects of Galactic environment*.

Ellison S. L., Patton D. R., Simard L., McConnachie A. W., 2008. *AJ*, **135**, 1877. *Galaxy Pairs in the Sloan Digital Sky Survey. I. Star Formation, Active Galactic Nucleus Fraction, and the Mass-Metallicity Relation*.

Ellison S. L., Patton D. R., Simard L., McConnachie A. W., Baldry I. K., Mendel J. T., 2010. *MNRAS*, **407**, 1514. *Galaxy pairs in the Sloan Digital Sky Survey - II. The effect of environment on interactions*.

Ellison S. L., Sánchez S. F., Ibarra-Medel H., Antonio B., Mendel J. T., Barrera-Ballesteros J., 2018. MNRAS, **474**, 2039. *Star formation is boosted (and quenched) from the inside-out: radial star formation profiles from MaNGA*.

Elmegreen D. M., Elmegreen B. G., 1982. *MNRAS*, **201**, 1021. *Flocculent and grand design spiral structure in field, binary and group galaxies*.

Elmegreen B. G., Elmegreen D. M., 1983. *ApJ*, **267**, 31. *Flocculent and grand design spiral galaxies in groups - Time scales for the persistence of grand design spiral structures*.

Elmegreen B. G., Elmegreen D. M., 1985. ApJ, **288**, 438. *Properties of barred spiral galaxies*.

Elmegreen B. G., Elmegreen D. M., 1986. *ApJ*, **311**, 554. *Do density waves trigger star formation?*

Elmegreen B. G., Elmegreen D. M., 1987a. *ApJ*, **320**, 182. *H I superclouds in the inner Galaxy*.

Elmegreen D. M., Elmegreen B. G., 1987b. *ApJ*, **314**, 3. *Arm classifications for spiral galaxies*.

Elmegreen D. M., Elmegreen B. G., Dressler A., 1982. MNRAS, **201**, 1035. *Flocculent and grand design spiral arm structure in cluster galaxies*.

Elmegreen D. M., Elmegreen B. G., Yau A., Athanassoula E., Bosma A., Buta R. J., Helou G., Ho L. C., Gadotti D. A., Knapen J. H., Laurikainen E., Madore B. F., Masters K. L., Meidt S. E., Menéndez-Delmestre K., Regan M. W., Salo H., Sheth K., Zaritsky D., Aravena M., Skibba R., Hinz J. L., Laine J., Gil de Paz A., Muñoz-Mateos J.-C., Seibert M., Mizusawa T., Kim T., Erroz Ferrer S., 2011. *ApJ*, **737**, 32. *Grand Design and Flocculent Spirals in the Spitzer Survey of Stellar Structure in Galaxies (S^4G)*.

Elmegreen B. G., 2002. *ApJ*, **577**, 206. *Star Formation from Galaxies to Globules*.

Elmegreen B. G., 2011. *Star Formation in Spiral Arms*, In: *EAS Publications Series*, p. 19, eds Charbonnel C., Montmerle T.

Emsellem E., Cappellari M., Krajnović D., van de Ven G., Bacon R., Bureau M., Davies R. L., de Zeeuw P. T., Falcón-Barroso J., Kuntschner H., McDermid R., Peletier R. F., Sarzi M., 2007. MNRAS, **379**, 401. *The SAURON project - IX. A kinematic classification for early-type galaxies*.

Emsellem E., Cappellari M., Krajnović D., Alatalo K., Blitz L., Bois M., Bournaud F., Bureau M., Davies R. L., Davis T. A., de Zeeuw P. T., Khochfar S., Kuntschner H., Lablanche P.-Y., McDermid R. M., Morganti R., Naab T., Oosterloo T., Sarzi M., Scott N., Serra P., van de Ven G., Weijmans A.-M., Young L. M., 2011. MNRAS, **414**, 888. *The ATLAS^{3D} project - III. A census of the stellar angular momentum within the effective radius of early-type galaxies: unveiling the distribution of fast and slow rotators*.

Engel H., Tacconi L. J., Davies R. I., Neri R., Smail I., Chapman S. C., Genzel R., Cox P., Greve T. R., Ivison R. J., Blain A., Bertoldi F., Omont A., 2010. *ApJ*, **724**, 233. *Most Submillimeter Galaxies are Major Mergers*.

Eskew M., Zaritsky D., Meidt S., 2012. AJ, **143**, 139. *Converting from 3.6 and 4.5 μm Fluxes to Stellar Mass*.

Evans, II N. J., Dunham M. M., Jørgensen J. K., Enoch M. L., Merín B., van Dishoeck E. F., Alcalá J. M., Myers P. C., Stapelfeldt K. R., Huard T. L., Allen L. E., Harvey P. M., van Kempen T., Blake G. A., Koerner D. W., Mundy L. G., Padgett D. L., Sargent A. I., 2009. ApJS, **181**, 321. *The Spitzer c2d Legacy Results: Star-Formation Rates and Efficiencies; Evolution and Lifetimes*.

Fall S. M., Efstathiou G., 1980. MNRAS, **193**, 189. *Formation and rotation of disc galaxies with haloes*.

Ferrarese L., Merritt D., 2000. ApJ, **539**, L9. *A Fundamental Relation between Supermassive Black Holes and Their Host Galaxies*.

Flores R. A., Primack J. R., 1994. *ApJL*, **427**, L1. *Observational and theoretical constraints on singular dark matter halos*.

Foyle K., Rix H.-W., Walter F., Leroy A. K., 2010. *ApJ*, **725**, 534. *Arm and Interarm Star Formation in Spiral Galaxies*.

Foyle K., Rix H.-W., Dobbs C. L., Leroy A. K., Walter F., 2011. *ApJ*, **735**, 101. *Observational Evidence Against Long-lived Spiral Arms in Galaxies*.

Fraser-McKelvie A., Brown M. J. I., Pimbblet K. A., Dolley T., Crossett J. P., Bonne N. J., 2016. *MNRAS*, **462**, L11. *A photometrically and spectroscopically confirmed population of passive spiral galaxies*.

Freeman K. C., 1970. ApJ, **160**, 811. *On the Disks of Spiral and S0 Galaxies*.

Fuchs B., 2001. *MNRAS*, **325**, 1637. *Density waves in the shearing sheet - III. Disc heating*.

Fujii M. S., Baba J., Saitoh T. R., Makino J., Kokubo E., Wada K., 2011. *ApJ*, **730**, 109. *The Dynamics of Spiral Arms in Pure Stellar Disks*.

Fujimoto M., 1968. *Modeling of gas flow through a spiral sleeve*, In: *Non-stable Phenomena in Galaxies*, 453.

Fukugita M., Nakamura O., Okamura S., Yasuda N., Barentine J. C., Brinkmann J., Gunn J. E., Harvanek M., Ichikawa T., Lupton R. H., Schneider D. P., Strauss M. A., York D. G., 2007. AJ, **134**, 579. *A Catalog of Morphologically Classified Galaxies from the Sloan Digital Sky Survey: North Equatorial Region*.

Gadotti D. A., 2009. *MNRAS*, **393**, 1531. *Structural properties of pseudo-bulges, classical bulges and elliptical galaxies: a Sloan Digital Sky Survey perspective*.

Galloway M. A., Willett K. W., Fortson L. F., Cardamone C. N., Schawinski K., Cheung E., Lintott C. J., Masters K. L., Melvin T., Simmons B. D., 2015. *MNRAS*, **448**, 3442. *Galaxy Zoo: the effect of bar-driven fuelling on the presence of an active galactic nucleus in disc galaxies*.

García-Benito R., González Delgado R. M., Pérez E., Cid Fernandes R., Cortijo-Ferrero C., López Fernández R., de Amorim A. L., Lacerda E. A. D., Vale Asari N., Sánchez S. F., 2017. A&A, **608**, A27. *The spatially resolved star formation history of CALIFA galaxies. Cosmic time scales*.

Garcia Gomez C., Athanassoula E., 1993. *A&AS*, **100**, 431. *Analysis of the distribution of H II regions in external galaxies. II - Analysis of the spiral structure*.

Garn T., Best P. N., 2010. *MNRAS*, **409**, 421. *Predicting dust extinction from the stellar mass of a galaxy*.

Gebhardt K., Bender R., Bower G., Dressler A., Faber S. M., Filippenko A. V., Green R., Grillmair C., Ho L. C., Kormendy J., Lauer T. R., Magorrian J., Pinkney J., Richstone D., Tremaine S., 2000. ApJ, **539**, L13. *A Relationship between Nuclear Black Hole Mass and Galaxy Velocity Dispersion*.

Genzel R., Tacconi L. J., Lutz D., Saintonge A., Berta S., Magnelli B., Combes F., García-Burillo S., Neri R., Bolatto A., Contini T., Lilly S., Boissier J., Boone F., Bouché N., Bournaud F., Burkert A., Carollo M., Colina L., Cooper M. C., Cox P., Feruglio C., Förster Schreiber N. M., Freundlich J., Gracia-Carpio J., Juneau S., Kovac K., Lippa M., Naab T., Salome P., Renzini A., Sternberg A., Walter F., Weiner B., Weiss A., Wuyts S., 2015. *ApJ*, **800**, 20. *Combined CO and Dust Scaling Relations of Depletion Time and Molecular Gas Fractions with Cosmic Time, Specific Star-formation Rate, and Stellar Mass*.

Ghosh S., Jog C. J., 2015. *MNRAS*, **451**, 1350. *Role of gas in supporting grand spiral structure*.

Ghosh S., Jog C. J., 2016. *MNRAS*, **459**, 4057. *Dynamical effect of gas on spiral pattern speed in galaxies*.

Giordano L., Tran K.-V. H., Moore B., Saintonge A., 2010. *ArXiv e-prints*. *Multi-Wavelength Properties of Barred Galaxies in the Local Universe. I: Virgo Cluster*.

Giovanelli R., Haynes M. P., Kent B. R., Perillat P., Saintonge A., Brosch N., Catinella B., Hoffman G. L., Stierwalt S., Spekkens K., Lerner M. S., Masters K. L., Momjian E., Rosenberg J. L., Springob C. M., Boselli A., Charmandaris V., Darling J. K., Davies J., Garcia Lambas D., Gavazzi G., Giovanardi C., Hardy E., Hunt L. K., Iovino A., Karachentsev I. D., Karachentseva V. E., Koopmann R. A., Marinoni C., Minchin

R., Muller E., Putman M., Pantoja C., Salzer J. J., Scodeggio M., Skillman E., Solanes J. M., Valotto C., van Driel W., van Zee L., 2005. *AJ*, **130**, 2598. *The Arecibo Legacy Fast ALFA Survey. I. Science Goals, Survey Design, and Strategy*.

Glass I. S., 1984. *MNRAS*, **211**, 461. *JHK colours of 'ordinary' galaxies*.

Glazebrook K., Abraham R. G., McCarthy P. J., Savaglio S., Chen H.-W., Crampton D., Murowinski R., Jørgensen I., Roth K., Hook I., Marzke R. O., Carlberg R. G., 2004. Nature, **430**, 181. *A high abundance of massive galaxies 3-6 billion years after the Big Bang*.

Goerdt T., Moore B., Read J. I., Stadel J., Zemp M., 2006. *MNRAS*, **368**, 1073. *Does the Fornax dwarf spheroidal have a central cusp or core?*

Goldreich P., Lynden-Bell D., 1965. *MNRAS*, **130**, 125. *II. Spiral arms as sheared gravitational instabilities*.

Gonzalez-Perez V., Castander F. J., Kauffmann G., 2011. MNRAS, **411**, 1151. *Colour gradients within SDSS DR7 galaxies: hints of recent evolution*.

Governato F., Brook C., Mayer L., Brooks A., Rhee G., Wadsley J., Jonsson P., Willman B., Stinson G., Quinn T., Madau P., 2010. *Nature*, **463**, 203. *Bulgeless dwarf galaxies and dark matter cores from supernova-driven outflows*.

Grabelsky D. A., Cohen R. S., Bronfman L., Thaddeus P., May J., 1987. *ApJ*, **315**, 122. *Molecular clouds in the Carina arm - Large-scale properties of molecular gas and comparison with H I*.

Grand R. J. J., Kawata D., Cropper M., 2012a. *MNRAS*, **421**, 1529. *The dynamics of stars around spiral arms*.

Grand R. J. J., Kawata D., Cropper M., 2012b. *MNRAS*, **426**, 167. *Dynamics of stars around spiral arms in an N-body/SPH simulated barred spiral galaxy*.

Grand R. J. J., Kawata D., Cropper M., 2013. *A&A*, **553**, A77. *Spiral arm pitch angle and galactic shear rate in N-body simulations of disc galaxies*.

Grosbøl P., Dottori H., 2012. *A&A*, **542**, A39. *Star formation in grand-design, spiral galaxies. Young, massive clusters in the near-infrared*.

Grosbøl P., Patsis P. A., Pompei E., 2004. *A&A*, **423**, 849. *Spiral galaxies observed in the near-infrared K band. I. Data analysis and structural parameters*.

Guo K., Zheng X. Z., Fu H., 2013. *ApJ*, **778**, 23. *The Intrinsic Scatter along the Main Sequence of Star-forming Galaxies at z ˜ 0.7*.

Hao C.-N., Kennicutt R. C., Johnson B. D., Calzetti D., Dale D. A., Moustakas J., 2011. *ApJ*, **741**, 124. *Dust-corrected Star Formation Rates of Galaxies. II. Combinations of Ultraviolet and Infrared Tracers*.

Häring N., Rix H.-W., 2004. ApJ, **604**, L89. *On the Black Hole Mass-Bulge Mass Relation*.

Hart R. E., Bamford S. P., Willett K. W., Masters K. L., Cardamone C., Lintott C. J., Mackay R. J., Nichol R. C., Rosslowe C. K., Simmons B. D., Smethurst R. J., 2016. *MNRAS*, **461**, 3663. *Galaxy Zoo: comparing the demographics of spiral arm number and a new method for correcting redshift bias*.

Hart R. E., Bamford S. P., Casteels K. R. V., Kruk S. J., Lintott C. J., Masters K. L., 2017a. *MNRAS*, **468**, 1850. *Galaxy Zoo: star formation versus spiral arm number*.

Hart R. E., Bamford S. P., Hayes W. B., Cardamone C. N., Keel W. C., Kruk S. J., Lintott C. J., Masters K. L., Simmons B. D., Smethurst R. J., 2017b. *MNRAS*, **472**, 2263. *Galaxy Zoo and sparcfire: constraints on spiral arm formation mechanisms from spiral arm number and pitch angles*.

Hart R. E., Bamford S. P., Keel W. C., Kruk S. J., Masters K. L., Simmons B. D., Smethurst R. J., 2018. *Galaxy Zoo: constraining the origin of spiral arms*.

Hawarden T. G., Mountain C. M., Leggett S. K., Puxley P. J., 1986. MNRAS, **221**, 41P. *Enhanced star formation - The importance of bars in spiral galaxies*.

Haynes M. P., Giovanelli R., 1984. *AJ*, **89**, 758. *Neutral hydrogen in isolated galaxies. IV - Results for the Arecibo sample*.

Haynes M. P., Giovanelli R., Martin A. M., Hess K. M., Saintonge A., Adams E. A. K., Hallenbeck G., Hoffman G. L., Huang S., Kent B. R., Koopmann R. A., Papastergis E., Stierwalt S., Balonek T. J., Craig D. W., Higdon S. J. U., Kornreich D. A., Miller J. R., O'Donoghue A. A., Olowin R. P., Rosenberg J. L., Spekkens K., Troischt P., Wilcots E. M., 2011. *AJ*, **142**, 170. *The Arecibo Legacy Fast ALFA Survey: The α.40 H I Source Catalog, Its Characteristics and Their Impact on the Derivation of the H I Mass Function*.

Heckman T. M., Robert C., Leitherer C., Garnett D. R., van der Rydt F., 1998. *ApJ*, **503**, 646. *The Ultraviolet Spectroscopic Properties of Local Starbursts: Implications at High Redshift*.

Helmboldt J. F., Walterbos R. A. M., Bothun G. D., O'Neil K., de Blok W. J. G., 2004. *ApJ*, **613**, 914. *Star Formation in H I-Selected Galaxies. I. Sample Characteristics*.

Helmboldt J. F., Walterbos R. A. M., Bothun G. D., O'Neil K., 2005. *ApJ*, **630**, 824. *Star Formation in H I-selected Galaxies. II. H II Region Properties*.

Helou G., Roussel H., Appleton P., Frayer D., Stolovy S., Storrie-Lombardi L., Hurt R., Lowrance P., Makovoz D., Masci F., Surace J., Gordon K. D., Alonso-Herrero A., Engelbracht C. W., Misselt K., Rieke G., Rieke M., Willner S. P., Pahre M., Ashby M. L. N., Fazio G. G., Smith H. A., 2004. *ApJS*, **154**, 253. *The Anatomy of Star Formation in NGC 300*.

Hernquist L., 1990. *ApJ*, **356**, 359. *An analytical model for spherical galaxies and bulges*.

Herrera-Endoqui M., Díaz-García S., Laurikainen E., Salo H., 2015. *A&A*, **582**, A86. *Catalogue of the morphological features in the Spitzer Survey of Stellar Structure in Galaxies (S^4G)*.

Hocking A., Geach J. E., Sun Y., Davey N., 2018. *MNRAS*, **473**, 1108. *An automatic taxonomy of galaxy morphology using unsupervised machine learning*.

Hodge P. W., Merchant A. E., 1966. *ApJ*, **144**, 875. *Photometry of so Galaxies. II. The Peculiar Galaxy NGC 128*.

Hohl F., 1971. ApJ, **168**, 343. *Numerical Experiments with a Disk of Stars*.

Hohl F., 1976. AJ, **81**, 30. *Suppression of bar instability by a massive halo*.

Holincheck A. J., Wallin J. F., Borne K., Fortson L., Lintott C., Smith A. M., Bamford S., Keel W. C., Parrish M., 2016. MNRAS, **459**, 720. *Galaxy Zoo: Mergers - Dynamical models of interacting galaxies*.

Holmberg E., 1958. *Meddelanden fran Lunds Astronomiska Observatorium Serie II*, **136**, 1. *A photographic photometry of extragalactic nebulae.*

Holwerda B. W., González R. A., van der Kruit P. C., Allen R. J., 2005. *A&A*, **444**, 109. *The opacity of spiral galaxy disks. VI. Extinction, stellar light and color*.

Hopkins P. F., Kereš D., Oñorbe J., Faucher-Giguère C.-A., Quataert E., Murray N., Bullock J. S., 2014. *MNRAS*, **445**, 581. *Galaxies on FIRE (Feedback In Realistic Environments): stellar feedback explains cosmologically inefficient star formation*.

Hopkins P. F., Quataert E., Murray N., 2011. MNRAS, **417**, 950. *Self-regulated star formation in galaxies via momentum input from massive stars*.

Hoyle F., Schwarzschild M., 1955. ApJ, **121**, 776. *On the Evolution of Type II Stars.*

Hoyle B., Masters K. L., Nichol R. C., Edmondson E. M., Smith A. M., Lintott C., Scranton R., Bamford S., Schawinski K., Thomas D., 2011. *MNRAS*, **415**, 3627. *Galaxy Zoo: bar lengths in local disc galaxies*.

Huang S., Haynes M. P., Giovanelli R., Brinchmann J., Stierwalt S., Neff S. G., 2012. *AJ*, **143**, 133. *Gas, Stars, and Star Formation in ALFALFA Dwarf Galaxies*.

Huang K.-H., Fall S. M., Ferguson H. C., van der Wel A., Grogin N., Koekemoer A., Lee S.-K., Pérez-González P. G., Wuyts S., 2017. *ApJ*, **838**, 6. *Relations between the Sizes of Galaxies and Their Dark Matter Halos at Redshifts $0 < z < 3$*.

Hubble E. P., 1926a. ApJ, **63**. *A spiral nebula as a stellar system: Messier 33.*

Hubble E. P., 1926b. *ApJ*, **64**. *Extragalactic nebulae.*

Hubble E. P., 1929. ApJ, **69**. *A spiral nebula as a stellar system, Messier 31.*

Hubble E. P., 1936. *Realm of the Nebulae*.

Hughes A., Meidt S., Colombo D., Schruba A., Schinnerer E., Leroy A., Wong T., 2016. *Giant Molecular Cloud Populations in Nearby Galaxies*, In: *From Interstellar Clouds to Star-Forming Galaxies: Universal Processes?*, p. 30, eds Jablonka P., André P., van der Tak F.

Ivezić Ž., Connolly A., Vanderplas J., Gray A., 2014. *Statistics, Data Mining, and Machine Learning in Astronomy*, Princeton University Press.

Jarrett T. H., Masci F., Tsai C. W., Petty S., Cluver M. E., Assef R. J., Benford D., Blain A., Bridge C., Donoso E., Eisenhardt P., Koribalski B., Lake S., Neill J. D., Seibert M., Sheth K., Stanford S., Wright E., 2013. *AJ*, **145**, 6. *Extending the Nearby Galaxy Heritage with WISE: First Results from the WISE Enhanced Resolution Galaxy Atlas*.

Jog C. J., 1992. *ApJ*, **390**, 378. *Swing amplification of nonaxisymmetric perturbations in stars and gas in a sheared galactic disk*.

Jog C. J., 1993. *Bulletin of the Astronomical Society of India*, **21**, 437. *Swing amplification in stars and gas: Origin of local spirit structure in galaxies*.

Jones T., Ellis R., Leethochawalit N., Stark D., Treu T., Schmidt K., 2016. *Early Disk Galaxies Revealed By Gravitational Lensing: What Did The Milky Way Look Like At Z 2?*, In: *Discs in galaxies (Discs 2016)*, 7.

Julian W. H., Toomre A., 1966. ApJ, **146**, 810. *Non-Axisymmetric Responses of Differentially Rotating Disks of Stars*.

Kalnajs A. J., Athanassoula-Georgala E., 1974. MNRAS, **168**, 287. *The bar modes of uniformly rotating stellar disks*.

Katz N., Quinn T., Bertschinger E., Gelb J. M., 1994. MNRAS, **270**, L71. *Formation of Quasars at High Redshift*.

Katz H., Lelli F., McGaugh S. S., Di Cintio A., Brook C. B., Schombert J. M., 2017. *MNRAS*, **466**, 1648. *Testing feedback-modified dark matter haloes with galaxy rotation curves: estimation of halo parameters and consistency with ΛCDM scaling relations*.

Katz N., Quinn T., Gelb J. M., 1993. MNRAS, **265**, 689. *Galaxy Formation and the Peaks Formalism*.

Kauffmann G., Heckman T. M., White S. D. M., Charlot S., Tremonti C., Brinchmann J., Bruzual G., Peng E. W., Seibert M., Bernardi M., Blanton M., Brinkmann J., Castander F., Csábai I., Fukugita M., Ivezic Z., Munn J. A., Nichol R. C., Padmanabhan N., Thakar A. R., Weinberg D. H., York D., 2003. MNRAS, **341**, 33. *Stellar masses and star formation histories for 10^5 galaxies from the Sloan Digital Sky Survey*.

Kauffmann G., White S. D. M., Heckman T. M., Ménard B., Brinchmann J., Charlot S., Tremonti C., Brinkmann J., 2004. *MNRAS*, **353**, 713. *The environmental dependence of the relations between stellar mass, structure, star formation and nuclear activity in galaxies*.

Kaviraj S., 2014. *MNRAS*, **440**, 2944. *The importance of minor-merger-driven star formation and black hole growth in disc galaxies*.

Kawata D., Cen R., Ho L. C., 2007. ApJ, **669**, 232. *Gravitational Stability of Circumnuclear Disks in Elliptical Galaxies*.

Kelvin L. S., Driver S. P., Robotham A. S. G., Graham A. W., Phillipps S., Agius N. K., Alpaslan M., Baldry I., Bamford S. P., Bland-Hawthorn J., Brough S., Brown M. J. I., Colless M., Conselice C. J., Hopkins A. M., Liske J., Loveday J., Norberg P., Pimbblet K. A., Popescu C. C., Prescott M., Taylor E. N., Tuffs R. J., 2014a. *MNRAS*, **439**, 1245. *Galaxy And Mass Assembly (GAMA): ugrizYJHK Sérsic luminosity functions and the cosmic spectral energy distribution by Hubble type*.

Kelvin L. S., Driver S. P., Robotham A. S. G., Taylor E. N., Graham A. W., Alpaslan M., Baldry I., Bamford S. P., Bauer A. E., Bland-Hawthorn J., Brown M. J. I., Colless M., Conselice C. J., Holwerda B. W., Hopkins A. M., Lara-López M. A., Liske J., López-Sánchez Á. R., Loveday J., Norberg P., Phillipps S., Popescu C. C., Prescott M., Sansom A. E., Tuffs R. J., 2014b. *MNRAS*, **444**, 1647. *Galaxy And Mass Assembly (GAMA): stellar mass functions by Hubble type*.

Kendall S., Clarke C., Kennicutt R. C., 2015. *MNRAS*, **446**, 4155. *Spiral structure in nearby galaxies - II. Comparative analysis and conclusions*.

Kendall S., Kennicutt R. C., Clarke C., 2011. *MNRAS*, **414**, 538. *Spiral structure in nearby galaxies - I. Sample, data analysis and overview of results*.

Kennedy R., Bamford S. P., Baldry I., Häußler B., Holwerda B. W., Hopkins A. M., Kelvin L. S., Lange R., Moffett A. J., Popescu C. C., Taylor E. N., Tuffs R. J., Vika M., Vulcani B., 2015. MNRAS, **454**, 806. *Galaxy And Mass Assembly (GAMA): the wavelength dependence of galaxy structure versus redshift and luminosity*.

Kennedy R., Bamford S. P., Häußler B., Brough S., Holwerda B., Hopkins A. M., Vika M., Vulcani B., 2016. A&A, **593**, A84. *Galaxy And Mass Assembly (GAMA): Galaxy colour gradients versus colour, structure, and luminosity*.

Kennicutt R. C., Evans N. J., 2012. *ARAA*, **50**, 531. *Star Formation in the Milky Way and Nearby Galaxies*.

Kennicutt, Jr. R., Hodge P., 1982. ApJ, **253**, 101. *A comparison of measured spiral arm properties with model predictions*.

Kennicutt, Jr. R. C., 1981. *AJ*, **86**, 1847. *The shapes of spiral arms along the Hubble sequence*.

Kennicutt, Jr. R. C., 1983. ApJ, **272**, 54. *The rate of star formation in normal disk galaxies*.

Kennicutt, Jr. R. C., 1998. *ApJ*, **498**, 541. *The Global Schmidt Law in Star-forming Galaxies*.

Kereš D., Katz N., Weinberg D. H., Davé R., 2005. MNRAS, **363**, 2. *How do galaxies get their gas?*

Khoperskov S. A., Vasiliev E. O., 2017. MNRAS, **468**, 920. *A Kennicutt-Schmidt relation at molecular cloud scales and beyond*.

Kim W.-T., Ostriker E. C., 2002. ApJ, **570**, 132. *Formation and Fragmentation of Gaseous Spurs in Spiral Galaxies*.

Kollmeier J. A., Zasowski G., Rix H.-W., Johns M., Anderson S. F., Drory N., Johnson J. A., Pogge R. W., Bird J. C., Blanc G. A., Brownstein J. R., Crane J. D., De Lee N. M., Klaene M. A., Kreckel K., MacDonald N., Merloni A., Ness M. K., O'Brien T., Sanchez-Gallego J. R., Sayres C. C., Shen Y., Thakar A. R., Tkachenko A., Aerts C., Blanton M. R., Eisenstein D. J., Holtzman J. A., Maoz D., Nandra K., Rockosi C., Weinberg D. H., Bovy J., Casey A. R., Chaname J., Clerc N., Conroy C., Eracleous M., Gänsicke B. T., Hekker S., Horne K., Kauffmann J., McQuinn K. B. W., Pellegrini E. W., Schinnerer E., Schlafly E. F., Schwope A. D., Seibert M., Teske J. K., van Saders J. L., 2017. *ArXiv e-prints*. *SDSS-V: Pioneering Panoptic Spectroscopy*.

Kong X., Charlot S., Brinchmann J., Fall S. M., 2004. *MNRAS*, **349**, 769. *Star formation history and dust content of galaxies drawn from ultraviolet surveys*.

Kormendy J., Bender R., 2012. ApJS, **198**, 2. *A Revised Parallel-sequence Morphological Classification of Galaxies: Structure and Formation of S0 and Spheroidal Galaxies*.

Kormendy J., Norman C. A., 1979. *ApJ*, **233**, 539. *Observational constraints on driving mechanisms for spiral density waves*.

Kormendy J., Richstone D., 1995. ARA&A, **33**, 581. *Inward Bound—The Search For Supermassive Black Holes In Galactic Nuclei*.

Kormendy J., 1977. ApJ, **217**, 406. *Brightness distributions in compact and normal galaxies. III - Decomposition of observed profiles into spheroid and disk components*.

Kregel M., van der Kruit P. C., Freeman K. C., 2005. *MNRAS*, **358**, 503. *Structure and kinematics of edge-on galaxy discs - V. The dynamics of stellar discs*.

Krips M., Crocker A. F., Bureau M., Combes F., Young L. M., 2010. MNRAS, **407**, 2261. *Molecular gas in SAURON early-type galaxies: detection of ^{13}CO and HCN emission*.

Krishna Swamy K. S., 1968. PASP, **80**, 406. *Line Blanketing in Stars*.

Kroupa P., 2001. *MNRAS*, **322**, 231. *On the variation of the initial mass function*.

Kruijssen J. M. D., Longmore S. N., Elmegreen B. G., Murray N., Bally J., Testi L., Kennicutt R. C., 2014. MNRAS, **440**, 3370. *What controls star formation in the central 500 pc of the Galaxy?*

Kruk S. J., Lintott C. J., Simmons B. D., Bamford S. P., Cardamone C. N., Fortson L., Hart R. E., Häußler B., Masters K. L., Nichol R. C., Schawinski K., Smethurst R. J., 2017. MNRAS, **469**, 3363. *Galaxy Zoo: finding offset discs and bars in SDSS galaxies*.

Kruk S. J., Lintott C. J., Bamford S. P., Masters K. L., Simmons B. D., Häußler B., Cardamone C. N., Hart R. E., Kelvin L., Schawinski K., Smethurst R. J., Vika M., 2018. MNRAS, **473**, 4731. *Galaxy Zoo: secular evolution of barred galaxies from structural decomposition of multiband images*.

Krumholz M. R., Kruijssen J. M. D., 2015. MNRAS, **453**, 739. *A dynamical model for the formation of gas rings and episodic starbursts near galactic centres*.

Kuchner U., Ziegler B., Verdugo M., Bamford S., Häußler B., 2017. *A&A*, **604**, A54. *The effects of the cluster environment on the galaxy mass-size relation in MACS J1206.2-0847*.

Kuijken K., Heymans C., Hildebrandt H., Nakajima R., Erben T., de Jong J. T. A., Viola M., Choi A., Hoekstra H., Miller L., van Uitert E., Amon A., Blake C., Brouwer M., Buddendiek A., Conti I. F., Eriksen M., Grado A., Harnois-Déraps J., Helmich E., Herbonnet R., Irisarri N., Kitching T., Klaes D., La Barbera F., Napolitano N., Radovich M., Schneider P., Sifón C., Sikkema G., Simon P., Tudorica A., Valentijn E., Verdoes Kleijn G., van Waerbeke L., 2015. MNRAS, **454**, 3500. *Gravitational lensing analysis of the Kilo-Degree Survey*.

La Vigne M. A., Vogel S. N., Ostriker E. C., 2006. ApJ, **650**, 818. *A Hubble Space Telescope Archival Survey of Feathers in Spiral Galaxies*.

Lada C. J., Margulis M., Sofue Y., Nakai N., Handa T., 1988. *ApJ*, **328**, 143. *Observations of molecular and atomic clouds in M31*.

Lahav O., Naim A., Buta R. J., Corwin H. G., de Vaucouleurs G., Dressler A., Huchra J. P., van den Bergh S., Raychaudhury S., Sodre, Jr. L., Storrie-Lombardi M. C., 1995. *Science*, **267**, 859. *Galaxies, Human Eyes, and Artificial Neural Networks*.

Land K., Slosar A., Lintott C., Andreescu D., Bamford S., Murray P., Nichol R., Raddick M. J., Schawinski K., Szalay A., Thomas D., Vandenberg J., 2008. *MNRAS*, **388**, 1686. *Galaxy Zoo: the large-scale spin statistics of spiral galaxies in the Sloan Digital Sky Survey*.

Larson R. B., 1974. MNRAS, **169**, 229. *Effects of supernovae on the early evolution of galaxies*.

Lelli F., McGaugh S. S., Schombert J. M., 2016. *AJ*, **152**, 157. *SPARC: Mass Models for 175 Disk Galaxies with Spitzer Photometry and Accurate Rotation Curves*.

Leroy A. K., Walter F., Brinks E., Bigiel F., de Blok W. J. G., Madore B., Thornley M. D., 2008. AJ, **136**, 2782. *The Star Formation Efficiency in Nearby Galaxies: Measuring Where Gas Forms Stars Effectively*.

Li C., Kauffmann G., Heckman T. M., Jing Y. P., White S. D. M., 2008. *MNRAS*, **385**, 1903. *Interaction-induced star formation in a complete sample of 10^5 nearby star-forming galaxies*.

Lian J., Yan R., Blanton M., Kong X., 2017. MNRAS, **472**, 4679. *Inside-out growth or inside-out quenching? Clues from colour gradients of local galaxies*.

Lilly S. J., Carollo C. M., Pipino A., Renzini A., Peng Y., 2013. *ApJ*, **772**, 119. *Gas Regulation of Galaxies: The Evolution of the Cosmic Specific Star Formation Rate, the Metallicity-Mass-Star-formation Rate Relation, and the Stellar Content of Halos*.

Lin C. C., Shu F. H., 1964. *ApJ*, **140**, 646. *On the Spiral Structure of Disk Galaxies.*

Lin C. C., Shu F. H., 1967. *Density waves in disk galaxies.*, In: *Radio Astronomy and the Galactic System*, 313, ed. van Woerden H.

Lindblad B., 1927. *MNRAS*, **87**, 420. *On the nature of the spiral nebulae*.

Lindblad B., 1963. *Stockholms Observatoriums Annaler*, **22**. *On the possibility of a quasi-stationary spiral structure in galaxies*.

Lindblad B., 1964. *Astrophysica Norvegica*, **9**, 103. *On the circulation theory of spiral structure*.

Lintott C. J., Schawinski K., Slosar A., Land K., Bamford S., Thomas D., Raddick M. J., Nichol R. C., Szalay A., Andreescu D., Murray P., Vandenberg J., 2008. *MNRAS*, **389**, 1179. *Galaxy Zoo: morphologies derived from visual inspection of galaxies from the Sloan Digital Sky Survey*.

Lintott C., Schawinski K., Bamford S., Slosar A., Land K., Thomas D., Edmondson E., Masters K., Nichol R. C., Raddick M. J., Szalay A., Andreescu D., Murray P., Vandenberg J., 2011. *MNRAS*, **410**, 166. *Galaxy Zoo 1: data release of morphological classifications for nearly 900 000 galaxies*.

Lupton R., Blanton M. R., Fekete G., Hogg D. W., O'Mullane W., Szalay A., Wherry N., 2004. PASP, **116**, 133. *Preparing Red-Green-Blue Images from CCD Data*.

Lynds B. T., 1970. *The Distribution of Dark Nebulae in Late-Type Spirals*, In: *The Spiral Structure of our Galaxy*, 26, eds Becker W., Kontopoulos G. I.

Macciò A. V., Dutton A. A., van den Bosch F. C., Moore B., Potter D., Stadel J., 2007. MNRAS, **378**, 55. *Concentration, spin and shape of dark matter haloes: scatter and the dependence on mass and environment*.

Maller A. H., 2008. *Halo Mergers, Galaxy Mergers, and Why Hubble Type Depends on Mass*, In: *Formation and Evolution of Galaxy Disks*, 251, eds Funes J. G., Corsini E. M.

Mandelbaum R., Seljak U., Cool R. J., Blanton M., Hirata C. M., Brinkmann J., 2006. *MNRAS*, **372**, 758. *Density profiles of galaxy groups and clusters from SDSS galaxy-galaxy weak lensing*.

Martig M., Bournaud F., Teyssier R., Dekel A., 2009. ApJ, **707**, 250. *Morphological Quenching of Star Formation: Making Early-Type Galaxies Red*.

Martig M., Crocker A. F., Bournaud F., Emsellem E., Gabor J. M., Alatalo K., Blitz L., Bois M., Bureau M., Cappellari M., Davies R. L., Davis T. A., Dekel A., de Zeeuw P. T., Duc P.-A., Falcón-Barroso J., Khochfar S., Krajnović D., Kuntschner H., Morganti R., McDermid R. M., Naab T., Oosterloo T., Sarzi M., Scott N., Serra P., Griffin K. S., Teyssier R., Weijmans A.-M., Young L. M., 2013. MNRAS, **432**, 1914. *The ATLAS^{3D} project - XXII. Low-efficiency star formation in early-type galaxies: hydrodynamic models and observations*.

Martin D. C., Fanson J., Schiminovich D., Morrissey P., Friedman P. G., Barlow T. A., Conrow T., Grange R., Jelinsky P. N., Milliard B., Siegmund O. H. W., Bianchi L., Byun Y.-I., Donas J., Forster K., Heckman T. M., Lee Y.-W., Madore B. F., Malina R. F., Neff S. G., Rich R. M., Small T., Surber F., Szalay A. S., Welsh B., Wyder T. K., 2005. *ApJL*, **619**, L1. *The Galaxy Evolution Explorer: A Space Ultraviolet Survey Mission*.

Martínez-García E. E., 2012. *ApJ*, **744**, 92. *Testing Theories in Barred-spiral Galaxies*.

Martinsson T. P. K., Verheijen M. A. W., Westfall K. B., Bershady M. A., Andersen D. R., Swaters R. A., 2013. *A&A*, **557**, A131. *The DiskMass Survey. VII. The distribution of luminous and dark matter in spiral galaxies*.

Masset F., Tagger M., 1997. A&A, **322**, 442. *Non-linear coupling of spiral waves in disk galaxies: a numerical study.*

Masters K. L., Mosleh M., Romer A. K., Nichol R. C., Bamford S. P., Schawinski K., Lintott C. J., Andreescu D., Campbell H. C., Crowcroft B., Doyle I., Edmondson E. M., Murray P., Raddick M. J., Slosar A., Szalay A. S., Vandenberg J., 2010a. MNRAS, **405**, 783. *Galaxy Zoo: passive red spirals*.

Masters K. L., Nichol R., Bamford S., Mosleh M., Lintott C. J., Andreescu D., Edmondson E. M., Keel W. C., Murray P., Raddick M. J., Schawinski K., Slosar A., Szalay A. S., Thomas D., Vandenberg J., 2010b. *MNRAS*, **404**, 792. *Galaxy Zoo: dust in spiral galaxies*.

Masters K. L., Nichol R. C., Hoyle B., Lintott C., Bamford S. P., Edmondson E. M., Fortson L., Keel W. C., Schawinski K., Smith A. M., Thomas D., 2011. *MNRAS*, **411**, 2026. *Galaxy Zoo: bars in disc galaxies*.

Masters K. L., Nichol R. C., Haynes M. P., Keel W. C., Lintott C., Simmons B., Skibba R., Bamford S., Giovanelli R., Schawinski K., 2012. MNRAS, **424**, 2180. *Galaxy Zoo and ALFALFA: atomic gas and the regulation of star formation in barred disc galaxies*.

Masters K. L., Lintott C. J., Hart R. E., Kruk S. J., Smethurst R. J., Casteels K. R. V., Keel W. C., Willett K. W., in prep. *The Galaxy Zoo view of the Hubble sequence*.

McGee R. X., Milton J. A., 1964. *Australian Journal of Physics*, **17**, 128. *A sky survey of neutral hydrogen at λ 21 cm. III. Gas at higher radial velocities*.

Meidt S. E., Schinnerer E., Knapen J. H., Bosma A., Athanassoula E., Sheth K., Buta R. J., Zaritsky D., Laurikainen E., Elmegreen D., Elmegreen B. G., Gadotti D. A., Salo H., Regan M., Ho L. C., Madore B. F., Hinz J. L., Skibba R. A., Gil de Paz A., Muñoz-Mateos J.-C., Menéndez-Delmestre K., Seibert M., Kim T., Mizusawa T., Laine J., Comerón S., 2012. ApJ, **744**, 17. *Reconstructing the Stellar Mass Distributions of Galaxies Using S^4G IRAC 3.6 and 4.5 μm Images. I. Correcting for Contamination by Polycyclic Aromatic Hydrocarbons, Hot Dust, and Intermediate-age Stars*.

Meidt S. E., Schinnerer E., García-Burillo S., Hughes A., Colombo D., Pety J., Dobbs C. L., Schuster K. F., Kramer C., Leroy A. K., Dumas G., Thompson T. A., 2013. ApJ, **779**, 45. *Gas Kinematics on Giant Molecular Cloud Scales in M51 with PAWS: Cloud Stabilization through Dynamical Pressure*.

Melbourne W. G., 1960. ApJ, **132**, 101. *Line-Blanketing Effects on A-G Dwarfs.*

Melvin T., Masters K., Lintott C., Nichol R. C., Simmons B., Bamford S. P., Casteels K. R. V., Cheung E., Edmondson E. M., Fortson L., Schawinski K., Skibba R. A., Smith A. M., Willett K. W., 2014. *MNRAS*, **438**, 2882. *Galaxy Zoo: an independent look at the evolution of the bar fraction over the last eight billion years from HST-COSMOS*.

Mendel J. T., Simard L., Palmer M., Ellison S. L., Patton D. R., 2014. *ApJS*, **210**, 3. *A Catalog of Bulge, Disk, and Total Stellar Mass Estimates for the Sloan Digital Sky Survey*.

Merrifield M. R., Rand R. J., Meidt S. E., 2006. *MNRAS*, **366**, L17. *The lifetime of grand design*.

Meurer G. R., Heckman T. M., Calzetti D., 1999. *ApJ*, **521**, 64. *Dust Absorption and the Ultraviolet Luminosity Density at z ˜ 3 as Calibrated by Local Starburst Galaxies*.

Michikoshi S., Kokubo E., 2014. *ApJ*, **787**, 174. *Pitch Angle of Galactic Spiral Arms*.

Michikoshi S., Kokubo E., 2016. *ApJ*, **823**, 121. *Swing Amplification of Galactic Spiral Arms: Phase Synchronization of Stellar Epicycle Motion*.

Miller R. H., Prendergast K. H., Quirk W. J., 1970. ApJ, **161**, 903. *Numerical Experiments on Spiral Structure*.

Moles M., Marquez I., Perez E., 1995. ApJ, **438**, 604. *The relation between dynamical perturbations, morphology, and nuclear activity in spiral galaxies*.

Moore T. J. T., Urquhart J. S., Morgan L. K., Thompson M. A., 2012. *MNRAS*, **426**, 701. *The effect of spiral arms on star formation in the Galaxy*.

More S., van den Bosch F. C., Cacciato M., Skibba R., Mo H. J., Yang X., 2011. *MNRAS*, **410**, 210. *Satellite kinematics - III. Halo masses of central galaxies in SDSS*.

Morgan W. W., Whitford A. E., Code A. D., 1953. *ApJ*, **118**, 318. *Studies in Galactic Structure. I. a Preliminary Determination of the Space Distribution of the Blue Giants.*

Morselli L., Renzini A., Popesso P., Erfanianfar G., 2016. *MNRAS*, **462**, 2355. *The effect of disc inclination on the main sequence of star-forming galaxies*.

Muñoz-Mateos J. C., Sheth K., Gil de Paz A., Meidt S., Athanassoula E., Bosma A., Comerón S., Elmegreen D. M., Elmegreen B. G., Erroz-Ferrer S., Gadotti D. A., Hinz J. L., Ho L. C., Holwerda B., Jarrett T. H., Kim T., Knapen J. H., Laine J., Laurikainen E., Madore B. F., Menendez-Delmestre K., Mizusawa T., Regan M., Salo H., Schinnerer E., Seibert M., Skibba R., Zaritsky D., 2013. *ApJ*, **771**, 59. *The Impact of Bars on Disk Breaks as Probed by S^4G Imaging*.

Muñoz-Mateos J. C., Sheth K., Regan M., Kim T., Laine J., Erroz-Ferrer S., Gil de Paz A., Comeron S., Hinz J., Laurikainen E., Salo H., Athanassoula E., Bosma A., Bouquin A. Y. K., Schinnerer E., Ho L., Zaritsky D., Gadotti D. A., Madore B., Holwerda B., Menéndez-Delmestre K., Knapen J. H., Meidt S., Querejeta M., Mizusawa

T., Seibert M., Laine S., Courtois H., 2015. *ApJS*, **219**, 3. *The Spitzer Survey of Stellar Structure in Galaxies (S^4G): Stellar Masses, Sizes, and Radial Profiles for 2352 Nearby Galaxies*.

Murphy E. J., Condon J. J., Schinnerer E., Kennicutt R. C., Calzetti D., Armus L., Helou G., Turner J. L., Aniano G., Beirão P., Bolatto A. D., Brandl B. R., Croxall K. V., Dale D. A., Donovan Meyer J. L., Draine B. T., Engelbracht C., Hunt L. K., Hao C.-N., Koda J., Roussel H., Skibba R., Smith J.-D. T., 2011. *ApJ*, **737**, 67. *Calibrating Extinction-free Star Formation Rate Diagnostics with 33 GHz Free-free Emission in NGC 6946*.

Mutlu-Pakdil B., Seigar M. S., Hewitt I. B., Treuthardt P., Berrier J. C., Koval L. E., 2018. *MNRAS*, **474**, 2594. *The Illustris simulation: supermassive black hole-galaxy connection beyond the bulge*.

Naim A., Lahav O., Buta R. J., Corwin, Jr. H. G., de Vaucouleurs G., Dressler A., Huchra J. P., van den Bergh S., Raychaudhury S., Sodre, Jr. L., Storrie-Lombardi M. C., 1995. MNRAS, **274**, 1107. *A comparative study of morphological classifications of APM galaxies*.

Nair P. B., Abraham R. G., 2010. *ApJS*, **186**, 427. *A Catalog of Detailed Visual Morphological Classifications for 14,034 Galaxies in the Sloan Digital Sky Survey*.

Navarro J. F., Frenk C. S., White S. D. M., 1996. *ApJ*, **462**, 563. *The Structure of Cold Dark Matter Halos*.

Navarro J. F., Frenk C. S., White S. D. M., 1997. *ApJ*, **490**, 493. *A Universal Density Profile from Hierarchical Clustering*.

Noeske K. G., Faber S. M., Weiner B. J., Koo D. C., Primack J. R., Dekel A., Papovich C., Conselice C. J., Le Floc'h E., Rieke G. H., Coil A. L., Lotz J. M., Somerville R. S., Bundy K., 2007a. ApJ, **660**, L47. *Star Formation in AEGIS Field Galaxies since z=1.1: Staged Galaxy Formation and a Model of Mass-dependent Gas Exhaustion*.

Noeske K. G., Weiner B. J., Faber S. M., Papovich C., Koo D. C., Somerville R. S., Bundy K., Conselice C. J., Newman J. A., Schiminovich D., Le Floc'h E., Coil A. L., Rieke G. H., Lotz J. M., Primack J. R., Barmby P., Cooper M. C., Davis M., Ellis R. S., Fazio G. G., Guhathakurta P., Huang J., Kassin S. A., Martin D. C., Phillips A. C., Rich R. M., Small T. A., Willmer C. N. A., Wilson G., 2007b. ApJ, **660**, L43. *Star Formation in AEGIS Field Galaxies since z=1.1: The Dominance of Gradually Declining Star Formation, and the Main Sequence of Star-forming Galaxies*.

Ogle P. M., Lanz L., Nader C., Helou G., 2016. *ApJ*, **817**, 109. *Superluminous Spiral Galaxies*.

Oh S. H., Kim W.-T., Lee H. M., Kim J., 2008. ApJ, **683**, 94. *Physical Properties of Tidal Features in Interacting Disk Galaxies*.

Oh S.-H., Brook C., Governato F., Brinks E., Mayer L., de Blok W. J. G., Brooks A., Walter F., 2011. *AJ*, **142**, 24. *The Central Slope of Dark Matter Cores in Dwarf Galaxies: Simulations versus THINGS*.

Oh S. H., Kim W.-T., Lee H. M., 2015. ApJ, **807**, 73. *Physical Properties of Tidal Features of Interacting Disk Galaxies: Three-dimensional Self-consistent Models*.

Oh S., Oh K., Yi S. K., 2012. *ApJS*, **198**, 4. *Bar Effects on Central Star Formation and Active Galactic Nucleus Activity*.

Onodera S., Kuno N., Tosaki T., Kohno K., Nakanishi K., Sawada T., Muraoka K., Komugi S., Miura R., Kaneko H., Hirota A., Kawabe R., 2010. ApJ, **722**, L127. *Breakdown of Kennicutt-Schmidt Law at Giant Molecular Cloud Scales in M33*.

Oort J. H., 1962. *Spiral Structure*, In: *The Distribution and Motion of Interstellar Matter in Galaxies*, 234, ed. Woltjer L.

Ostriker J. P., Peebles P. J. E., 1973. ApJ, **186**, 467. *A Numerical Study of the Stability of Flattened Galaxies: or, can Cold Galaxies Survive?*

Overzier R. A., Heckman T. M., Wang J., Armus L., Buat V., Howell J., Meurer G., Seibert M., Siana B., Basu-Zych A., Charlot S., Gonçalves T. S., Martin D. C., Neill J. D., Rich R. M., Salim S., Schiminovich D., 2011. *ApJL*, **726**, L7. *Dust Attenuation in UV-selected Starbursts at High Redshift and Their Local Counterparts: Implications for the Cosmic Star Formation Rate Density*.

Padoan P., Juvela M., Pan L., Haugbølle T., Nordlund Å., 2016. ApJ, **826**, 140. *Supernova Driving. III. Synthetic Molecular Cloud Observations*.

Parravano A., Hollenbach D. J., McKee C. F., 2003. *ApJ*, **584**, 797. *Time Dependence of the Ultraviolet Radiation Field in the Local Interstellar Medium*.

Pasha I. I., 2004. *ArXiv Astrophysics e-prints*. *Density-Wave Spiral Theories in the 1960s. I*.

Patton D. R., Qamar F. D., Ellison S. L., Bluck A. F. L., Simard L., Mendel J. T., Moreno J., Torrey P., 2016. *MNRAS*, **461**, 2589. *Galaxy pairs in the Sloan Digital Sky Survey - XI. A new method for measuring the influence of the closest companion out to wide separations*.

Pawlik M. M., Wild V., Walcher C. J., Johansson P. H., Villforth C., Rowlands K., Mendez-Abreu J., Hewlett T., 2016. MNRAS, **456**, 3032. *Shape asymmetry: a morphological indicator for automatic detection of galaxies in the post-coalescence merger stages*.

Pedregosa F., Varoquaux G., Gramfort A., Michel V., Thirion B., Grisel O., Blondel M., Prettenhofer P., Weiss R., Dubourg V., Vanderplas J., Passos A., Cournapeau D., Brucher M., Perrot M., Duchesnay E., 2011. *Journal of Machine Learning Research*, **12**, 2825. *Scikit-learn: Machine Learning in Python*.

Peng Y., Maiolino R., Cochrane R., 2015. *Nature*, **521**, 192. *Strangulation as the primary mechanism for shutting down star formation in galaxies*.

Pérez-Villegas A., Pichardo B., Moreno E., Peimbert A., Velázquez H. M., 2012. *ApJL*, **745**, L14. *Pitch Angle Restrictions in Late-type Spiral Galaxies Based on Chaotic and Ordered Orbital Behavior*.

Pety J., Schinnerer E., Leroy A. K., Hughes A., Meidt S. E., Colombo D., Dumas G., García-Burillo S., Schuster K. F., Kramer C., Dobbs C. L., Thompson T. A., 2013. ApJ, **779**, 43. *The Plateau de Bure + 30 m Arcsecond Whirlpool Survey Reveals a Thick Disk of Diffuse Molecular Gas in the M51 Galaxy*.

Planck Collaboration, Ade P. A. R., Aghanim N., Arnaud M., Ashdown M., Aumont J., Baccigalupi C., Banday A. J., Barreiro R. B., Bartlett J. G., et al., 2016. *A&A*, **594**, A13. *Planck 2015 results. XIII. Cosmological parameters*.

Pontzen A., Governato F., 2012. *MNRAS*, **421**, 3464. *How supernova feedback turns dark matter cusps into cores*.

Popescu C. C., Misiriotis A., Kylafis N. D., Tuffs R. J., Fischera J., 2000. A&A, **362**, 138. *Modelling the spectral energy distribution of galaxies. I. Radiation fields and grain heating in the edge-on spiral NGC 891*.

Postman M., Geller M. J., 1984. *ApJ*, **281**, 95. *The morphology-density relation - The group connection*.

Pour-Imani H., Kennefick D., Kennefick J., Davis B. L., Shields D. W., Shameer Abdeen M., 2016. ApJ, **827**, L2. *Strong Evidence for the Density-wave Theory of Spiral Structure in Disk Galaxies*.

Pozzetti L., Bolzonella M., Zucca E., Zamorani G., Lilly S., Renzini A., Moresco M., Mignoli M., Cassata P., Tasca L., Lamareille F., Maier C., Meneux B., Halliday C., Oesch P., Vergani D., Caputi K., Kovač K., Cimatti A., Cucciati O., Iovino A., Peng Y., Carollo M., Contini T., Kneib J.-P., Le Févre O., Mainieri V., Scodeggio M., Bardelli S., Bongiorno A., Coppa G., de la Torre S., de Ravel L., Franzetti P., Garilli B., Kampczyk P., Knobel C., Le Borgne J.-F., Le Brun V., Pellò R., Perez Montero E., Ricciardelli E., Silverman J. D., Tanaka M., Tresse L., Abbas U., Bottini D., Cappi A., Guzzo L., Koekemoer A. M., Leauthaud A., Maccagni D., Marinoni C., McCracken H. J., Memeo P., Porciani C., Scaramella R., Scarlata C., Scoville N., 2010. *A&A*, **523**, A13. *zCOSMOS - 10k-bright spectroscopic sample. The bimodality in the galaxy stellar mass function: exploring its evolution with redshift*.

Prendergast K. H., Burbidge G. R., 1960. *ApJ*, **131**, 243. *The Persistence of Spiral Structure.*

Puerari I., Dottori H. A., 1992. *A&AS*, **93**, 469. *Fourier analysis of structure in spiral galaxies*.

Querejeta M., Meidt S. E., Schinnerer E., Cisternas M., Muñoz-Mateos J. C., Sheth K., Knapen J., van de Ven G., Norris M. A., Peletier R., Laurikainen E., Salo H., Holwerda B. W., Athanassoula E., Bosma A., Groves B., Ho L. C., Gadotti D. A., Zaritsky D., Regan M., Hinz J., Gil de Paz A., Menendez-Delmestre K., Seibert M., Mizusawa T., Kim T., Erroz-Ferrer S., Laine J., Comerón S., 2015. *ApJS*, **219**, 5. *The Spitzer Survey of Stellar Structure in Galaxies (S^4G): Precise Stellar Mass Distributions from Automated Dust Correction at 3.6 μm*.

Rautiainen P., Salo H., 1999. A&A, **348**, 737. *Multiple pattern speeds in barred galaxies. I. Two-dimensional models*.

Read J. I., Gilmore G., 2005. *MNRAS*, **356**, 107. *Mass loss from dwarf spheroidal galaxies: the origins of shallow dark matter cores and exponential surface brightness profiles*.

Rieke G. H., Alonso-Herrero A., Weiner B. J., Pérez-González P. G., Blaylock M., Donley J. L., Marcillac D., 2009. *ApJ*, **692**, 556. *Determining Star Formation Rates for Infrared Galaxies*.

Rix H.-W., Zaritsky D., 1995. *ApJ*, **447**, 82. *Nonaxisymmetric Structures in the Stellar Disks of Galaxies*.

Roberts M. S., Haynes M. P., 1994. *ARAA*, **32**, 115. *Physical Parameters along the Hubble Sequence*.

Roberts M. S., 1963. ARA&A, **1**, 149. *The Content of Galaxies: Stars and Gas*.

Roberts W. W., 1969. ApJ, **158**, 123. *Large-Scale Shock Formation in Spiral Galaxies and its Implications on Star Formation*.

Robotham A., Driver S. P., Norberg P., Baldry I. K., Bamford S. P., Hopkins A. M., Liske J., Loveday J., Peacock J. A., Cameron E., Croom S. M., Doyle I. F., Frenk C. S., Hill D. T., Jones D. H., van Kampen E., Kelvin L. S., Kuijken K., Nichol R. C., Parkinson H. R., Popescu C. C., Prescott M., Sharp R. G., Sutherland W. J., Thomas D., Tuffs R. J., 2010. *PASA*, **27**, 76. *Galaxy and Mass Assembly (GAMA): Optimal Tiling of Dense Surveys with a Multi-Object Spectrograph*.

Roca-Fàbrega S., Valenzuela O., Figueras F., Romero-Gómez M., Velázquez H., Antoja T., Pichardo B., 2013. *MNRAS*, **432**, 2878. *On galaxy spiral arms' nature as revealed by rotation frequencies*.

Romanishin W., 1985. *ApJ*, **289**, 570. *Star formation in grand design and flocculent spiral galaxies*.

Romanishin W., 1990. *Star Formation, Metallicity, and the Colors of Spiral Galaxies*, In: *Bulletin of the American Astronomical Society*, 865.

Romero-Gómez M., Masdemont J. J., Athanassoula E., García-Gómez C., 2006. *A&A*, **453**, 39. *The origin of rR_1 ring structures in barred galaxies*.

Romero-Gómez M., Athanassoula E., Masdemont J. J., García-Gómez C., 2007. *A&A*, **472**, 63. *The formation of spiral arms and rings in barred galaxies*.

Rosse T. E. O., 1850. *Philosophical Transactions of the Royal Society of London Series I*, **140**, 499. *Observations on the Nebulae*.

Rots A. H., Shane W. W., 1974. *A&A*, **31**, 245. *A high resolution map of the distribution of neutral hydrogen in the spiral galaxy M81.*

Rots A. H., Shane W. W., 1975. *A&A*, **45**, 25. *Distribution and kinematics of neutral hydrogen in the spiral galaxy M 81. I - Observations*.

Roussel H., Gil de Paz A., Seibert M., Helou G., Madore B. F., Martin C., 2005. ApJ, **632**, 227. *Extinction Law Variations and Dust Excitation in the Spiral Galaxy NGC 300*.

Roškar R., Debattista V. P., Quinn T. R., Stinson G. S., Wadsley J., 2008a. ApJ, **684**, L79. *Riding the Spiral Waves: Implications of Stellar Migration for the Properties of Galactic Disks*.

Roškar R., Debattista V. P., Stinson G. S., Quinn T. R., Kaufmann T., Wadsley J., 2008b. ApJ, **675**, L65. *Beyond Inside-Out Growth: Formation and Evolution of Disk Outskirts*.

Roškar R., Debattista V. P., Quinn T. R., Wadsley J., 2012. MNRAS, **426**, 2089. *Radial migration in disc galaxies - I. Transient spiral structure and dynamics*.

Rowlands K., Dunne L., Maddox S., Bourne N., Gomez H. L., Kaviraj S., Bamford S. P., Brough S., Charlot S., da Cunha E., Driver S. P., Eales S. A., Hopkins A. M., Kelvin L., Nichol R. C., Sansom A. E., Sharp R., Smith D. J. B., Temi P., van der Werf P., Baes M., Cava A., Cooray A., Croom S. M., Dariush A., de Zotti G., Dye S., Fritz J., Hopwood R., Ibar E., Ivison R. J., Liske J., Loveday J., Madore B., Norberg P., Popescu C. C., Rigby E. E., Robotham A., Rodighiero G., Seibert M., Tuffs R. J., 2012. *MNRAS*, **419**, 2545. *Herschel-ATLAS/GAMA: dusty early-type galaxies and passive spirals*.

Saintonge A., Kauffmann G., Wang J., Kramer C., Tacconi L. J., Buchbender C., Catinella B., Graciá-Carpio J., Cortese L., Fabello S., Fu J., Genzel R., Giovanelli R., Guo Q., Haynes M. P., Heckman T. M., Krumholz M. R., Lemonias J., Li C., Moran S., Rodriguez-Fernandez N., Schiminovich D., Schuster K., Sievers A., 2011. *MNRAS*, **415**, 61. *COLD GASS, an IRAM legacy survey of molecular gas in massive galaxies - II. The non-universality of the molecular gas depletion time-scale*.

Saintonge A., Tacconi L. J., Fabello S., Wang J., Catinella B., Genzel R., Graciá-Carpio J., Kramer C., Moran S., Heckman T. M., Schiminovich D., Schuster K., Wuyts S., 2012. *ApJ*, **758**, 73. *The Impact of Interactions, Bars, Bulges, and Active Galactic Nuclei on Star Formation Efficiency in Local Massive Galaxies*.

Saintonge A., Lutz D., Genzel R., Magnelli B., Nordon R., Tacconi L. J., Baker A. J., Bandara K., Berta S., Förster Schreiber N. M., Poglitsch A., Sturm E., Wuyts E., Wuyts S., 2013. *ApJ*, **778**, 2. *Validation of the Equilibrium Model for Galaxy Evolution to z ˜ 3 through Molecular Gas and Dust Observations of Lensed Star-forming Galaxies*.

Saintonge A., Catinella B., Cortese L., Genzel R., Giovanelli R., Haynes M. P., Janowiecki S., Kramer C., Lutz K. A., Schiminovich D., Tacconi L. J., Wuyts S., Accurso G., 2016. *MNRAS*, **462**, 1749. *Molecular and atomic gas along and across the main sequence of star-forming galaxies*.

Salim S., Rich R. M., Charlot S., Brinchmann J., Johnson B. D., Schiminovich D., Seibert M., Mallery R., Heckman T. M., Forster K., Friedman P. G., Martin D. C., Morrissey P., Neff S. G., Small T., Wyder T. K., Bianchi L., Donas J., Lee Y.-W., Madore B. F., Milliard B., Szalay A. S., Welsh B. Y., Yi S. K., 2007. *ApJS*, **173**, 267. *UV Star Formation Rates in the Local Universe*.

Salim S., Lee J. C., Janowiecki S., da Cunha E., Dickinson M., Boquien M., Burgarella D., Salzer J. J., Charlot S., 2016. *ApJS*, **227**, 2. *GALEX-SDSS-WISE Legacy*

Catalog (GSWLC): Star Formation Rates, Stellar Masses, and Dust Attenuations of 700,000 Low-redshift Galaxies.

Salo H., Laurikainen E., 2000. *MNRAS*, **319**, 377. *N-body model for M51 - I. Multiple encounter versus single passage?*

Salo H., Laurikainen E., Buta R., Knapen J. H., 2010. ApJ, **715**, L56. *Bars do Drive Spiral Density Waves*.

Salo H., Laurikainen E., Laine J., Comerón S., Gadotti D. A., Buta R., Sheth K., Zaritsky D., Ho L., Knapen J., Athanassoula E., Bosma A., Laine S., Cisternas M., Kim T., Muñoz-Mateos J. C., Regan M., Hinz J. L., Gil de Paz A., Menendez-Delmestre K., Mizusawa T., Erroz-Ferrer S., Meidt S. E., Querejeta M., 2015. *ApJS*, **219**, 4. *The Spitzer Survey of Stellar Structure in Galaxies (S^4G): Multi-component Decomposition Strategies and Data Release*.

Sandage A., Smith L. L., 1966. ApJ, **144**, 886. *The color-magnitude diagram of the metal-rich globular cluster NGC 6712*.

Sandage A., 1961. *The Hubble atlas of galaxies*.

Sanders D. B., Mirabel I. F., 1996. *ARAA*, **34**, 749. *Luminous Infrared Galaxies*.

Saraiva Schroeder M. F., Pastoriza M. G., Kepler S. O., Puerari I., 1994. *A&AS*, **108**. *The distribution of light in the spiral galaxy NGC 7412.*

Savchenko S. S., Reshetnikov V. P., 2013. *MNRAS*, **436**, 1074. *Pitch angle variations in spiral galaxies*.

Schawinski K., Urry C. M., Simmons B. D., Fortson L., Kaviraj S., Keel W. C., Lintott C. J., Masters K. L., Nichol R. C., Sarzi M., Skibba R., Treister E., Willett K. W., Wong O. I., Yi S. K., 2014. *MNRAS*, **440**, 889. *The green valley is a red herring: Galaxy Zoo reveals two evolutionary pathways towards quenching of star formation in early- and late-type galaxies*.

Schinnerer E., Meidt S. E., Colombo D., Chandar R., Dobbs C. L., Garcia-Burillo S., Hughes A., Leroy A. K., Pety J., Querejeta M., Kramer C., Schuster K. F., 2017. *ArXiv e-prints*. *The PdBI Arcsecond Whirlpool Survey (PAWS). The Role of Spiral Arms in Cloud and Star Formation*.

Schmidt M. *Rotation Parameters and Distribution of Mass in the Galaxy*, 513. the University of Chicago Press, 1965.

Schruba A., Leroy A. K., Walter F., Sandstrom K., Rosolowsky E., 2010. ApJ, **722**, 1699. *The Scale Dependence of the Molecular Gas Depletion Time in M33*.

Seiden P. E., Gerola H., 1979. *ApJ*, **233**, 56. *Properties of spiral galaxies from a stochastic star formation model*.

Seigar M. S., James P. A., 1998a. *MNRAS*, **299**, 672. *The structure of spiral galaxies - I. Near-infrared properties of bulges, discs and bars*.

Seigar M. S., James P. A., 1998b. *MNRAS*, **299**, 685. *The structure of spiral galaxies - II. Near-infrared properties of spiral arms*.

Seigar M. S., James P. A., 2002. *MNRAS*, **337**, 1113. *A test of arm-induced star formation in spiral galaxies from near-infrared and Hα imaging*.

Seigar M. S., Chorney N. E., James P. A., 2003. *MNRAS*, **342**, 1. *Near-infrared constraints on the driving mechanisms for spiral structure*.

Seigar M. S., Bullock J. S., Barth A. J., Ho L. C., 2006. *ApJ*, **645**, 1012. *Constraining Dark Matter Halo Profiles and Galaxy Formation Models Using Spiral Arm Morphology. I. Method Outline*.

Seigar M. S., Kennefick D., Kennefick J., Lacy C. H. S., 2008. *ApJL*, **678**, L93. *Discovery of a Relationship between Spiral Arm Morphology and Supermassive Black Hole Mass in Disk Galaxies*.

Seigar M. S., Davis B. L., Berrier J., Kennefick D., 2014. *ApJ*, **795**, 90. *Constraining Dark Matter Halo Profiles and Galaxy Formation Models Using Spiral Arm Morphology. II. Dark and Stellar Mass Concentrations for 13 Nearby Face-on Galaxies*.

Seigar M. S., 2005. *MNRAS*, **361**, L20. *The connection between shear and star formation in spiral galaxies*.

Sellwood J. A., Athanassoula E., 1986. MNRAS, **221**, 195. *Unstable modes from galaxy simulations*.

Sellwood J. A., Carlberg R. G., 1984. *ApJ*, **282**, 61. *Spiral instabilities provoked by accretion and star formation*.

Sellwood J. A., Carlberg R. G., 2014. *ApJ*, **785**, 137. *Transient Spirals as Superposed Instabilities*.

Sellwood J. A., Sparke L. S., 1988. MNRAS, **231**, 25P. *Pattern speeds in barred spiral galaxies*.

Sellwood J. A., Wilkinson A., 1993. *Reports on Progress in Physics*, **56**, 173. *Dynamics of barred galaxies*.

Sellwood J. A., 1985. MNRAS, **217**, 127. *The global stability of our Galaxy*.

Sellwood J. A., 2011. *MNRAS*, **410**, 1637. *The lifetimes of spiral patterns in disc galaxies*.

Semczuk M., Łokas E. L., del Pino A., 2017. *ApJ*, **834**, 7. *Tidal Origin of Spiral Arms in Galaxies Orbiting a Cluster*.

Sheth K., Regan M., Hinz J. L., Gil de Paz A., Menéndez-Delmestre K., Muñoz-Mateos J.-C., Seibert M., Kim T., Laurikainen E., Salo H., Gadotti D. A., Laine J., Mizusawa T., Armus L., Athanassoula E., Bosma A., Buta R. J., Capak P., Jarrett T. H., Elmegreen D. M., Elmegreen B. G., Knapen J. H., Koda J., Helou G., Ho L. C., Madore B. F., Masters K. L., Mobasher B., Ogle P., Peng C. Y., Schinnerer E., Surace J. A., Zaritsky D., Comerón S., de Swardt B., Meidt S. E., Kasliwal M., Aravena M., 2010. *PASP*, **122**, 1397. *The Spitzer Survey of Stellar Structure in Galaxies (S4G)*.

Silk J., 2003. Ap&SS, **284**, 663. *Formation and evolution of disk galaxies*.

Silva L., Granato G. L., Bressan A., Danese L., 1998. ApJ, **509**, 103. *Modeling the Effects of Dust on Galactic Spectral Energy Distributions from the Ultraviolet to the Millimeter Band*.

Simard L., Willmer C. N. A., Vogt N. P., Sarajedini V. L., Phillips A. C., Weiner B. J., Koo D. C., Im M., Illingworth G. D., Faber S. M., 2002. ApJS, **142**, 1. *The DEEP Groth Strip Survey. II. Hubble Space Telescope Structural Parameters of Galaxies in the Groth Strip*.

Simard L., Mendel J. T., Patton D. R., Ellison S. L., McConnachie A. W., 2011. *ApJS*, **196**, 11. *A Catalog of Bulge+disk Decompositions and Updated Photometry for 1.12 Million Galaxies in the Sloan Digital Sky Survey*.

Simmons B. D., Lintott C., Schawinski K., Moran E. C., Han A., Kaviraj S., Masters K. L., Urry C. M., Willett K. W., Bamford S. P., Nichol R. C., 2013. *MNRAS*, **429**, 2199. *Galaxy Zoo: bulgeless galaxies with growing black holes*.

Simmons B. D., Melvin T., Lintott C., Masters K. L., Willett K. W., Keel W. C., Smethurst R. J., Cheung E., Nichol R. C., Schawinski K., Rutkowski M., Kartaltepe J. S., Bell E. F., Casteels K. R. V., Conselice C. J., Almaini O., Ferguson H. C., Fortson L., Hartley W., Kocevski D., Koekemoer A. M., McIntosh D. H., Mortlock A., Newman J. A., Ownsworth J., Bamford S., Dahlen T., Faber S. M., Finkelstein S. L., Fontana A., Galametz A., Grogin N. A., Grützbauch R., Guo Y., Häußler B., Jek K. J., Kaviraj S., Lucas R. A., Peth M., Salvato M., Wiklind T., Wuyts S., 2014. *MNRAS*, **445**, 3466. *Galaxy Zoo: CANDELS barred discs and bar fractions*.

Simmons B. D., Smethurst R. J., Lintott C., 2017. *MNRAS*, **470**, 1559. *Supermassive black holes in disc-dominated galaxies outgrow their bulges and co-evolve with their host galaxies*.

Skibba R. A., Bamford S. P., Nichol R. C., Lintott C. J., Andreescu D., Edmondson E. M., Murray P., Raddick M. J., Schawinski K., Slosar A., Szalay A. S., Thomas D., Vandenberg J., 2009. *MNRAS*, **399**, 966. *Galaxy Zoo: disentangling the environmental dependence of morphology and colour*.

Skibba R. A., Masters K. L., Nichol R. C., Zehavi I., Hoyle B., Edmondson E. M., Bamford S. P., Cardamone C. N., Keel W. C., Lintott C., Schawinski K., 2012. *MNRAS*, **423**, 1485. *Galaxy Zoo: the environmental dependence of bars and bulges in disc galaxies*.

Smethurst R. J., Lintott C. J., Simmons B. D., Schawinski K., Marshall P. J., Bamford S., Fortson L., Kaviraj S., Masters K. L., Melvin T., Nichol R. C., Skibba R. A., Willett K. W., 2015. *MNRAS*, **450**, 435. *Galaxy Zoo: evidence for diverse star formation histories through the green valley*.

Smethurst R. J., Lintott C. J., Bamford S. P., Hart R. E., Kruk S. J., Masters K. L., Nichol R. C., Simmons B. D., 2017. MNRAS, **469**, 3670. *Galaxy Zoo: the interplay of quenching mechanisms in the group environment*.

Somerville R. S., Behroozi P., Pandya V., Dekel A., Faber S. M., Fontana A., Koekemoer A. M., Koo D. C., Pérez-González P. G., Primack J. R., Santini P., Taylor E. N., van der Wel A., 2018. MNRAS, **473**, 2714. *The relationship between galaxy and dark matter halo size from z 3 to the present*.

Sonnenfeld A., Treu T., Marshall P. J., Suyu S. H., Gavazzi R., Auger M. W., Nipoti C., 2015. *ApJ*, **800**, 94. *The SL2S Galaxy-scale Lens Sample. V. Dark Matter Halos and Stellar IMF of Massive Early-type Galaxies Out to Redshift 0.8*.

Sparke L. S., Sellwood J. A., 1987. MNRAS, **225**, 653. *Dissection of an N-body bar*.

Speagle J. S., Steinhardt C. L., Capak P. L., Silverman J. D., 2014. *ApJS*, **214**, 15. *A Highly Consistent Framework for the Evolution of the Star-Forming "Main Sequence" from z ˜ 0-6*.

Spergel D. N., Verde L., Peiris H. V., Komatsu E., Nolta M. R., Bennett C. L., Halpern M., Hinshaw G., Jarosik N., Kogut A., Limon M., Meyer S. S., Page L., Tucker G. S., Weiland J. L., Wollack E., Wright E. L., 2003. *ApJS*, **148**, 175. *First-Year Wilkinson Microwave Anisotropy Probe (WMAP) Observations: Determination of Cosmological Parameters*.

Springel V., 2005. MNRAS, **364**, 1105. *The cosmological simulation code GADGET-2*.

Sreejith S., Pereverzyev, Jr. S., Kelvin L. S., Marleau F. R., Haltmeier M., Ebner J., Bland-Hawthorn J., Driver S. P., Graham A. W., Holwerda B. W., Hopkins A. M., Liske J., Loveday J., Moffett A. J., Pimbblet K. A., Taylor E. N., Wang L., Wright A. H., 2018. *MNRAS*, **474**, 5232. *Galaxy And Mass Assembly: automatic morphological classification of galaxies using statistical learning*.

Stark A. A., Elmegreen B. G., Chance D., 1987. *ApJ*, **322**, 64. *Molecules in galaxies. V - CO observations of flocculent and grand-design spirals*.

Strateva I., Ivezić Ž., Knapp G. R., Narayanan V. K., Strauss M. A., Gunn J. E., Lupton R. H., Schlegel D., Bahcall N. A., Brinkmann J., Brunner R. J., Budavári T., Csabai I., Castander F. J., Doi M., Fukugita M., Győry Z., Hamabe M., Hennessy G., Ichikawa T., Kunszt P. Z., Lamb D. Q., McKay T. A., Okamura S., Racusin J., Sekiguchi M., Schneider D. P., Shimasaku K., York D., 2001. AJ, **122**, 1861. *Color Separation of Galaxy Types in the Sloan Digital Sky Survey Imaging Data*.

Strauss M. A., Weinberg D. H., Lupton R. H., Narayanan V. K., Annis J., Bernardi M., Blanton M., Burles S., Connolly A. J., Dalcanton J., Doi M., Eisenstein D., Frieman J. A., Fukugita M., Gunn J. E., Ivezić Ž., Kent S., Kim R. S. J., Knapp G. R., Kron R. G., Munn J. A., Newberg H. J., Nichol R. C., Okamura S., Quinn T. R., Richmond M. W., Schlegel D. J., Shimasaku K., SubbaRao M., Szalay A. S., Vanden Berk D., Vogeley M. S., Yanny B., Yasuda N., York D. G., Zehavi I., 2002. *AJ*, **124**, 1810. *Spectroscopic Target Selection in the Sloan Digital Sky Survey: The Main Galaxy Sample*.

Struck C., Dobbs C. L., Hwang J.-S., 2011. *MNRAS*, **414**, 2498. *Slowly breaking waves: the longevity of tidally induced spiral structure*.

Sundelius B., Thomasson M., Valtonen M. J., Byrd G. G., 1987. *A&A*, **174**, 67. *Tidal spiral arms in two-component galaxies - Density waves and swing amplification*.

Swaters R. A., Madore B. F., van den Bosch F. C., Balcells M., 2003. *ApJ*, **583**, 732. *The Central Mass Distribution in Dwarf and Low Surface Brightness Galaxies*.

Tabor M., Merrifield M., Aragón-Salamanca A., Cappellari M., Bamford S. P., Johnston E., 2017. MNRAS, **466**, 2024. *Untangling galaxy components: full spectral bulge-disc decomposition*.

Tagger M., Sygnet J. F., Athanassoula E., Pellat R., 1987. ApJ, **318**, L43. *Nonlinear coupling of galactic spiral modes*.

Tan J. C., 2000. ApJ, **536**, 173. *Star Formation Rates in Disk Galaxies and Circumnuclear Starbursts from Cloud Collisions*.

Teimoorinia H., Ellison S. L., Patton D. R., 2017. *MNRAS*, **464**, 3796. *Pattern recognition in the ALFALFA.70 and Sloan Digital Sky Surveys: a catalogue of 500 000 H I gas fraction estimates based on artificial neural networks*.

Theis C., Spinneker C., 2003. *A&AS*, **284**, 495. *M51 revisited: A genetic algorithm approach of its interaction history*.

Thornley M. D., 1996. *ApJL*, **469**, L45. *Uncovering Spiral Structure in Flocculent Galaxies*.

Tojeiro R., Masters K. L., Richards J., Percival W. J., Bamford S. P., Maraston C., Nichol R. C., Skibba R., Thomas D., 2013. *MNRAS*, **432**, 359. *The different star formation histories of blue and red spiral and elliptical galaxies*.

Toomre A., Toomre J., 1972a. *ApJ*, **178**, 623. *Galactic Bridges and Tails*.

Toomre A., Toomre J., 1972b. *Model of the Encounter Between NGC 5194 and 5195.*, In: *Bulletin of the American Astronomical Society*, 214.

Toomre A., 1964. *ApJ*, **139**, 1217. *On the gravitational stability of a disk of stars*.

Toomre A., 1981. *What amplifies the spirals*, In: *Structure and Evolution of Normal Galaxies*, p. 111, eds Fall S. M., Lynden-Bell D.

Tremonti C. A., Heckman T. M., Kauffmann G., Brinchmann J., Charlot S., White S. D. M., Seibert M., Peng E. W., Schlegel D. J., Uomoto A., Fukugita M., Brinkmann J., 2004. ApJ, **613**, 898. *The Origin of the Mass-Metallicity Relation: Insights from 53,000 Star-forming Galaxies in the Sloan Digital Sky Survey*.

Tuffs R. J., Popescu C. C., Völk H. J., Kylafis N. D., Dopita M. A., 2004. *A&A*, **419**, 821. *Modelling the spectral energy distribution of galaxies. III. Attenuation of stellar light in spiral galaxies*.

Tully R. B., 1974. ApJS, **27**, 449. *The Kinematics and Dynamics of M51. III. The Spiral Structure*.

Unterborn C. T., Ryden B. S., 2008. *ApJ*, **687**, 976. *Inclination-Dependent Extinction Effects in Disk Galaxies in the Sloan Digital Sky Survey*.

van den Bosch F. C., Robertson B. E., Dalcanton J. J., de Blok W. J. G., 2000. AJ, **119**, 1579. *Constraints on the Structure of Dark Matter Halos from the Rotation Curves of Low Surface Brightness Galaxies*.

van der Wel A., Chang Y.-Y., Bell E. F., Holden B. P., Ferguson H. C., Giavalisco M., Rix H.-W., Skelton R., Whitaker K., Momcheva I., Brammer G., Kassin S. A., Martig M., Dekel A., Ceverino D., Koo D. C., Mozena M., van Dokkum P. G., Franx M., Faber S. M., Primack J., 2014. ApJ, **792**, L6. *Geometry of Star-forming Galaxies from SDSS, 3D-HST, and CANDELS*.

Veilleux S., Kim D.-C., Sanders D. B., 2002. ApJS, **143**, 315. *Optical and Near-Infrared Imaging of the IRAS 1 Jy Sample of Ultraluminous Infrared Galaxies. II. The Analysis*.

Vogel S. N., Kulkarni S. R., Scoville N. Z., 1988. *Nat*, **334**, 402. *Star formation in giant molecular associations synchronized by a spiral density wave*.

Vulcani B., Bamford S. P., Häußler B., Vika M., Rojas A., Agius N. K., Baldry I., Bauer A. E., Brown M. J. I., Driver S., Graham A. W., Kelvin L. S., Liske J., Loveday J., Popescu C. C., Robotham A. S. G., Tuffs R. J., 2014. *MNRAS*, **441**, 1340. *Galaxy And Mass Assembly (GAMA): the wavelength-dependent sizes and profiles of galaxies revealed by MegaMorph*.

Wada K., Baba J., Saitoh T. R., 2011. *ApJ*, **735**, 1. *Interplay between Stellar Spirals and the Interstellar Medium in Galactic Disks*.

Wang B., Heckman T. M., 1996. *ApJ*, **457**, 645. *Internal Absorption and the Luminosity of Disk Galaxies*.

Wang J., Fu J., Aumer M., Kauffmann G., Józsa G. I. G., Serra P., Huang M.-l., Brinchmann J., van der Hulst T., Bigiel F., 2014. *MNRAS*, **441**, 2159. *An observational and theoretical view of the radial distribution of H I gas in galaxies*.

Wang L., Dutton A. A., Stinson G. S., Macciò A. V., Penzo C., Kang X., Keller B. W., Wadsley J., 2015. *MNRAS*, **454**, 83. *NIHAO project - I. Reproducing the inefficiency of galaxy formation across cosmic time with a large sample of cosmological hydrodynamical simulations*.

Weaver H. F., 1970. *Some Characteristics of Interstellar Gas in the Galaxy*, In: *Interstellar Gas Dynamics*, 22, ed. Habing H. J.

Weigel A. K., Schawinski K., Bruderer C., 2016. *MNRAS*, **459**, 2150. *Stellar mass functions: methods, systematics and results for the local Universe*.

Weinberg M. D., 1985. MNRAS, **213**, 451. *Evolution of barred galaxies by dynamical friction*.

Weinzirl T., Jogee S., Khochfar S., Burkert A., Kormendy J., 2009. ApJ, **696**, 411. *Bulge n and B/T in High-Mass Galaxies: Constraints on the Origin of Bulges in Hierarchical Models*.

White S. D. M., Rees M. J., 1978. MNRAS, **183**, 341. *Core condensation in heavy halos - A two-stage theory for galaxy formation and clustering*.

Whitmore B. C., Gilmore D. M., 1991. *ApJ*, **367**, 64. *On the interpretation of the morphology-density relation for galaxies in clusters*.

Whitmore B. C., Gilmore D. M., Jones C., 1993. ApJ, **407**, 489. *What determines the morphological fractions in clusters of galaxies?*

Wild V., Groves B., Heckman T., Sonnentrucker P., Armus L., Schiminovich D., Johnson B., Martins L., Lamassa S., 2011. MNRAS, **410**, 1593. *Optical versus infrared studies of dusty galaxies and active galactic nuclei - I. Nebular emission lines*.

Willett K. W., Lintott C. J., Bamford S. P., Masters K. L., Simmons B. D., Casteels K. R. V., Edmondson E. M., Fortson L. F., Kaviraj S., Keel W. C., Melvin T., Nichol R. C., Raddick M. J., Schawinski K., Simpson R. J., Skibba R. A., Smith A. M., Thomas D., 2013. *MNRAS*, **435**, 2835. *Galaxy Zoo 2: detailed morphological classifications for 304 122 galaxies from the Sloan Digital Sky Survey*.

Willett K. W., Schawinski K., Simmons B. D., Masters K. L., Skibba R. A., Kaviraj S., Melvin T., Wong O. I., Nichol R. C., Cheung E., Lintott C. J., Fortson L., 2015. *MNRAS*, **449**, 820. *Galaxy Zoo: the dependence of the star formation-stellar mass relation on spiral disc morphology*.

Williams J. P., Blitz L., McKee C. F., 2000. *Protostars and Planets IV. The Structure and Evolution of Molecular Clouds: from Clumps to Cores to the IMF*.

Wright E. L., Eisenhardt P. R. M., Mainzer A. K., Ressler M. E., Cutri R. M., Jarrett T., Kirkpatrick J. D., Padgett D., McMillan R. S., Skrutskie M., Stanford S. A., Cohen M., Walker R. G., Mather J. C., Leisawitz D., Gautier, III T. N., McLean I., Benford D., Lonsdale C. J., Blain A., Mendez B., Irace W. R., Duval V., Liu F., Royer D., Heinrichsen I., Howard J., Shannon M., Kendall M., Walsh A. L., Larsen M., Cardon J. G., Schick S., Schwalm M., Abid M., Fabinsky B., Naes L., Tsai C.-W., 2010. *AJ*, **140**, 1868. *The Wide-field Infrared Survey Explorer (WISE): Mission Description and Initial On-orbit Performance*.

Yan L., Donoso E., Tsai C.-W., Stern D., Assef R. J., Eisenhardt P., Blain A. W., Cutri R., Jarrett T., Stanford S. A., Wright E., Bridge C., Riechers D. A., 2013. *AJ*, **145**, 55. *Characterizing the Mid-infrared Extragalactic Sky with WISE and SDSS*.

York D. G., Adelman J., Anderson, Jr. J. E., Anderson S. F., Annis J., Bahcall N. A., Bakken J. A., Barkhouser R., Bastian S., Berman E., Boroski W. N., Bracker S., Briegel C., Briggs J. W., Brinkmann J., Brunner R., Burles S., Carey L., Carr M. A., Castander F. J., Chen B., Colestock P. L., Connolly A. J., Crocker J. H., Csabai I., Czarapata P. C., Davis J. E., Doi M., Dombeck T., Eisenstein D., Ellman N., Elms B. R., Evans M. L., Fan X., Federwitz G. R., Fiscelli L., Friedman S., Frieman J. A., Fukugita M., Gillespie B., Gunn J. E., Gurbani V. K., de Haas E., Haldeman M., Harris F. H., Hayes J., Heckman T. M., Hennessy G. S., Hindsley R. B., Holm S., Holmgren D. J., Huang C.-h., Hull C., Husby D., Ichikawa S.-I., Ichikawa T., Ivezić Ž., Kent S., Kim R. S. J., Kinney E., Klaene M., Kleinman A. N., Kleinman S., Knapp G. R., Korienek J., Kron R. G., Kunszt P. Z., Lamb D. Q., Lee B., Leger R. F., Limmongkol S., Lindenmeyer C., Long D. C., Loomis C., Loveday J., Lucinio R., Lupton R. H., MacKinnon B., Mannery E. J., Mantsch P. M., Margon B., McGehee

P., McKay T. A., Meiksin A., Merelli A., Monet D. G., Munn J. A., Narayanan V. K., Nash T., Neilsen E., Neswold R., Newberg H. J., Nichol R. C., Nicinski T., Nonino M., Okada N., Okamura S., Ostriker J. P., Owen R., Pauls A. G., Peoples J., Peterson R. L., Petravick D., Pier J. R., Pope A., Pordes R., Prosapio A., Rechenmacher R., Quinn T. R., Richards G. T., Richmond M. W., Rivetta C. H., Rockosi C. M., Ruthmansdorfer K., Sandford D., Schlegel D. J., Schneider D. P., Sekiguchi M., Sergey G., Shimasaku K., Siegmund W. A., Smee S., Smith J. A., Snedden S., Stone R., Stoughton C., Strauss M. A., Stubbs C., SubbaRao M., Szalay A. S., Szapudi I., Szokoly G. P., Thakar A. R., Tremonti C., Tucker D. L., Uomoto A., Vanden Berk D., Vogeley M. S., Waddell P., Wang S.-i., Watanabe M., Weinberg D. H., Yanny B., Yasuda N., SDSS Collaboration, 2000. AJ, **120**, 1579. *The Sloan Digital Sky Survey: Technical Summary*.

Yuan T., Richard J., Gupta A., Federrath C., Sharma S., Groves B. A., Kewley L. J., Cen R., Birnboim Y., Fisher D. B., 2017. ApJ, **850**, 61. *The Most Ancient Spiral Galaxy: A 2.6-Gyr-old Disk with a Tranquil Velocity Field*.

Zahid H. J., Dima G. I., Kewley L. J., Erb D. K., Davé R., 2012. *ApJ*, **757**, 54. *A Census of Oxygen in Star-forming Galaxies: An Empirical Model Linking Metallicities, Star Formation Rates, and Outflows*.

Zang T. A., 1976. *PhD thesis*, , Massachussetts Institute of Technology, Cambrigde, MA.